

Copyright
by
Nat Ativitavas
2002

**The Dissertation Committee for Nat Ativitavas certifies that this is the approved
version of the following dissertation:**

**ACOUSTIC EMISSION SIGNATURE ANALYSIS OF FAILURE
MECHANISMS IN FIBER REINFORCED PLASTIC STRUCTURES**

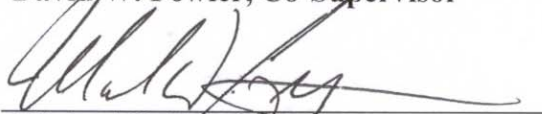
Committee:



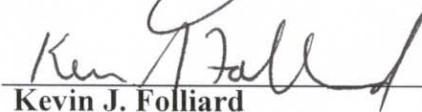
Timothy J. Fowler, Supervisor



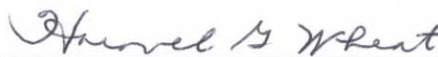
David W. Fowler, Co-Supervisor



Michael D. Engelhardt



Kevin J. Folliard



Harovel G. Wheat

**ACOUSTIC EMISSION SIGNATURE ANALYSIS OF FAILURE
MECHANISMS IN FIBER REINFORCED PLASTIC STRUCTURES**

by

Nat Ativitavas, B.Eng., M.S.

Dissertation

Presented to the Faculty of the Graduate School of

The University of Texas at Austin

in Partial Fulfillment

of the Requirements

for the Degree of

Doctor of Philosophy

The University of Texas at Austin

December 2002

Dedication

To my mother and my father

Acknowledgements

I wish to express my gratitude and appreciation to my advisor, Professor Timothy Fowler, for his guidance, friendship and support throughout this research. His optimistic way of thinking was always a source of motivation for me. It has been an honor working under his supervision. I also thank his wife, Marie, for the support and happiness she provided.

I wish to express my thanks to Dr. Michael Engelhardt who also provided advice and encouragement during the course of this research. I thank Dr. David Fowler, Dr. Kevin Folliard, and Dr. Harovel Wheat for their valuable guidance.

Financial support for this research project was provided by the Texas Department of Transportation. Special thanks to Robert Sarcinella and Paul McDad for all encouragement and friendship received during this period. I also wish to thank the TxDOT staff that provided tremendous technical support, which are Edward Morgan and Michael Dawidczik, James Kosel, Travis Saengerhousen, James Barton, and Kristina Figueroa. I also would like to thank Mike Smith and Agata La Rue for their wonderful guidance.

I wish to express my appreciation to Petroleum Authority of Thailand for financial support and for the opportunity to pursue my doctoral degree.

I also wish to acknowledge the following people who provided instrument, materials, specimens, and technical support:

Mark Carlos of Physical Acoustics Corporation

Carl Ricco of Industrial Pipe and Plastics of Texas, Inc.

Sib Banerjee of Molded Fiber Glass Research Company

Jason Lakes of Dow Chemical Company

Jim Miller and the staff at Austin Waterjet, Inc. and

Blake Stasney, Mike Bell, Dennis Fillip, and the staff at Ferguson Lab.

I would like to thank Brian Tinkey, Matthew Memberg, Lisa Novak, Jenny Tanner, and Anna Boenig for proof reading this dissertation.

I would like to mention my friends who helped me with my work and made my life in Austin enjoyable. To my great friends, Dr. Yajai Promboon (my AE mentor), Jenny Tanner, and Brian Tinkey, for guidance and wonderful moment these years. To Dr. Fernando Ulloa, Professor Paul Ziehl, and Piya Chotickai for technical help, sharing experiences, and friendship.

To all my roommates, Anna, Michele, Jen, Gina, Jenny, and Rubén, as well as my friends in the US, Kan, Taichiro, Jorge, Pachara, Lisa & Rick, Siriporn, and Manoj, who gave me happiness and was always concerned about me.

To Chalamporn Kasetsiri for all the patience, support, laughter, and inspiration she gave me especially during the past two years.

To the Mavichak family, especially Dr. Viroj Mavichak, Neil, and Euay for their motivation and support. To my sister, Pornpat, and brother, Touch, for their encouragement and wonderful help, especially during the last minutes.

And to my parents for their endless love and support throughout my studies in the US. Without them, I would not have made it this far. I love you.

Nat Ativitavas

December, 2002

**ACOUSTIC EMISSION SIGNATURE ANALYSIS OF FAILURE
MECHANISMS IN FIBER REINFORCED PLASTIC STRUCTURES**

Publication No. _____

Nat Ativitavas, Ph.D.

The University of Texas at Austin, 2002

Co-Supervisors: Timothy J. Fowler

David W. Fowler

The objective of the research program was to develop reliable pattern recognition and neural network analysis methods to determine the failure mechanism signatures in fiber reinforced plastic structures from acoustic emission (AE) data.

The AE database was collected from a range of test specimens. Visual inspection and observation with a scanning electron microscope were performed to identify failure mechanisms in the specimens at various load levels. It was found that different types of specimen and structural loading yielded different types of failure. The failure mechanisms of interest were matrix cracking, debonding, delamination, and fiber breakage.

Two methods of analysis were used to determine the AE signatures. The first was visual AE pattern recognition. This analysis used a comparison of dissimilarities among AE correlation plots of data from different specimens. The results showed several AE signatures. The analysis also explains the correlation of material properties to failure mechanism evolution.

The second analysis method was the use of neural networks to perform AE pattern recognition. The neural networks were trained using AE data in order to perform two tasks: determine the failure mechanisms and to assess the damage severity. The performance of the networks was found to be excellent for the first task and promising for the second task.

The neural network was also applied to additional AE data from full-scale and coupon tests. By comparing the results from the network with visually observed damage, the network results are shown to be very reliable in determining failure mechanisms.

Table of Contents

List of Tables	xvi
List of Figures	xix
CHAPTER 1: Introduction	1
1.1 General Background.....	1
1.2 Research Significance.....	3
1.3 Research Methodology.....	4
CHAPTER 2: Background and Literature Review	6
2.1 Fiber Reinforced Plastic.....	6
2.1.1 Materials Constitution.....	6
2.1.1.1 Fibers.....	6
2.1.1.2 Resins.....	8
2.1.2 Manufacturing.....	9
2.1.2.1 Hand Lay-up.....	9
2.1.2.2 Pultrusion.....	9
2.1.2.3 Filament Winding.....	10
2.1.3 Failure Mechanisms in Composites.....	11
2.1.4 Failure Progression.....	13
2.1.5 Fiber Breakage Study.....	16
2.2 Nondestructive Inspection of Fiber Reinforced Plastics.....	19
2.2.1 Introduction.....	19
2.2.2 NDT Methods.....	20
2.2.2.1 Radiography.....	20
2.2.2.2 Magnetic Particle.....	20
2.2.2.3 Ultrasonics.....	21
2.2.2.4 Liquid Penetrant.....	21
2.2.2.5 Eddy Current.....	21

2.2.2.6 Leak Testing.....	22
2.2.2.7 Acoustic Emission.....	22
2.2.2.8 Visual Examination.....	22
2.2.3 Causes of Damage to FRP Structures.....	22
2.2.3.1 Mechanical.....	22
2.2.3.2 Chemical Attack.....	23
2.2.3.3 Environmental Exposure.....	23
2.2.3.4 Fabrication Effects.....	23
2.2.4 Failure Rate.....	23
2.2.5 Factors Affecting NDT Performance.....	24
2.2.5.1 Human Factors.....	24
2.2.5.2 Method Selection.....	25
2.2.5.3 Qualifications of NDT Personnel.....	26
2.3 Acoustic Emission.....	26
2.3.1 Introduction.....	26
2.3.2 Acoustic Emission Applications.....	27
2.3.3 Instrumentation.....	29
2.3.3.1 AE sensors.....	29
2.3.3.2 Preamplifier.....	31
2.3.3.3 AE Data Acquisition.....	31
2.3.4 AE Parameters.....	31
2.3.4.1 Basic AE Parameters.....	32
2.3.4.2 Modified Parameters.....	35
2.3.5 Correlation Plots.....	38
2.3.5.1 Amplitude Distribution.....	38
2.3.5.2 Cumulative Amplitude Distribution.....	39
2.3.5.3 Amplitude vs Duration Plot.....	43
2.3.5.4 Cumulative Signal Strength vs. Load (or Hits).....	44

2.3.6 Literature Review.....	45
2.3.6.1 Literature Review of Source Identification in FRP Based of b-Value.....	45
2.3.6.2 Literature Review of Source Identification in FRP Based on AE Parameters.....	49
2.4 Neural Networks.....	68
2.4.1 Introduction.....	68
2.4.2 Artificial Networks.....	69
2.4.3 Bias.....	71
2.4.4 Activation Function.....	71
2.4.5 Training.....	73
2.4.6 Backpropagation Neural Networks.....	74
2.4.6.1 Network Architecture.....	74
2.4.6.2 Delta Rule.....	78
2.4.7 Probabilistic Neural Networks.....	79
2.4.7.1 Bayes Decision Strategy.....	79
2.4.7.2 Constructing PDFs.....	81
2.4.7.3 Network Architecture.....	84
2.4.8 Literature Review of Neural Networks.....	85
2.4.8.1 Literature Review of Backpropagation Networks.....	85
2.4.8.2 Literature Review of Neural Network/pattern Recognition for Failure Mechanism Classification.....	86
2.4.8.3 Literature Review of PNN.....	90
2.5 Summary.....	91
CHAPTER 3: Materials and Instrumentations.....	94
3.1 Materials.....	94
3.2 AE Instrumentations.....	98
3.2.1 AE Data Acquisition System.....	98

3.2.2 AE Sensors.....	100
3.3 Testing Facilities.....	101
CHAPTER 4: Fiber Breakage.....	106
4.1 Low Amplitude Filtering Technique.....	106
4.1.1 Concept of Technique.....	106
4.1.2 Experimental Program.....	109
4.1.3 Physical Results.....	112
4.1.4 SEM Results.....	112
4.1.5 AE Results.....	126
4.1.6 Discussion.....	129
4.2 Experimental Program for Fiber Breakage Database.....	133
4.2.1 Experimental Program.....	133
4.2.1.1 Coupon Specimens.....	133
4.2.1.2 Full-Scale Specimens.....	137
4.2.2 Results.....	142
4.2.2.1 Coupon Specimens.....	142
4.2.2.2 Full-Scale Specimen Results.....	149
4.2.3 Discussion.....	157
4.3 Summary.....	162
CHAPTER 5: Matrix Cracking and Debonding.....	163
5.1 SEM Study.....	163
5.1.1 Experimental Program.....	164
5.1.2 Physical Results.....	166
5.1.3 SEM Results.....	167
5.1.4 AE Results.....	175
5.1.5 Discussion.....	176
5.2 Experimental Program for Fiber Breakage Database.....	178
5.2.1 Experimental Program.....	178

5.2.2 Results.....	181
5.2.3 Discussion.....	186
5.3 Summary.....	189
CHAPTER 6: Delamination and Additional Specimens with	
Unknown Failure Mechanisms.....	191
6.1 Delamination.....	192
6.1.1 Short Beam Shear Test.....	192
6.1.1.1 Experimental Program.....	192
6.1.1.2 Physical Results.....	195
6.1.1.3 Visual and SEM Observation.....	199
6.1.1.4 AE Results.....	202
6.1.1.5 Discussion.....	204
6.1.2 Tension Test of “T” Specimens.....	206
6.1.2.1 Experimental Program.....	207
6.1.2.2 Physical Results.....	209
6.1.2.3 AE Results.....	213
6.1.2.4 Discussion.....	214
6.2 Additional Specimens with Unknown Failure Mechanism Evolution.....	215
6.2.1.1 Specimens Subjected to Compression Loading.....	216
6.2.1.2 Specimen SW2 Subjected to Four-Point Bending Test.....	219
6.2.1.3 Chopped Strand Fiber and Woven Roving FRP	
Coupons Subjected to Direct Tension Test.....	227
6.3 Summary.....	235
CHAPTER 7: Visual Pattern Recognition.....	237
7.1 Organization.....	237
7.2 The Plots for Visual Pattern Recognition.....	240
7.3 Discussion.....	274

7.3.1 Stress vs. Strain.....	274
7.3.2 Amplitude vs. Time or Load.....	276
7.3.3 Amplitude Distribution.....	278
7.3.4 Progression of Amplitude Distribution.....	279
7.3.5 Cumulative Amplitude Distribution.....	281
7.3.6 Progression of Cumulative Amplitude Distribution.....	282
7.3.7 Cumulative Hits vs. Load, Cumulative Signal Strength vs. Load, and Historic Index vs. Load.....	285
7.3.8 Amplitude vs. Duration.....	287
7.3.9 Duration Distribution.....	290
7.3.10 Duration Distribution of High Amplitude Hits.....	290
7.3.11 Signal Strength Distribution.....	292
7.3.12 Signal Strength Distribution of High Amplitude Hits.....	292
7.3.13 Rise Time Distribution.....	293
7.4 Summary.....	296
CHAPTER 8: Neural Networks for AE Pattern Recognition.....	300
8.1 Preliminary Neural Network System.....	300
8.1.1 Primary Networks.....	302
8.1.1.1 Primary Network Organization.....	303
8.1.1.2 Results of Primary Neural Networks.....	320
8.1.2 Secondary Neural Network.....	329
8.1.2.1 Secondary Network Organization.....	329
8.1.2.2 Results of Secondary Networks.....	331
8.2 Failure Mechanism Determination of Additional Specimens Using Neural Network.....	332
8.3 Final Network System.....	337
8.3.1 Final Network System for Determination of Failure Mechanisms.....	338

8.3.2 Final Network System for Determination of Damage Severity..	339
8.3.2.1 Primary and Secondary Network Organization of Final Network.....	339
8.3.2.2 Testing Results of Final Primary and Secondary Networks.....	343
8.4 Summary.....	345
CHAPTER 9: Neural Network Applications.....	349
9.1 Trapezoidal Girder.....	349
9.1.1 Test Setup and Instrumentations.....	349
9.1.2 Test Results.....	356
9.1.3 Failure Mechanism and Damage Severity Determined by Neural Networks.....	359
9.2 Rail Shear Tests.....	366
9.2.1 Test Setup and Instrumentations.....	366
9.2.2 Test Results.....	368
9.2.3 Failure Mechanism and Damage Severity Determined by Neural Networks.....	373
9.3 Comparison of Damage Severity Determination.....	377
9.4 Summary.....	384
CHAPTER 10: Summary and Conclusions.....	386
10.1 Summary.....	386
10.2 Significant Findings.....	388
10.2.1 AE Database Collection.....	388
10.2.2 AE Visual Pattern Recognition.....	390
10.2.3 Neural Network for AE Pattern Recognition.....	393
10.3 Directions for Future Research.....	396
References.....	397
VITA.....	413

List of Tables

Table 2.1	Physical Properties of FRP Compared with Concrete and Steel.....	7
Table 2.2	Physical Properties of Glass and Carbon Fibers.....	8
Table 2.3	K Value for Historic Index.....	36
Table 2.4	J Value for Severity.....	37
Table 2.5	AE Characteristics of Equipment Damage.....	53
Table 2.6	Feature Extraction.....	89
Table 4.1	Summary of Test Program.....	111
Table 4.2	Summary of AE Results Including Load and Total Number of AE Hits.....	126
Table 4.3	Material Information and Specimen Dimensions (inches).....	134
Table 4.4	Summary of Ultimate Stress, Ultimate Strain, and Elastic Modulus of Specimens.....	143
Table 4.5	Summary of AE Data.....	146
Table 4.6	Summary of Total AE Hits.....	152
Table 4.7	Summary of Low Amplitude Filtering Results.....	158
Table 5.1	Summary of the Test Program.....	165
Table 5.2	Summary of the Test Results.....	167
Table 5.3	Summary of Total Number of AE Hits of Each Specimen.....	175
Table 5.4	Material Information and Specimen Dimensions (inches).....	179
Table 5.5	Summary of AE Data.....	186
Table 6.1	Material Information and Specimen Dimensions (inches).....	193
Table 6.2	Summary of Short Beam Shear Test Results.....	199
Table 6.3	Summary of AE Data.....	203
Table 6.4	Summary of the Test Results.....	209
Table 6.5	Summary of Total AE Hits.....	213

Table 6.6	Summary of Ultimate Load and AE Data.....	218
Table 6.7	Number of AE Hits of Sensors 7,11, and 15 of Specimen SW2.....	226
Table 7.1	Specimen Summary for Research Program Database.....	238
Table 7.2	Summary of Representative Specimens and Basic Properties.....	241
Table 7.3	Summary of b-Value of Failure Mechanisms Found in Research Program.....	285
Table 7.4	Summary of Knee from Cumulative Hits vs. Load, Cumulative Signal Strength vs. Load, and Historic Index Plots.....	286
Table 7.5	Summary of Duration Range of Each Type of Specimens.....	291
Table 7.6	Summary of Duration Range of High Amplitude Hits from Each Type of Specimens.....	292
Table 7.7	Summary of Range of Signal Strength from Each Type of Specimens.....	292
Table 7.8	Summary of Signal Strength Range of High Amplitude Hits from Each Type of Specimen.....	293
Table 8.1	Specimen Summary for Neural Network.....	306
Table 8.2	Linear Conversion Table for Amplitude vs. Duration.....	314
Table 8.3	Log Conversion Table for Amplitude vs. Duration.....	315
Table 8.4	Summary of Primary Neural Network Testing Performance.....	321
Table 8.5	Summary of Secondary Neural Network Testing Performance.....	332
Table 8.6	Failure Mechanism Determination of Specimens BHV1, BHV2,BHV3, and SW2.....	334

Table 8.7	Failure Mechanism Determination of Specimen Chop and Wov.....	335
Table 8.8	Testing Performance of Final Primary and Secondary Networks.....	339
Table 8.9	Summary of Testing Performance of Final Primary Neural Networks (with Load Level Determination).....	343
Table 8.10	Testing Performance of Final Secondary Network.....	344
Table 9.1	Network Determination of Sensors 13 and 15.....	360
Table 9.2	Network Determination of Sensors 7 and 14 of Specimen TK1.....	365
Table 9.3	Physical Results of Three-Rail Shear Test.....	369
Table 9.4	Network Determination of Three-Rail Shear Specimens.....	374
Table 9.5	Network Determination of Sensors 13 and 15 of Specimen TK1.....	378
Table 9.6	Network Determination of Sensors 7 and 14 of Specimen TK1.....	379
Table 9.7	Network Determination of Three-Rail Shear Specimens.....	380
Table 10.1	Summary of b-Values of Failure Mechanisms Found in Research Program.....	393

List of Figures

Figure 2.1	Schematic Illustration of Pultrusion Process.....	10
Figure 2.2	Schematic of Filament Winding (Classic Helical) Process.....	11
Figure 2.3	Schematic Illustration of Failure Mechanisms in Composites...	12
Figure 2.4	Single and Multiple Fracture.....	14
Figure 2.5	Failure Progressive Diagram.....	15
Figure 2.6	Tensile Failure Model for the Cumulative Fracture of Fibers...	16
Figure 2.7	Typical Failure Rate Curve.....	24
Figure 2.8	Acoustic Emission Instrument.....	30
Figure 2.9	Acoustic Emission Waveform Parameters.....	32
Figure 2.10	Example of Historic Index Superimposed with Cumulative Signal Strength and Loading Profile vs. Time of Glass FRP Specimen Tested in Tension.....	37
Figure 2.11	Differential Amplitude Distribution of Fiber Glass Composite Tensioned Perpendicular to the Fiber Direction.....	39
Figure 2.12	Cumulative Amplitude Distribution Plot.....	40
Figure 2.13	Amplitude vs. Duration Plot Showing Good Data and Two Types of Unwanted Noise.....	43
Figure 2.14	Normalized Cumulative Signal Strength vs. Normalized Load Plot of Fiber Glass Composite Loaded in Tension Perpendicular to the Fiber Direction.....	44
Figure 2.15	Variation of the Coefficient b_1 as a Function of θ for the Unidirectional and Crossply Composites.....	46
Figure 2.16	Plot of Distribution Function Corresponding to the Modified Power Law Showing the Effect of the Parameters b and x_a	48
Figure 2.17	Three Different Types of Amplitude Distribution.....	51

Figure 2.18	Duration and Rise Time Distribution Plot After Removing Hits from Matrix Cracking.....	54
Figure 2.19	Four Types of Specimens from Li's Research.....	57
Figure 2.20	AE Waveform of SiC Fiber/Metallic Matrix Composite.....	59
Figure 2.21	Force vs. Displacement Diagram from the Fiber Pull-Out Tests.....	60
Figure 2.22	Amplitude Distribution Plot of Fiberglass Showing Triple Peaks.....	61
Figure 2.23	C-Ratio vs. Stress for Kevlar Epoxy Composite Loaded in Tension.....	62
Figure 2.24	Proposed New Technique to Present Amplitude Distribution...	64
Figure 2.25	Illustration Description of Energy Moment T_{em}	67
Figure 2.26	Basic Architecture of a Simple Neural Network.....	70
Figure 2.27	Artificial Neuron.....	70
Figure 2.28	Binary Step Function.....	72
Figure 2.29	Binary Sigmoid Function.....	72
Figure 2.30	Bipolar Sigmoid Function.....	73
Figure 2.31	Backpropagation Neural Network with One Hidden Layer.....	75
Figure 2.32	Simplified Diagram Showing Local and Global Minimums of Neural Network Performance.....	77
Figure 2.33	Decision Function for a One Dimensional Data, x	80
Figure 2.34	Effect of Smoothing Parameter on a Two Dimensional PDF...	83
Figure 2.35	Probabilistic Neural Network Architecture Having a p Dimensions, m Training Samples, and 2 Categories.....	85
Figure 3.1	Glass Fiber Reinforced Isophthalic Polyester Pultruded Beam (FG).....	95
Figure 3.2	Layer Arrangement of FG Beam.....	95
Figure 3.3	Glass Fiber Reinforced Vinyl Ester Pultruded Beam (IKG).....	96

Figure 3.4	Carbon and Glass Fiber Reinforced Vinyl Ester Pultruded Beam (SW).....	97
Figure 3.5	Transportation Instrument.....	99
Figure 3.6	MISTRAS System.....	99
Figure 3.7	AE Sensors and External Preamplifier.....	101
Figure 3.8	Universal Testing Machine 600HVL.....	102
Figure 3.9	Four-Point Loading Frame for Coupon Specimens.....	103
Figure 3.10	Full-Scale Loading Frame.....	103
Figure 3.11	Universal Testing Machine, Instron 4208.....	104
Figure 3.12	Scanning Electron Microscope, Hitachi S-3200N.....	105
Figure 4.1	Idealized Schematic Plots of Normalized Cumulative Hits and Signal Strength vs. Load.....	108
Figure 4.2	Coupon Specimen.....	110
Figure 4.3	Test Setup.....	111
Figure 4.4	Maximum Stresses and Strains of the Specimens L1 to L5....	112
Figure 4.5	Typical View of Fibers and Matrix of Specimen L1 Before Testing.....	113
Figure 4.6	Typical Damages on Specimen L1 Before Testing.....	114
Figure 4.7	View of the Side of Specimen L1 Showing Damage from Waterjet Cut and Air Voids Around a Stitch.....	115
Figure 4.8	Typical Matrix Cracks Observed in Specimen L1.....	116
Figure 4.9	Fiber Breakage in the Specimen L1.....	117
Figure 4.10	Matrix Cracking with Larger Crack Openings of Specimen L2.....	118
Figure 4.11	Fiber Breakage Continued with Matrix Cracking in Specimen L2.....	119
Figure 4.12	Overview of Specimen L2.....	119
Figure 4.13	Fiber Breakage and Fiber/Matrix Debonding in Specimen L3	120

Figure 4.14	Overview of Specimen L3.....	121
Figure 4.15	Fiber Breakage Associated with Fiber/Matrix Debonding in Specimen L4.....	122
Figure 4.16	Fiber Breaks with Several Matrix Cracks in Specimen L4.....	123
Figure 4.17	Overview of Specimen L4.....	123
Figure 4.18	Visible Fiber Breakage in Specimen L5.....	124
Figure 4.19	Overview of Specimen L5.....	125
Figure 4.20	A Side of Specimen L5 Showing Delamination.....	125
Figure 4.21	Cumulative Signal Strength vs. Load for All Specimens.....	127
Figure 4.22	Amplitude vs. Load Plot.....	128
Figure 4.23	Plot of Cumulative Hits vs. Load Before and After Filtering...	131
Figure 4.24	Number of Fiber Breaks Plot from Zweben's Study and from Cumulative High Amplitude Hits.....	132
Figure 4.25	Representative Samples for Coupon Tension Test.....	135
Figure 4.26	Sensor Locations on the Specimen.....	136
Figure 4.27	Test Setup of Coupon Specimens.....	137
Figure 4.28	Specimen FGV.....	138
Figure 4.29	Four-Point Bending Test Specimen.....	139
Figure 4.30	Specimen FGI with Increased Buckling Resistance.....	140
Figure 4.31	Test Setup of Beam FGV.....	141
Figure 4.32	Sensor Locations on Specimen FGI.....	141
Figure 4.33	Stress-Strain Curves for All Specimens.....	142
Figure 4.34	Tensile Failure of the Specimens.....	144
Figure 4.35	Tensile Failure and Delamination on the Side of Specimen LGV1.....	145
Figure 4.36	Fiber Breakage on Specimen LGI1.....	145

Figure 4.37	Visual Damage Evolution on Specimen LGI2 Corresponding with AE Amplitude/Cumulative Signal Strength vs. Normalized Load.....	147
Figure 4.38	Amplitude Superimposed with Cumulative Signal Strength vs. Load.....	148
Figure 4.39	Beam FGI at Failure.....	149
Figure 4.40	Bottom Flange at Failure of Beam FGI.....	150
Figure 4.41	Beam FGV at Failure.....	150
Figure 4.42	Load Deflection Response at Midspan.....	151
Figure 4.43	First Observed Crack at the Circular Hole.....	153
Figure 4.44	Crack on Side of Bottom Flange.....	154
Figure 4.45	Additional Crack at Bottom Flange.....	154
Figure 4.46	Shear Failure (During the Load Hold).....	155
Figure 4.47	Amplitude Superimposed with Cumulative Signal Strength vs. Load of Break FGV.....	156
Figure 4.48	Amplitude Superimposed with Cumulative Signal Strength (with a Smaller Range) vs. Load of Beam FGV.....	156
Figure 4.49	Amplitude Superimposed with Cumulative Signal Strength vs. Load of Beam FGI.....	157
Figure 4.50	Summary of Failure Mechanisms of Specimen LGV.....	159
Figure 4.51	Number of Fiber Breaks Plots from Zweben's Study and from Cumulative High Amplitude Hits.....	160
Figure 5.1	Coupon Specimen.....	165
Figure 5.2	Test Setup of Coupon Specimen.....	166
Figure 5.3	Loading Geometry of Coupon Specimen.....	166
Figure 5.4	Crack at Ultimate Load.....	167
Figure 5.5	Cracks at the Edge of Specimen T1.....	168
Figure 5.6	Broken matrix Shell.....	169

Figure 5.7	Illustration of Cross Section Showing Failure Mechanisms Associated with Matrix Shells.....	169
Figure 5.8	Cracks at the Edge of Specimen T2.....	170
Figure 5.9	Broken Matrix Shell.....	171
Figure 5.10	Crack Opening of Specimen T3.....	172
Figure 5.11	Crack from the Side View of Specimen T3.....	172
Figure 5.12	Fiber Break Inside Crack of Specimen T3.....	173
Figure 5.13	View of Cross Section Showing Matrix Cracking and Air Voids.....	173
Figure 5.14	Pure Matrix and Shell Cracks.....	174
Figure 5.15	Fine Crack Near Edge of Specimen T3.....	175
Figure 5.16	Hit Amplitude vs. Strain Plot.....	176
Figure 5.17	Representative Samples for Coupon Tension Test.....	180
Figure 5.18	Sensor Location on the Specimen.....	181
Figure 5.19	Stress-Strain Curves of Tension Tests.....	182
Figure 5.20	Tensile Failure on Specimen TGI2.....	183
Figure 5.21	Tensile Fracture and Multiple Crazeing of Specimen TGV.....	184
Figure 5.22	SEM View of the Fracture of Specimen TGI1.....	185
Figure 5.23	Amplitude Superimposed with Cumulative Signal Strength vs. Load (Normalized).....	187
Figure 5.24	Summary of Failure Mechanisms.....	189
Figure 6.1	Glass Fiber/Vinyl Ester Specimen.....	193
Figure 6.2	Short Beam Shear Test Setup of Specimen SGI1.....	194
Figure 6.3	Loading Geometry of Short Beam Shear Test.....	195
Figure 6.4	Glass/Isophthalic Polyester Specimen at Failure.....	196
Figure 6.5	Glass/Vinyl Ester Specimen at Failure.....	196
Figure 6.6	Hybrid/Vinyl Ester Specimen at Failure.....	197

Figure 6.7	Stress vs. Strain Relationship of Representative Glass Fiber/Isophthalic Polyester Specimen (Specimen SGI3).....	197
Figure 6.8	Stress vs. Strain Relationship of Representative Glass Fiber/Vinyl Ester specimen (Specimen SGV3).....	198
Figure 6.9	Stress vs. Strain Relationship of Representative Hybrid/Vinyl Ester Specimen (Specimen SHV3).....	198
Figure 6.10	Failure Surface of Specimen SGI1 After Breaking Off.....	200
Figure 6.11	Fiber Breaks in Specimen SGI1.....	201
Figure 6.12	SEM Photo Showing Fiber Imprint (Debonding) and Matrix Cracking of Specimen SGI1.....	201
Figure 6.13	SEM Photo Showing Fiber Breaks of Specimen SGI1.....	202
Figure 6.14	Amplitude Superimposed with Cumulative Signal Strength vs. Load of Representative Specimens.....	204
Figure 6.15	Summary of Failure Mechanisms on Amplitude Superimposed with Cumulative Signal Strength vs. Load of Representative Specimens.....	206
Figure 6.16	“T” Sample.....	207
Figure 6.17	“T” Specimen Dimensions.....	208
Figure 6.18	“T” Specimen Test Setup.....	209
Figure 6.19	First Crack of Specimen Tee1.....	210
Figure 6.20	Crack Propagation of Specimen Tee1.....	211
Figure 6.21	Opening of Entire Bonding Interface of Specimen Tee1.....	211
Figure 6.22	Wide Opening of the Interface Showing Fiber Bridging from Upper Portion to Lower Portion of Specimen Tee1.....	212
Figure 6.23	Bonding Surface After the Test of Specimen Tee1.....	212
Figure 6.24	Amplitude Superimposed with Load vs. Time.....	214
Figure 6.25	Summary of Failure Mechanisms of Representative Tee Specimen.....	215

Figure 6.26	Compression Buckling Specimen, Dimension and Test Setup.....	216
Figure 6.27	Specimen BHV2 Showing Web Buckling Test Failure.....	217
Figure 6.28	Amplitude Superimposed with Normalized Load vs. Time of Specimen BHV1.....	218
Figure 6.29	Four-Point Bending Test Setup and Dimensions of Specimen SW2.....	220
Figure 6.30	AE Sensor Locations on Specimen SW2.....	221
Figure 6.31	AE Sensor Locations on Specimen SW2.....	222
Figure 6.32	Specimen SW2 During Testing.....	223
Figure 6.33	Specimen SW2 Load-Deflection Relationship.....	223
Figure 6.34	Specimen SW2 Top Flange Early Delamination.....	224
Figure 6.35	Delamination at Top Flange of Specimen SW2.....	224
Figure 6.36	Delamination at Top Flange of Specimen SW2 Where Buckling Occurred.....	225
Figure 6.37	Amplitude Superimposed with Normalized vs. Time of Specimen SW2.....	226
Figure 6.38	Dimension of Specimens Chop and Wov.....	227
Figure 6.39	Specimen Chop (Chopped Strand Fiber Structure).....	228
Figure 6.40	Specimen Wov (Woven Roving Fiber Structure).....	228
Figure 6.41	Stress vs. Displacement Plot of Specimen Chop.....	229
Figure 6.42	Stress vs. Displacement Plot of Specimen Wov.....	230
Figure 6.43	Tensile Failure of Specimen Chop.....	231
Figure 6.44	Fracture of Specimen Chop Showing Delamination and Surrounding Matrix Cracking.....	231
Figure 6.45	Delamination at Other End of Narrowed Section of Specimen Chop.....	232
Figure 6.46	Tensile Failure of Specimen Wov.....	233

Figure 6.47	Fracture and Longitudinal Delamination of Specimen Wov...	233
Figure 6.48	Amplitude Superimposed with Cumulative Signal Strength vs. Load of Specimen Chop.....	234
Figure 6.49	Amplitude Superimposed with Cumulative Signal Strength vs. Load of Specimen Wov.....	235
Figure 7.1	Display of a Series of One Correlation Plots.....	239
Figure 7.2	Pictures of Test Specimens.....	242
Figure 7.3	Stress vs. Strain of Representative Specimens.....	244
Figure 7.4	Amplitude vs. Time (or Load) of Representative Specimens.....	246
Figure 7.5	Amplitude Distribution of Representative Specimens.....	248
Figure 7.6	Progression of Amplitude Distribution of Representative specimen.....	250
Figure 7.7	Cumulative Amplitude Distribution of Representative Specimens.....	252
Figure 7.8	Progression of Cumulative Amplitude Distribution of Representative Specimen.....	254
Figure 7.9	Cumulative Hits vs. Load of Representative Specimens.....	256
Figure 7.10	Cumulative Signal Strength vs. Load of Representative Specimens.....	258
Figure 7.11	Historic Index vs. Load of Representative Specimens.....	260
Figure 7.12	Amplitude vs. Duration of Representative Specimens.....	262
Figure 7.13	Duration Distribution of Representative Specimens.....	264
Figure 7.14	Duration Distribution of High Amplitude Hits of Representative Specimens.....	266
Figure 7.15	Signal Strength Distribution of Representative Specimens.....	268
Figure 7.16	Signal Strength Distribution of High Amplitude Hits of Representative Specimens.....	270

Figure 7.17	Rise Time Distribution of Representative Specimens.....	272
Figure 7.18	Example of How to Calculative the b-Value or Slope of Cumulative Amplitude Distribution Plot.....	283
Figure 7.19	Progression of Amplitude vs. Duration Plot for Specimen LGI1 at Different Loads.....	289
Figure 7.20	Progression of Rise Time Distribution of Specimen LGI1, Sensor 1.....	294
Figure 7.21	Rise Time vs. Amplitude Plot of Specimen LGI1.....	295
Figure 7.22	Rise Time vs. Duration Plot of Specimen LGI1.....	295
Figure 7.23	Rise Time vs. Signal Strength of Specimen LGI1.....	296
Figure 8.1	Flow Chart of Network System Consisting of Primary and Secondary Neural Network.....	302
Figure 8.2	Typical Primary Neural Network Diagram.....	303
Figure 8.3	Process of Preparing Input Data for a Primary Network.....	307
Figure 8.4	Transformation of Normalized Amplitude Distribution Plot to Data Array.....	309
Figure 8.5	Amplitude vs. Duration Plot Mapped by 12x14 Matrix.....	311
Figure 8.6	12x14 Matrix containing Numbers of Hits that Fall into Amplitude and Duration Intervals.....	311
Figure 8.7	12x14 Matrix Normalized by Total Number of Hits.....	312
Figure 8.8	Cells Used as Input Neurons for Networks. Shaded Cells (Low Amplitude/High Duration and High Amplitude/ Long Duration) are not Used.....	313
Figure 8.9	Transformation of Matrix of Specimen TGI2 at Ultimate Load into Data Array.....	313
Figure 8.10	Original Values vs. Values Used in Amplitude vs. Duration Network with Linear Conversion.....	315

Figure 8.11	Original Values vs. Values Used in Amplitude vs. Duration Network with Log Conversion.....	316
Figure 8.12	Transformation of Historic Index vs. Load and Severity vs. Load Plot into Data Arrays.....	317
Figure 8.13	Waveform Centroid and Waveform Centriod Ratio Parameters.....	319
Figure 8.14	Example of a Waveform Centroid Distribution Plot.....	320
Figure 8.15	Overall Performance of Primary Neural Networks Trained by Backpropagation and PNN.....	324
Figure 8.16	Primary Network Performance for Each Failure Mechanism Combination.....	326
Figure 8.17	Secondary Neural Network Diagram.....	330
Figure 8.18	Amplitude Superimposed with Cumulative Signal Strength vs. Load Plot of Specimen Chop Showing Failure Mechanisms Determined by Neural Network.....	336
Figure 8.19	Amplitude Superimposed with Cumulative Signal Strength vs. Load Plot of Specimen Wov Showing Failure Mechanisms Determined by Neural Network and Its Correction.....	337
Figure 8.20	First Scheme of Primary Network Using AE data and Material Information as Network Input.....	340
Figure 8.21	Second Scheme of Primary Network Using AE data, Material, and Failure Mechanism Information as Network Input.....	341
Figure 8.22	Third Scheme of Primary Network Only Using Data From 0% to 70% of Ultimate Load.....	342
Figure 8.23	Performance of Final Network for Failure Mechanism Determination.....	347

Figure 8.24	Performance of Final Network for Level of Load Determination.....	348
Figure 9.1	Dimensions of Specimen TK1.....	351
Figure 9.2	Specimen TK1 Cross Sections.....	352
Figure 9.3	Bracing FRP Tubes of Specimen TK1.....	353
Figure 9.4	Tree Bracing Steel Rods on Specimen TK1.....	353
Figure 9.5	Carpenter Clamp on Specimen TK1.....	354
Figure 9.6	Specimen Test Setup.....	354
Figure 9.7	Specified Load Schedule.....	355
Figure 9.8	Sensor Locations of Specimen.....	355
Figure 9.9	Load-Deflection Response at Midspan.....	356
Figure 9.10	Buckling Delamination at Top Flange (East Side).....	357
Figure 9.11	Cracks Under Top Flange Where Delamination Occurred.....	357
Figure 9.12	Cracks at Steel Rod (East Side).....	358
Figure 9.13	Cracks at Web Where Web Joins Bottom Flange of Girder.....	358
Figure 9.14	Illustration of Damage Propagation on East Side of Girder....	362
Figure 9.15	Three-Rail Shear Test Setup (ASTM D 4255).....	367
Figure 9.16	Specimen Layout and Dimensions.....	368
Figure 9.17	Shear Stress vs. Strain Curve of Specimen SHEAR2.....	370
Figure 9.18	Shear Stress vs. Strain Curve of Specimen SHEAR3.....	370
Figure 9.19	Specimen SHEAR2 After Testing.....	371
Figure 9.20	Specimen SHEAR3 After Testing.....	371
Figure 9.21	Autopsy of Specimen SHEAR3 Showing Interior Inclined Crack and Exterior Vertical and Horizontal Crack.....	372
Figure 9.22	Amplitude vs. Load Plot of Specimen SHEAR1.....	375
Figure 9.23	Amplitude vs. load Plot of Specimen SHEAR3.....	376

Figure 9.24	Comparison of Backpropagation Network Results with Peak Hold, PNN Network Results with Peak Hold, and Theory of Specimen TK1.....	382
Figure 9.25	Comparison of Backpropagation Network Results with Peak Hold, PNN Network Results with Peak Hold, and Theory of Specimen SHEAR1 and SHEAR 3.....	383

CHAPTER 1

Introduction

1.1 GENERAL BACKGROUND

Fiber reinforced plastic (FRP) is a constantly developing material combining two desired qualities: the strength of fibers and durability of resin. FRP is well known for having high corrosion resistance, and high strength-to-weight ratio. Accordingly, this material has been used in many applications that require these benefits. Typical examples of FRP construction are tanks, pressure vessels, vehicle components, and military airplanes. Bridges, and highway structures are also FRP applications, but are only economically practical in corrosive environments. In Texas, two structural applications, short span bridge members and concrete reinforcing bars are being implemented.

Initially, FRP equipment had a poor in-service performance record. This was due to many factors such as improper design, poor quality manufacturing, and in-service abuse (Fowler and Gray, 1979). Experience has shown that using nondestructive testing (NDT) for quality control of FRP components, and for periodic in-service inspection of structures has greatly improved the performance record, and is necessary for successful use of FRP.

Many nondestructive techniques have been used for FRP inspection. However, several nondestructive techniques are not suitable for field use. This is because some techniques work well only in the laboratory environment but not in the field. Other techniques can be used only for a specific purpose and cannot be used for general applications. Some require a traffic interruption and highly experienced operators. Other techniques are time-consuming, which makes them

very expensive for large structures. Over the past twenty years, new technologies have been developed and introduced leading to more reliable methods, better inspection, and safer operation. One of the major successes of the new nondestructive techniques is acoustic emission.

Acoustic emission (AE) is used to detect stress waves generated by structural discontinuities. AE is considered a “global method” since the entire structure is evaluated by a single test. The method is fast, less labor intensive than competitive evaluation techniques and, in many cases, able to be performed without a service shutdown. These qualities have led to widespread adoption of AE as a practical method of assuring the structural integrity of FRP structural components. In 1978, the Committee on Acoustic Emission from Reinforced Plastics (CARP) was formed by the Society of the Plastics Industry, Inc. (SPI). With the effort of the committee members, which consisted of a number of chemical companies, fiberglass equipment fabricators, materials suppliers, instrument manufacturers, and academic and research institutions, the CARP Recommended Practice was published in 1982 (CARP, 1982). The CARP Recommended Practice has been used successfully and has shown excellent results. This led to the development of additional standards, which use AE as a primary test for FRP tank, pressure vessel inspection (ASME Section V, Article 11, ASME Section X), highway tankers (ASNT, 1993), manlifts (ASTM F 914), and cooling tower fan blades (ASTM E 2076). AE is also used in other ASTM procedures such as ASTM E 1067 and ASTM E 1118 (for FRP tanks/vessels and for thermosetting resin pipe, respectively). In addition, a number of researchers have used AE as a laboratory tool to study the behavior of FRP materials (Ziehl, 2000).

Currently, AE is found to be a reliable and cost effective method for use with FRP components and has developed into a mature technology. AE

instruments, including hardware and software, are constantly being upgraded. Other nondestructive methods, which are complementary to AE can also be used to perform follow-up local inspection.

1.2 RESEARCH SIGNIFICANCE

Currently, there are several standard procedures for assessing the significance of defects detected by acoustic emission. Examples are the American Society of Mechanical Engineers Code (ASME Section V, Article 11 and ASME Section X) and the American Society for Nondestructive Testing Recommended Practice (CARP, 1999). One drawback of these procedures is that none of them provides a method to determine the type and size of defects. If this information is needed, other methods such as ultrasonic, radiography, or impact echo must be used to accurately measure the size and identify the defect types. Unfortunately, these local NDT methods are slow and labor intensive.

It would be ideal for AE testing to be able to identify defect types. This would be especially beneficial for composite material where several local methods such as eddy current, magnetic, and thermography cannot easily be applied. There is an indication that AE testing has this potential. Research has shown that each type of defect exhibits different AE characteristics. Many techniques such as graphical visualization and neural networks (see Chapter 2, Section 2.4 for more details) have been applied to AE data to perform pattern recognition. However, many of these studies are preliminary and AE defect identification (source identification or signature analysis) is a subject that could benefit from further exploration.

The principal objective of the research program reported in this dissertation is to develop reliable pattern recognition and neural network analysis methods to determine failure mechanism signatures in FRP structures from AE

data. Failure mechanisms that are addressed include matrix cracking, debonding between fibers and matrix, delamination, and fiber breakage.

1.3 RESEARCH METHODOLOGY

This research program focuses on development of simple and practical methods. Instrumentation and test procedure used must be simple and be in accordance with common AE standards. Representative specimens are made by commercially available FRP fabricators, and cover different types of materials and manufacturing processes.

The experimental set-up follows ASTM standards. The one exception is that coupon sizes are as large as possible to reduce wave reflections within the coupons. The larger-size coupons also better represent the behavior of full-scale components.

AE field practice uses narrow band resonant sensors in order to standardize data, minimize the influence of background noise, and overcome attenuation problems. In the field, the distance from the AE source to the sensor can vary from zero to 20 feet. For these reasons, waveform and frequency spectrum analyses, which require the use of wideband sensors and a known distance between AE source and sensor, cannot be used in the field. Accordingly, these techniques are not used in this study.

Pattern recognition is applied to a group of AE bursts rather than to individual sensor hits. This is because an individual hit, which may be one among thousands, is not likely to be representative of the emission.

To perform reliable analyses, AE data must be closely correlated with the actual defects occurring during the tests. The method used in this research for identifying the actual micro-defect mechanisms is the scanning electron microscope (SEM).

The following is an outline of the research program:

1. Literature review of AE source signature analysis and pattern recognition for FRP (Chapter 2).
2. Conduct an experimental program based on the “Recommended Practice for Acoustic Emission Evaluation of Fiberglass Reinforced Plastic (FRP) Tanks and Pressure Vessels” procedure (CARP, 1999). The purpose of these tests is to develop an AE database of different types of failure mechanisms (Chapter 3). The experimental work includes testing of:
 - a) Unidirectional fiber specimens tested in tension parallel to the fiber direction (Chapter 4).
 - b) Unidirectional fiber specimens tested in tension perpendicular to the fiber direction (Chapter 5).
 - c) Specimens in which delamination is the main failure mode (Chapter 6).
 - d) Specimens with other common types of fiber structure such as chopped strand fiber and woven roving (Chapter 6).
3. Perform SEM scanning to confirm the failure mechanisms that exist in the specimen.
4. Develop AE correlation plots for the AE data generated under item 2. Compare the plots to determine dissimilarities between the data patterns that can be attributed to different failure mechanisms (Chapter 7).
5. Apply the selected neural network methods to develop the pattern recognition based on the AE database (Chapters 8).
6. Apply the technology developed under item 5 to the AE data from more complex specimens and evaluate the results (Chapter 9).

CHAPTER 2

Background and Literature Review

This chapter is divided into four parts. The first part discusses background information on fiber reinforced plastic (FRP) and its failure mechanisms. The second part provides general information on nondestructive inspection of FRP structures. The third part covers acoustic emission (AE) background information and source identification in FRP. The fourth part covers basic neural networks, with emphasis on backpropagation and probabilistic networks.

2.1 FIBER REINFORCED PLASTIC

FRP is a type of composite material. It is also referred to as a structural plastic and has been used in many structural applications such as bridges, tanks, pressure vessels, aircraft, and structures. It is also used for structural repair and strengthening. Composites are well known for having corrosion resistance, high strength-to-weight ratio, and on-site formability. As a result, structural plastics are widely used, especially in corrosive environments and aerospace engineering. Disadvantages of composites include low modulus of elasticity, high creep, difficulty in joining, and lack of design methods. FRP can give a wide range of structural properties depending on the types of materials, manufacturing processes, and fiber volume fractions. The Table 2.1 provides a general idea of FRP material properties compared with other structural materials.

Table 2.1: Physical Properties of FRP Compared with Concrete and Steel

Properties	FRP		Normal weight concrete	Structural steel A-36	High strength structural steel A514
	Glass FRP	Graphite FRP			
Tensile modulus of elasticity (ksi)	1,500-5,500	10,000-26,000	3,300-4,300	29,000	29,000
Tensile strength (ksi)	10-150	40-200	0.3-0.6	58-70	120
Compressive strength (ksi)	10-90	40-150	1.5-10	58-70	120
Density (lbs/ft ³)	95-115	95-105	150	490	490

2.1.1 Materials Constitution

The two main constituents of fiber reinforced plastics are fiber and resin. The fibers act as reinforcement. In addition to transferring load between fibers and resisting shear, the resins behave as a protective binder. Characteristics of both materials are described below:

2.1.1.1 Fibers

Fibers can be made from many kinds of material. Glass, carbon, and graphite fibers are the most common types for commercial products. Besides glass and carbon, other materials such as boron, ceramic, aramid, aluminum, and steel have been used (ASCE, 1982). Three types of glass fibers are now available. E-glass fibers (E stands for electrical) are used for many structural

applications. C-glass fibers (C stands for chemical) are best for highly corrosive environments. S-glass fibers (high silica) have improved structural properties, and heat resistance (ASCE, 1982). Type E and C are most commonly used in structural applications. The properties of E glass fiber are shown in Table 2.2

Carbon fibers are manufactured by the pyrolysis of organic precursor fiber (i.e. rayon, polyacrylonitrile) in an inert atmosphere (Harper, 1996). Carbon fibers have a much higher modulus of elasticity, but smaller diameter than glass fibers. The structural properties of carbon fibers are also described in Table 2.2.

Table 2.2: Physical Properties of Glass and Carbon Fibers

Properties	E-Glass fiber	Carbon and graphite fiber
Modulus of Elasticity (ksi)	10,500	34,100-55,000
Tensile strength (ksi)	500	250-580
Ultimate strain (%)	4.8	1.6
Diameter (inch)	0.00091	0.000276

Generally, the carbon and graphite fibers possess better properties, but are a lot more expensive than the glass fibers. Therefore, the carbon fibers are mainly used for aerospace applications, where cost is not the main concern (Chawla, 1998).

2.1.1.2 Resins

There are many kinds of resin materials available in the market giving composites a wide range of structural properties. Polyester, epoxy, and vinyl ester are the most common types. Epoxies bond well to the fibers, are heat resistant, but are more expensive (Structural Plastics Design Manual, 1982).

Polyester is inexpensive, and has some chemical resistance (Chawla, 1998). Polyester can be produced by many methods, which make its properties range from brittle/hard to ductile/ flexible (ASCE, 1982). Vinyl ester is a modified epoxy designed to provide a wide range of corrosion resistance. The other superior properties of vinyl ester are low viscosity, high impact resistance, high corrosion resistance to many chemicals (at room and elevated temperatures), strong adhesion to glass fibers, and outstanding high-temperature aging (Harper, 1996).

2.1.2 Manufacturing

There are many ways to manufacture composites. Care should be taken to select a suitable method in order to achieve the design properties within a reasonable expense. In this section, only 3 processes, based on the manufacturing methods of the specimens in the research program, will be explained.

2.1.2.1 Hand Lay-up

Hand lay-up method is the simplest way to produce a composite, however, it is the most labor-intensive method. It is done by laying a fiber sheet (mat, woven roving, fabric, or combination) in a mold, and saturating the layer with liquid resin. The advantage of the hand lay-up method is freedom to make as many layers in whatever shape is desired. The curing process of this method commonly does not include heat and pressure (ASCE, 1982).

2.1.2.2 Pultrusion

Pultrusion is a continuous process of passing continuous fibers through a system. First, the fibers are soaked in the resin impregnator, and then they are pulled through a heated die. The heated die will remove all the excess resin, and form the shape of the composite (see Fig 2.1). Because of the continuous molding

cycle, the cross section will be the same dimension and will have similar properties along the length of the product. Pultruded composites mainly consist of unidirectional fibers in the pulling direction because continuous fibers are used. However, other mat sheets such as random chopped strand mats can be inserted to improve the properties of the perpendicular direction. Fiber contents can be controlled from 25 to 70 percent by weight. Currently, there are pultruded structural composites available in many shapes like structural steel. The advantages of this technique are that it is not labor intensive, and the product has a consistent quality.

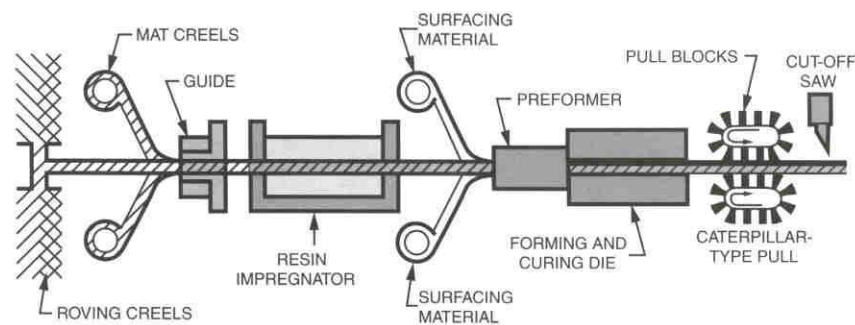


Figure 2.1: Schematic Illustration of Pultrusion Process (Strongwell Extren Design Manual)

2.1.2.3 Filament Winding

Filament winding is another automated process using continuous roving. The roving is soaked with the resin and wound over a rotating mandrel as shown in Fig. 2.2 (Chawla, 1998). Because of this, the fiber configuration can be adjusted according to the speed of the mandrel rotation and the speed of the filament dispensing mechanism (ASCE, 1982). Then, the resin is cured and the

mandrel is removed. This technique is commonly used to produce cylindrical vessels and pipes.

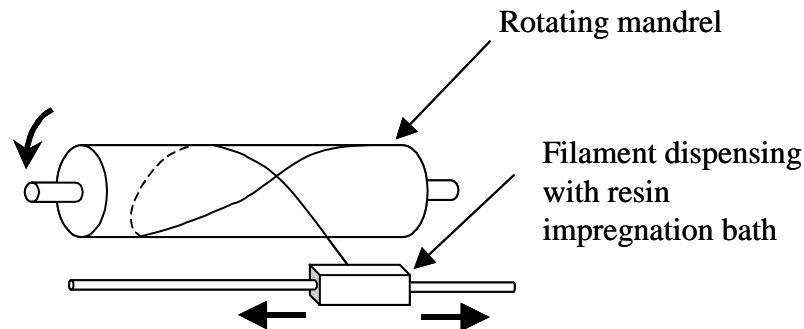


Figure 2.2: Schematic of Filament Winding (Classic Helical) Process (Adapted From ASCE, 1982)

2.1.3 Failure Mechanisms in Composites

FRP consists of more than one material. As a result, the failure mechanisms can occur in one material or in a combination of materials. There are many research papers describing the various types of damage mechanisms.

Matrix Cracking: Matrix or resin cracking is the term describing failure when the matrix strain reaches the ultimate strain. Figure 2.3a is a drawing of matrix cracking.

Fiber Breakage: Fiber breakage or fiber fracture occurs when an FRP component is under tensile stress and the fiber strain reaches the ultimate stress.

Fiber-Matrix Debonding: Separation of the interface between the fiber and the matrix can occur, and is shown in Fig. 2.3a.

Delamination: Some researchers describe delamination as a combination of fiber-matrix debonding and matrix cracking. Typically, delamination means the separation between two layers as illustrated in Fig. 2.3c (Chen, 1992, Suzuki, 2000).

Fiber Pull-Out: Fiber pull-out is the phenomenon that occurs when the tension force at fiber is higher than the friction between fiber-matrix interface. Fiber pull-out occurs at the end of a fiber, or at a break in the fiber. Figure 2.3d shows a sketch of fiber pullout. Failure mechanisms in FRP are discussed in detail in Chapters 4 to 6.

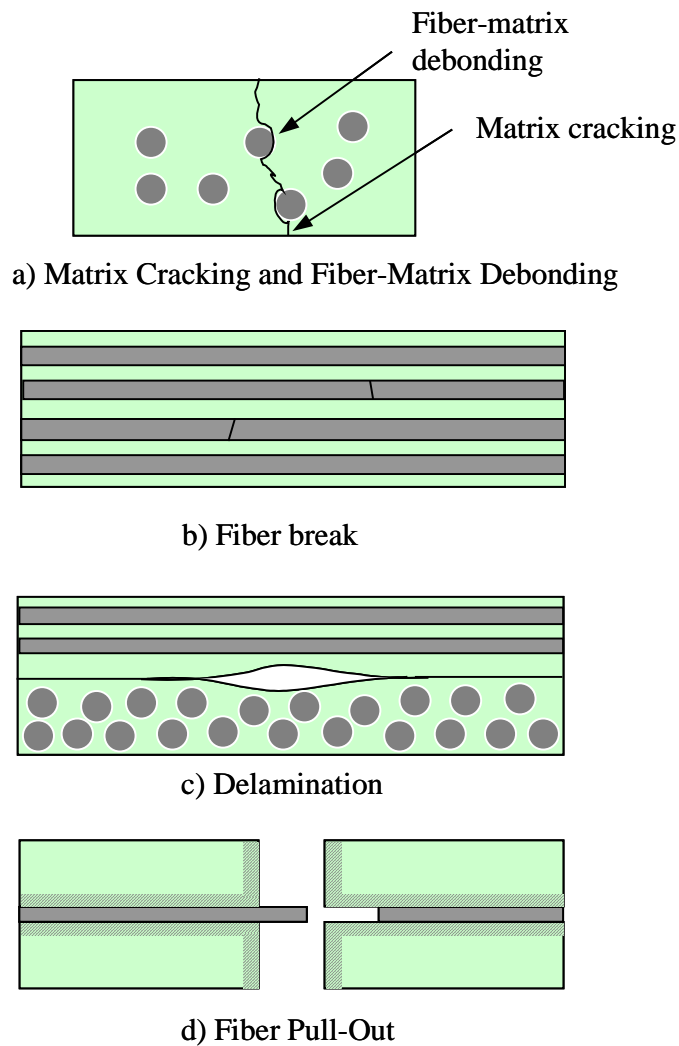


Figure 2.3: Schematic Illustration of Failure Mechanisms in Composites

2.1.4 Failure Progression (McGowan, 1983)

During loading, the sequence of failure mechanisms depends upon the strain property of the fibers and the matrix. When an FRP specimen with unidirectional fibers in the direction of the applied stress is loaded in tension, the fibers will carry a much greater proportion of the load than the matrix because of the much higher modulus of the fibers. However, the strain of both materials must be constant over the cross section. Therefore, if the fibers are more ductile than the matrix, the matrix will reach the ultimate strain first, causing matrix cracking. At this point, the load, which used to be carried by the matrix, will be transferred to the fibers. If the volume of the fibers in the specimen is adequate, the structure will remain stable. Then, as the load is increased, multiple matrix cracking will occur until the stress in the fibers reaches its ultimate. Alternatively, if the fibers cannot support the load transferred due to the first matrix cracks, the entire structure will fracture as soon as the first matrix cracks.

This is depicted on Figure 2.4. A similar behavior is observed if the fibers are more brittle than the matrix. In this instance, the fibers fail first. Figure 2.5a is a diagram of the failure progression versus the fiber volume fraction. The left side of the diagram is pure matrix strength (fiber volume fraction = 0), while the right side is pure fiber strength (fiber volume fraction = 1). With a brittle matrix at low fiber volumes, the fibers will fail as soon as the matrix cracks. At high fiber volumes, multiple matrix cracks will occur.

Unlike ductile fibers, when brittle fibers are used in composites, low percentage of fiber volume will cause multiple fractures of the fibers. When the strain of the matrix reaches the ultimate, the entire structure will fail. However, if the fiber volume fraction is high, the matrix cannot carry the transferred load after the first fiber break. This leads to the sudden failure of the composite. Diagram

in Fig. 2.5b represents the case of brittle fibers in composites by fiber volume fraction.

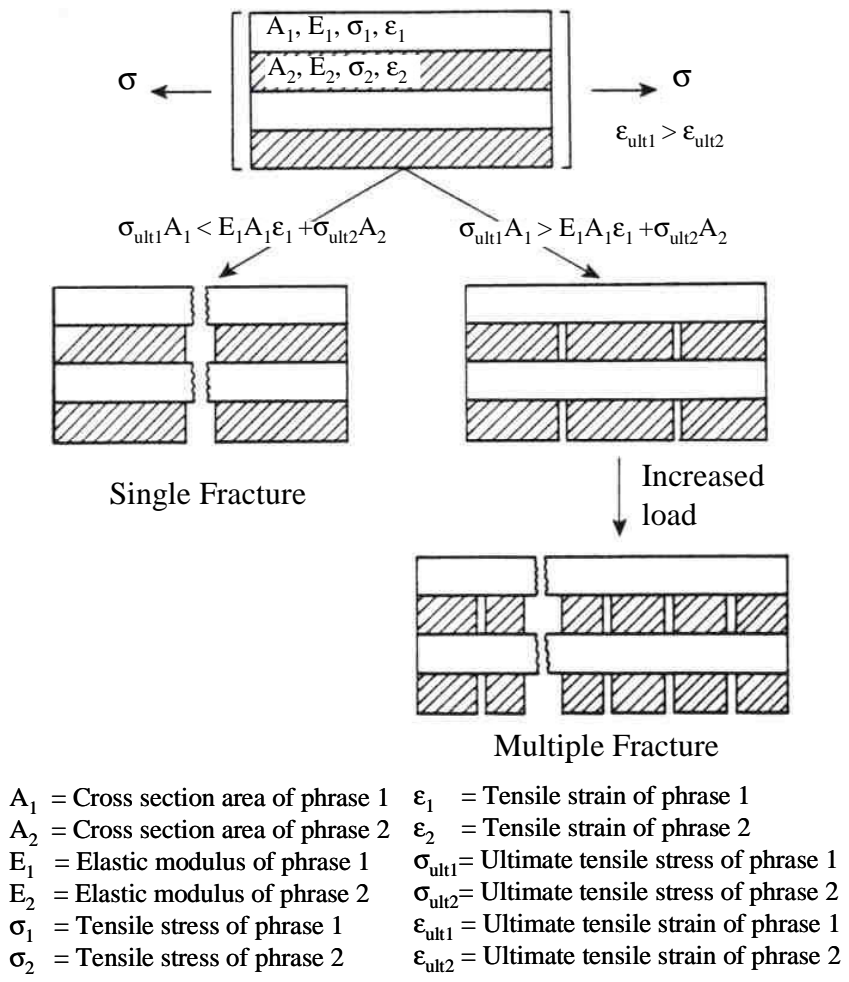
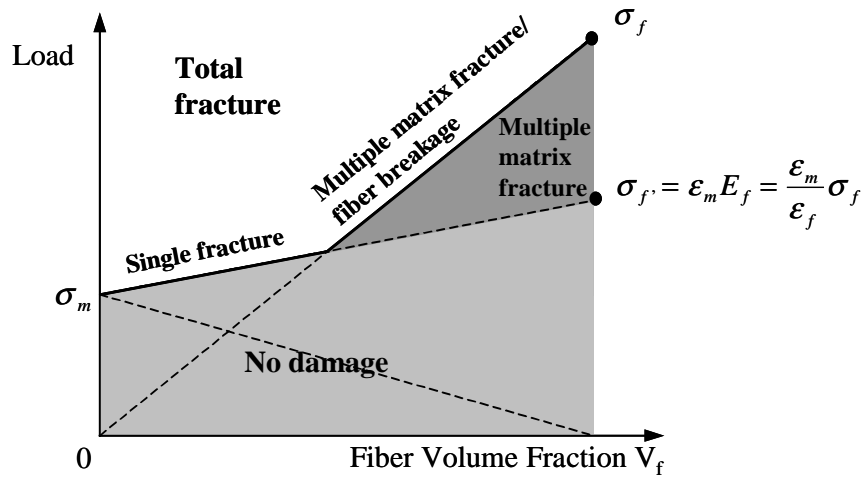
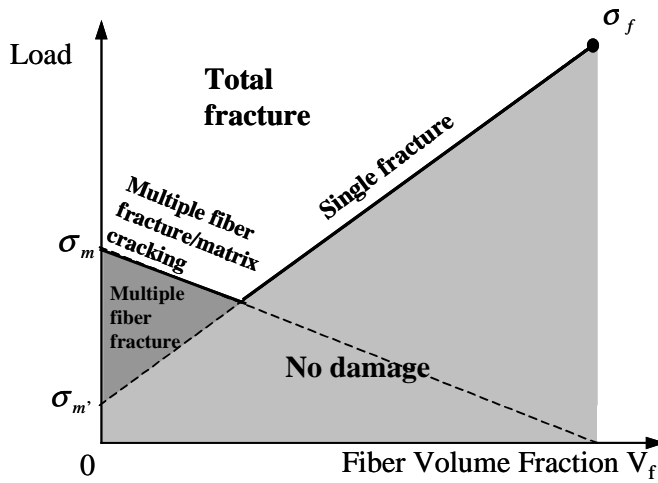


Figure 2.4: Single and Multiple Fracture: The More Brittle Phase is Shaded
 (Adapted From McGowan, 1983)



a) Brittle Matrix



b) Brittle Fiber

σ_m = Resin matrix strength

σ_f = fiber strength

$\sigma_{f'}$ = Composite stress at matrix failure

ϵ_m = resin matrix strain at σ_m

ϵ_f = Fiber strain at σ_f

E_f = fiber's Young modulus

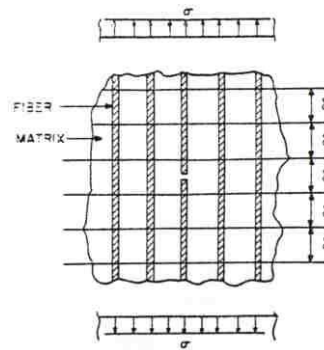
$\sigma_{m'}$ = Stress in composite at fiber failure

Figure 2.5: Failure Progressive Diagram (Adapted From McGowan, 1983)

2.1.5 Fiber Breakage Study

Rosen (1964) studied tensile failure of unidirectional composites and published a paper, which plays an important role for this research program. He stated that fibers normally had flaws or imperfections, so the strength of the fibers was distributed statistically. As a result, some fibers started to fracture early, before failure of the structure, due to these imperfections. This agreed with the series of microphotographs taken during his tensile tests.

Based on Rosen's model, the stress at the end of the fiber break was zero and increased as it moved further away from the break point. The length of a fiber from the end to maximum stress was called "ineffective length", δ . Within this ineffective length, there would be no fiber breaks. Therefore, Rosen suggested dividing composite into layers (see Fig. 2.6), which had a thickness of δ each.



**Figure 2.6: Tensile Failure Model for the Cumulative Fracture of Fibers
(Zweben, 1968)**

Each layer was then divided into small elements equal to the number of the fibers in the cross section. Therefore, a composite of length L having N fibers would

have total number of MN elements, where $M = L/ \delta$. Zweben (1968) suggested the ineffective length as:

$$\delta = d_f \left\{ \frac{1}{2} \times \frac{E_f}{G_b} \times \left[\frac{(1 - v_f^{1/2})}{v_f^{1/2}} \right] \right\}^{1/2}$$

where

δ = Ineffective length

d_f = Fiber diameter

E_f = Young's modulus

G_b = Matrix shear modulus

v_f = Fiber volume fraction

And the fiber strength was distributed according to the Weibull distribution:

$$f(\sigma) = \alpha \delta \beta \sigma^{\beta-1} e^{-\alpha \delta \sigma^\beta}$$

and

$$F(\sigma) = 1 - e^{-\alpha \delta \sigma^\beta}$$

where

$f(\sigma)$ = Weibull probability density function

$F(\sigma)$ = Weibull cumulative distribution function

α and β = Weibull distribution parameters

δ = Ineffective length

σ = Fiber stress

The parameters α and β can be obtained from testing the virgin fibers. Generally, β is an inverse measure of dispersion. The lower β is associated with the wider distribution in failure stress level of fibers. Therefore, within MN elements, the expected number of fiber breaks (B_1) at stress σ would be:

$$B_1 = M N F(\sigma)$$

Rosen assumed that after a fiber had broken, the load in a broken fiber was transferred equally among the rest of the fibers in a cross section. This means the load in a broken element would be transferred equally to the rest of the elements in that layer. As the load increases, an increasing accumulation of fiber fractures would occur. At the end, the ultimate stress would exceed the weakest cross section strength causing composite failure.

This model was modified by Zweben (1968). Zweben stated that after the fiber broke, the load would be distributed to adjacent elements with some load intensity. The closer adjacent elements were subjected to the higher intensity. According to Zweben, the load intensity equation was given by the following equation:

$$K_r = \frac{4 \cdot 6 \cdot 8 \cdot \dots \cdot (2r + 2)}{3 \cdot 5 \cdot 7 \cdot \dots \cdot (2r + 1)}$$

where

r = Number of broken fibers

K_r = Load-concentration factor of adjacent fibers

Given that a single element is broken, the probability that one of the two adjacent fibers will break due to the load concentration is:

$$p_{2/1} = 2[F(K_1 \sigma) - F(\sigma)] - 2[F(K_1 \sigma) - F(\sigma)]^2$$

The probability that both adjacent fibers will break simultaneously is:

$$p_{3/1} = [F(K_1 \sigma) - F(\sigma)]^2$$

Therefore, the probability that a given element will break followed by the fracture of at least one adjacent element is:

$$p_2 = F(\sigma) (p_{2/1} + p_{3/1})$$

For the entire composite, the expected number of groups of two or more broken fibers (B_2) is:

$$B_2 = M N p_2$$

Using the above equations, the expected number of fiber breaks at different load levels could be predicted. It was shown that the prediction fitted well with the experimental results, especially at high stresses.

2.2 NONDESTRUCTIVE INSPECTION OF FIBER REINFORCED PLASTICS

2.2.1 Introduction

It is generally accepted that every structure or component in the real world always has some imperfections. The imperfections in a structure may or may not be visible, or harmful. Accordingly, nondestructive testing (NDT) or nondestructive inspection (NDI) or nondestructive evaluation (NDE) can be performed to ensure that structures can be safely operated for a certain period of time. In general, the roles of NDT are to help detect, locate, and evaluate the significance of the flaws in in-service structures. NDT also plays a role of quality control in the manufacturing process. It is used to ensure that imperfections in every part of a structure are below an accepted tolerance before installation. Detecting flaws after the installation is harder and difficult to repair.

Benefits of NDT include life extension and cost savings. Preventive maintenance associated with inspections will reduce the cost of major repairs, such as repairing leaks. NDT for quality control provides more confidence in the design process, thus leading to a reduced factor of safety and construction cost. In addition, NDT prevents leaks from a tank or pressure vessel, which can generate product wastes, and environmental pollution (Bray and Stanley, 1997).

NDT can be categorized into 2 groups: active and passive. Active NDT is the technique that sends energy in some form into or onto the specimen. Flawed and unflawed specimens respond differently to this energy, which will be observed by a trained inspector. The examples of this method are ultrasonic, impact echo, radiography, and eddy current. The passive method observes acoustic or visual changes in a specimen under either a normal load condition or a proof cycle. A defect in the structure will reveal itself naturally. These passive methods include acoustic emission, visual inspection, dye-penetrant, and leak detection (Bray and Stanley, 1997).

2.2.2 NDT Methods

The most common nondestructive testing methods are summarized below. Each method has strengths and weaknesses and are complementary to one another.

2.2.2.1 Radiography

Radiography (ASNT Vol. 3, 2002) utilizes the penetration of X or gamma radiation to the specimens. The X ray is radiated from an X-ray machine or radioactive isotope, and is received by film on the other side of the specimen. The film will show the density of the radiation by the color of the gray tone. A crack or imperfection usually reduces the thickness of the material. This causes a higher density of radiation, and a darker mark on the film.

2.2.2.2 Magnetic Particle

Magnetic particle method (ASNT Vol. 6, 1989) induces a magnetic field in a ferro-magnetic specimen and dusts the surface with iron particles. If surface discontinuities are present, a distortion of iron particle arrangement will be seen due to the disturbance of the magnetic field. The magnetic particle method is not

suitable for using with FRP materials, which except for steel FRPs are not ferromagnetic.

2.2.2.3 Ultrasonics

Ultrasonic testing (ASNT Vol. 7, 1991) is done by transmitting high frequency sound waves into a material. The waves can be detected by a receiver on the opposite side of the specimen or hit the back wall of the specimen and reflect back to a receiver on the same side as the transmitter. An imperfection within the thickness can also interrupt or reflect the signal. The times of flight are used to calculate the thickness of the part, or the depth of the imperfection.

2.2.2.4 Liquid Penetrant

In this test (ASNT Vol. 2, 1999), the specimen is coated by a visible or fluorescent dye solution. For composite material, the excess dye on the surface is wiped or washed off. If there are surface cracks, the dye will penetrate and leave the marks on the surface. Fluorescent dyes give better sensitivity than the normal dye, but an ultraviolet lamp must be used. Fluorescent dye is needed for carbon FRP because it is difficult to observe the normal dye on carbon fibers, which are dark color.

2.2.2.5 Eddy Current

The eddy current method (ASNT Vol.4, 1982) uses electrical current generated in a conductive material by inducing a magnetic field. The electrical current (eddy current) will be continuously monitored during the test. Imperfections on or near the surface of a specimen will cause the change of the magnetic field, thus changing the level of eddy current. Eddy current techniques are not used with glass FRP because the glass is nonconductive. However, the technique can be used with carbon or graphite FRP materials.

2.2.2.6 *Leak Testing*

Leaking of a liquid from a tank or pressure vessel can be inspected by several methods. Examples include listening devices, pressure gauge measurements, liquid and gas penetrant techniques, and soap bubble test (ASNT Vol. 1, 1997).

2.2.2.7 *Acoustic Emission*

AE is explained in detail in Section 2.3.

2.2.2.8 *Visual Examination*

Visual examination (ASNT Vol. 8, 1993) is the oldest and the most widely used method of NDT. It can detect most of the serious defects on or near the surface of a structure. Visual examination may require tools to enhance the performance. These tools include a flashlight, knife, hand held magnifying glass, and hardness impressor. Visual examination is particularly important for FRP structures, because other NDT techniques are often less effective on FRP materials than on metals.

2.2.3 Causes of Damage to FRP Structures

2.2.3.1 *Mechanical*

Mechanical damage is the most common type in FRP structures. FRP materials are typically brittle. As a result, FRP components are very sensitive to fatigue, overstress, and impact loading. It is common to see cracks at the high stressed areas and areas under mechanical impact (Niesse and Ahluwalia, 2001).

2.2.3.2 Chemical Attack

Chemical attack usually occurs in FRP tanks and pressure vessels. It can take the form of permeation, chemical changes, and dissolution. The permeation in FRP can cause blisters, delamination, swelling, softening of resin, and attack of fiberglass. The chemical changes can cause weakening or softening of the resin. Some can cause cracking or crazing at the surface. The dissolution removes the resin, and leaves fibers hanging down from the laminate (Niesse and Ahluwalia, 2001).

2.2.3.3 Environmental Exposure

FRP material is very sensitive to environmentally induced degradation. Ultraviolet light, and overheating can degrade the resin. The effect includes changing the color, initial softening and later hardening of resin. In addition, abrasion resulting from a sand storm can cause surface damage (Niesse and Ahluwalia, 2001).

2.2.3.4 Fabrication Effects

Inexperienced labor can leave several types of defects in the structure such as inclusions, the use of the wrong resin, misalignment, and the improper curing technique. Moreover, incorrect on-site installation, and shipping can cause some locally over-stressed areas increasing the chance of damage (Niesse and Ahluwalia, 2001).

2.2.4 Failure Rate (Bray and Stanley, 1997)

It is helpful to understand the nature of structural failure rate so that future inspection can be planned. The typical relationship between the failure rate and time for structures and components is referred to as the “bath tub curve” as shown in Fig. 2.7. The first part, which counts from time zero to T_E , is called the “burn-

in” region. These very early failures are associated with either manufacturing defects, improper installation, shipping damage, improper design, or severe overload. NDT can reduce the failure rate in this region by performing the quality control of the new product before it is installed in the on-site structure. The mid-zone of the curve represents the useful life or constant failure rate portion. This portion covers a long period of time. Periodic inspection or continuous monitoring can be performed in this portion. In the last region, the failure rate starts to increase again after time T_w , which generally is a result of fatigue failure. Time T_m is the point where half of the components in a structure fail, and the curve rises sharply after that. The NDT must contribute in this region by determining time T_w and managing to repair the structure before time T_m is reached.

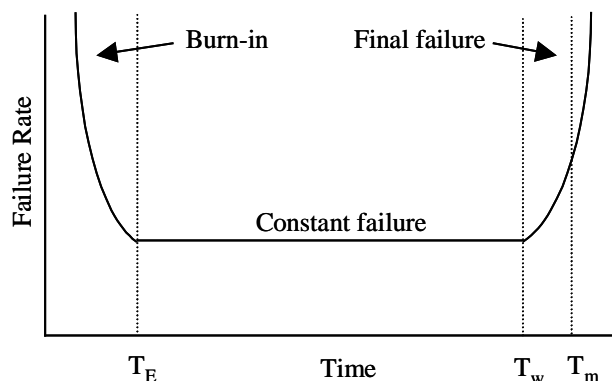


Figure 2.7: Typical Failure Rate Curve (Bray and Stanley, 1997)

2.2.5 Factors Affecting NDT Performance

2.2.5.1 Human Factors (Dickens and Bray, 1994)

The accuracy of the NDT is most affected by inspectors. There are three ideal conditions for performing perfect NDT:

1. Person is highly skilled and motivated
2. Activity is familiar
3. Environmental conditions are favorable

In practice, it is hard to find these conditions at the same time. If the weather is too cold, windy, and the site is hard to access, some flaws can be missed. Some of the tasks require the judgment of the inspectors. For example, it may be the inspector's decision to accept or reject the structure based on the "critical flaw size". Under bad conditions, the accuracy of the detected flaw size can be low leading to either incorrectly rejecting or accepting the structure. Working in pairs can significantly reduce errors of inconsistency in the inspectors' judgment.

2.2.5.2 Method Selection

Each NDT method has different capabilities and has strengths and weaknesses, which determine its ability to detect certain types of defect, location, size, and severity. For example, dye-penetrant, which is a simple technique, can only detect surface defects and cannot give information about the crack depth. In addition, it has limited application for follow up inspection of FRP structures, which can have a large number of surface microcracks from weathering. Dye-penetrant enhanced X-ray radiography is likely to be the most reliable technique for composite inspection in laboratory conditions (Fowler, 1999). However, it is expensive, requires heavy instruments, and requires access to both sides of the structure. Visual inspection is the simplest method, but the size of the flaws to be detected by this method is large and close to the critical flaw size. In general, the detection of smaller flaws requires more sophisticated and probably more expensive techniques.

2.2.5.3 Qualifications of NDT Personnel

NDT techniques require special skill for operating the instruments, and interpreting the results. Therefore, NDT engineers and technicians must be trained and qualified for any technique they will be operating. The American Society for Nondestructive Testing provides guidelines for establishment of a qualification and certification program in “Recommended Practice No. SNT-TC-1A: Personnel Qualification and Certification in Nondestructive Testing”. There are three levels of qualification. An NDT level I inspector should be able to perform specific calibrations, specific NDT, and specific evaluations. An NDT level II inspector must be able to run the complete tests, and evaluate results with respect to applicable codes, standards, and specifications. An NDT level III inspector should be able to establish techniques and procedures; interpret codes, standards, specifications, and procedures; and designate the particular NDT methods, techniques, and procedures to be used.

2.3 ACOUSTIC EMISSION

2.3.1 Introduction

AE is defined as “the class of phenomena whereby transient elastic waves are generated by the rapid release of energy from localized sources within a material, or the transient waves so generated” (ASTM E1316).

Acoustic emission is generated by the material itself, unlike other types of stress wave nondestructive testing techniques such as impact echo and ultrasonics, which require external input sources. The source of acoustic emission can be from many phenomena, depending on the type of material. In metals, AE sources can be from dislocation movements, cracks, fractures, and even corrosion. In

concrete, microcracking and macrocracking as well as debonding or movement of reinforcement can cause emissions. For composites, AE comes from matrix cracking, delamination, debonding of the matrix from the fibers, fiber breakage, and fiber pullout (Fowler, 1977). In liquids, AE can be from fluid leakage and turbulence (Bray and Stanley, 1997). In addition to internal acoustic emission sources, external noise (background noise) such as mechanical rubbing, wind, air hoses, and moving trucks can create elastic waves, which interfere with the genuine data. These background noises have to be prevented or filtered out before the AE data is analyzed.

2.3.2 Acoustic Emission Applications

AE is emitted from a structural imperfection earlier than from unflawed material under the same applied stress. Accordingly, the AE technique is used to evaluate the integrity of a structure (Boogaard, 1989). The time of flight of the stress wave can also be used to identify the location of the source (Promboon, 2000). AE can also be used to indicate the level of strain when a specific material becomes significantly damaged, which is useful for design criteria (Zeihl, 2000).

Acoustic emission has been used to evaluate many types of structures such as pressure vessels, storage tanks, railroad tank cars, manlift booms, and bridges. It also has been used with a variety of material such as steel, concrete, composites, and even ice. As a result, AE standards have been established and developed. In 1982, the Committee on Acoustic Emission from Reinforced Plastics (CARP) developed “Recommended Practice for Acoustic Emission Testing of Fiberglass Tanks/Vessels”, which was the first procedure for testing composite structures. AE is also a mandatory test for ASME Code, Section X, class II composite pressure vessels. Other important applications of AE testing of FRP structures are manlift booms (ASTM F 914), cooling tower fan blades

(ASTM E 2076), aerospace (Hamstad, 1983, Whalley and Cole, 1983), pipe (Droge, 1983), downhole tubing (Peckering, 1983), and FRP bridge beams (TxDOT, 2002).

The advantage of AE is that it is a global method rather than a local method meaning that the technique monitors a large area of the structure, rather than a small local area. As a result, the monitoring can be done within a short period of time and, is not labor intensive.

However, the disadvantage of this technology is that the acoustic emission is dependent on the applied load. This means, some discontinuities may not generate detectable AE under a certain types or level of load. Other areas of the acoustic emission technique that need more research are:

1. **Source Location:** The ability to locate the position of discontinuities in a structure. This is beneficial particularly for large structures since it is time consuming to locate the area to be repaired. Source location in metal tank cars was successfully developed at the University of Texas at Austin, however, more research is needed for the other materials such as composites (Promboon, 2000).
2. **Source Identification:** The ability to determine the type of discontinuities within a structure. With current AE technology, only the severity of the discontinuities can be evaluated (CARP, MONPAC). However, if the type of discontinuities is required, other local methods such as ultrasonic must be used. These local methods are time and labor intensive. It would be beneficial if source identification could be determined from the AE data. This area is also referred to as “signature analysis” or “failure mode classification”. In most cases, AE from different failure modes

exhibits a different pattern of data, therefore, “AE pattern recognition” is another term used for source identification. This area is the subject of the research reported in this dissertation.

3. **Size and Orientation Determination of Defects:** The size and orientation of a defect is valuable for fracture mechanics analysis, which is used to determine the structural significance of a defect. This area has not been studied intensively since current acoustic emission procedures such as those set out in the MONPAC and CARP documents can already provide intensity information on the defects. However, it would still be valuable if this information could be found by the AE technique.
4. **Probability of Detection (POD):** Probability of detection using the round robin method cannot be done by AE because a defect emits less acoustic emission as more tests are conducted (known as Kaiser effect). Therefore, other methods based on theoretical studies with benchmark experimental testing have been developed and included into some test procedures (Fowler, 1996, and AAR, 1999).

2.3.3 Instrumentation

2.3.3.1 AE Sensors

Acoustic emission sensors are mounted on the surface of the structure being tested. When transient waves propagate through the structure, the piezoelectric crystal in an AE sensor will resonate in response to the structure’s surface motion. The change in stress in the crystal will generate an electric current, which can be monitored. This information will then be stored by the AE data acquisition system (see Fig. 2.8).

Resonant sensors are sensitive to only a small range of frequencies. Whereas, a stress wave consists of many frequency components. The higher frequency components will attenuate more quickly as the wave travels and can only be detected close to the source. Background noise such as that from external sources like passing trucks and air hose sound, will be lower frequency. Therefore, the resonant frequency of the sensor is chosen to give maximum sensitivity without background noise.

In concrete, low frequency sensors (60 kHz) are used because the inhomogeneity of the concrete attenuates the signal (and also the background noise) more quickly than homogeneous materials.

In some metal applications, such as nuclear reactors, 300 kHz sensors are used because of the high background noise from the reactor.

In composites, 100-200 kHz sensors are typically used (CARP, 1999).

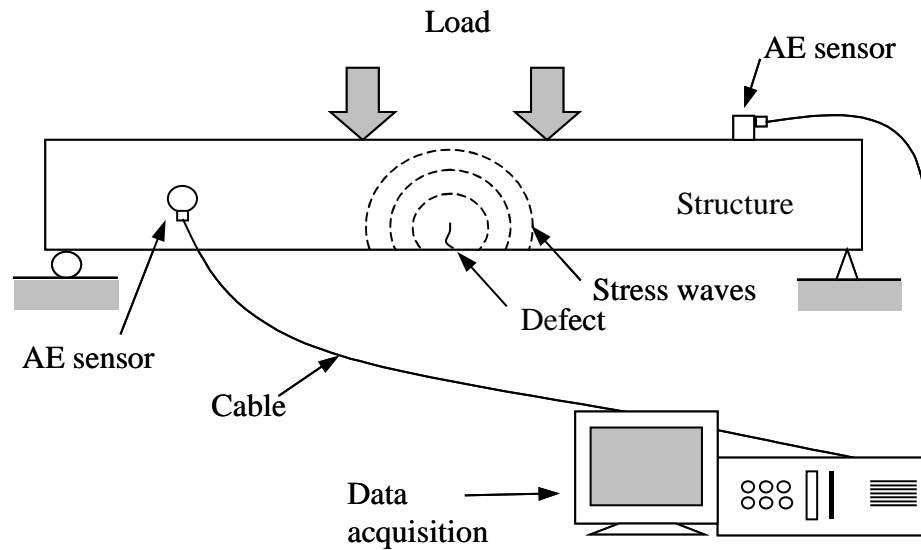


Figure 2.8: Acoustic Emission Instrument

Beside resonant sensors, wideband sensors are produced in a way that the resonance is damped out. This way, all the frequencies of the wave are recorded at the same sensitivity, and as a result, a wideband sensor is useful when a frequency spectrum analysis is required (Halmshaw, 1991). The disadvantage of this type of sensor is that it is a lot less sensitive to the emission than resonant sensors. Therefore, some emission might not be detected by wideband sensors.

2.3.3.2 Preamplifier

The piezoelectric material in the AE sensor transforms the signal to a voltage. Since the magnitude of the voltage is very small, a preamplifier is required to amplify the voltage to a more suitable range. Usually, the preamplifier is mounted integral in the sensor.

2.3.3.3 AE Data Acquisition

After the preamplifier, the AE signal is transmitted to the AE data acquisition system by a cable. The data acquisition system can filter (eliminate unwanted signals or frequencies), or amplify the signals. It will also record, and organize the AE data. Most of the time data acquisition software can instantly plot graphs and analyze the data, which is helpful for inspectors to understand what is happening during the test.

2.3.4 AE Parameters

An AE waveform of a noise is normally displayed on a voltage vs. time plot. From this waveform, basic AE parameters can be measured. To help visualize the AE data, an idealized waveform of a typical AE hit is shown in Fig. 2.9.

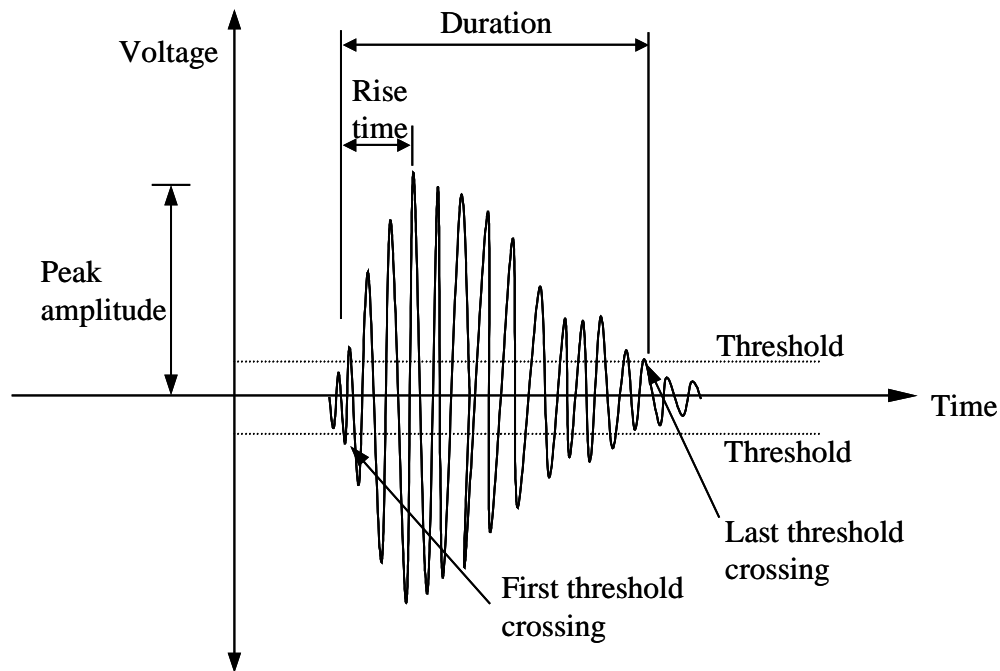


Figure 2.9: Acoustic Emission Waveform Parameters

2.3.4.1 Basic AE Parameters

Threshold (Voltage Threshold): “A voltage level on an electronic comparator such that signals with amplitudes larger than this level will be recognized. The voltage threshold may be user adjustable, fixed, or automatic floating.” (ASTM E 1316). The threshold is set for eliminating electronic background noise, which normally has low amplitude.

Count (AE count): “The number of times the acoustic emission signal exceeds a preset threshold during any selected portion of a test” (ASTM E 1316).

Peak amplitude (AE Signal Amplitude): “The peak voltage of the largest excursion attained by the signal waveform from an emission event” (ASTM E 1316). In other words, peak amplitude is the highest point of the signal. It is the absolute value on either positive or negative side of a waveform.

The peak amplitude is usually reported in decibels (dB) due to the wide range of typical values in voltage unit. Voltage is converted to decibels using the following equation:

$$A = 20 \log \left(\frac{V}{V_{ref}} \right)$$

where

A = Amplitude in decibels

V = Voltage of peak excursion

V_{ref} = Reference voltage, typically 1 μ V (Voltage generated by 1 mbar pressure of the face of sensor).

Duration (Hit Duration): “The time between AE signal start and AE signal end” (ASTM E 1316). It is the time from the first to the last threshold crossing and is typically displayed in microseconds.

Risetime (AE Signal Rise Time): “The time between AE signal start and the peak amplitude of that AE signal” (ASME E 1316). Risetime is also measured in microseconds.

Signal Strength: The area under the envelope of the linear voltage signal. Specifically, the signal strength (Fowler et al.,1989) is:

$$S_0 = \frac{1}{2} \int_{t_1}^{t_2} f_+(t) dt - \frac{1}{2} \int_{t_1}^{t_2} f_-(t) dt$$

where

f_+ = positive signal envelope function

f_- = negative signal envelope function

t_1 = time at first threshold crossing

t_2 = time at last threshold crossing

The signal strength is the parameter that is related to the energy of the hit (Fowler et al., 1989). The important point of the signal strength is that when a material fractures, there will be strain energy released, part of which becomes AE. Therefore there is a “constant relation” between the energy release from the defects and AE energy (Rotem, 1979). Signal strength is sometimes referred to as relative energy.

MARSE: The area under the envelope of the rectified voltage signal (ASME V, article 12). Specifically, MARSE is defined as:

$$S_r = \frac{1}{2} \int_{t_1}^{t_2} f_r(t) dt$$

where

f_r = rectified signal envelope function

MARSE is an approximation of signal strength. It could be slightly different but is generally acceptable (Fowler et al., 1989)

Energy (AE Signal Energy): “The energy contained in a detected acoustic emission burst signal, with units usually reported in joules and values which can be expressed in logarithmic form (dB, decibels)” (ASTM E 1316). Specifically, energy is defined as:

$$E_t = \frac{1}{2} \int_{t_1}^{t_2} f_+^2(t) dt - \frac{1}{2} \int_{t_1}^{t_2} f_-^2(t) dt$$

Hit (Sensor Hit): “The detection and measurement of an AE signal on a channel” (ASTM E 1316).

Frequency: The number of cycles per second of the pressure variation in a wave. Commonly, an AE wave consists of several frequency components.

Event (AE Event): “A local material change giving rise to acoustic emission” (ASTM E 1316).

Source (AE Source): “The position of one or more AE events” (CARP, 1999)

2.3.4.2 Modified Parameters

Kaiser and Felicity Effects:

The Kaiser effect is defined as “The absence of detectable acoustic emission at a fixed sensitivity level, until previously applied stress levels are exceeded (ASTM E 1316). The presence of the Kaiser effect generally indicates good integrity of the structure (Halmshaw, 1991)

The Felicity effect is described as “ the presence of detectable acoustic emission at a fixed predetermined sensitivity level at stress levels below those previously applied (ASTM E 1316). The Felicity effect is a breakdown of the Kaiser effect. That means that the structure generates emission during reloading, before the previous maximum stress is reached (Fowler, 1977, and Fowler, 1979).

The Felicity ratio is an indication of the amount of damage, and is defined as the ratio of the load at which emissions occur to the previous maximum load:

$$\text{Felicity ratio} = \frac{\text{load at which emissions occur}}{\text{Previous maximum load}}$$

A low Felicity ratio is generally associated with more damage in the structure.

Historic Index: Historic index is a parameter to determine the changes of signal strength rate throughout a test. Specifically, it measures changes in slope of the cumulative signal strength vs. hits plot. The CARP procedure defines historic index as

$$H(t) = \frac{N}{N - K} \frac{\sum_{i=K+1}^N S_{0i}}{\sum_{i=1}^N S_{0i}}$$

where

$H(t)$ = the historic index at time t .

N = the number of hits up to and including time t

S_{0i} = the signal strength of the i^{th} hit.

For fiber reinforced composite materials, K is defined as in Table 2.3.

Table 2.3: K Value for Historic Index (CARP, 1999)

Number of Hits	K
< 20	Not applicable
20 to 100	0
101 to 500	0.8N
>500	N-100

Normally, historic index is low at the beginning of test, and increases when the load increases. Once the structure starts to have significant damage, the cumulative signal strength curve (see Section 2.3.5.4 for more details) will show a rapid change of slope (knee). At this point, a jump of historic index can be seen. Figure 2.10 is an example plot of historic index vs. time of a glass FRP specimen tested in tension (Ziehl, 2000). The plot also superimposes cumulative signal strength and the loading schedule.

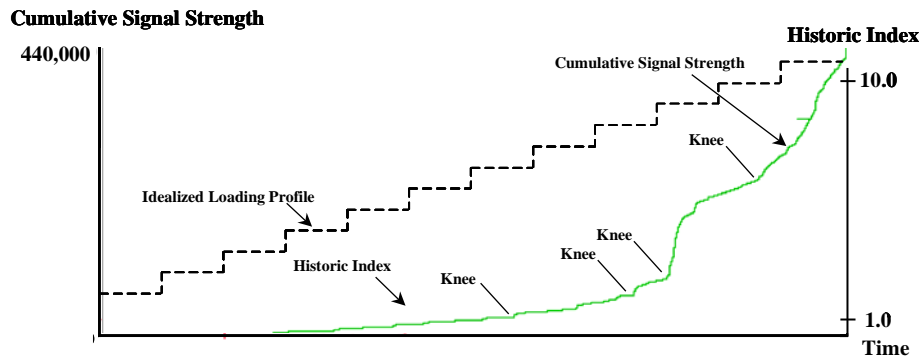


Figure 2.10: Example of Historic Index Superimposed with Cumulative Signal Strength and Loading Profile vs. Time of a Glass FRP Specimen Tested in Tension (Ziehl, 2000)

Severity (Sr): The average signal strength of J hits having the maximum numerical value of signal strength (MONPAC-PLUS, 1992). Severity index is defined as:

$$S_r = \frac{1}{J} \sum_{i=1}^J S_{oi}$$

where

S_{oi} = the signal strength of the i^{th} hit

J, for composite materials, is defined as shown in the Table 2.4.

Table 2.4: J Value for Severity (CARP, 1999)

Number of Hits	J
< 20	Not applicable
> 20	20

A large increase of severity corresponds with the onset of structural damage. Normally, severity increases rapidly at the knee of cumulative signal strength vs hits curve. After that, if the damage becomes more serious, the severity will keep increasing, but at a slower rate. Severity is also a tool to identify the onset of emission for Felicity ratio (MONPAC-PLUS, 1992).

2.3.5 Correlation Plots

Plots of the correlation between two or more AE parameters can help understand the phenomena or failure mechanisms in a structure during loading. There are many plots used in the field of acoustic emission, but only selected plots, which were used for this research program are described here:

2.3.5.1 Amplitude Distribution

The amplitude is the most fundamental parameter for acoustic emission since the threshold amplitude is the parameter that the data acquisition system uses to decide whether or not an emission will be recorded. Therefore, it is not surprising that amplitude distribution (or amplitude histogram) has been a basic study in many AE applications. Examples are source identification and failure load prediction (Pollock, 1978, Hill, 1995, Valentin, 1985, Hill et al, 1996, and Hill et al, 1998). Amplitude distribution is a histogram of the number of hits (plotted on a log scale) at different amplitude levels. Figure 2.11 is an example of this plot. Amplitude distribution is sometimes called a “differential amplitude distribution”.

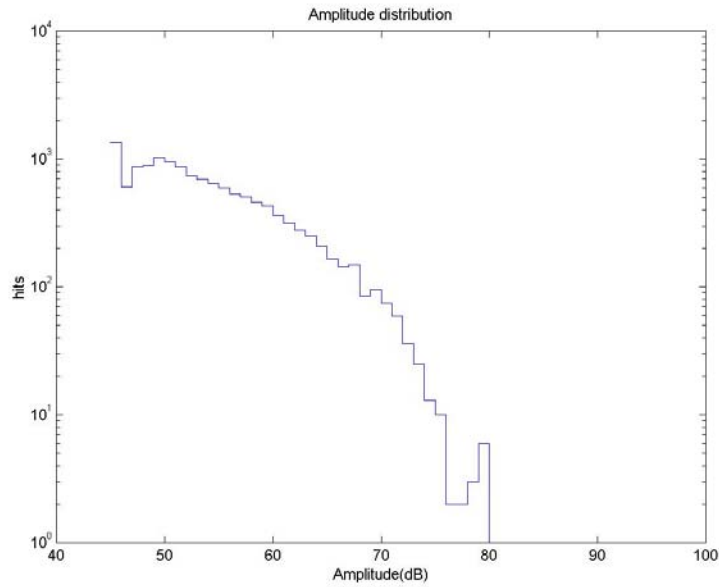


Figure 2.11: Differential Amplitude Distribution of Fiber Glass Composite Tensioned Perpendicular to the Fiber Direction

Several researchers have studied source identification by looking at humps in this plot. It was found that different humps represent different failure mechanism (Pollock, 1978, Hill, 1995, and Valentin, 1985).

2.3.5.2 Cumulative Amplitude Distribution

2.3.5.2.1 Background

It is known that the attenuation in a material decreases the amplitude of emissions as the wave travels (Elmore and Heald, 1969). Therefore, a sensor closer to the source will detect higher amplitudes of an event than sensors further away. This means that away from the source, the amplitude parameter itself cannot be referred to as a certain type of failure mechanism. This has made many researchers find a new way to analyze the AE amplitude. As a result, cumulative

amplitude distribution and b-value have been successfully developed and, applied to AE source identification (Pollock, 1981). Cumulative amplitude distribution was first developed for seismology applications, and was later adopted for AE technology. Cumulative amplitude distribution is a log plot of the histogram of the number of hits at a specified amplitude or higher (See Fig. 2.12). The slope of the plot is called b-value and will be discussed in the next section.

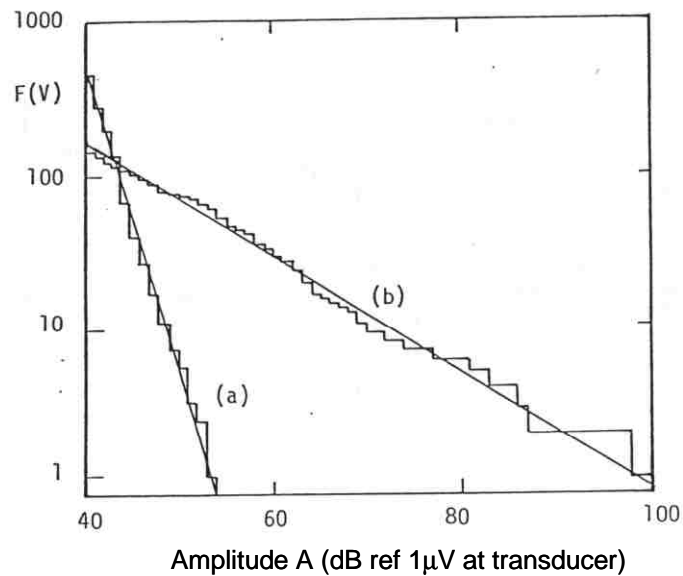


Figure 2.12: Cumulative Amplitude Distribution Plot a) plastic zone Growth in A516 Steel b) Stress Corrosion Cracking in 4340 Steel (Pollock, 1978)

2.3.5.2.2 Theory of b-Value

The AE data acquisition system normally records the amplitude in voltage (V) or decibel (dB) units. The relationship between these units is:

$$A = 20 \log \left(\frac{V}{V_{ref}} \right)$$

where

$$V_{ref} = 1\mu V,$$

A = amplitude in decibels

V = amplitude in voltage units

To simplify the explanation, voltage units will be discussed first.

Given $f(V)$ is an amplitude distribution function, such that $f(V)$ is the number of hits for which the amplitude is equal to the value V and that $F(V)$ is a cumulative amplitude distribution plot of the number of hits for which the amplitudes are equal to or higher than the value V . Then the two functions are related by the equation:

$$f(V) = -\frac{dF(V)}{dV}$$

Given $\Phi(V)$ is a normalized function representing the probability that an emission's amplitude exceeds V , and V_0 is the smallest detected amplitude (typically threshold), which gives $\Phi(V_0) = 1$. The problem arises in developing a function $\Phi(V)$ that describes the nature of failure detection. For composite materials, Pollock, 1981, suggested use of the function:

$$\Phi(V) = \left(\frac{V}{V_0} \right)^{-b}$$

where

b = parameter characteristic of the distribution function

$F(V)$ and $\Phi(V)$ are related by the equation:

$$F(V) = N_0 \Phi(V)$$

where

N_0 = total number of hits

Therefore

$$F(V) = N_0 \left(\frac{V}{V_0} \right)^{-b}$$

The advantage of this function is that if plotted on a log-log scale, the function will be seen as a straight line with the slope of “- b”. This can be called “power law”.

$$\log \left(\frac{F(V)}{N_0} \right) = -b \log \left(\frac{V}{V_0} \right)$$

Now, if the amplitude in a decibel unit is replaced, the equation will be:

$$\log \left(\frac{F(A)}{N_0} \right) = -B(A - A_0)$$

where

$$B = b \frac{\log 10}{20}$$

A_0 = threshold amplitude (decibel)

It is postulated by Pollock (Pollock, 1981) that this b or B value is unique for each failure mechanism, and the log scale will remove the effect of wave attenuation. Therefore, the b or B value will not change with the distance between source to sensor, if all signals are attenuated equally (Pollock, 1981).

The b value can change during a test, which can be explained as the transition from one mechanism to another. Pollock stated that most of the b-values range is between 0.7-1.5, but it could be as low as 0.4 or as high as 4.0. The lower values are usually associated with discontinuous crack growth in high-strength brittle metals, whereas the high values can be from plastic zone growth prior to crack extension.

2.3.5.3 Amplitude vs Duration Plot

The plot of amplitude vs. log duration plot is useful for determining whether or not the AE data is genuine. The genuine data generally creates a triangle cluster on the plot (see Fig. 2.13), while the nongenuine hits such as mechanical rubbing and electromagnetic interference (EMI) appear in the area outside the triangle (Fowler, 1986).

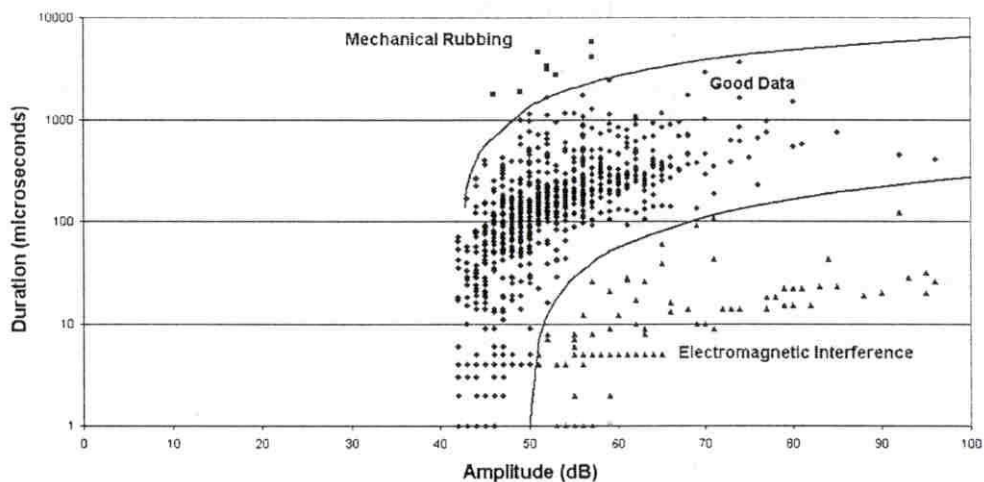


Figure 2.13: Amplitude vs Duration Plot Showing Good Data and Two Types of Unwanted Noise (Harvey, 2001)

2.3.5.4 Cumulative Signal Strength vs. Load (or Hits)

When damage occurs in a structure under an applied load, there will be some energy release. Part of this energy is transformed into the acoustic emission. Thus, the energy of the hits is directly related with the severity of the damage (Rotem and Altus, 1979, Bray and Stanley, 1997). Therefore, signal strength has become an important parameter for AE applications. As the load increases, more damages occur, and the graph of cumulative signal strength vs load generally shows the rise of the curve. At the ultimate load, the curve usually yields the steep rise as shown in Fig. 2.14. The historic index is the measurement of the rate of the slope, which some researchers used it to determine the onset of significant damage (CARP, 1999, Zeihl, 1998, and Tinkey, 2000).

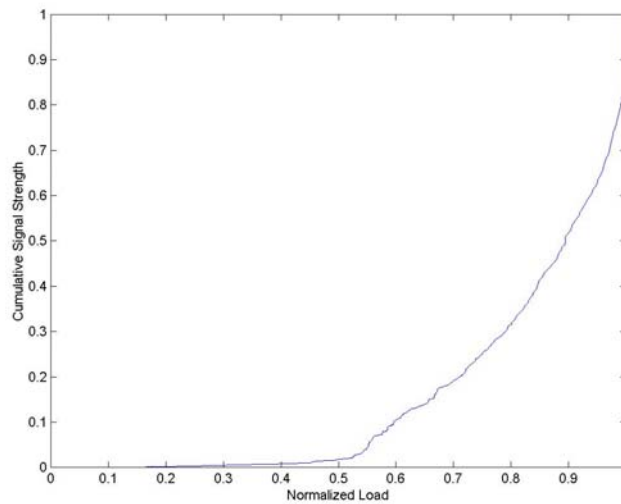


Figure 2.14: Normalized Cumulative Signal Strength vs Normalized Load Plot of Fiber Glass Composite Loaded in Tension Perpendicular to the Fiber Direction

2.3.6 Literature Review

2.3.6.1 Literature Review of Source Identification in FRP Based of b-Value

Pollock, A. A.

In the 1970s, Pollock published a paper on the application of the power law and b-value to acoustic emission (Pollock, 1978) and as discussed in Section 2.3.5.2.2, he expanded on this in a later paper (Pollock, 1981). The paper suggested other $\Phi(V)$ functions as described below:

1. log-normal model by Holt et al.:

$$\Phi(V) = \frac{1}{V\sigma\sqrt{2\pi}} e^{-(\ln(V/V_p))^2 / 2\sigma^2}$$

where

V_p = peak amplitude of the amplitude distribution function

σ = standard deviation of the natural logarithm of the peak amplitude.

2. Weibull distribution:

$$\Phi(V) = e^{-(V/V_p)^q}$$

where

q = parameter characteristic of the distribution function

3. Power law distribution:

$$\Phi(V) = \left(\frac{V}{V_o} \right)^{-b}$$

where

b = parameter characteristic of the distribution function

4. Statistical extreme value function proposed by Evans and Graham:

$$\Phi(V) = 1 - e^{-(V/V_p)^b}$$

where

b = parameter characteristic of the distribution function (because this model converges to a power law with exponent $-b$ in the high-amplitude range).

Valentin, D.

Valentin et al., 1983, conducted tensile tests on two types of composites, unidirectional and crossplied (0° , 90°) carbon FRP. He varied the direction of tension force from parallel to perpendicular to the fibers. The cumulative amplitude distribution plots of unidirectional composites were found to be linear, while they were bilinear for crossplied specimens. The relationship between initial b -values (b_1) and the angles (θ) between the fibers and the load are shown in Fig. 2.15. It was observed that the plot is not symmetric for the crossplied (0° , 90°) material. The authors attributed this to the confinement of the outer layer.

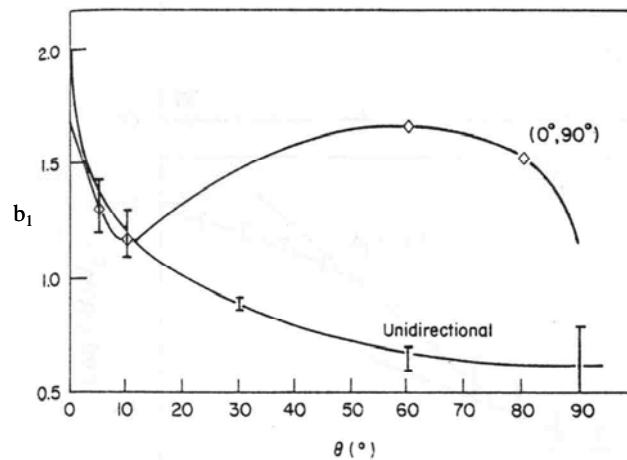


Figure 2.15: Variation of the Coefficient b_1 as a Function of θ for the Unidirectional and Crossply Composites (Valentin, 1983)

In addition, the unidirectional specimens emitted a large proportion of low amplitude hits when loaded in the parallel direction. From this, he concluded that

the carbon fibers, which have a very small diameter compared to glass fibers, generate low amplitude hits when fractured. A bigger proportion of high amplitude hits occurred when the angle is closer to 90 degrees. This suggested that the high amplitude hits were from matrix cracking parallel to the fiber. Matrix cracking perpendicular to the fiber was believed to be insignificant (Valentin et al., 1983).

Valentin (Valentin et al., 1984, and Valentin, 1985) stated the limitation of Pollock's equation and proposed the modified equation shown below:

$$F(V) = N_0 \left(\frac{V}{V_0} \right)^{-b} \frac{V_a^{-b} - V_0^{-b}}{V_a^{-b} - V^{-b}}$$

where

N_0 = total number of hits

V = amplitude in voltage units

V_0 = threshold amplitude in voltage units

V_a = a constant number

b = power law parameter

for a decibel units, the equation would be:

$$F(A) = N_0 \left(\frac{1 - \tanh B [(A - A_a) / 2]}{1 - \tanh B [(A_0 - A_a) / 2]} \right)$$

where

A = amplitude in decibel units

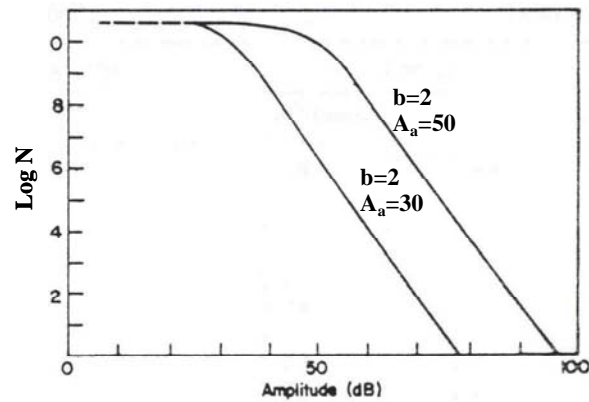
A_0 = threshold amplitude in decibel units

A_a = a constant number

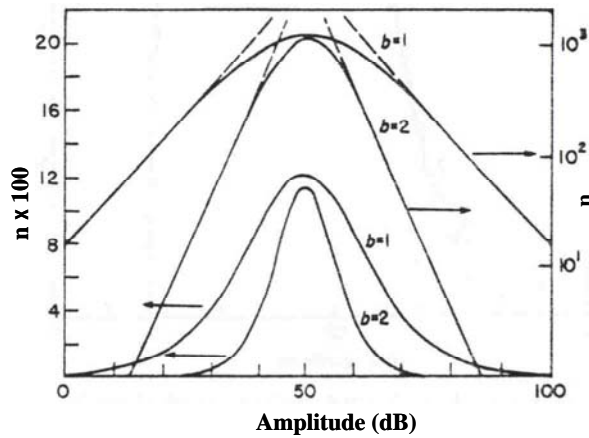
The cumulative distribution function is plotted in Fig. 2.16a, it was noticed that there was a small curve at the lower amplitude, while it was straight at the higher amplitude. The amplitude distribution function is:

$$f(A) = n_0 \left(1 - \tanh^2 B \frac{(A - A_a)}{2} \right)$$

The curve of this function looks like a normal distribution with a maximum point of “ n_0 ” at amplitude A_a (see Fig 2.16b).



a) Cumulative Amplitude Distribution



b) Amplitude Distribution

Figure 2.16: Plot of Distribution Functions Corresponding to the Modified Power Law Showing the Effect of the Parameters b and A_a (Valentin, 1985).

Figure 2.16b Shows the Plots with $b = 1$ and 2 on Linear and Log Scales.

Valentin et al., 1984, stated that the cumulative amplitude distribution of crossplied composites (carbon fiber in polystyrylpyridine, PSP) gave a bilinear slope with b_1 (lower amplitude) = 1.7, and b_2 (higer amplitude) = 0.2. The point of the slope change was at 65 dB. The value of b_1 from the crossplied composites was found to be close to the slope of the unidirectional specimens. With the modified power law, A_a was measured to be 25-34 dB for matrix cracking while it was 40 dB for fiber breakage. The A_a of interfacial debonding was found to be 47, 55, and 60 dB (Valentin et al., 1984).

Scarpellini, R.S., Swanson, T.L, Fowler, T.J., 1983

In 1983, researchers at Monsanto company conducted research on AE signatures from different defects. Cumulative amplitude distributions were studied, and a summary of their conclusions is shown below:

Inclusion: The cumulative amplitude distribution showed a bilinear slope, with $b = 2$ at lower amplitude and $b = 1$ at higher amplitude. They suggested that there were 2 failure mechanisms in inclusion specimens.

Star Crack (Impact Induced Crack): Only one slope of $b = 2$ was found for this defect.

Delamination (Resin Rich Interface Layer): Only a slope of $b = 2$ was found.

Dry Spot (Resin Starved Inner Layer): A slope of $b = 1.4$ was shown.

2.3.6.2 Literature Review of Source Identification in FRP Based on AE Parameters

Barnes, C. A., and Ramirez, G., 1998

Barnes and Ramirez conducted a research at the University of Texas at Austin. Twenty-foot long, twenty-two inch diameter carbon fiber composite pipes were pressurized, and monitored with AE (by 150 kHz resonant sensors).

They stated that the results agreed with Monsanto's work (Scarpellini, Swanson, and Fowler, 1983) that AE hits with amplitude of 40-60 dB and duration of 2,000-10,000 microseconds were from delamination, whereas lower amplitude hits were from matrix cracking. It was also found that the carbon fiber composites gave more 100-dB hits than the glass fiber composites, from which they concluded that the carbon fiber breakage gave higher amplitude events than the glass fibers. Since the carbon fiber's diameter is smaller than the glass, it is believed that amplitude is more related to the stiffness of the strand than to its size. In addition, the waveform of the hits were recorded and they showed that delamination can be associated with low amplitude, long duration, and low frequency, while fiber breakage yielded high amplitude, short duration, and a wide range of frequencies.

It is note that the result from this paper does not agree with Valentin's paper (see 2.3.6.1, Valentin, 1983), which stated that the carbon fibers generated low amplitude hits.

Berthelot, J. M., and Billaud, J., 1983

Berthelot and Billaud conducted an experiment with steel fiber-epoxy composites. The amplitude distribution of the testes showed several peaks. Each peak was believed to represent a different failure mechanism. The peak of 21-24 dB was suggested to correspond with matrix cracking, while the 36-40 amplitude peak was believed to be from crack initiation in the matrix. The peak of 48-49 dB was suggested to be fiber end pulling out, whereas the peak of 60-62 dB was concluded as fiber fracture.

Berthelot, J. M., and Rhazi, J., 1986

Berthelot and Rhazi divided the paper into two parts. First, they categorized three types of amplitude distribution in composite materials as explained below:

1. Discontinuous distribution (Fig 2.17a)

2. Continuous distribution (Fig. 2.17b)
3. Intermediate distribution (Fig. 2.17c)

The continuous distribution is the most common type for composites. It involves a mix of several basic mechanisms in a complex rupture process. Discontinuous distributions were typically found in the laboratory experiment. Intermediate distributions were observed in the case of sheet molding compounds with good interlaminar bond.

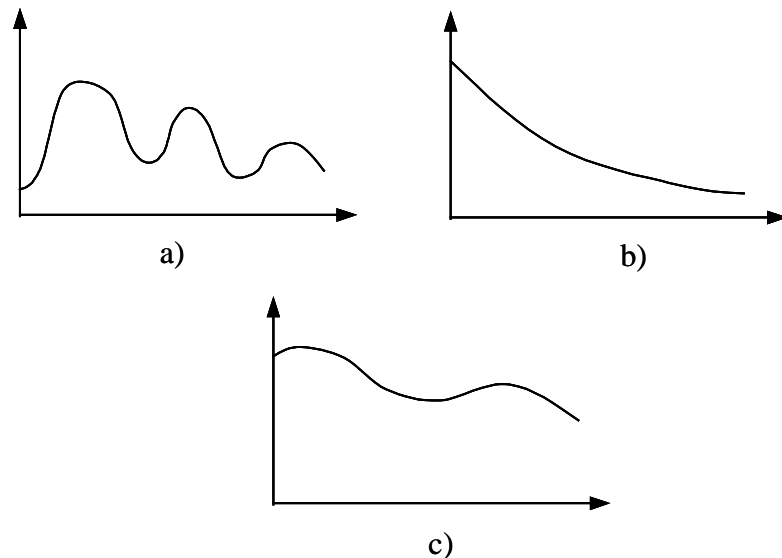


Figure 2.17: Three Different Types of Amplitude Distribution a) *Discontinuous* b) *Continuous* c) *Intermediate* (Adapted from *Berthelot and Rhazi, 1986*)

Second, Berthelot and Rhazi explained the detail of the rupture processes. Damage initiation occurred at low deformation. Only the microstructure was effected and AE was found to correspond with high amplitude. The propagation phrase occurred at a higher deformation and the scale was macroscopic. This phrase was associated with a low amplitude range of AE hits.

Crosbie, G. A., and Guild, F. J., 1983

Crosbie and Guild studied AE in glass fiber composites with a polyester resin. They suggested the use of amplitude distribution, and the plot of load vs. cumulative events to classify failure mechanism types. The onset of AE in various amplitude ranges was also suggested.

Crump, T. N.

Crump and his colleague (Crump and Droge, 1979) tested 243 FRP samples with AE. The samples were made of two types of resins, Atlac 382-05A and Derakane 411-45. Also, the samples had variations of glass content, and laminate structures. Part of the testing program was conducting tensile testing of samples with 3 different glass contents. They found that more AE activity was found in the higher glass content specimens. Thus, it was concluded that the majority of AE hits came from fiber breakage. Also, the amplitude of AE data was related to the level of stresses released.

Later in 1981, Crump (Crump, 1981) published another paper based on the same testing program. He stated that the FRP specimens did not exhibit any AE until the 0.55% strain was reached. Other AE characteristics of several damage mechanisms were identified as described in Table 2.5. This lab test program played an important role in the establishment of CARP Recommended Practice.

Table 2.5: AE Characteristics of Equipment Damage (Crump, 1981)

Anomalies	Area	Active sensors	Amplitude	AE counts	Type Damage
Mechanical damage	Usually localized	≥ 1	High	High	Fiber breakage
Defect in construction	Usually localized	1-3	Low	High	Resin and fiber bond breakage
Defective resin bond	Localized	1-3	Low	High	Resin bond breakage
Defective fiber reinforced bond	Localized	1-3	High	High	Fiber bond breakage
Overall chemical attack	Wide	Many	Low	High	Resin crack fiber bond break
Localized chemical attack	Localized	≥ 1	Low	High	Resin crack fiber bond break

Ely, T. M., Hill, E. v. K., 1992

Ely and Hill performed a tensile test of a graphite/epoxy composite, and tried to characterize its failure mechanisms. The main parameters used for the analysis were duration, risetime, and counts. After the duration distribution was plotted, it appeared that the majority of the durations fell between 0 to 40 microseconds. At this point, they made an assumption that those hits were matrix cracking. They decided to filter these hits (duration of 0-40 microseconds) to explore what other mechanisms also occurred. Surprisingly 3 humps appeared on the duration and risetime distribution plot as shown in Fig. 2.18.

The hits from the first hump (duration of 41 to 72 microseconds) were analyzed. It was found that the risetime fell between 1 to 24 microseconds, and

amplitude distribution plot showed that the peak amplitude fell around 58 dB. The authors concluded that these hits were fiber breakage.

The hits from the second hump (duration of 73 to 126 microseconds) were analyzed. It appeared that the risetime fell from 25 to 60 microseconds, and the amplitude distribution plot indicated the peak amplitude of 63 dB. It was concluded that these hits were from fiber pullout.

The hits from the last hump (duration more than 127 microseconds) were also analyzed. The risetime was found more than 61 microseconds, and the peak from the amplitude distribution plot was at 69 dB. This was believed to be longitudinal splitting.

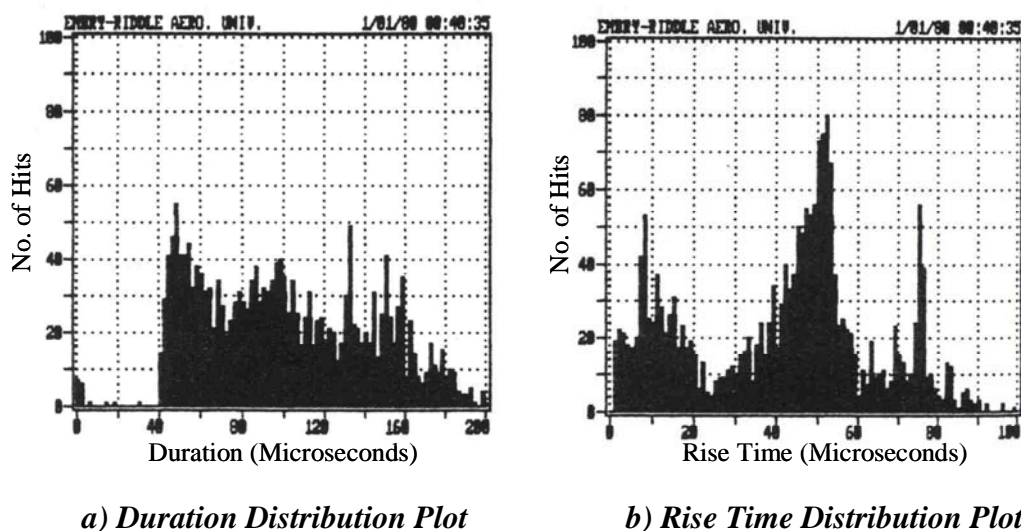


Figure 2.18: Duration and Rise Time Distribution Plot After Removing Hits from Matrix Cracking (Adapted From Ely, 1992)

Favre, J. P., and Laizet, J. C., 1989

AE analysis of crack accumulation in CFRP crossplied laminates under tensile loading was conducted. AE was compared with radiography to verify cracks. It was found that there was a direct relation between high amplitude hits and the number of cracks. They also stated that every high amplitude event was followed by a group of events with various amplitudes. This was believed to be due to 1) the microcracking on both sides of the crack when it propagated, and 2) the friction between the debonding or crack's surface.

Gorman, M. R.

Gorman and Foral, 1986, studied the amplitude distribution of glass/epoxy and graphite/PEEK composites. They found 3 peaks at 35, 44, and 70 dB for glass/epoxy composite, whereas only 2 peaks of 66 and 96 dB were found in graphite/PEEK specimens.

Gorman and Rytting, 1983, conducted research dealing with filament wound graphite/epoxy laminate tensile coupons. Resonant sensors of 150 kHz were used with band pass filter of 100-300 kHz. Long duration AE events (3 milliseconds) were found, which was associated with macroscopic matrix cracking. In addition, high amplitudes (85 dB or more), which normally were believed to be from fiber breaks, were found as matrix cracking.

Guild, F. J.

Guild, F. J., 1985, introduced new modified parameters, which were:

1. Cumulative event count by amplitude range: $N_R = \sum_{i=h}^k n_i$

where

h and k = the lower and upper limits of an amplitude range

2. Event count rate by amplitude range: $N_R = \frac{\Delta N_R}{\Delta t}$

where

Δt = a specified sampling interval, commonly 5 seconds

ΔN_R = the total increase of N_R within Δt

3. Share of cumulative event count by amplitude range: $C_R = \frac{N_R}{N} \times 100$

where

N = the total event count.

4. Share of differential event count by amplitude range: $D_R = \frac{\Delta N_R}{\Delta N} \times 100$

where

ΔN = a chosen increment in total event count, commonly 1000 events

ΔN_R = the total increase of N_R within ΔN .

Guild suggested that plotting the above parameters with stress would help better present AE data and failure mechanisms.

Harvey, D. W., 2001

Harvey conducted research based on AE background noise during an aerospace composite fatigue test. Harvey introduced the Average Slope of Wave Rise (ASOWR), which is the average slope between the beginning to the peak of the waveform or:

$$\frac{\textit{Amplitude} - \textit{Threshold}}{\textit{Risetime}}$$

A very high value of ASOWR indicated acoustic emission from EMI, while a very low ASOWR indicated mechanical rubbing. This parameter was useful for filtering unwanted data. However, more research was needed to apply ASOWR with the full-scale specimens.

Kwon, O., and Yoon, D. J., 1989

Their paper presents the introduction of energy distribution plot, which was obtained from CFRP tensile test. It was found that the energy distribution plots of (0°/90°) crossply laminates did not show high energy signal compared to the ones of ±45° samples.

Li, L., and Zhao, J. H., 1986

Li and Zhao monitored damage growth processes in 4 types of specimens, which are described below (also see Fig. 2.19).

1. **Pure resin:** Most of the hits detected from this specimen were lower than 40 dB.
2. **Pure fiber:** Eighty percent of the hits were higher than 76 dB.
3. **Debonding:** Amplitude was broadly distributed.
4. **Delamination:** A peak between 52 to 78 dB on the amplitude distribution plot was detected.

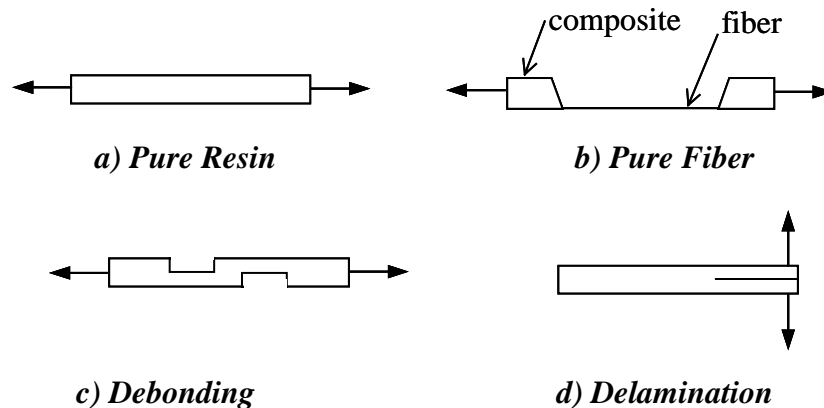


Figure 2.19: Four Types of Specimens from Li's Research (Adapted from Li, and Zhao, 1986)

Mason, J. J., Valentin, D., 1989

Mason and Valentin did an experiment on proof testing unidirectional glass fiber reinforced plastic. Eleven specimens were tested up to 50 percent of their ultimate load. It was found that fiber ruptures were the main AE mechanism of the test. However, matrix cracking around broken fibers, interface decohesion, and fiber pullout could also be found. The main peak of amplitude distribution plot was about 40 to 50 dB, which was believed to correspond with a single fiber failure. The highest amplitude peak was around 70 dB referring to simultaneous fiber breakage.

Merienne M. C, and Favre, J. P., 1989

Merienne and Favre studied signature analysis of AE signals from fiber ruptures. This study was conducted on SiC fiber/metallic matrix composites. The results were compared with scanning electron microscope (SEM). It was found that there were multiple cracks at the ends of a fiber break. This corresponds with the AE signal as shown in Fig 2.20. The picture also shows the comparison with the AE waveform of matrix dislocation. This signal consisted of multiple bursts, which were close to each other and could not be distinguished.

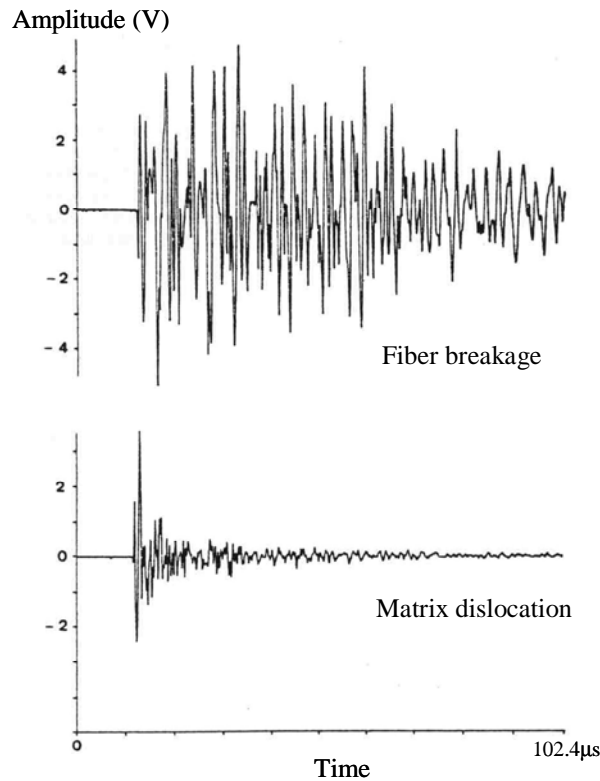


Figure 2.20: AE Waveforms of SiC Fiber/Metallic Matrix Composite (Merienne and Favre, 1989)

Mielke, W., et al , 1989

Mielke et al. conducted research on single fiber pullout tests, in which a fiber was partially embedded in a thermoplastic matrix. It was found that there were 2 types of pullout mechanisms: single pullout, and multiple pullouts as shown in Fig. 2.21.

Fiber breaks occurred in some tests. They stated that the pullout mechanisms could not be identified by amplitude or energy because there was an overlapping of fiber pullout and fiber breaks on the same energy and amplitude scale. However, frequency analysis could differentiate between these mechanisms, because fiber rupture yielded high frequency components.

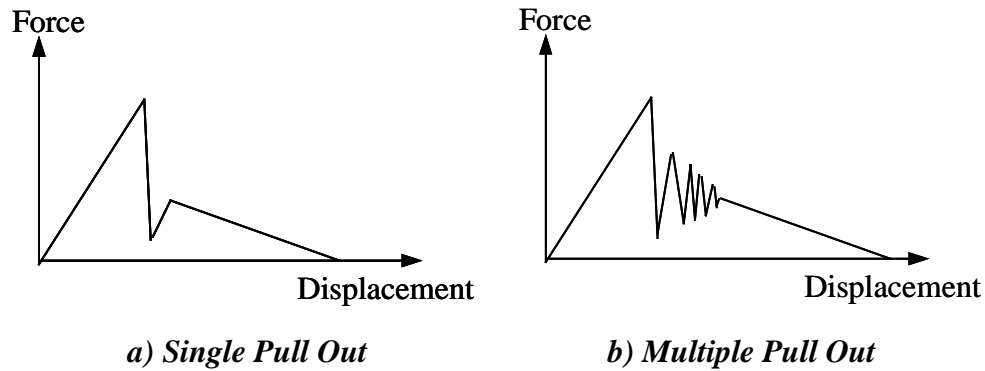


Figure 2.21: Force vs. Displacement Diagram from the Fiber Pull-Out Tests
(Adapted From Mielke, 1989)

Pollock, A. A.

Besides his introduction of cumulative amplitude distributions and b-values described earlier, Pollock (1981) suggested the “average amplitudes”, which is described as equation:

$$\bar{A} = A_0 + \frac{20}{b \ln 10}$$

where

\bar{A} = average amplitude

A_0 = threshold amplitude

He stated that the plot of the graph $\log \bar{A}$ vs. time was a very promising way to analyze AE data. The advantages of this method are that it is easy to compute, can be performed in real time, and is easy to understand.

In 1978, he published a paper, which presents the amplitude distribution plot of a bending test on a fiberglass specimen with ± 70 degree fiber orientation

The plot in Fig. 2.22 shows 3 peaks, which usually represent matrix crazing, debonding/delamination, and fiber breakage. This distribution is sometimes referred to as the Wadin “W” in recognition of the contribution of Jim Wadin, a colleague of Dr. Pollock.

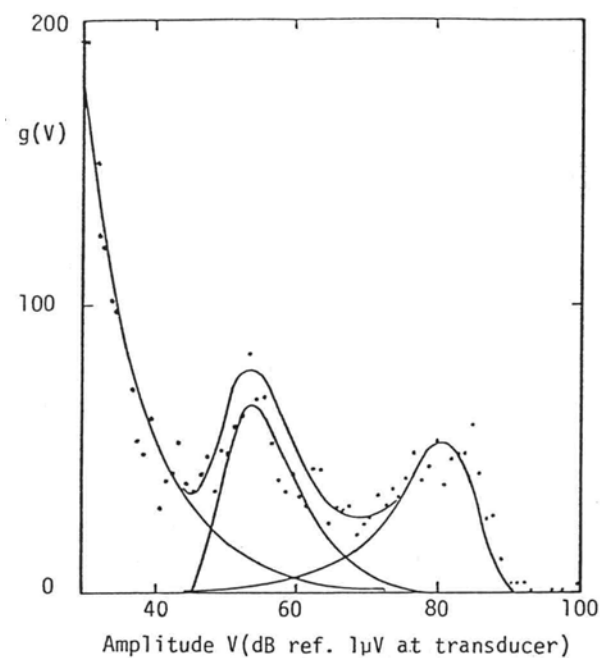


Figure 2.22: Amplitude Distribution Plot of Fiberglass Showing Triple Peaks (Pollock, 1978)

Roman, I., et al., 1986

Roman studied the AE signature of Kevlar-epoxy composites (unidirectional) loaded in tension. Resonant sensors and a 250-500 kHz filter were used. The stress-strain curve of the test was bilinear, with a change point at about 70 percent of the ultimate load. This was because the specimen became stiffer due to straightening of the fibers. It was also found that Kevlar fiber

strength did not vary much since less than 2 percent of the fibers broke before the maximum load. The plot of count rate vs. stress of the specimens showed that the count rate increased at the beginning of the test up to 30 percent of the load, then it dropped. At 60 to 70 percent of the ultimate load, the count rate started to pick up again and finally reached its maximum at failure.

The author introduced a new parameter, C-ratio, which is described as:

$$C - ratio = \frac{\text{No. of hits below } 65 \text{ dB}}{\text{No. of hits higher } 65 \text{ dB}}$$

As plotted in Fig. 2.23, it was shown that the first part of the plot (C-ratio decreased) represented the debonding stage of fibers that were already straightened. After reaching 70 percent of the load, the C-ratio increased. This was believed to be from matrix fractures, debonding, and friction. At failure, the C-ratio dropped suddenly, which corresponds with fiber breaks.

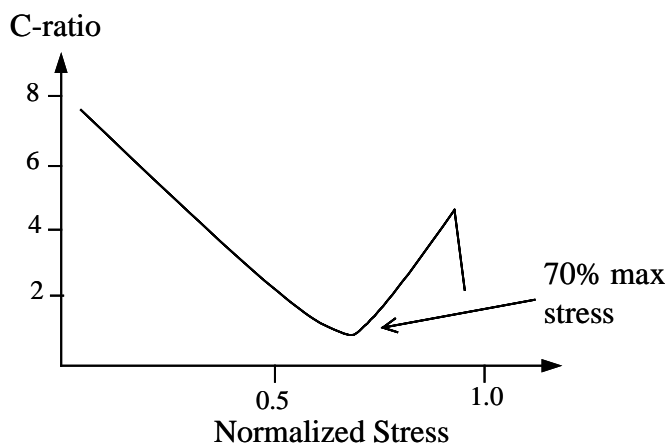


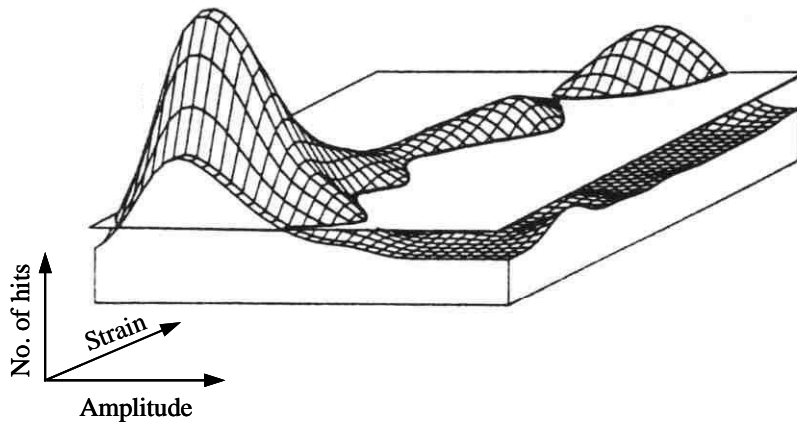
Figure 2.23: C-Ratio vs. Stress for Kevlar Epoxy Composite Loaded in Tension
(Adapted From Roman et al., 1986)

Shiwa, M., et al ., 1986

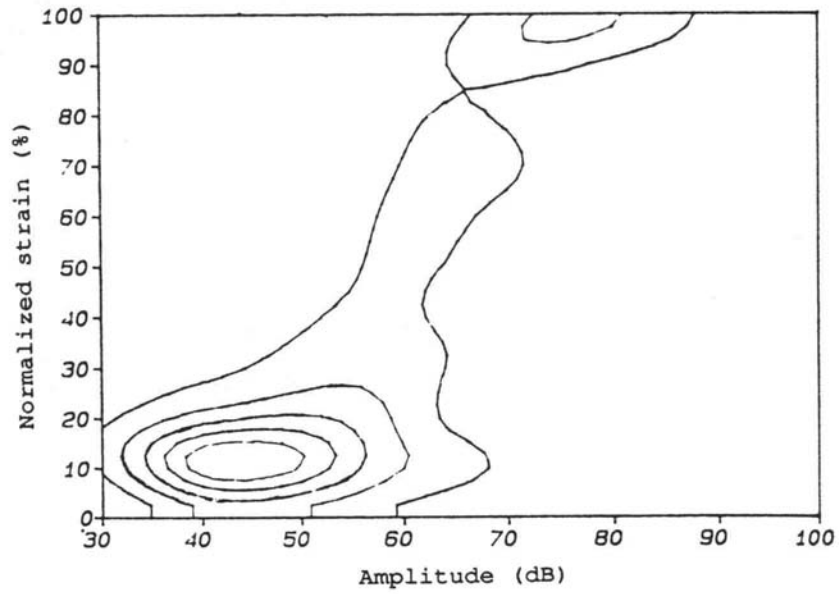
Shiwa et al., 1986, conducted AE research with tensile loading and load holds of laminated fiberglass epoxy composites. Two types of specimens (notched and unnotched specimens) were tested. It was found that for both specimens, AE counts increased rapidly at 60 percent of ultimate strength. The amplitude distribution curves were plotted showing that the peak of the curve was at 60 dB (at failure) for the notched specimen, while it was at 50 dB for the unnotched specimen.

Surrel, Y., and Vautrin, A., 1989

A new way of displaying the amplitude distribution plot was introduced in this paper. A series of amplitude distributions were made along with the stress (or strain) as shown in Fig. 2.24a. Then the plot was transformed to be a contour mapping as shown in Fig. 2.24b. However, it was stated in the paper that this map was not very successful in presenting data.



a) 3-Dimension



b) Contour Map

Figure 2.24: Proposed New Technique to Present Amplitude Distribution
(Adapted From Surrel, 1989)

Wagner, J., et al ., 1992

Wagner and his co-authors pointed out four very interesting statements, which were:

1. When comparing AE from the lab environment (small scale) to the field (full-size specimen), three problems had to be considered:
 - a. Distance from source to sensor
 - b. Dispersion
 - c. Attenuation

These effects alter the shape of the waveforms significantly as the waves travel longer in the full-size specimens.

2. Parameters that were affected by the size of the specimens were:
 - a. Time of arrival source location
 - b. Rise time analysis
 - c. Sensor and array lockouts
 - d. Guard sensors
 - e. Frequency analysis
 - f. Long dead time
 - g. Event definition time
 - h. b-value analysis
3. Parameters that were not affected by the size of specimens were:
 - a. AE during load hold
 - b. Felicity effect
 - c. Number of high amplitude events
4. For composite materials, it has been reported that moving AE from a small scale to a full-scale specimen seemed to be successful. An example is the CARP Recommended Practice.

Walker, J. L., and Hill, E. v. K., 1992

Walker and Hill conducted research predicting ultimate strength of the 6-graphite/epoxy tensile specimens based on statistics of AE parameters. The specimens were made of unidirectional graphite in epoxy resin. From the AE data, amplitude distributions at 25% of the ultimate load were plotted. Then, the plots were modeled by using Weibull distribution, which had 3 parameters (b as a skewness of the curve, A_0 as an amplitude at threshold, and θ as an average amplitude). The results showed that the parameter b correlated well with the ultimate strength of the specimens. They also explained that the higher b (skewness) was associated with high amplitude activities. This indicated that the specimens were subjected to a more evenly distributed loading, which can be inferred as better quality structures. In contrary, a lower value of b indicated a large number of low amplitude matrix cracking around a stress concentration. Thus, the quality of the structure was low with the low b value. In the author's (Ativitavas) opinion, this does not seem to be correct, as it could be other factors such as type of reinforcement (woven roving, mat, or unidirectional) and orientation of fibers.

The value θ did not correlate well with the ultimate strength but it was believed to be a parameter that was dependent to the material attenuation. They also suggested adding the energy parameter to the analysis since energy was not as affected by attenuation and dispersion as was the amplitude. Therefore, using the number of high-energy events could improve the ultimate load prediction if full-scale tests were conducted.

In addition, they stated that matrix cracking generally had low energy, short-to-moderate duration, and low amplitude hits, whereas fiber breakage yielded high energy, short duration, and moderate-to-high amplitude hits.

Delaminations, however, were identified as high energy, long duration, and moderate-to-high amplitude hits.

Yamaguchi, K.

Yamaguchi and his coworkers (Sakakibara et al., 1984, Yamaguchi et al., 1984a, and Yamaguchi et al., 1984b) invented an interesting parameter called energy moment (T_{em}). This parameter is a ratio of signal moment area under a waveform envelope to the energy of that particular hit as shown in the equation and Fig. 2.25 below.

Energy, E_t

$$E_t = \int_{t_1}^{t_2} f^2(t) dt$$

Energy moment, T_{em}

$$T_{em} = \int_{t_1}^{t_2} f^2(t)t dt / E_t$$

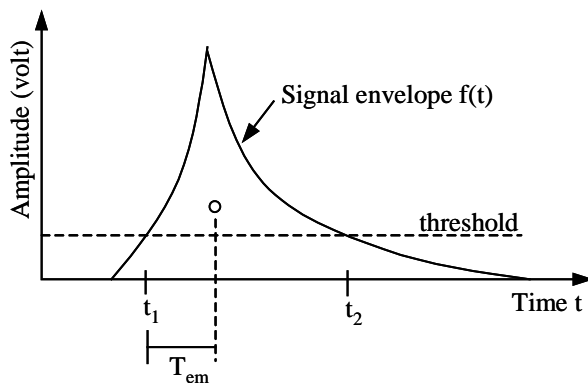


Figure 2.25: Illustration Description of Energy Moment T_{em}

This technique is essentially the center of gravity of the energy versus time plot. The authors conducted a fatigue test of an austenitic stainless steel pipe with AE monitoring. The energy moment distributions of various levels of cycles were plotted. It was found that at different cycles, the distribution curves peaked at slightly different values of energy moment (Yamaguchi, 1984).

2.4 NEURAL NETWORKS

2.4.1 Introduction

The field of neural networks has been developing for more than 50 years in the attempt to simulate the human brain on computers. The inspiration for developing neural networks came from the fact that a human's brain can do many things without mathematical explanation, such as recognizing friends' faces or differentiating between cats and dogs. These abilities come from past personal experience (Fausett, 1994).

Likewise, a neural network is a computerized program that arranges its structure based on a database and is able to give the "most-likely" correct answer. For example, if a record of weather in the past 200 years is available, neural networks can learn the pattern of weather, and be able to predict the pattern of the future weather based on the pattern of the present and immediately preceding weather. Therefore, larger databases are preferred to achieve better accuracy. Neural networks not only can perform prediction problems, but they can also solve pattern recognition, classification, and optimizing problems. Pattern recognition of AE defect data by neural networks is an area in this research program.

2.4.2 Artificial Networks

As discussed previously, artificial networks are modified from biological neural systems. A biological neural network consists of biological neurons (i.e., a brain or nerve cell). A signal, which is in a form of electric impulses, is transmitted from a neuron to another by means of a chemical process. The incoming signal can be modified by scaling the signal's frequency. Then all the incoming signals are summed in a neuron. When sufficient input is received, the cell fires a signal to the next neuron.

An artificial neural net consists of several artificial neurons connected to each other. Input information, which could be a series of numbers, is received at the input neurons. Then the information is transferred through subsequent neurons to the end. As the data travels through the net, the information is modified, and mathematical operations are performed. At the end, the output neurons will show a series of simple numbers, which indicate the answer. For example, if the outcomes of the two output neurons are 0 and 1, it may indicate "not raining", while 1 and 0 may indicate "raining".

Usually the neurons are arranged into different layers (see Fig. 2.26). Each neuron in each layer performs a different activity as described below:

1. Input neurons only receive information in the form of numbers. They transfer the data to the next layer. Neurons in the input layer perform no calculation.
2. Hidden neurons receive information from the input neurons or other hidden neurons through the connections. Each connection has a multiplier (weight) to multiply the signal before entering the hidden neuron (see Fig. 2.27). A hidden neuron usually receives more than one signal. The entire signals will be combined together and substituted into an activation function. The output of the activation function will then be transferred to the following neurons (usually output neurons but sometimes hidden neurons). At this point, many

calculations are performed in the hidden layer giving ability to neural networks to solve many complex problems.

3. Output layer neurons behave similarly to the ones in the hidden layer except that the pattern of the outcome from output neurons indicates the answer of the problem.

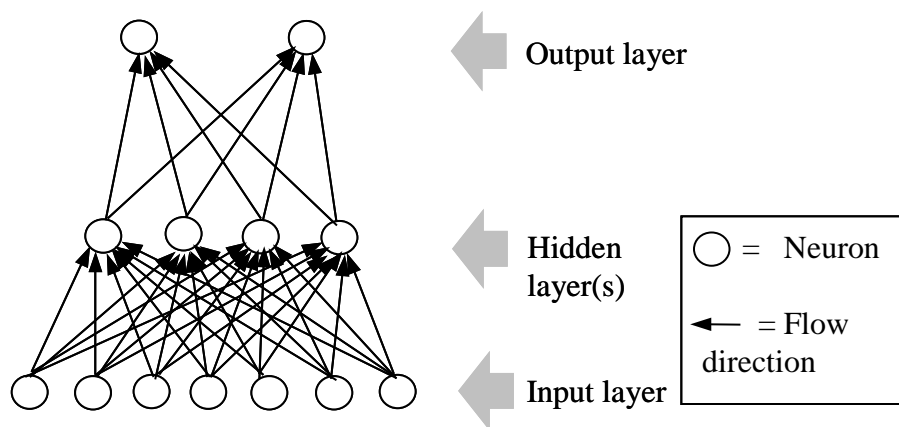
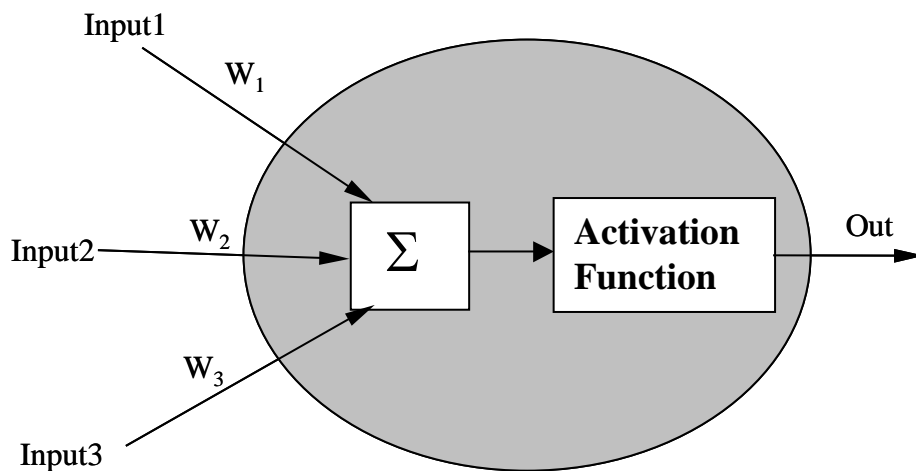


Figure 2.26: Basic Architecture of a Simple Neural Network (Fausett, 1994)



$$\Sigma = \text{Input1} \times W_1 + \text{Input2} \times W_2 + \text{Input3} \times W_3$$

Figure 2.27: Artificial Neuron (Fausett, 1994)

The networks that have only input and output layers are called single-layer networks, whereas the networks with one or more hidden layers are called multilayer networks. Single-layer networks are crude, and are limited in solving basic problems such as exclusive OR problem (XOR). Multilayer networks, however, are powerful, and can solve more complicated problems. Normally, one hidden layer is sufficient to solve most of the complex problems. Two hidden layers can solve some special cases, however it takes more time to train these networks (Fausett, 1994).

2.4.3 Bias

A bias can be included in the network by adding a neuron, which its activation is always 1. Therefore, a bias behaves as a weight input to the following neuron, which helps adjust the summation value as shown below.

$$\Sigma = 1 \times W_0 + \text{Input1} \times W_1 + \text{Input2} \times W_2 + \dots$$

2.4.4 Activation Function

As discussed in 2.4.2, the activation function is a part of an artificial neuron. Normally, all the neurons in a network have the same activation function. There are several types of activation functions:

1. Binary Step Function (with Threshold θ)

$$f(x) = \begin{cases} 1 & \text{if } x \geq \theta \\ 0 & \text{if } x < \theta \end{cases}$$

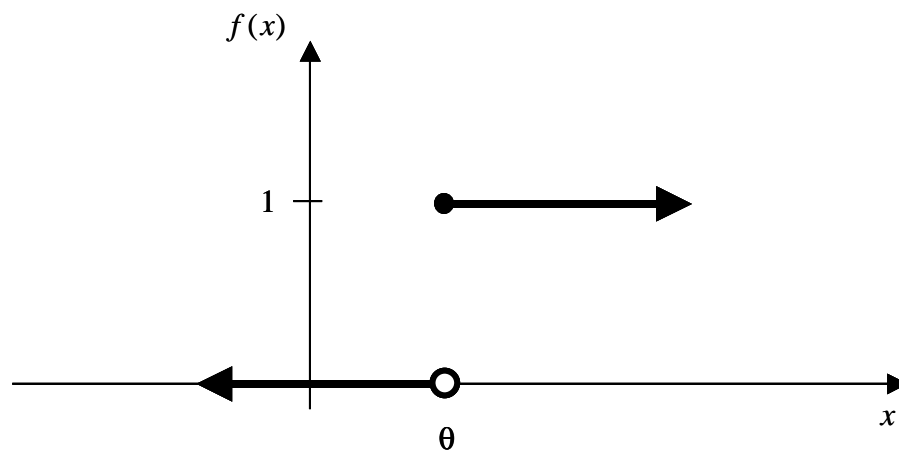


Figure 2.28: Binary Step Function

2. Binary Sigmoid:

$$f(x) = \frac{1}{1 + \exp(-\alpha x)}$$

and

$$f'(x) = \alpha f(x)[1 - f(x)]$$

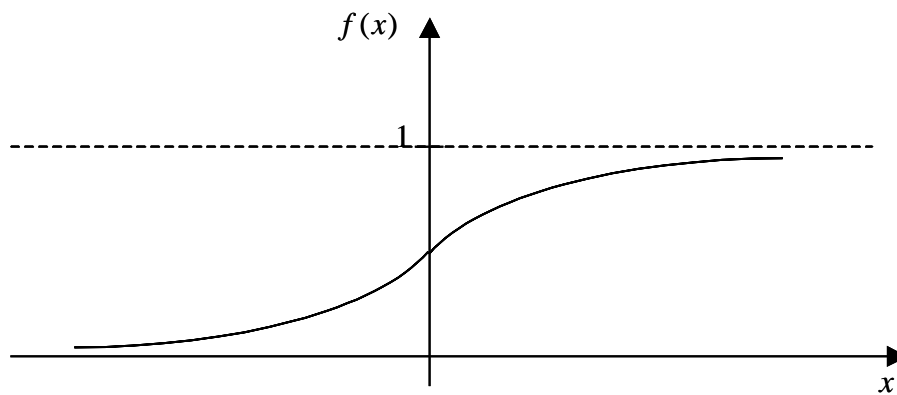


Figure 2.29: Binary Sigmoid Function

3. Bipolar Sigmoid:

$$\begin{aligned}g(x) &= 2f(x) - 1 = \frac{2}{1 + \exp(-\alpha x)} - 1 \\ &= \frac{1 - \exp(-\alpha x)}{1 + \exp(-\alpha x)}\end{aligned}$$

and
$$g'(x) = \frac{\alpha}{2} [1 + g(x)][1 - g(x)]$$

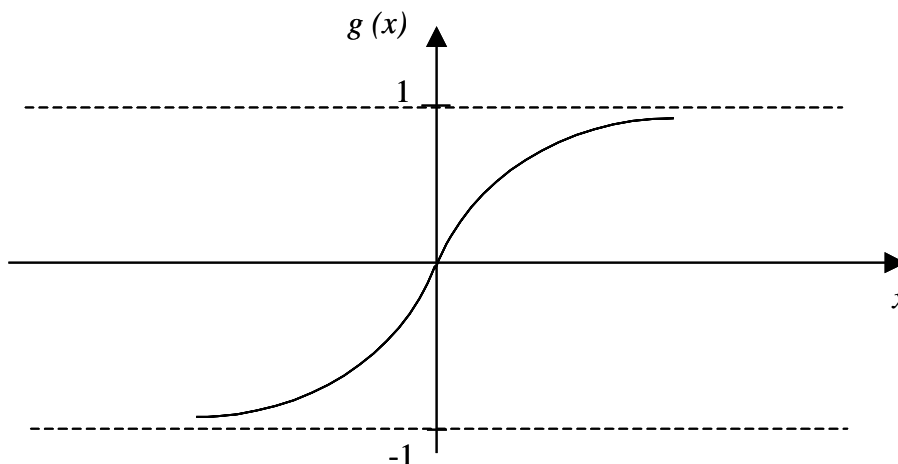


Figure 2.30: Bipolar Sigmoid Function

2.4.5 Training

Training the networks is the key to making the networks work. There are two major methods to train the networks.

The supervised training method allows networks to compare the output result with the real answer for every set of training input. The difference between the output and the answer is called “error”. The computer will adjust the weight of each connection in such a way to reduce the error. At the beginning, the

networks might experience a large error. However, after several cycles of training with the set of data, the error will be reduced.

Unlike supervised, the unsupervised training method does not depend of comparing the answer to the output. The networks will organize the data in a way they see fit (NeuralWare, 2000). A self-organizing map, which is a program that performs classification problems, is an example of this type of training. It works by arranging the input data into different groups or clusters depending on similarity.

In this dissertation, only backpropagation and probabilistic based training methods (supervised) will be discussed.

2.4.6 Backpropagation Neural Networks

2.4.6.1 Network Architecture

Backpropagation nets utilize a training method using backward error distribution (Fausett, 1994). The training of a network has three steps (see Fig. 2.31):

1. Feedforward of the Input Training Pattern

Each input neuron (\mathbf{X}_i) reads an input signal from the data file and feeds the signal to each hidden neuron ($\mathbf{Z}_1, \dots, \mathbf{Z}_p$). Each hidden neuron will sum the receiving signal and pass it to the activation function. The output from the activation function (z_j) will be fed to the output neuron. Each output neuron (\mathbf{Y}_k) will sum the receiving signal and compute its activation (y_k), which become the output of the network.

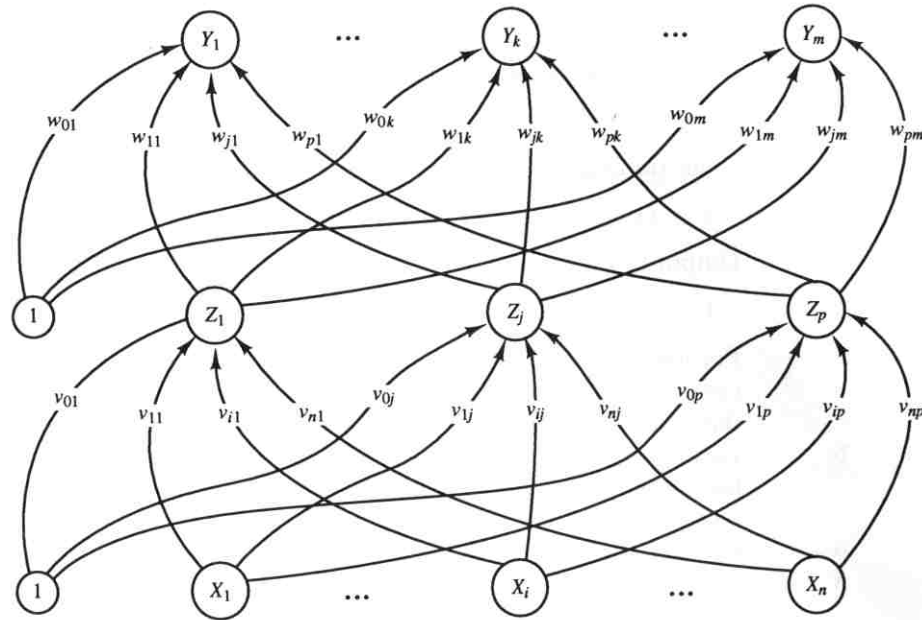


Figure 2.31: Backpropagation Neural Network with One Hidden Layer
(Fausett, 1994)

Algorithm:

Each hidden neuron (Z_j , $j = 1, \dots, p$) sums its weighted input signals from the input neurons (X_i , $i = 1, \dots, n$),

$$z_in_j = v_{0j} + \sum_{i=1}^n x_i v_{ij}$$

and applies its activation function to compute its output signal,

$$z_{jk} = f(z_in_j)$$

Each output neuron (Y_k , $k = 1, \dots, m$) sums its weighted input signals,

$$y_in_k = w_{0k} + \sum_{j=1}^p z_j w_{jk}$$

and applies its activation function to compute its output signal,

$$y_k = f(y_{in_k})$$

2. Backpropagation of the Error

At this step, each output neuron compares its output y_k with the actual answer (target), t_k . The error, or the difference, will be determined and the correction factor δ_k ($k = 1, \dots, m$) is computed based on this error. This factor, δ_k , which carries the error information is then distributed back to all the hidden neurons z_j . Similarly, each hidden neuron Z_j will sum the error input and compute δ_j and distribute it back to the input layer.

Algorithm:

Each output neuron (Y_k , $k = 1, \dots, m$) compares the output with the real answer and compute the correction factor accordingly,

$$\delta_k = (t_k - y_k) f'(y_{in_k})$$

Each hidden neuron (Z_j , $j = 1, \dots, p$) sums its error inputs,

$$\delta_{in_j} = \sum_{k=1}^m \delta_k w_{jk}$$

and multiplies by the derivative of its activation function to compute its error factor,

$$\delta_j = \delta_{in_j} f'(z_{in_j})$$

3. Weight Adjustment

While the correction factor δ_k is being distributed back to the hidden neurons, it will adjust the weight, w_{jk} . Likewise, the weight, v_{ij} , between input layer and hidden layer will be adjusted according to the correction error δ_j .

Algorithm:

The weight adjustment term for the weight between hidden and output layer is calculated.

$$\Delta w_{jk} = \alpha \delta_k z_j$$

where

α is learning rate

Then the weight adjustment term for the weight between input and hidden layer is calculated.

$$\Delta v_{ij} = \alpha \delta_j x_i$$

The learning rate is a factor to decide how big the weight adjustment can be at a time. If the adjustment is too big, the error might not fall to the global minimum. However, if the adjustment is too small, it might take a long time for the error to fall to the global minimum or the error might get stuck at the local minimum (see the simplified model in Fig. 2.32).

After the first training set, a better network (the weights are adjusted) will be obtained. Then additional training sets will be applied to the network to reduce more and more error, and eventually the network will become an optimized network with a very small error.

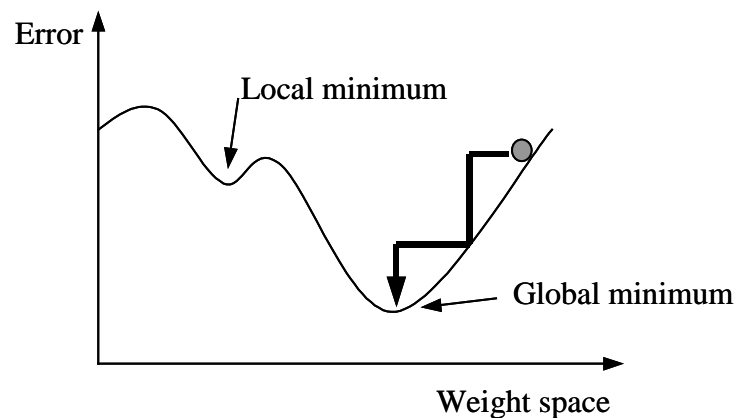


Figure 2.32: Simplified Diagram Showing Local and Global Minimums of Neural Network Performance (Miikkulainen, 1999)

2.4.6.2 Delta Rule

The weight adjustment technique mentioned in the backpropagation neural networks section is called the “delta rule”, which is one of the methods normally used for backpropagation networks. The delta rule is based on minimization of the squared error for each training set.

The squared error for a particular training set is

$$E = (t - f(y_in))^2$$

Fausett stated that

“E is a function of all of the weights, w_i , $i = 1, \dots, n$. The gradient of E is the vector consisting of the partial derivatives of E with respect to each of the weights. The gradient gives the direction of most rapid increase in E: the opposite direction gives the most rapid decrease in the error” (Fausett, 1994).

Therefore, if the weights are adjusted in the direction of $-\frac{\partial E}{\partial w}$, the error will be decreased.

Thus,

$$-\frac{\partial E}{\partial w_i} = -2(t - f(y_in)) \frac{\partial f(y_in)}{\partial w_i}$$

where

$$f(y_in) = y_k$$

and

$$y_in = \sum_{i=1}^n x_i w_i$$

Therefore,

$$-\frac{\partial E}{\partial w_i} = -2(t - y_k) x_i f'(y_{in})$$

Given

$$\delta_i = (t - y_k) f'(y_{in})$$

Therefore,

$$\Delta w = \alpha \delta_i x_i$$

2.4.7 Probabilistic Neural Networks

Unlike backpropagation networks, probabilistic neural networks (PNN) provide a different way of training. PNN constructs probability density functions (PDFs) based on training samples, and these functions in turn act as classifiers. The training process for PNN is more time efficient than back propagation since it requires only one time calculation. PNN was introduced by Specht using Bayes decision strategy and nonparametric estimators of probability density functions (Specht, 1990).

2.4.7.1 Bayes Decision Strategy

This decision rule is mainly used for classification problems. It is simple, but can be applied to a multi-category problem. To simplify the explanation, only a two-category case (A and B) will be discussed here.

If the decision maker is θ , then θ can be either θ_A or θ_B based on a set of p -dimensional input $\mathbf{X}_t = [x_1 \dots x_j \dots x_p]$. Now, Bayes decision rule is

$$\begin{aligned} \theta &= \theta_A & \text{if } h_A l_A f_A(X) > h_B l_B f_B(X) \\ \theta &= \theta_B & \text{if } h_A l_A f_A(X) < h_B l_B f_B(X) \end{aligned}$$

where

$f_A(x)$ and $f_B(x)$ = probability density functions (PDFs) for categories A and B respectively

l_A = loss function associated with the decision $\theta = \theta_A$

l_B = loss function associated with the decision $\theta = \theta_B$

h_A and h_B = priori probability of category A and B respectively

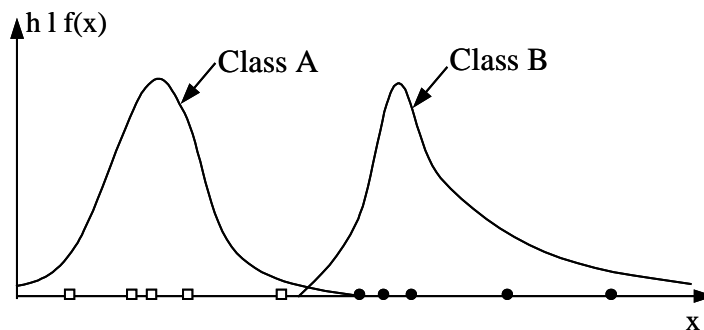
Then the decision boundary will be

$$f_A(X) = K f_B(X)$$

where

$$K = h_B l_B / h_A l_A$$

The priori probabilities are usually known and the loss functions are subjective, therefore, the key of this decision rule is the PDF. Figure 2.33 below is a diagram showing how the decision rule works based on one-dimensional input data, x .



□ = Data From Class A

• = Data From Class B

Figure 2.33: Decision Function for a One Dimensional Data, x (Adapted From Meisel, 1972)

PDFs have to be constructed based on the training pattern. They must be non-negative, integrable, and their integral over all space must be unity (Specht, 1990).

2.4.7.2 Constructing PDFs

The main concern with the Bayes decision strategy is obtaining PDFs. Parzen (1962) suggested a way to construct or estimate the PDFs for a one-dimensional case as shown below

$$f_A(x) = \frac{1}{n\lambda} \sum_{i=1}^n \omega\left(\frac{x-x_{Ai}}{\lambda}\right)$$

where

n = number of training sets

$x_{A1}, \dots, x_{Ai}, \dots, x_{An}$ = training samples

The equation above is commonly called the “Parzen estimator”. It was proved that the estimators become more accurate when the training set gets bigger. The function inside the summation function is called “Parzen window” (Grabec, 1997).

The Parzen estimator can be extended to apply to multidimensional cases as shown in the equation below. Usually a Gaussian function is used as a Parzen window because it makes the networks simpler than other windows.

$$f_A(X) = \frac{1}{(2\pi)^{p/2} \sigma^p} \frac{1}{m} \sum_{i=1}^m \exp\left[-\frac{(X - X_{Ai})^T (X - X_{Ai})}{2\sigma^2}\right]$$

where

i = pattern number

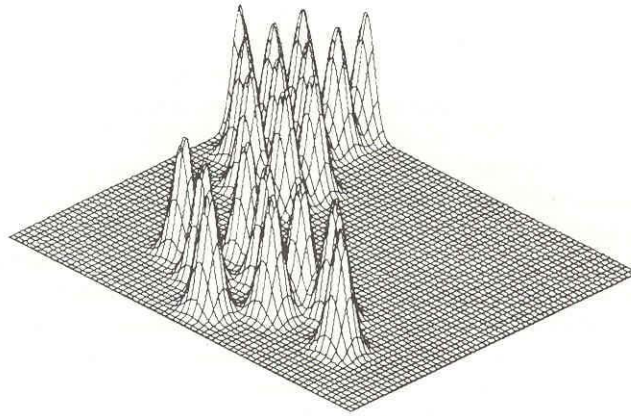
m = total number of training patterns

x_{Ai} = i th training pattern from category θ_A

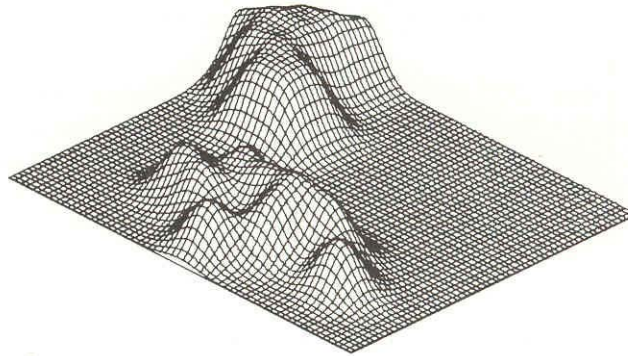
σ = “smoothing parameter” or parzen window

p = dimensions of measurement space

Figure 2.33 is an example of a Parzen estimator applied to a 2-dimensional sample. Basically the estimator is the summation product of small multivariate Gaussian distributions (kernels), which have center points at each training sample (Specht, 1990). Once the training set is gathered, the only one thing left is to select the smoothing parameter. The smoothing parameter can be from 0 to ∞ . It is the key to choose how much all the small kernels can be interpolated. With a small value of the smoothing parameter, the degree of interpolation is small, and each kernel becomes distinct (see Fig. 2.34a). When the smoothing parameter gets larger, more interpolation can be seen, including the neighborhood area. Therefore, any set of input that falls close to the training samples will have about the same probability as the training samples (See Fig. 2.34b). This is the ideal case for a smoothing parameter. A very large value of smoothing parameter, on the other hand, gives a high interpolation regardless of real underlying distribution as shown in Fig. 2.34c (Specht, 19990). As a result, neither an extremely low nor extremely high value of the smoothing parameter provides an optimal PDF. The best value of the smoothing parameter varies with the particular problem since this parameter is a function of the dimension, p , and the number of training samples, n (Specht, 1990).

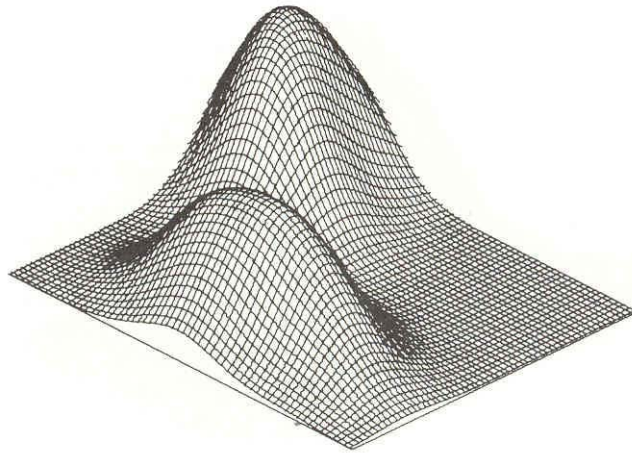


a) A Small Value of σ



b) A Larger Value of σ

***Figure 2.34: Effect of Smoothing Parameter on a Two Dimensional PDF
(From Meisel, 1972)***



c) a Very Large Value of σ

Figure 2.34 (cont'd): Effect of Smoothing Parameter on a Two Dimensional PDF (From Meisel, 1972)

2.4.7.3 Network Architecture

PNN can be designed as a four-layer network. The data from the training samples (with p dimensions) are received at the input layer as shown in Fig. 2.35. With the weights at input neurons, the dot product of each training sample is performed. At this point, each kernel of each sample has been constructed, and stored in each pattern neuron. Summation neurons are the place where all the kernels of the same category are combined together. The number of the summation neurons, therefore, must be equal to the number of the categories. Finally, the output neurons compare the probability of occurrence from the summation neurons and make the decision based on Bayes strategy (Specht, 1990).

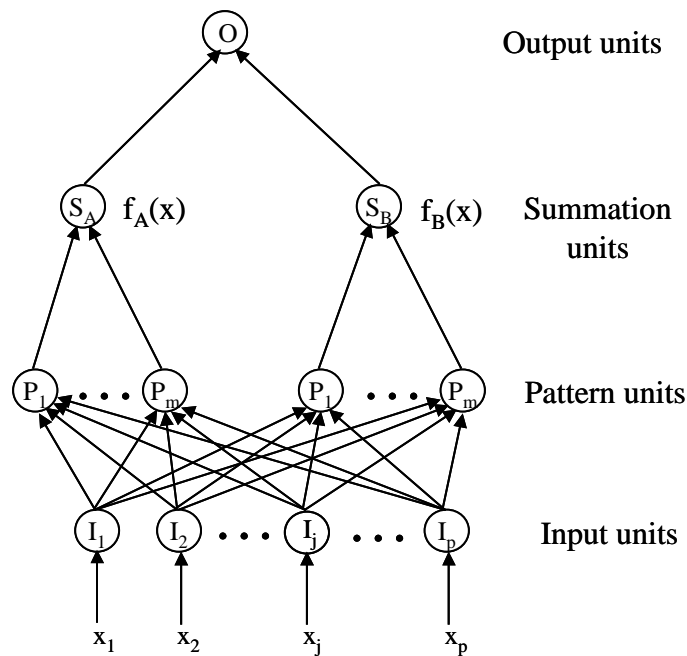


Figure 2.35: Probabilistic Neural Network Architecture Having p dimensions, m Training Samples, and 2 Categories (Adapted From Specht, 1990)

2.4.8 Literature Review of Neural Networks

2.4.8.1 Literature Review of Backpropagation Networks

The field of neural networks started with single-layer nets, which have many limitations, and therefore this field did not gain popularity in the 1970s (Fausett, 1994). However, the discovery of backpropagation by David Parker, 1985, and by Lecun, 1986, made neural networks popular again. Backpropagation networks are considered to be the most popular method at this time (Miikkulainen, 1999). This is because the backpropagation networks require multiple layers, which can solve complex problems. In addition, the backpropagation method uses the delta rule for training, which reduces the error rapidly (Fausett, 1994).

Hidden layers in backpropagation networks should be minimized as much as possible, since adding more layers to the networks will require more time for training. Fausett stated that two or more hidden layers may be of benefit for some applications, however, one hidden layer is usually sufficient (Fausett, 1994). NeuralWare Company, a neural network software development firm, suggested that hidden layers should be limited to only 1 or 2 (NeuralWare, 2000).

The number of the neurons in the hidden layer should range between the number of input and output neurons (NeuralWare, 2000). To find the optimum number of hidden neurons, NeuralWare suggests a trial-error method by changing the number of hidden neurons until the least total error was found.

2.4.8.2 Literature Review of Neural Network/pattern Recognition for Failure Mechanism Classification

Belchamber, R. M., et al., 1983

In 1983, Belchamber et al. published an early work on pattern recognition of AE from different composites. AE data was from testing ten composite materials with a polypropylene resin base. They used wideband sensors, and three pattern recognition techniques. These techniques were:

1. Linear learning machine networks (LLN)
2. K^{th} Nearest neighbor (KNN)
3. SIMCA

The AE parameters used as input for the pattern recognition were: average of amplitude, variance, half life, median frequency, and bandwidth. They found that LLN, which is the crudest technique, performed best for differentiating the resin types.

Fowler, T. J.

Fowler et al., 1989, suggested that the new direction in analyzing acoustic emission data was neural networks. In controlled tests, such as those reported by Scarpellini et al., 1983, it was found that experienced field test inspectors could accurately identify the defect types by only looking at the AE plots. The authors added that this skill was accumulated from many years of AE experience, and it was difficult to teach to new inspectors. Therefore, it was suggested that neural networks, which is a pattern recognition tool based on the human mind, could be applied to perform AE pattern recognition of failure mechanisms. The important point to consider is to select the right AE parameters.

Hill, E. v. K.

Eric v. K. Hill has published many papers on the use of AE and backpropagation neural networks to predict the ultimate strength of specimens. In 1993, Hill et al. conducted tensile loading experiments on aluminum-lithium weld specimens (5 specimens). The AE was monitored from the beginning up to 25% of the ultimate load. The amplitude distribution information was then calculated from the AE data and used as an input to the neural networks. They found that using one hidden layer of 9 neurons and a sigmoid activation function, the maximum error of the results were 2.6%. They also recommended use of another AE parameter in addition to the amplitude distribution parameter.

In 1996, Hill et al. applied neural networks to predict the burst pressure of pressure vessels based on AE data. Nine graphite/epoxy pressure vessels with different resin types were tested to the ultimate load, but AE was only monitored up to 25%. Forty-seven neurons from the amplitude distribution data and one neuron representing the resin type were used as the input layer. They found that using one hidden layer with 15 neurons optimized their backpropagation network.

The resulting error was 3.89%. They also suggested that more bad-condition samples should be tested in future experiments.

In December, 1998, Hill and Fisher published additional work from 1996. This time, the pressure vessels were tested at 3 different temperatures, with 2 pressurization schemes, and with 2 transducer configurations. They also included two “simulated manufacturing anomalies”. It was found that the pressurization scheme, and the transducer configuration did not have a significant effect on the strength prediction. In addition, having temperature as an additional input could slightly improve accuracy.

Grabec, I, Sachse, W., and Govekar, E., 1991

Grabec, Sachse, and Govekar, 1991, conducted research using a neural network adaptive learning system (backpropagation based) with the delta rule correction. The research was divided into 2 parts.

The first part involved the AE source location of a pencil lead break. They broke pencil leads at various locations on an aluminum block and recorded the AE with 2 sensors. With the AE waveform as network input, the network could estimate source orientations as well as locations of the pencil lead breaks.

In the second part, a mild steel plate was drilled while AE was monitored. The drilling involved 3 conditions, which were free run (the machine was turned on, but no drilling), drill, and drill with a worn out bit. Spectral densities of the AE hits (20 dimensions) were used as the network input, whereas the network output was drilling position and condition. They found that the prediction accuracy was 90%.

Promboon, Y., 2000

Promboon conducted acoustic emission source location research at the University of Texas at Austin. The main part of her research was dealing with steel, and a time of arrival/group velocity technique. However, she also did some

source location research on glass fiber reinforced epoxy pipe by using neural networks. She stated the two main reasons for using neural networks rather than a time of arrival technique for FRP were that:

1. The modulus of the fibers and resin are so different that it was difficult to calculate the dispersive group velocity.
2. The velocity and attenuation are different in different directions making it more complicated to use the time of arrival method.

Promboon divided a pipe into 24 zones (6 longitudinal sections, and 4 circumferential sections). She generated artificial sources by breaking pencil leads at various zones (1100 events). AE was monitored with 3 wideband sensors. With the backpropagation network, it was found that a combination input of amplitude, duration, and rise time from all sensors (9 neurons) made the best source locator. The error of this network was 3% for circumferential section, and 38% for longitudinal section (see Table 2.6). At the end of the research, the network was able to locate an impact on the pipe with very good results.

Table 2.6: Feature Extraction (Promboon, 2000)

Input Combinations	Misclassification Error	
	Circumferential Section	Sections along the length
ΔT and Δ Amplitude (6 inputs)	5%	55%
ΔT only (3 inputs)	6%	40%
All inputs from 1 sensor (arrival time, amplitude, duration, rise time, avg. freq., and signal strength)	25%	60%
Amplitude, duration, rise time (9 inputs)	3%	38%

Chen, H. L., and Chen, C. L., 1992

A backpropagation neural network was applied to classify 8 different types of timber samples, and also predict their ultimate strengths. The AE data was collected within the loading range between 500 to 2,000 lbs. The parameters considered in this research were number of events, ring down counts, duration, amplitude, rise time, and mid-span displacement. Each parameter was averaged over 100 lb load steps. They found that with 50 training samples, 8 testing samples, a learning rate of 0.02, and 4 to 6 hidden neurons, the accuracy was 75% for classification rate and 80% for strength prediction (Chen, 1992).

2.4.8.3 Literature Review of PNN

Specht, D. F., 1990

Specht reported that with 113 training sets for a 6-category problem, the performance of PNN was 85% while backpropagation yielded 82% (the training set for backpropagation was reduced due to the time limit, so the actual performance should probably be about the same as PNN). However, the calculation speed of the PNN was 200,000 times faster than the backpropagation method (Specht, 1990).

Grabec, I. and Sachse, W., 1997

Grabec and Sachse (1997) published a book “Synergetics of Measurement, Prediction and Control”. The book is focused on a quantitative description of nature using statistic and neural networks approaches. One type of neural network discussed in the book is Parzen’s window approach to general regression, which the authors referred to as PNN. The authors applied this networks to an AE problem.

An aluminum plate with asymmetrical shape was prepared. A steel ball was dropped at various locations on the surface of the plate and AE was

monitored by two wideband sensors. The size of the ball was also changed to determine the effect of the source dimension. The network was trained by the waveforms of AE hits (30 training sets). It was found that the network could predict the source location with 100% accuracy, and the ball size with 90% accuracy. Later on, the noisy signals were included in the training set. It was found that the accuracy was slightly reduced.

The author also applied the PNN to perform recognition of defects from ultrasonic testing. It was discovered that the proposed network can perfectly estimate the size and type of an inclusion in an aluminum block.

2.5 SUMMARY

Background information on FRP and its failure mechanisms are discussed in this chapter, which is divided into four sections. The first section provides an overview of FRP materials including their manufacture and failure. The second section describes nondestructive inspection methods for FRP and summarizes factors that influence the effectiveness of the various techniques. The third section describes AE technology and reviews literature on the application of signature analysis to FRP materials. The final section covers neural networks.

It is concluded that AE is one of the most reliable methods for inspecting FRP structures. The method is widely specified in codes and standards covering manufacture and inspection of FRP structures. In addition, AE is a global test that is well suited for FRP structures, which are usually large.

The literature review provides important background information for this research program. The extensive number of studies, and the conflicting results indicate the need for a broader approach to AE source identification. The following is a summary of the literature review:

1. Numerous research investigations and studies have attempted to relate specific emission sources to specific AE patterns. These studies are referred to as signature analysis.
2. A wide range of signature analysis techniques have been proposed ranging from statistical analysis of AE parameters, through visual pattern recognition, to personal experience.
3. Conflicting results have been obtained from the signature analysis studies. No clear consensus has emerged of specific AE patterns for specific sources.
4. The Zweben fiber breakage theory has the potential to predict the percentage of fiber breaks at a given load, which could correlate with the pattern of AE.
5. Conventional AE waveform parameters such as amplitude, duration, and energy have been studied. In addition, new parameters such as energy moment, event count by energy range, and duration distribution have been proposed.
6. In general, techniques that analyze the entire data set such as b-value analysis, cumulative signal strength, and distribution plots give better results than techniques that analyze parameters of “representative” hits.
7. The most promising methods for FRP signature analysis are the determination of the b-value and neural networks.
8. The size difference between laboratory specimens and field structures must be taken into account in the development of practical field methods of signature analysis.
9. Field test inspectors with experience in AE testing have been able to accurately identify source mechanisms from AE data, even though they are often unable to define the AE patterns that influence their conclusion. This

suggests that neural networks, the purpose of which is to simulate human thought processes, have the potential to be a valuable signature analysis tool.

CHAPTER 3

Materials and Instrumentations

This chapter addresses the material specification of the original full-scale beams, from which many of the coupon specimens were cut. In addition, AE equipment, including AE data acquisition systems and sensors, are described. This chapter also describes the testing facilities utilized in this research.

3.1 MATERIALS

Most of the specimens used in this research program were cut from original full-scale samples. These samples were made available from TxDOT project 0-1173 “Applications for Composite Materials in TxDOT”. The materials were selected based on the quality required for bridge construction and market availability. For this reason, the samples were considered appropriate to the goal of this research project. The original full-scale beams are as follows:

1. Glass fiber reinforced isophthalic polyester pultruded beams (FG1 and FG2). The two beams were fabricated by Strongwell Corporation and one is shown in Fig. 3.1.

Dimensions: Wide flange shape, 30 foot long, 12 inch flange width, 12 inch deep, and 0.5 inch thick.

Fabrication method: Pultrusion

Material specification:

Fiber: 366 type 30® E glass fiber (manufactured by Owens Corning)

Resin: AROPOL 2036C isophthalic polyester (manufactured by Ashland Chemical).

Fiber arrangement: Unidirectional fiber layers alternated with chopped random fiber layers. The fibers in the unidirectional fiber layers are oriented longitudinally along the length of the beam. Figure 3.2 shows the fiber layers of the material after the resin was removed by ignition.



Figure 3.1: Glass Fiber Reinforced Isophthalic Polyester Pultruded Beam (FG)

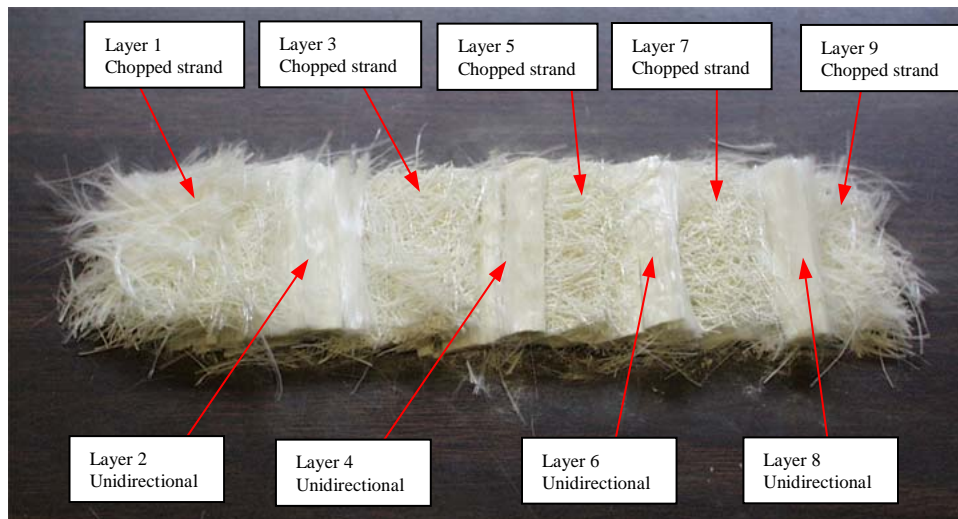


Figure 3.2: Layer Arrangement of FG Beam

2. Glass fiber reinforced vinyl ester pultruded beams (IKG). The two beams were fabricated by Bedford Reinforced Plastics Inc., and one is shown in Fig. 3.3.

Dimensions: Wide flange shape 30 foot long, 12 inch flange width, 12 inches deep, and 0.5 inch thick.

Fabrication method: Pultrusion

Material specification:

Fiber: 366 type 30@ E glass fiber (manufactured by Owens Corning).

Resin: CORVE 8182 vinyl ester (manufactured by Interplastic Corporation).

Fiber arrangement: Unidirectional fiber layers alternated with chopped random fiber layers like beam FG. The fibers in the unidirectional fiber layers are oriented longitudinally along the length of the beam.



Figure 3.3: Glass Fiber Reinforced Vinyl Ester Pultruded Beam (IKG)

3. Carbon and glass fiber reinforced vinyl ester pultruded beams (SW). The two beams were fabricated by Strongwell Corporation and one is shown in Figure 3.4.

Dimensions: Wide flange shape with double webs, 30 foot long, 6 inch flange width, 0.6 inch thick, and 8 inches deep.

Fabrication method: Pultrusion

Material specification:

Fiber: Hybrid with HERCULES AS 4 (36K) carbon fiber and E glass fiber.

Resin: Dow Chemical Derakane 411-350 vinyl ester with 10% styrene

Fiber arrangement: Unidirectional fiber layers alternated with chopped random fiber layers. The fibers in the unidirectional fiber layers are oriented longitudinally along the length of the beam.



Figure 3.4: Carbon and Glass Fiber Reinforced Vinyl Ester Pultruded Beam (SW)

3.2 AE INSTRUMENTATIONS

3.2.1 *AE Data Acquisition System*

Two AE data acquisition systems were used for this research. Physical Acoustic Corporation (PAC), Princeton, New Jersey, manufactured both of them. Details are given below:

1. Twenty-four channel Transportation Instrument. The instrument is shown in Figure 3.5. The Transportation Instrument is a basic general purpose AE data acquisition system that is widely used for field testing. It is easy to use, set up, and transport. The 24 channels provide very good coverage for full-scale specimens. Data from this instrument can be analyzed with the widely used VTRNSMON software that runs on PC style computers. The drawback of this system is that it has a 16 bit architecture, which can record any information only up to the maximum value of 65,535 or $(2^{16} - 1)$. This directly affects the recording performance of AE duration, which can be longer than 100,000 microseconds in some tests.
2. Six channel MISTRAS system. The state-of-the-art MISTRAS system has all of the Transportation Instrument's functions, and can acquire digital waveforms (Fig. 3.6). The MISTRAS has adjustable settings (threshold, hit definition time, etc.) and is capable of very high data acquisition rates. Also, it has a very short rearm time. The MISTRAS includes an extensive suite of software programs that can be run on any Windows based computer.



Figure 3.5: Transportation Instrument

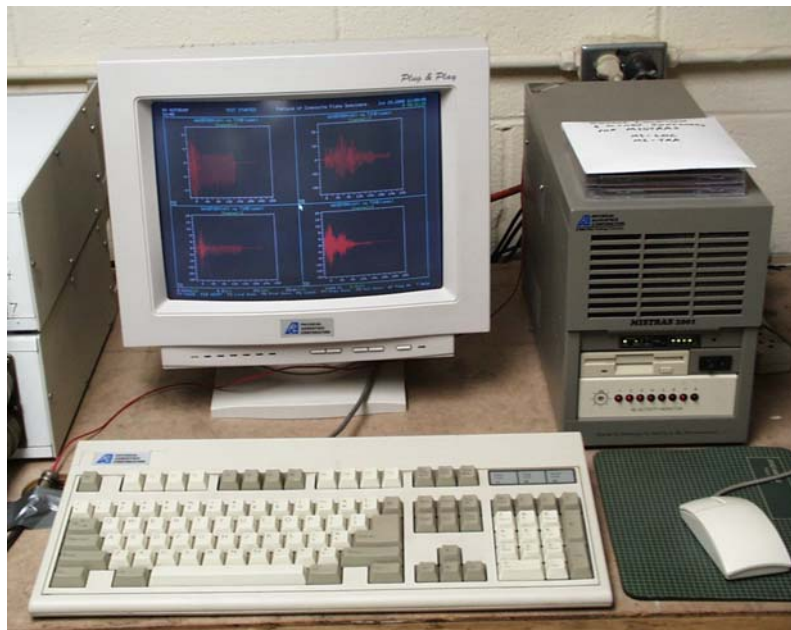


Figure 3.6: MISTRAS System

The Transportation Instrument has the following factory settings.

1. Test threshold = 40 dB
2. Peak definition time (PDT) = 200 microseconds
3. Hit definition time (HDT) = 400 microseconds
4. Hit lockout time (HLT or REARM time) \cong 180 microseconds

The MISTRAS hardware parameters and a signal-processing filter were set as described below:

1. Test threshold = 40 dB if the background noise was minimized, otherwise 45 dB.
2. Signal processing filter = 100-200 kHz
3. Peak definition time = 200 microseconds
4. Hit definition time = 400 microseconds
5. Hit lockout time = 40 microseconds

For both instruments, MARSE is used as a measure of signal strength.

3.2.2 AE Sensors

R15I sensors which have resonant response centered on 150 kHz were primarily used with the FRP specimens, as required by the CARP Recommendation Practice. Each R15I sensor was manufactured by Physical Acoustic Corporation (PAC) and had a preamplifier incorporated within the shielded casing. An R15 sensor was used where the mounting space was limited. These sensors do not have an integral preamplifier, making their size smaller than the R15I sensor.

Wideband and R6I (resonant at 60 kHz) sensors are not recommended by CARP and were only used in this research study to compare the attenuation characteristics of FRP specimens. The R15I, R15, R6I, and wideband sensors as well as the external preamplifier are shown in Figure 3.7.

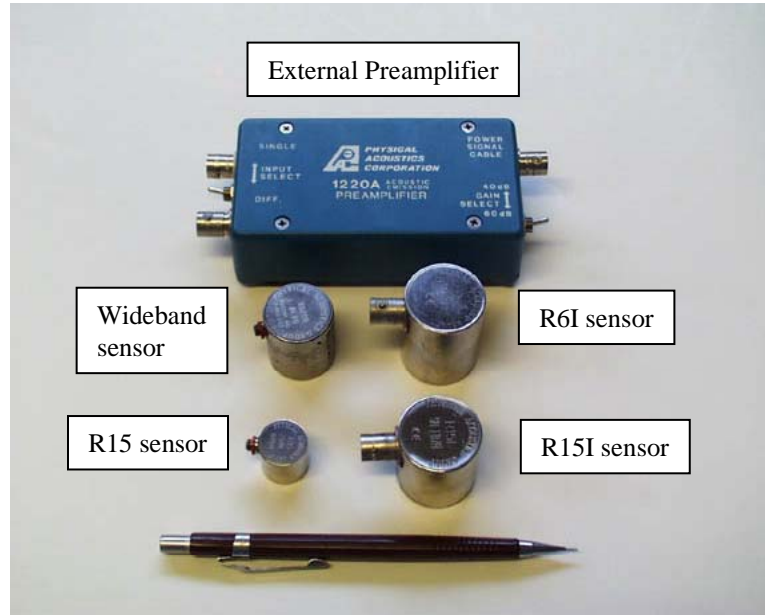


Figure 3.7: AE Sensors and External Preamplifier

3.3 TESTING FACILITIES

Most of the experiments were conducted in the Ferguson Structural Engineering Laboratory at the University of Texas at Austin, Pickle Research Campus. The testing machines used in the program included:

1. **Universal Testing Machine 600HVL:** The machine was manufactured by Satec Systems, Inc. (see Fig. 3.8). It has hydraulic wedge grip mechanism with 600 kips maximum capacity for tension loading.
2. **Four-Point Loading Frame for Coupon Specimens:** The load was controlled by a hydraulic ram and a hand pump. A load cell, which is placed on the top of the ram, is used for load readings (see Fig. 3.9).
3. **Full-Scale Loading Frame:** The test setup consisted of a steel frame, to which a hydraulic ram was attached at the midspan of the girder. The frame has 200 kips maximum capacity (see Fig. 3.10).



Figure 3.8: Universal Testing Machine 600HVL

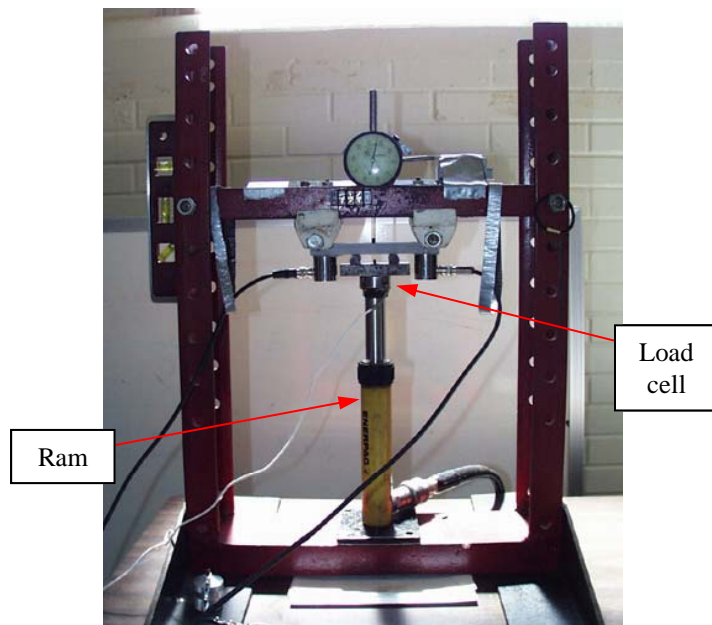


Figure 3.9: Four-Point Loading Frame for Coupon Specimens



Figure 3.10: Full-Scale Loading Frame

Additional experiments were carried out at the Texas Department of Transportation Cedar Park Campus. The details of the facilities are:

1. **Universal Testing Machine, Instron 4208:** The machine had 60 kips maximum capacity (see Fig. 3.11). Its grips for tensile testing were mechanical wedge.
2. **Hitachi S-3200N Scanning Electron Microscope:** The machine was able to scan an object up to 5000x magnification (see Fig.3.12).



Figure 3.11: Universal Testing Machine, Instron 4208



Figure 3.12: Scanning Electron Microscope, Hitachi S-3200N

CHAPTER 4

Fiber Breakage

This chapter focuses on the AE characteristics of the fiber breakage mechanism. It is not practical to design a specimen and test that can be monitored for AE and exhibits only fiber breakage. Specimens with pure unidirectional fibers, the simplest form for the study of fiber breakage, were subjected to tension tests as reported in Section 4.1. The failure mechanisms from these specimens included both fiber breakage and non-fiber breakage. As a result, the objective of Section 4.1 is to develop a technique to investigate the AE characteristics of fiber breaks and to sort them out from the entire AE data set. Section 4.2 applies the technique and the knowledge developed in Section 4.1 to determine failure mechanisms of the more complex, realistic specimens. These AE data are used for visual pattern recognition (Chapter 7) and for neural networks performing pattern recognition (Chapter 8).

4.1 LOW AMPLITUDE FILTERING TECHNIQUE

4.1.1 Concept of the Technique

When a unidirectional FRP is tested in tension, the expected failure mechanisms from the tests include matrix cracking, fiber breakage, fiber/matrix debonding, delamination, and fiber pullout.

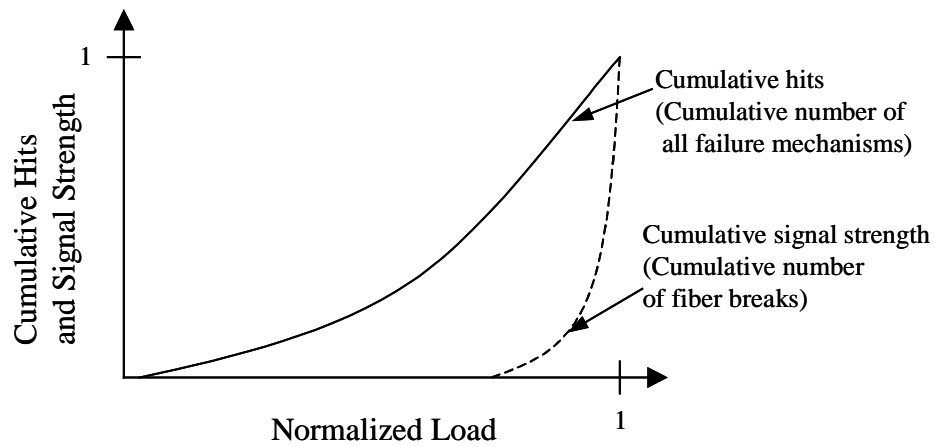
Many researchers (i.e. Berthelot and Billaud, 1983, Li and Zhao, 1986, Marianne and Favre, 1989, Pollock, 1981, and Crump, 1981) have shown that fiber breakage is associated with high amplitude hits. This conclusion will be examined in this chapter.

Young's modulus and the tensile strength of the fibers are much higher than that of the matrix, while the typical ultimate strains of the fiber and matrix are about the same. Therefore, the majority of strain energy released during the test comes from the fiber breakage. As the strain energy transforms to the AE signal strength, it can be concluded that the majority of the AE signal strength comes from the fiber breakage as well (Bray and Stanley, 1997).

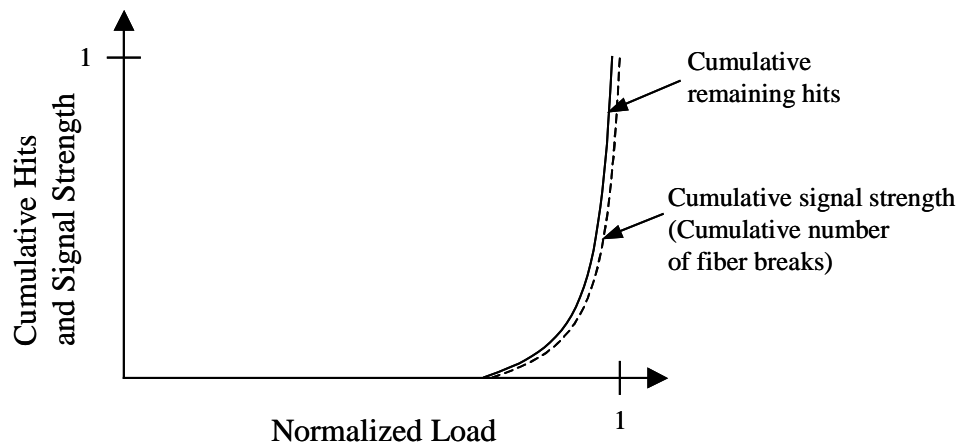
As discussed in Chapter 2, studies by Rosen (1964) and Zweben (1968) have predicted that fiber breaks can be seen in early stages of the test, and the number of fiber breaks increases exponentially with the load. This is attributed to the scattering of the fiber strength.

If the above statements are correct, a plot of cumulative signal strength vs. load should provide an approximation of the plot of cumulative number of fiber breaks vs. load. In contrast, a plot of cumulative hits vs. load should provide an approximation of the cumulative number of all failure mechanisms including, but not limited to fiber breaks (see Fig. 4.1a).

This leads to the concept of that if the low amplitude hits (non-fiber break hits) are filtered out, the cumulative plot of the remaining hits vs. load should coincide the cumulative signal strength vs. load plot. All the axes of both plots must be normalized to eliminate the difference in units (see Fig. 4.1b). The lowest amplitude remaining after filtering is the borderline between the fiber break and non-fiber break hits.



a) Before Low Amplitude Hits are Filtered



b) After Low Amplitude Hits are Filtered

Figure 4.1: Idealized Schematic Plots of Normalized Cumulative Hits and Signal Strength vs. Load

In order to further evaluate this concept, two important additional steps are necessary:

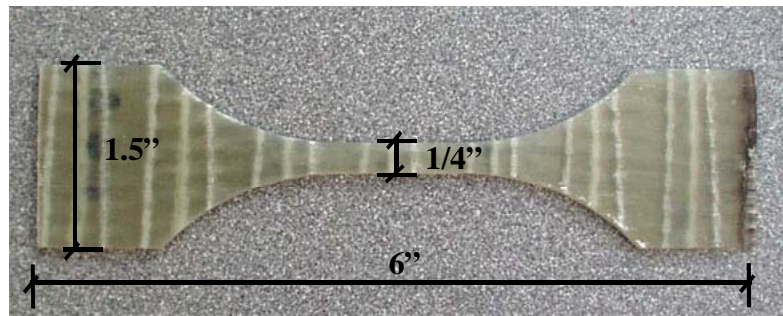
1. Conduct tension tests of coupon specimens having fibers only in the direction parallel to the tensile stress. This type of specimen is the simplest form for fiber breakage investigation.

2. Conduct extensive scanning electron microscope (SEM) studies of the failure progression in order to demonstrate the relationship between fiber breakage, high amplitude AE hits, and the shape of the cumulative signal strength curve.

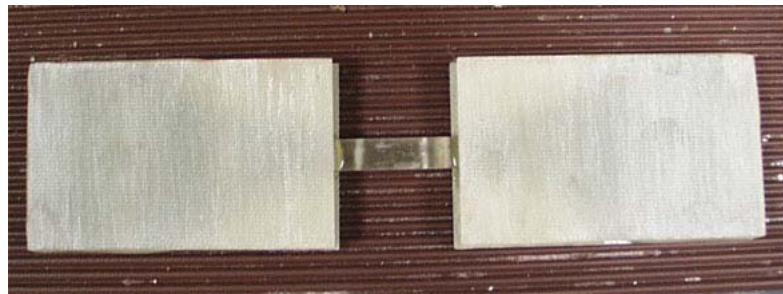
4.1.2 Experimental Program

Five FRP coupon specimens were made of a vinyl ester resin (Derakane 411-100) that was reinforced with glass fibers only in the longitudinal direction. MFG (An Entity of Molded Fiber Glass Companies) fabricated all these specimens. The size of the specimens follows ASTM D 638, which was 6 in. long, 1.5 in. wide, and 0.1 in. thick. A dog-bone coupon was waterjet cut from each specimen (see Fig. 4.2a) producing a constant width of ¼ inch in the middle. The white lines running across the coupon, approximately perpendicular to the longitudinal fibers, are the stitching holding the fiber bundles together. The surface of the coupon had a rough texture due to the profile of fiber strands. Accordingly, tabs were used to obtain a full contact between the specimens and the grips of the testing machine (see Fig. 4.2b). Tabs were made from G-10 laminate composite. The G-10 material is manufactured from epoxy resin and reinforced with glass fiber fabric. The size of the tabs was 2¼-inch long, 1.5-inch wide, and 1/8-inch thick, bonded at both sides and both ends of the specimens. The adhesive used for bonding was Bondo Marine™ Epoxy (Product No. 3202, Bondo Corporation).

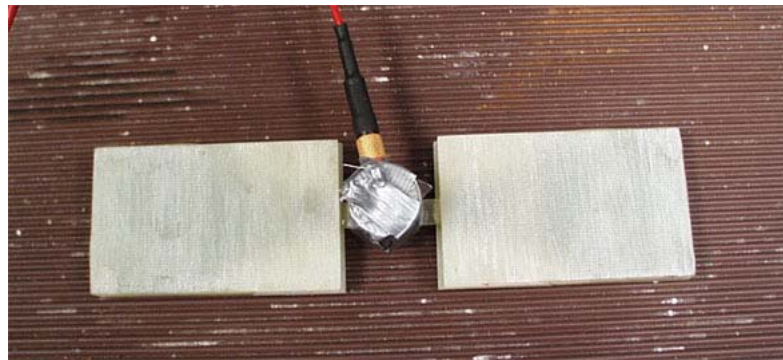
The testing machine used for this experiment was an Instron 4208 facilitated by the Texas Department of Transportation, Cedar Park Campus. The machine had a maximum capacity of 60 kips. The grips were normal wedge mechanisms. The crosshead speed was 0.0125 in/min. A picture of the test setup is shown in Figure 4.3



a) Top View of the Dog-Bone Coupon



b) Dog-Bone Coupon With Tabs on Both Sides and Both Ends



c) R15 Sensor Mounted on the Specimen

Figure 4.2: Coupon Specimen

AE was monitored during the tests. The Mistras AE data acquisition system was used. The space for mounting an AE sensor was very limited due to the size of the specimen. Therefore, an R15 sensor with an external preamplifier was used rather than bigger R15I integral sensor (see Fig. 4.2c).

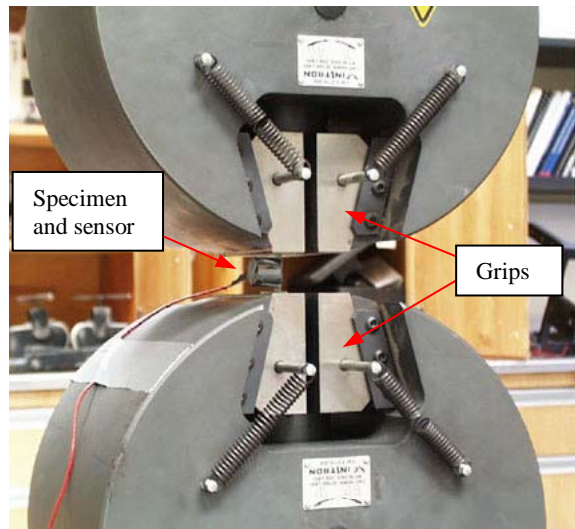


Figure 4.3: Test Setup

Each specimen was loaded to different maximum loads. This way, microscopic failure mechanisms of the specimens could be observed at different stages by SEM. Table 4.1 is a summary of the test specimens and their maximum loads.

Table 4.1: Summary of the Test Program

Specimen	Maximum Load (% of ultimate load)
L1	45.
L2	60
L3	85
L4	87.5
L5	100

After loading, the specimens were unloaded and examined with a scanning electron microscope to observe the damage evolution. The SEM cannot scan the entire body of the specimens. Therefore, only damage on the surface could be observed.

4.1.3 Physical Results

Figure 4.4 is a summary of the tensile tests showing the maximum stresses, and maximum strains (based on 1-inch gage length).

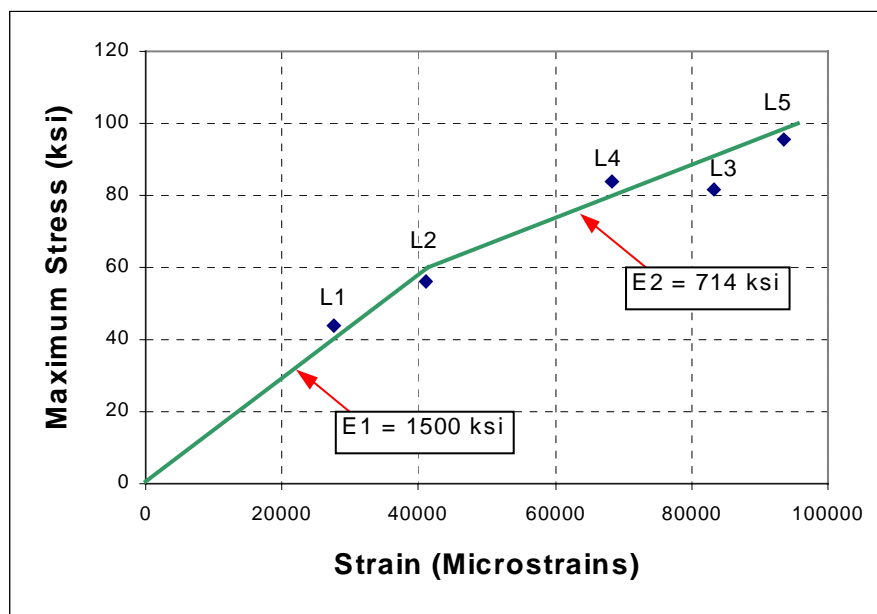


Figure 4.4: Maximum Stresses and Strains of the Specimens L1 to L5

4.1.4 SEM Results

The damage evolution observed with the aid of the SEM is described below:

Specimen L1 Before the Test

Overall, the specimen was in almost perfect condition. Most of the fibers had no imperfections, and the matrix showed no sign of cracks. Figure 4.5 shows a typical top view scan of specimen L1 before the test. The picture shows a group of undamaged fibers running in the unidirectional direction. The picture also shows a perfect condition of the matrix. It was also quite normal to see dust particles on the surface of the specimen.

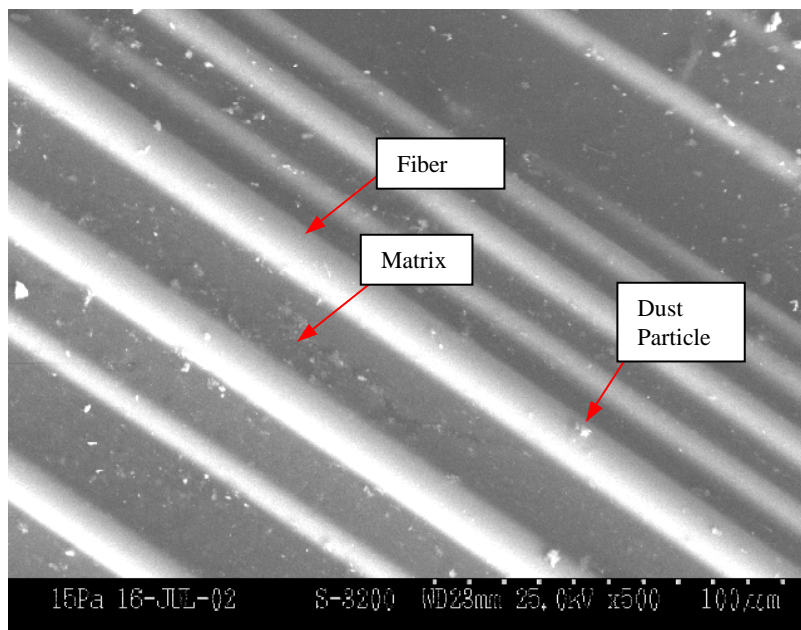


***Figure 4.5: Typical View of Fibers and Matrix of Specimen L1 Before Testing
(500x Magnification)***

Only a few fibers were found to have any damage. The damage could have resulted from manufacturing, fabrication, machinery, or handling. A typical fiber break and fiber/matrix debonding is shown in Figure 4.6. Also, non-parallel fibers are visible in the photo. The fibers are normally manufactured in bundles connected by stitches. Each bundle consists of many fiber strands. Therefore, it

is likely that there is some twisting due to handling during the fiber manufacturing process (before stitching) or twisting due to the FRP fabrication process.

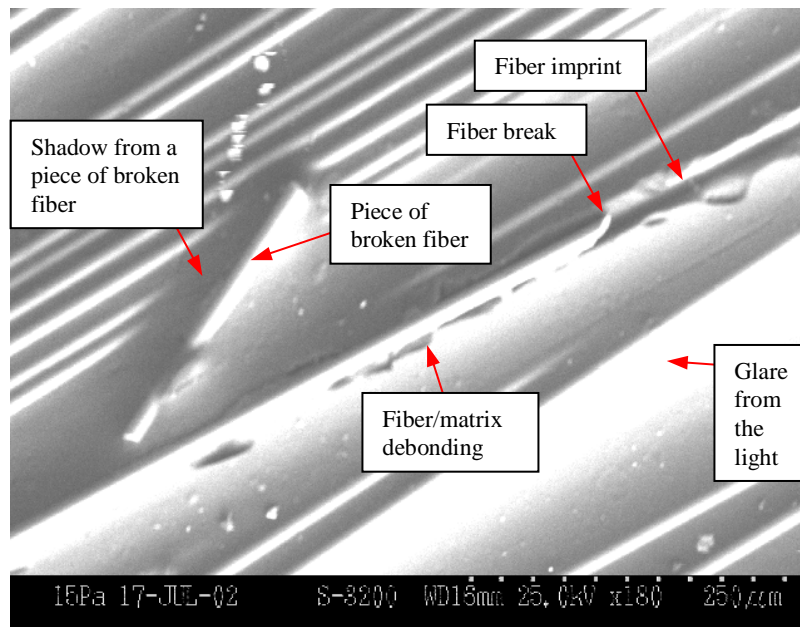


Figure 4.6: Typical Damages on Specimen L1 Before Testing (180x Magnification)

The side of the specimen was also observed. A number of damage sites involving fiber breaks due to the waterjet cut can be seen (see Fig. 4.7). As a result, the side of the specimen is not a proper area to observe the damage evolution. There are typical air voids on both sides of the stitch. These air voids can be attributed to absorbance of the resin into the stitch during the curing process.

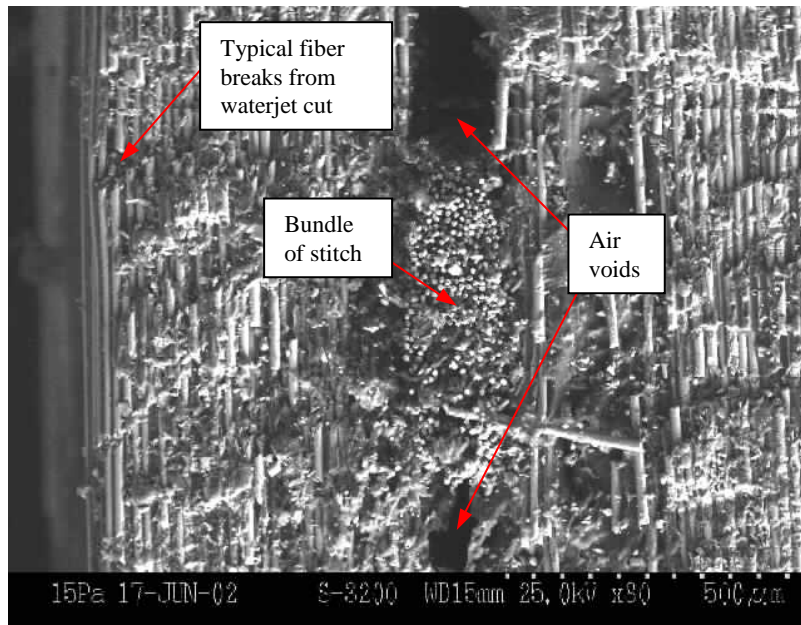


Figure 4.7: View of the Side of Specimen L1 Showing Damage from Waterjet Cut and Air Voids Around a Stitch (80x Magnification)

Specimen L1 After the Test (45% of the Ultimate Load)

A number of matrix cracks were observed. These matrix cracks appeared as white lines between the fibers, as shown in Fig. 4.8. A few fiber breaks could also be seen. Some of them were in the form of cracks perpendicular to the fiber direction. These cracks appeared as black lines (see Fig. 4.9a) rather than white lines like matrix cracks. Other forms of fiber breakage in this specimen were break/offset and break/debonding. Typical fiber break/offset and fiber break/debonding are shown in Figure 4.9b, and 4.9c respectively.

The sides of the specimen were also scanned. No appearance of damage development, beyond that seen in the original unloaded specimen, could be seen.

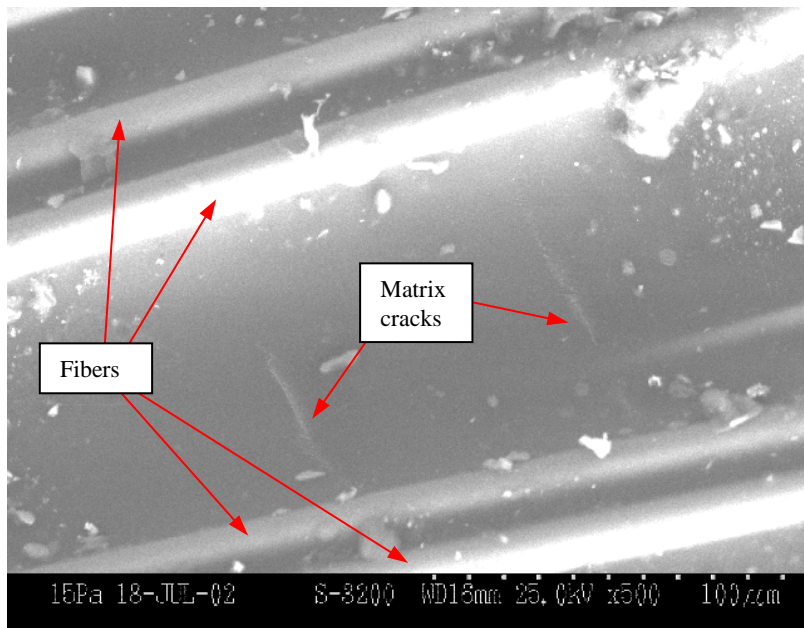
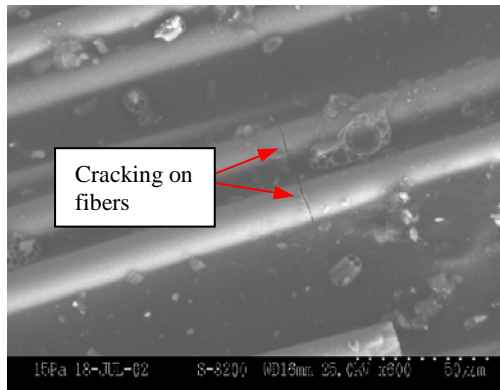
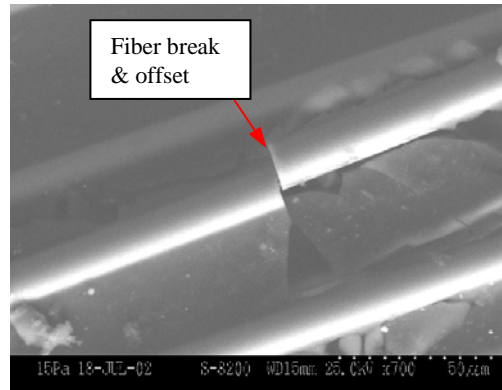


Figure 4.8: Typical Matrix Cracks Observed in Specimen L1 (500x Magnification)



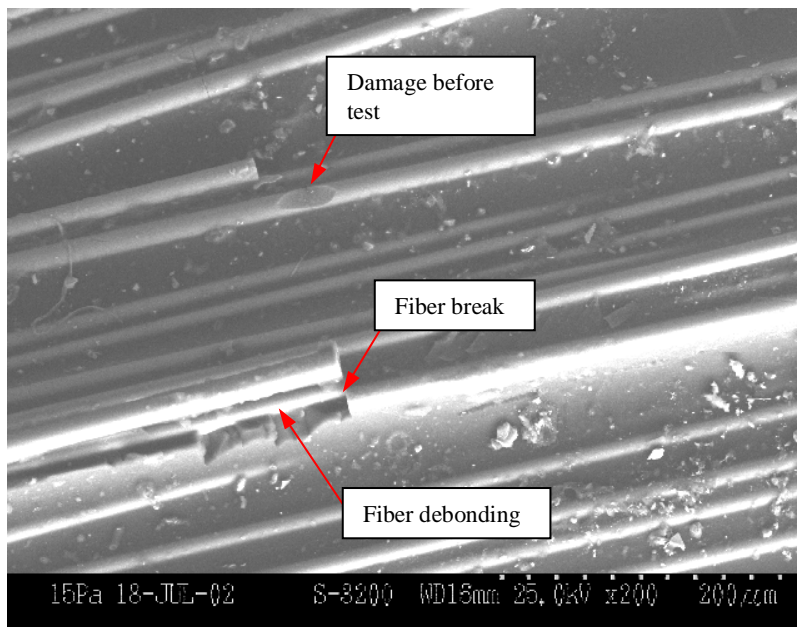
a) Cracking of Fibers

(600x Magnification)



b) Fiber Break/Offset

(700x Magnification)



c) Fiber Break/Debonding (200x Magnification)

Figure 4.9: Fiber Breakage in the Specimen L1

Specimen L2 (60% of the Ultimate Load)

Substantial numbers of matrix cracks could be seen. Some matrix cracks propagated, and larger crack openings could be noticed (see Figure 4.10). A few fiber breaks could also be seen. Most of the fiber breaks in this specimen were associated with a crack continuation into the matrix, as shown in Figure 4.11. Figure 4.12 shows the overall view of the specimen. It can be seen from the picture that most of the fibers were still in good condition. Also, the sides of the specimen showed no development of new defects.

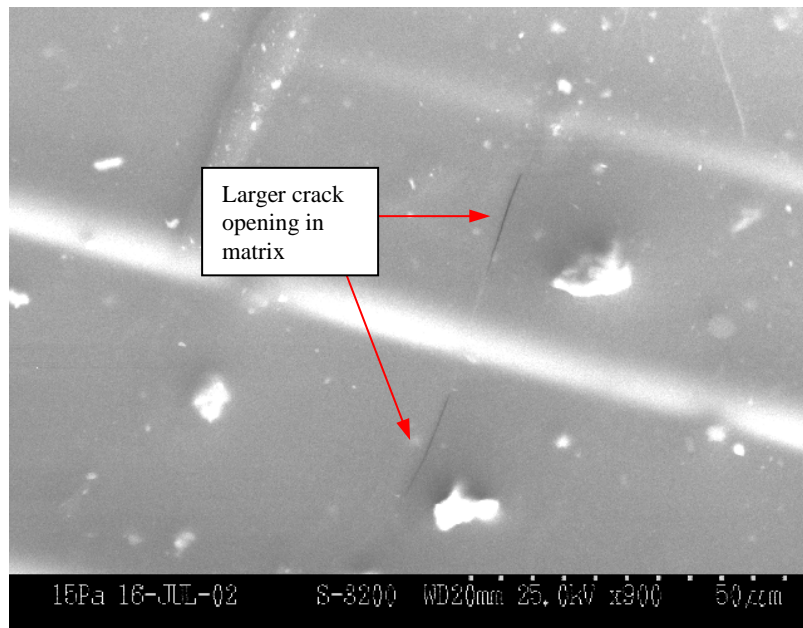


***Figure 4.10: Matrix Cracking with Larger Crack Openings of Specimen L2
(300x Magnification)***

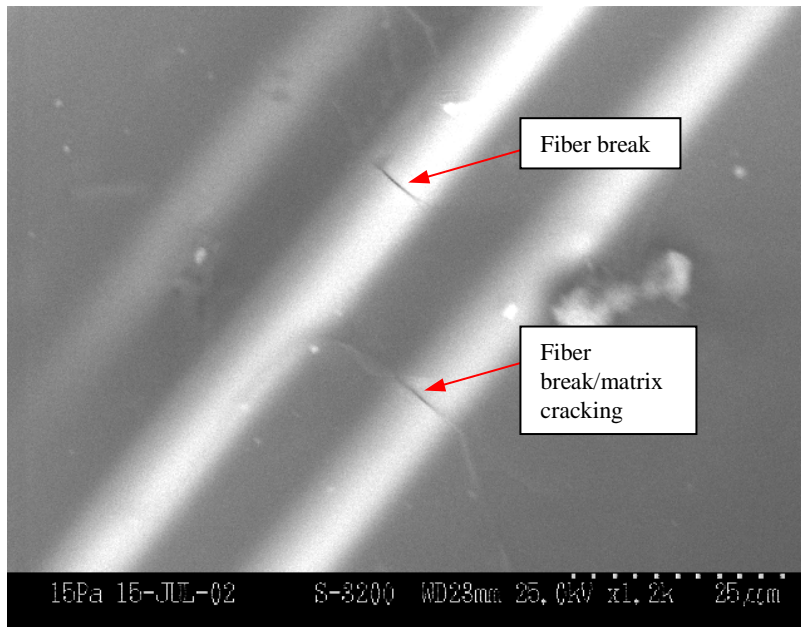


Figure 4.11: Fiber Breakage Continued with Matrix Cracking in Specimen L2 (1200x Magnification)

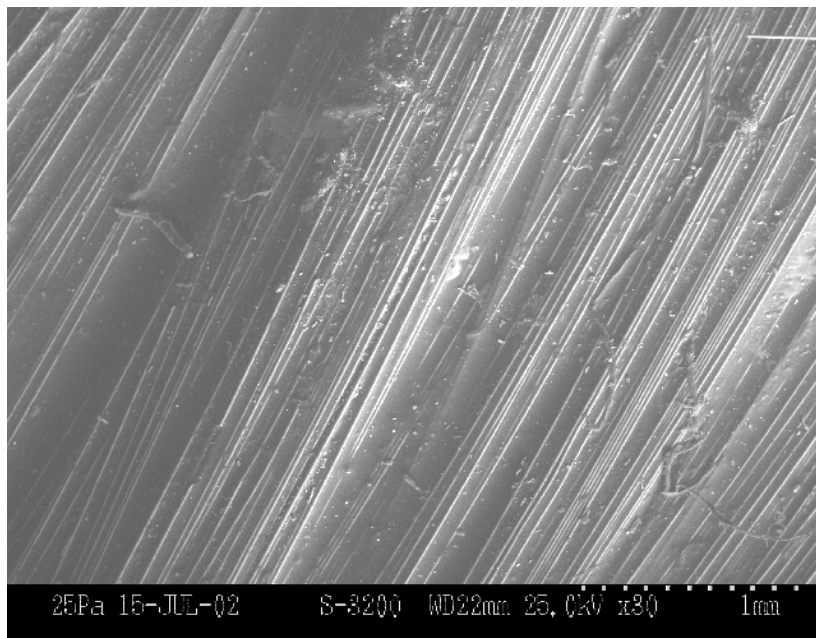


Figure 4.12: Overview of Specimen L2 (30x Magnification)

Specimen L3 (85% of the Ultimate Load)

Many more fiber breaks were observed in specimen L3 than in specimen L2. Most of the fiber breaks were associated with fiber/matrix debonding (see Figure 4.13). However, the cracks continuing from fiber breaks to the matrix could still be seen in this specimen. Figure 4.14 is an overall photograph of the specimen. It can be seen in this picture that many fibers had been broken. There was no appearance of damage developed on the sides of the specimen.

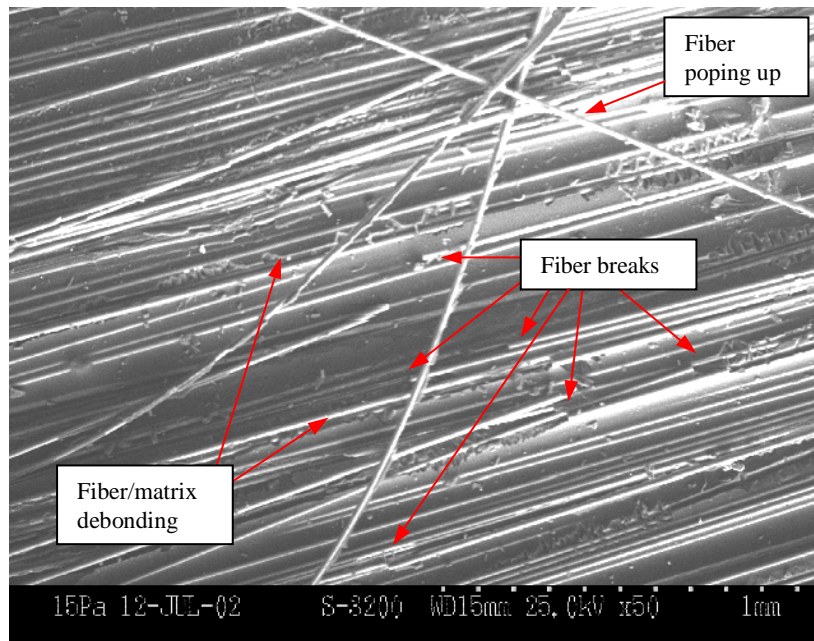


Figure 4.13: Fiber Breakage and Fiber/Matrix Debonding in Specimen L3 (50x Magnification)

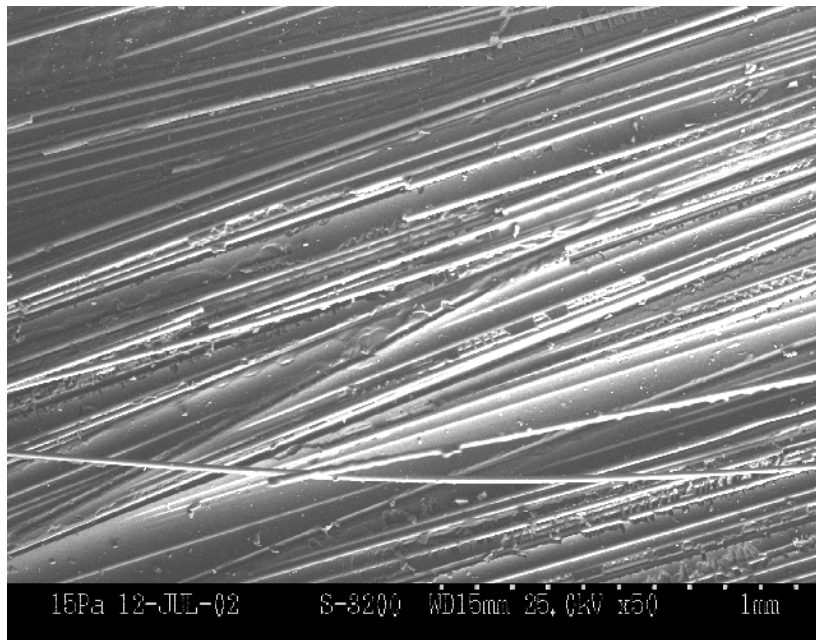


Figure 4.14: Overview of Specimen L3 (50x Magnification)

Specimen L4 (87.5% of the Ultimate Load)

Even though specimen L4 was loaded to the higher load level than specimen L3, fiber breaks in this specimen were found to be fewer than those in specimen L3. This was the case for all sites viewed with the SEM. The fewer fiber breaks is consistent with the higher apparent stiffness (Figure. 4.4) of this specimen at the test load. Most of the fiber breaks were observed with fiber/matrix debonding (see Figure 4.15). Some fiber breaks occurred with several matrix cracks (see Figure 4.16). A similar observation was made by Merienne and Farve (1989). Pure matrix cracking could still be found over the entire matrix area. Figure 4.17 is the overall view of this specimen, and shows a number of fiber breaks. The sides of the specimen were also scanned, however, no evidence of developed damage was found.

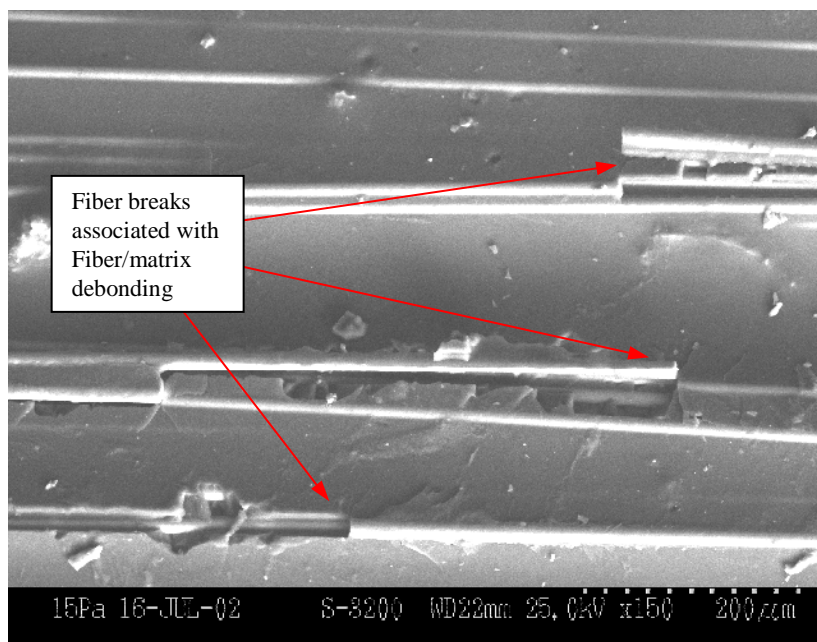


Figure 4.15: Fiber Breakage Associated with Fiber/Matrix Debonding in Specimen L4 (150x Magnification)

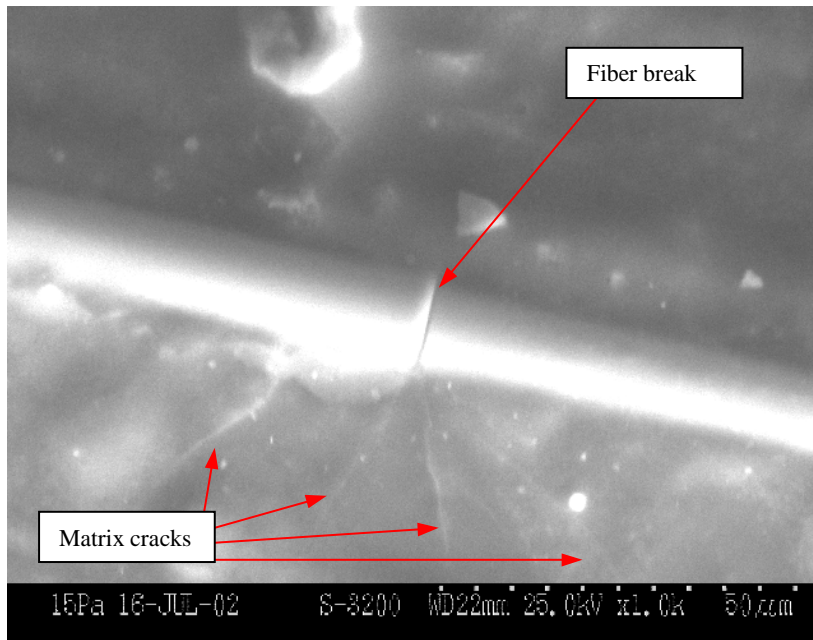


Figure 4.16: Fiber Breaks with Several Matrix Cracks in Specimen L4 (1000x Magnification)

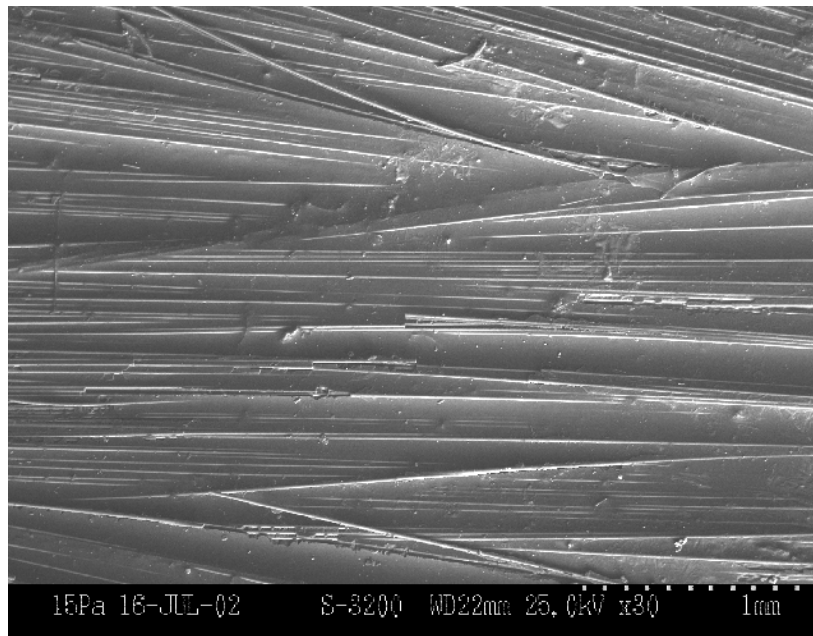


Figure 4.17: Overview of Specimen L4 (30x Magnification)

Specimen L5 (At Ultimate Load)

This specimen was tested to the ultimate load. Accordingly, breaking of the specimen involving fiber breakage and delamination could be seen (see Fig. 4.18). However, the narrow section area, in which fiber breakage was not easily seen, was examined by SEM.

The photographs from the SEM show fiber breaks on nearly all fibers (see Figure 4.19). These fiber breaks were associated with fiber/matrix debonding. Severe matrix cracking occurred over the entire area. Figure 4.20 shows a view of a side of the specimen, in which delamination and fiber breaks could be seen.

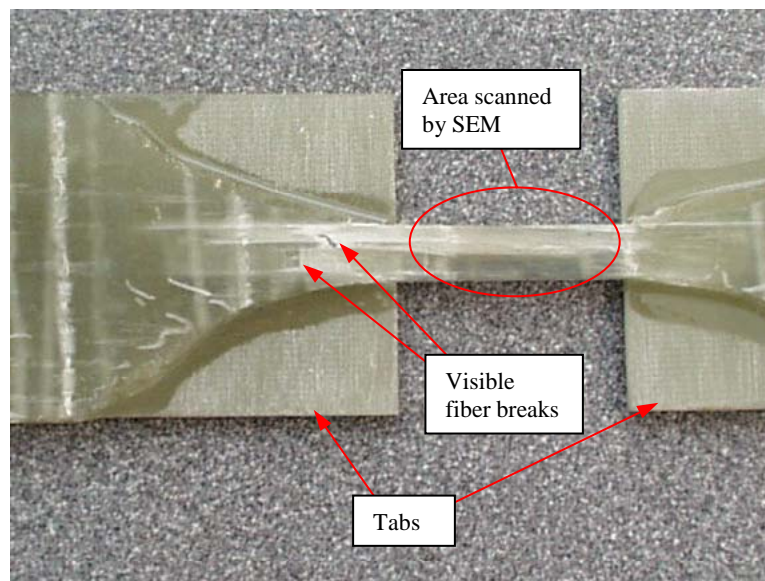


Figure 4.18: Visible Fiber Breakage in Specimen L5

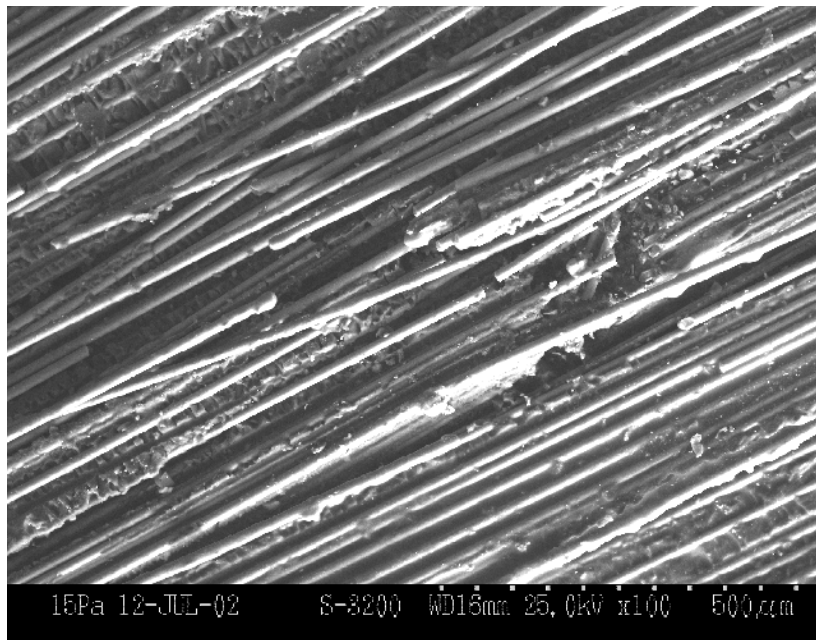


Figure 4.19: Overview of Specimen L5 (100x Magnification)

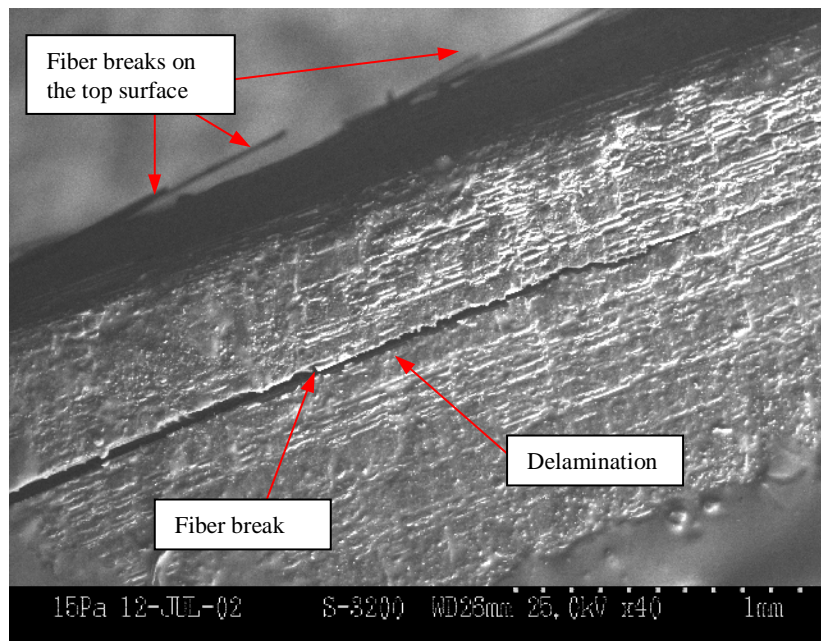


Figure 4.20: A Side of Specimen L5 Showing Delamination (40x Magnification)

4.1.5 AE Results

Table 4.2 is a summary of the total number of AE hits from all specimens. It is noted that the total number of AE hits of specimen L4 were lower than those of specimen L3, even though specimen L4 was loaded to the higher maximum stress. This is consistent with the fewer fiber breaks observed by the SEM inspection.

Table 4.2: Summary of AE results Including Load and Total Number of AE Hits

Specimen	Load (% of ultimate)	Total number of AE hits
L1	45	598
L2	60	1,649
L3	85	4,446
L4	87.5	3,149
L5	100	11,351

The plots of cumulative signal strength vs. load of each specimen are shown together in Figure 4.21. The curves of specimen L1 and L2 are flat compared with other specimens. The curve of specimen L4 ended just before reaching the knee of the curve, while the curve of specimen L3 passed the knee. This explains the reason that more fiber breaks were found in the specimen L3. The curve of specimen L5 rises steeply at ultimate, as commonly found in an AE test.

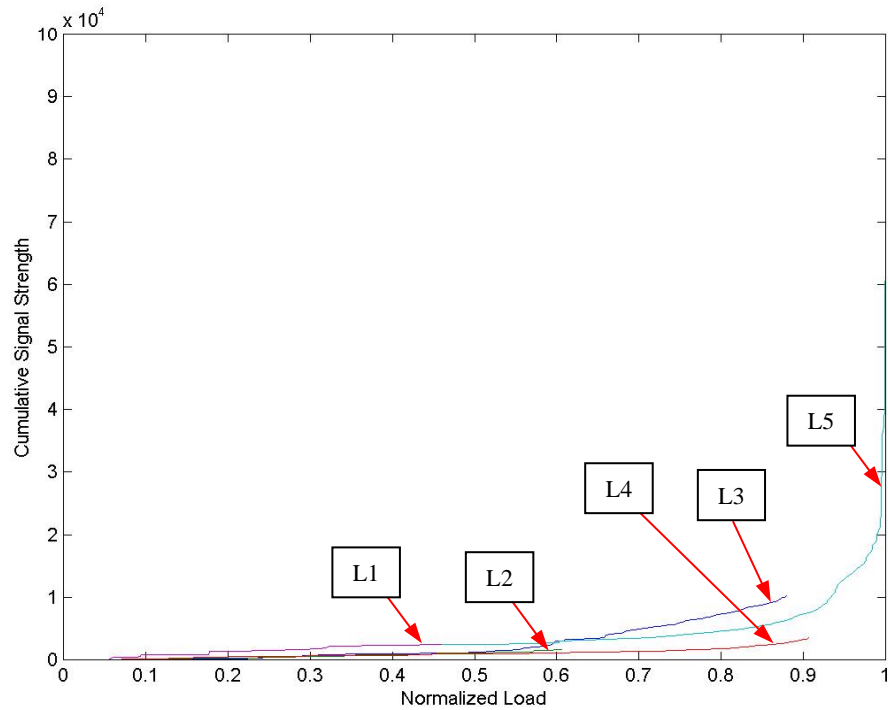
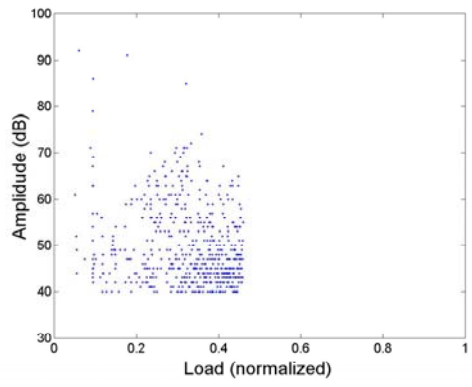
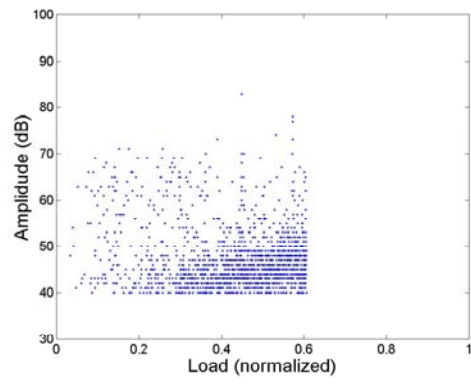


Figure 4.21: Cumulative Signal Strength vs. Load for All Specimens

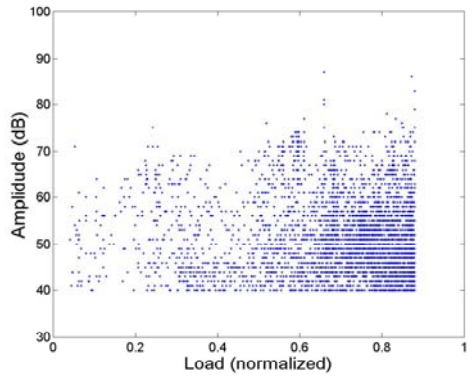
The amplitude vs. load plots of all specimens are shown in Figure 4.22. It was noticed that there were a few high amplitude hits (hits with an the amplitude greater than ≈ 70 dB) from specimens L1 and L2. The plot of specimen L3 shows a large number of high amplitude hits, whereas the number of high amplitude hits from specimen L4 fell between those from specimens L2 and L3. As expected, specimen L5 exhibited the greatest number of high amplitude hits.



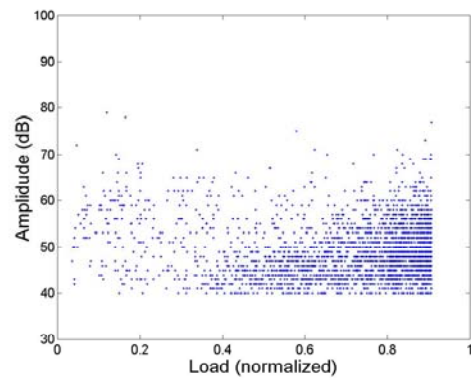
a) L1



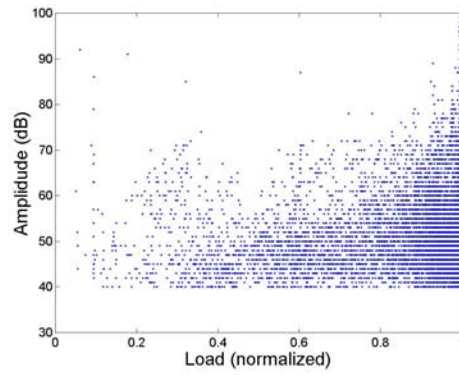
b) L2



c) L3



d) L4



e) L5

Figure 4.22: Amplitude vs. Load Plot

4.1.6 Discussion

As shown from the SEM, the first step of damage evolution was matrix cracking. Then, fiber breakage occurred when the fibers reached the ultimate strain. After that, fiber/matrix debonding took place. At the ultimate load, delamination and fiber pullout occurred almost at the same time.

The number of fiber breaks from the SEM photographs showed good agreement with the AE results. This relationship can be concluded as follows:

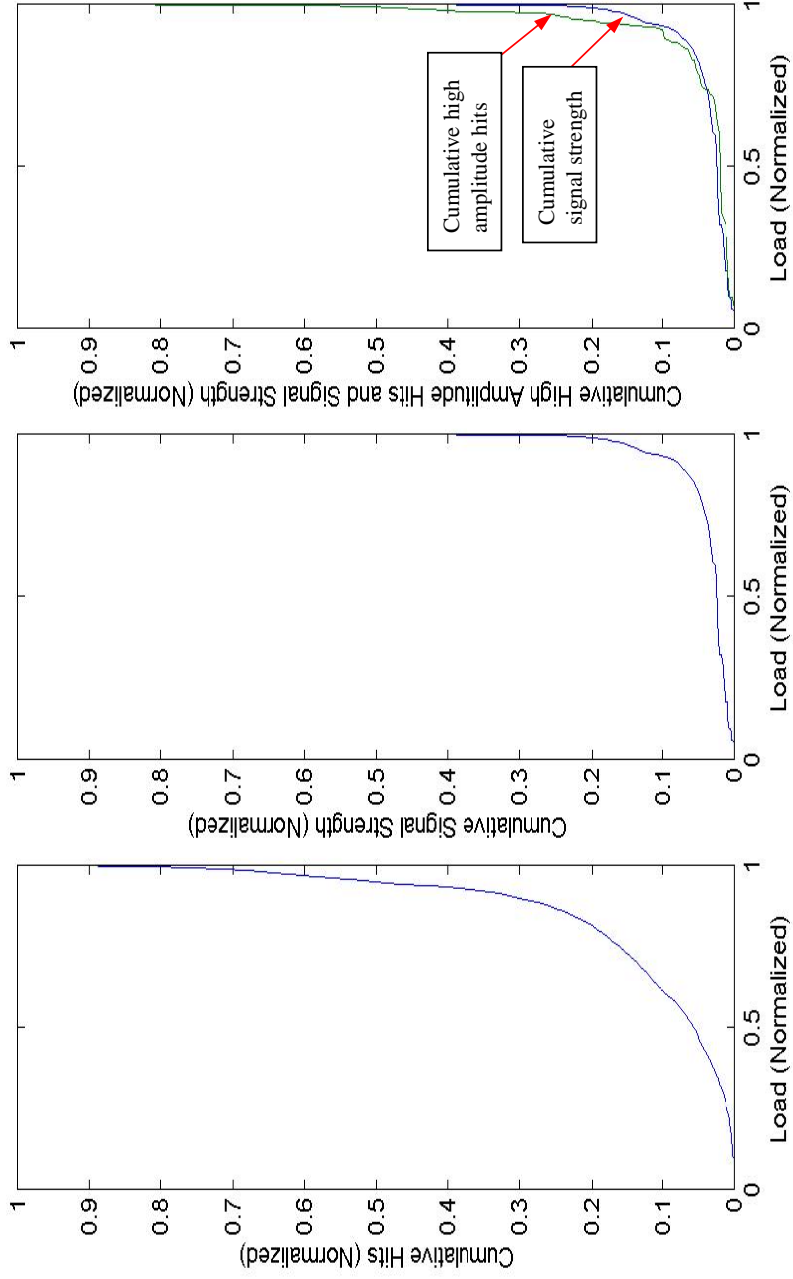
1. Only a few fiber breaks were found by the SEM in specimen L1. The AE cumulative signal strength showed a flat curve slightly above the x-axis. A few high amplitude hits were detected.
2. Approximately the same number of fiber breaks as specimen L1 was found in specimen L2. However, more matrix cracks were found in specimen L2. The AE cumulative signal strength still showed a flat curve slightly above the x-axis. Also, only a few high amplitude hits were detected, even though more matrix cracks were found.
3. A higher number of fiber breaks was found in specimen L4. This was associated with a slight increase of the cumulative signal strength curve and an increase of high amplitude hits detected from the test.
4. The substantial number of fiber breaks in specimen L3 can be related to the increase in the cumulative signal strength curve of the specimen. The amplitude vs. load plot showed a significant number of high amplitude hits.
5. Specimen L5 was taken to the ultimate load, and cross section breaks were visible. The cumulative signal strength curve showed a steep rise at ultimate. A much greater number of high amplitude hits than those of specimen L3 were found.

In conclusion, this experiment clearly indicated that the number of fiber breaks is related to the high amplitude hits and signal strength. Lower amplitude hits were attributed to other failure mechanisms such as matrix cracking, fiber/matrix debonding, and delamination.

At this point, the association of high amplitude hits with fiber breakage is validated and low amplitude filtering can be applied to eliminate data from other mechanisms. Figure 4.23a shows the normalized plot of cumulative AE hits vs. load for specimen L5. As indicated previously, this plot is an approximation of the cumulative damage in the specimen. Figure 4.23b shows the normalized plot of cumulative signal strength vs. load for the same specimen. Based on the SEM observations, this plot is an approximation of the cumulative number of fiber breaks. It is shown from these plots that there is a difference between the shapes of the curves.

When the low amplitude AE hits are filtered out, the shape of the plot of the cumulative remaining hits vs. load becomes similar to the shape of the plot of the cumulative signal strength vs. load. When the hits having amplitude below 74 dB are removed, the two plots become almost identical. This is shown in Figure 4.23c. This is another confirmation that high amplitude hits are related to the fiber breaks. In addition, the amplitude of 74 dB is a boundary between the hits from fiber breakage and non-fiber breakage.

At the beginning of the test, little fiber/matrix debonding was found. This mechanism always occurred after the fiber breakage. Accordingly, it is also concluded that the low amplitude hits detected before the occurrence of the first high amplitude hits were likely to be emitted from matrix cracking.



a) Cumulative Hits vs. Load b) Cumulative Signal Strength c) Cumulative High Amplitude Hit (≥ 74 dB) and Signal Strength vs. Load vs. Load

Figure 4.23: Plot of Cumulative Hits vs. Load Before and After Filtering

The study from Zweben (1968) is applied to the AE data from specimen T5. Figure 4.24 is the plot of number of fiber breaks vs. load, which are from 2 sources. The first source is the number of fiber breaks from the cumulative high amplitude hits vs. load plot. The other source is from the calculation based on Zweben's study. It is found that the Weibull parameters of Zweben's study that give good correlation to the cumulative signal strength vs. load curve is $\beta = 30$ and $\alpha^{-1/\beta} = 150$ kip-in. It is noted that the β value of 30 is quite high and explains that these glass fibers do not have much strength distribution. This can be attributed to the good fabrication and handling processes.

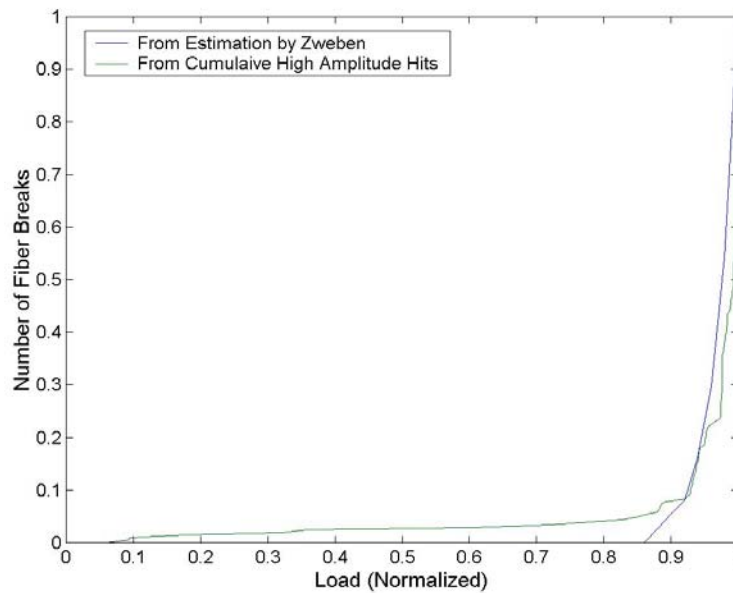


Figure 4.24: Number of Fiber Breaks Plot from Zweben's Study and from Cumulative High Amplitude Hits

4.2 EXPERIMENTAL PROGRAM FOR FIBER BREAKAGE DATABASE

In this experiment, dog-bone coupons were cut from the beams FG, IKG, and SW described in Chapter 3. They were tension tested in the longitudinal direction (fiber direction parallel to the stress direction). In addition to the coupon specimens, two full-scale beams (FGI and FGV) were also prepared and subjected to bending tests. These specimens were machined to ensure the tension failure from bending.

All the samples consisted of unidirectional fiber layers alternated with chopped strand mat layers. The chopped strand mat layers were added in order to gain strength in the transverse direction. As a result, these samples were more complex but more representative of actual construction than samples L1 to L5 described in the Section 4.1.

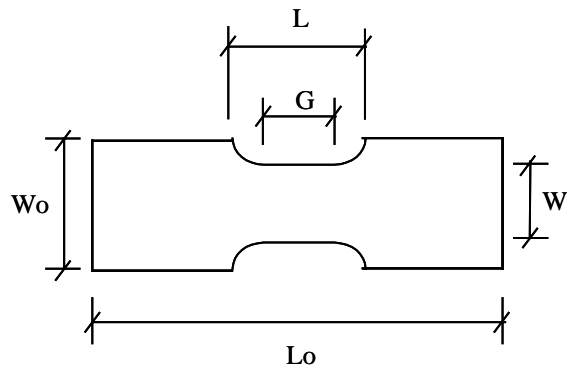
The low amplitude filtering technique and experience gained in Section 4.1 was applied to the AE data from these specimens in order to identify failure mechanisms of the specimen. The AE data and the failure mechanism information are used as a database for neural networks performing pattern recognition in Chapter 8.

4.2.1 Experimental Program

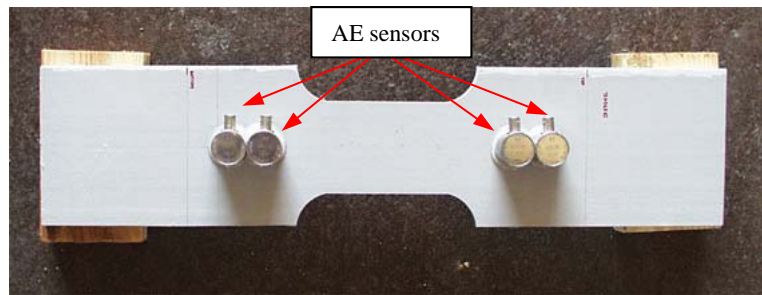
4.2.1.1 *Coupon Specimens*

Five coupons were cut from the original full-scale beams. The coupons were cut into dog-bone shapes. The dimensions and the material information are described in the Table 4.3. The coupons were made of three different materials. Representative samples of each material are shown in Figure 4.25.

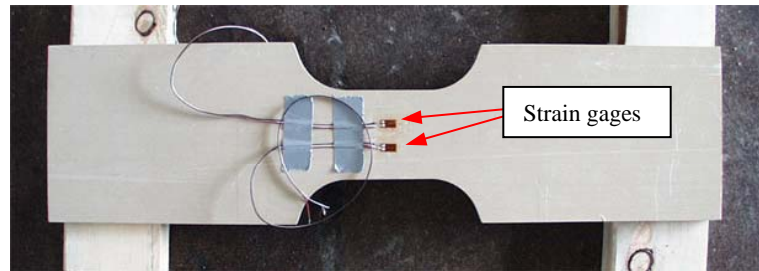
Table 4.3: Material Information and Specimen Dimensions (inches)



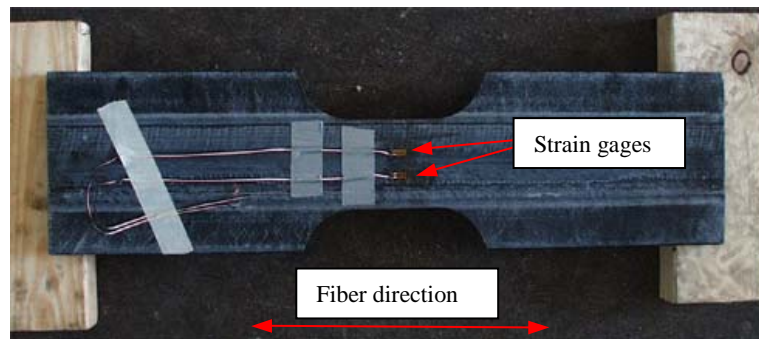
Specimen	LGI1	LGI2	LGV1	LGV2	LHV
Girder the specimen was cut from	FG1	FG1	IKG1	IKG1	SW2
Location of the cut	Web	Web	Web	Web	Flange
Material	Glass fiber/ isophthalic polyester	Glass fiber/ isophthalic polyester	Glass fiber/ vinyl ester	Glass fiber/ vinyl ester	Hybrid/ vinyl ester
Overall length (L_o)	19.5	23	23.25	30	23
Overall width (W_o)	5.25	5.5	6	6	6
Dogbone length (L)	6	6.25	6.5	5.5	6.5
Length of narrow section (G)	1	4	3	0	3
Width of narrow section (W)	3.125	3.25	3	3.25	3
Thickness	0.5	0.5	0.5	0.5	0.6



a) Specimen LGI2



b) Specimen LGVI



c) Specimen LHV

Figure 4.25: Representative Samples for Coupon Tension Test

Loading was applied to the longitudinal axis of the specimens. The load was applied monotonically up to failure. The testing machine used was the Universal Testing Machine 600HVL. Two strain gages were attached on each specimen to monitor longitudinal strains during the test.

AE was monitored during testing. The AE data acquisition system used was the Mistras system. Four R15I sensors were mounted on the specimens. The sensors were arranged in two pairs located at both ends of the reduced section, as shown in Figure 4.26. With this sensor arrangement, source location of the damage could be performed if needed. Figure 4.27 shows the coupon test setup.

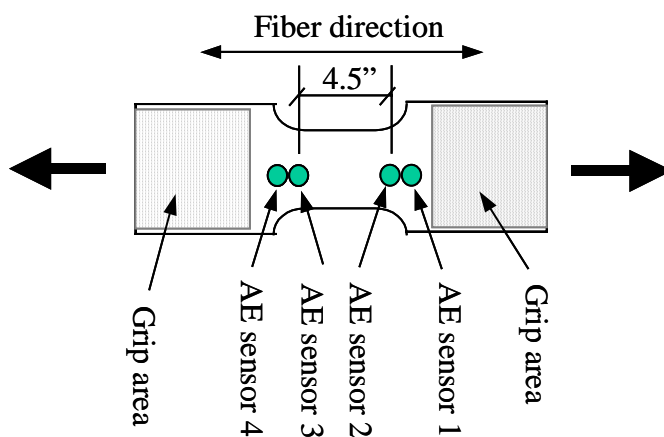


Figure 4.26: Sensor Locations on the Specimen

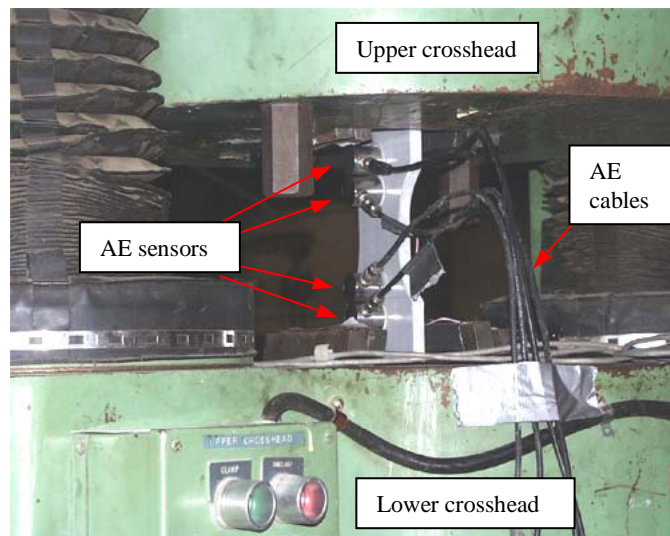
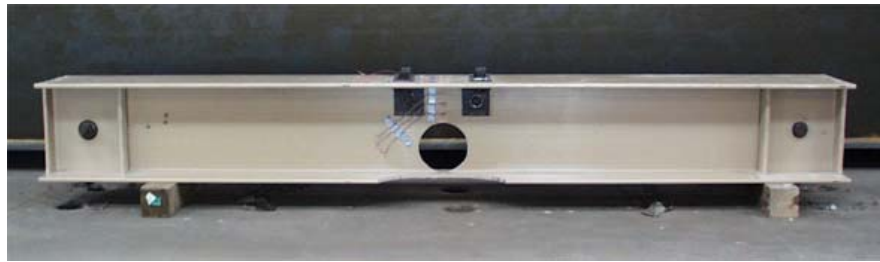


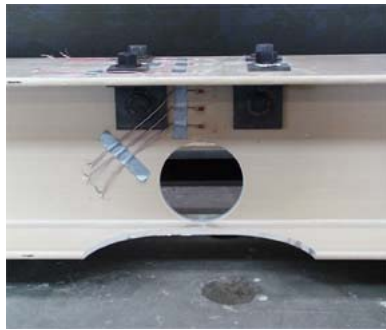
Figure 4.27: Test Setup of Coupon Specimens

4.2.1.2 Full-Scale Specimens

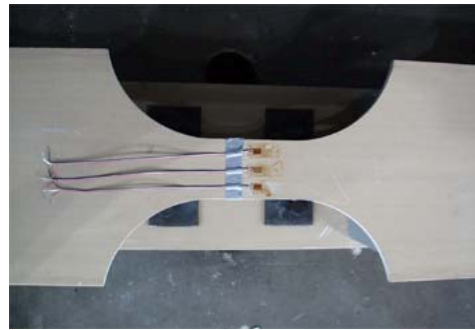
Larger specimens were tested to obtain a more realistic AE database for pattern recognition of fiber breakage. Two full-scale specimens were tested (FGI and FGV) having dog-bone sections at the bottom flange (midspan), and a circular hole at the lower part of the web (see Figure 4.28a, 4.28b, and 4.28c). This geometry was designed to reduce the strength of the bottom flange so that it reached its tensile capacity before the top flange buckled. Beam FGI and FGV were cut from the original beam FG, and IKG respectively. Therefore, beam FGI was made of glass fiber/isophthalic polyester, while beam FGV was made of glass/vinyl ester.



a) Overview



b) Circular Hole in the Web



c) Dog Bone Bottom Flange

Figure 4.28: Specimen FGV

Each beam was 98-inch long and had the cross section of the FRP beam, which was a WF 12 in x 12 in x ½ in. The narrow section of the bottom flange had a width of 3 inches. Also, there was a 4-inch diameter circular hole at midspan for specimen FGI, and a 6-inch diameter hole for specimen FGV. Figure 4.29 shows the typical dimensions of the specimens.

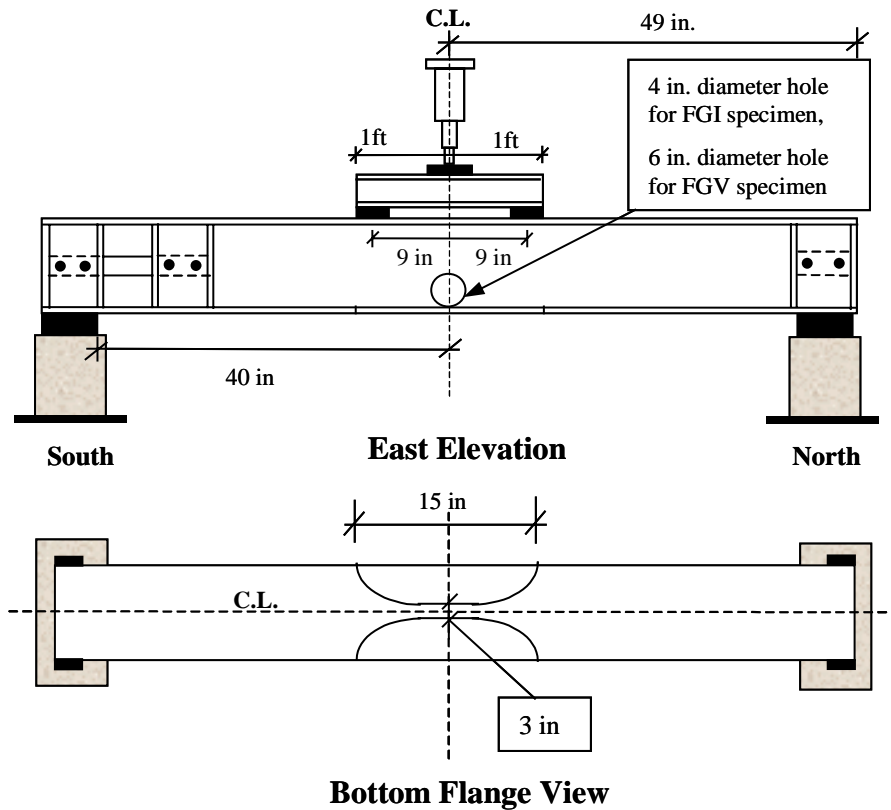


Figure 4.29: Four-Point Bending Test Specimen

Both specimens also had the web at each end braced to prevent it from buckling. FRP Structural channels were used on both sides of the web. FRP structural tubes of 3 in x 3 in x ¼ in were also braced under the ends of the spreader beam on both sides of the web. This essentially reduced the effective length of the specimen. A pair of steel angles was also attached on both sides of the web at the corner of the top flange and the web. The purpose of the angles was to decrease the chance of the top flange buckling. The resulting test configuration is shown in Figure 4.30, and the overview test setup is shown in Figure 4.31.

Eight R15I sensors were used as primary sensors and were attached on each specimen. Two pairs of sensors were located on the bottom flange at both ends of the reduced section (see Fig. 4.32). Two sensors were located on the web and two were located on the top flange. These sensors were connected to the Mistras AE data acquisition system. Two additional R15I sensors were located on the bottom flange near the dog-bone area. These sensors were connected to the Transportation Instrument as backup for the AE data. Figure 4.32 shows the sensor locations on specimen FGI.

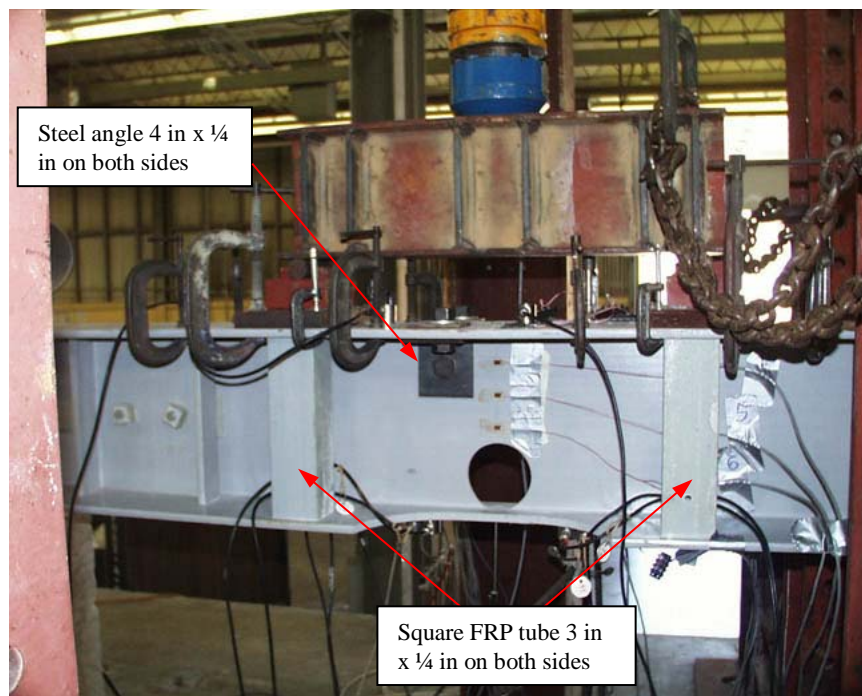


Figure 4.30: Specimen FGI with Increased Buckling Resistance

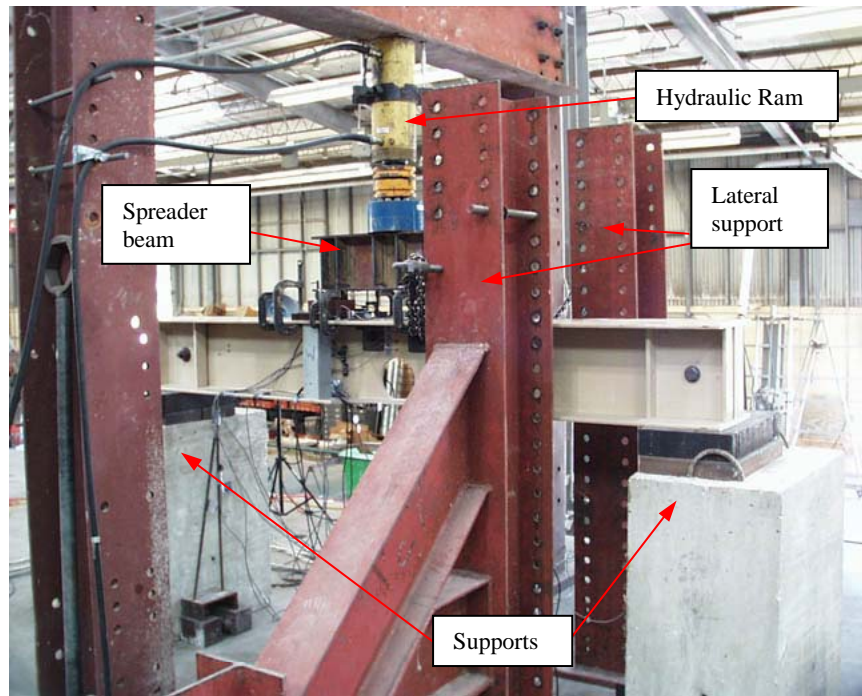


Figure 4.31: Test Setup of Beam FGV

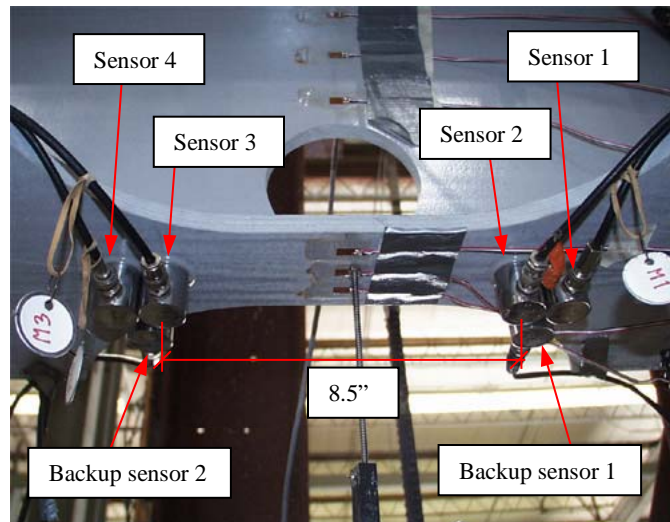


Figure 4.32: Sensor Locations on Specimen FGI

4.2.2 Results

4.2.2.1 Coupon Specimens

Stress-strain curves of the specimens are shown in Figure 4.33. Specimen LHV had the highest ultimate stress (61 ksi), while specimen LGV2 had the highest ultimate strain (12,000 microstrain). The elastic modulus of specimens LGI1 and LGI2 were approximately 3,500 ksi, while they were approximately 3,700 ksi for specimens LGV1 and LGV2. Specimen LHV gave an elastic modulus of 7,600 ksi. The carbon fibers in the specimen are the reason for the large modulus and higher ultimate stress. Table 4.4 summarizes ultimate stresses, ultimate strain, and elastic modulus of the specimens.

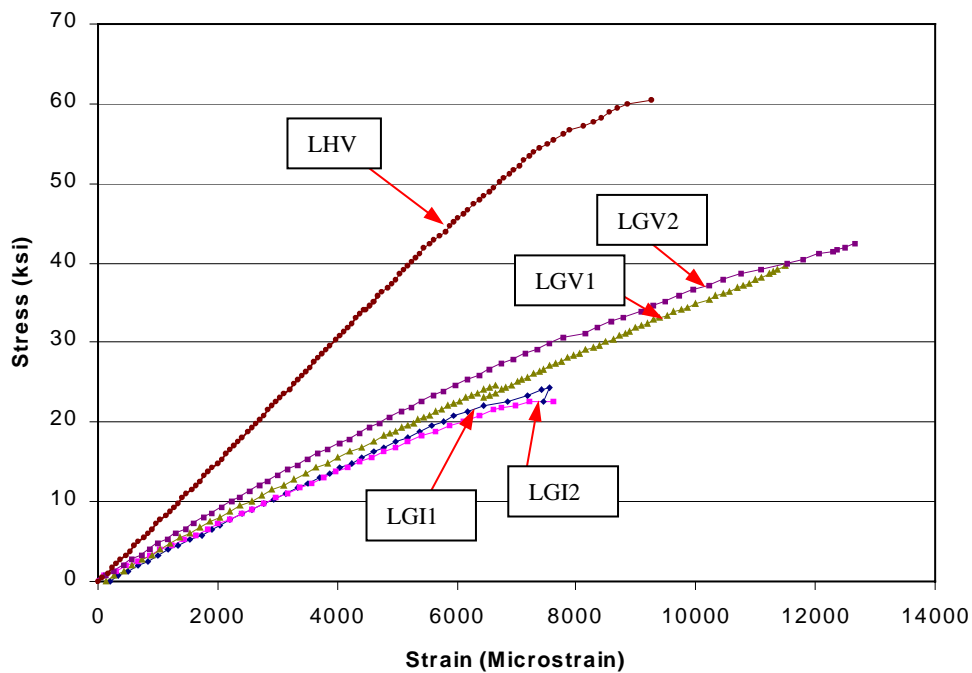


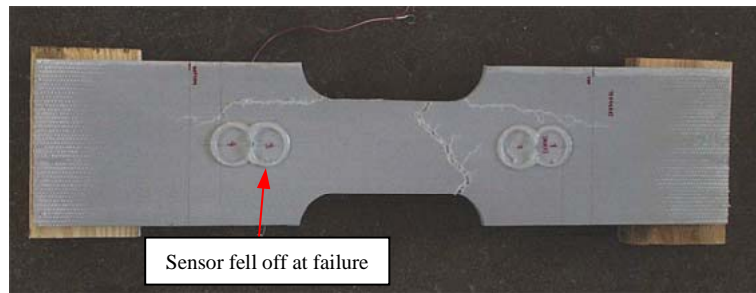
Figure 4.33: Stress-Strain Curves for All Specimens

Table 4.4: Summary of Ultimate Stress, Ultimate Strain, and Elastic Modulus of the Specimens

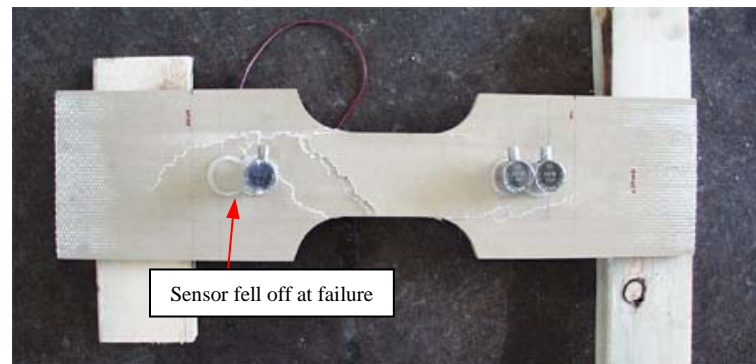
Specimens	Ultimate Stress (ksi)	Ultimate Strain (microstrains)	Elastic Modulus (ksi)
LGI1	24.36	7,547	3,630
LGI2	22.62	7,620	3,330
LGV1	39.53	11,492	3,510
LGV2	42.59	12,630	4,070
LHV	61.00	9,600	7,605

Pictures of failures of representative specimens after the test are shown in Figure 4.34. The majority of the visible fractures occurred at the ends of the narrow section in each specimen. Fiber breakage, matrix cracking, fiber/matrix debonding, and delamination could be seen by the naked eye. Figure 4.35 shows a typical failure on the side of the specimen, and Figure 4.36 is a close-up picture showing fiber breakage.

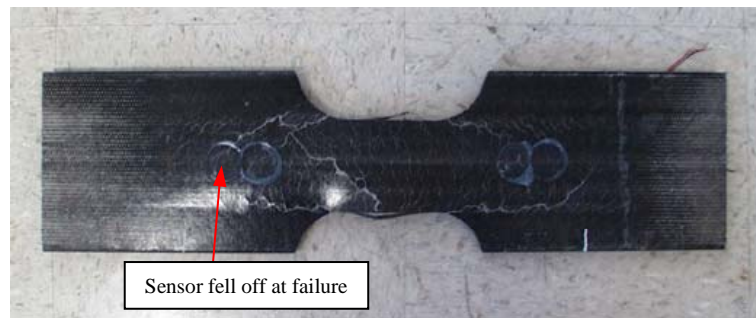
A summary of total AE hits from all specimens is shown in Table 4.5. Specimen LHV had the most AE hits, while the least number of hits occurred in specimen LGI1. The total number of hits depends on several factors such as size of the specimen, fiber fraction, number of fibers in a cross section area, number of cracks, and the length of the narrow section. Specimen LHV had some carbon fibers, which are smaller diameter than the glass fibers. Thus, for the same volume percentage of fiber, there are more carbon than glass fibers.



a) Specimen LGI2



b) Specimen LGV1



c) Specimen LHV

Figure 4.34: Tensile Failure of the Specimens



Figure 4.35: Tensile Failure and Delamination on the Side of Specimen LGVI

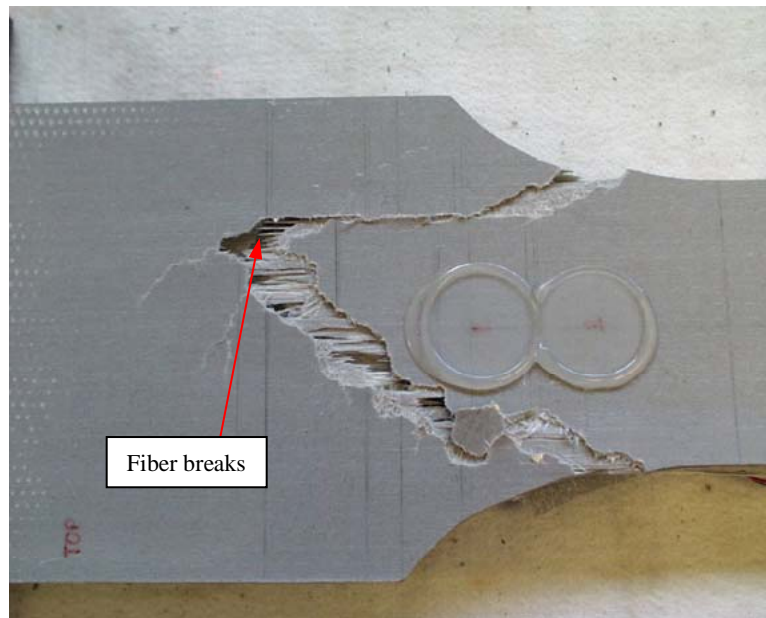


Figure 4.36: Fiber Breakage on Specimen LGII

Table 4.5: Summary of AE Data

Specimen	Average AE hits per sensor
LGI1	32,493
LGI2	78,312
LGV1	171,476
LGV2	189,536
LHV	244,237

The visual damage evolution of all specimens was documented in conjunction with the AE data. Only one representative specimen (LGI2) is described in detail in this section. The visual damage evolution was as follows:

1. The specimen was monotonically loaded with a constant crosshead speed. No damage was observed on the specimen from the beginning up to 24 kips (15.6 ksi), and only low amplitude AE hits were detected.
2. At the load of 24 kips (15.6 ksi and 4,624 microstrain), high amplitude hits started to occur, and a fine crack could be noticed at an end of the bottom curve of the dog-bone (see Fig. 4.37). Also, at this point, the cumulative signal strength curve started to increase.
3. As the load increased, the crack propagated, and other cracks were observed. This was associated with an increasing number of high amplitude hits, as can be seen from the amplitude vs. time plot.
4. At failure, the specimen was completely fractured, and the AE hits of 100 dB were detected.

A detailed summary of the visual damage evolution as well as AE amplitude data of specimen LGI2 is also shown in Fig. 4.37.

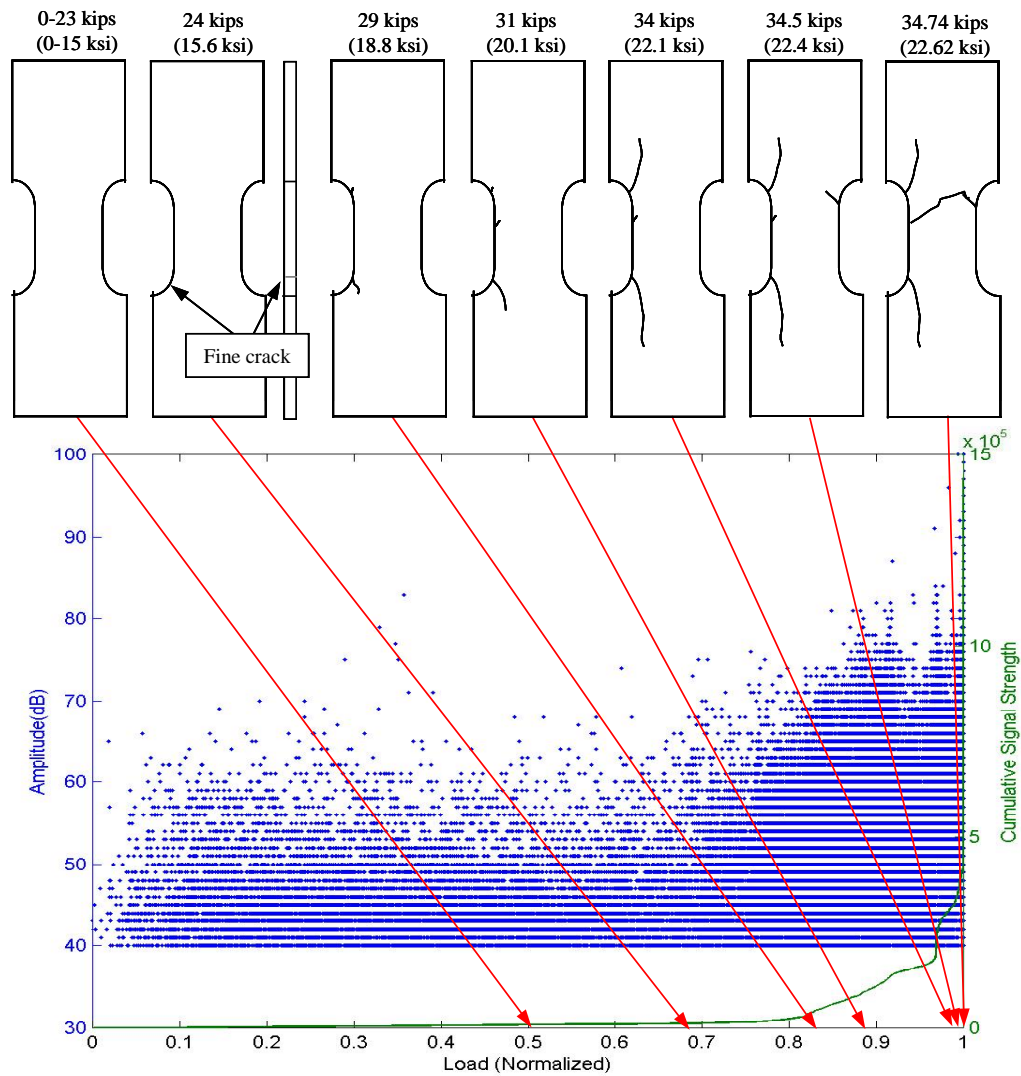
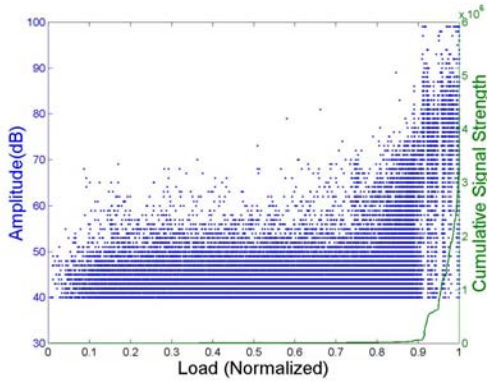


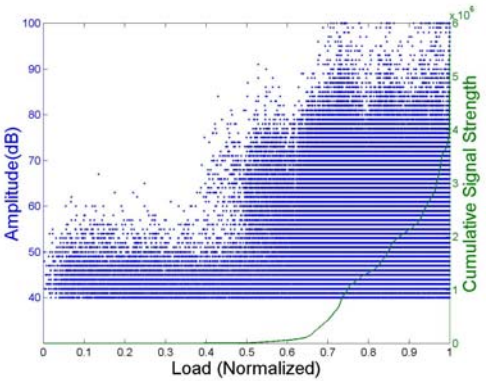
Figure 4.37: Visual Damage Evolution on Specimen LGI2 Corresponding with AE Amplitude/Cumulative Signal Strength vs. Normalized Load (Sensor 2)

The normalized plots of amplitude superimposed with cumulative signal strength vs. load of other specimens are shown in Fig. 4.38. It was noticed from all plots except specimen LHV that AE amplitudes were consistently low at the

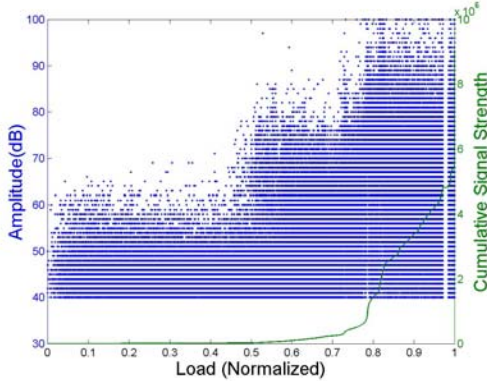
beginning of test, while high amplitude hits were consistently detected after the first crack was observed. In specimen LHV, however, high amplitude hits occurred earlier in the test. High amplitude hits were observed to be associated with the increase of cumulative signal strength for every specimen.



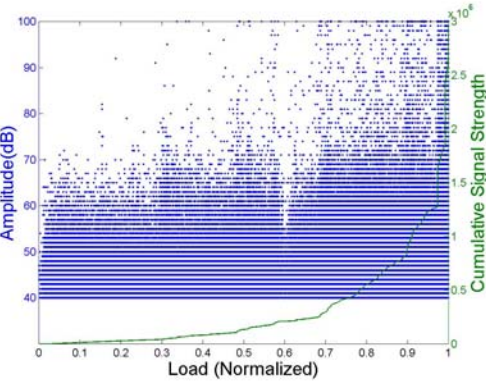
a) Specimen LGI1 (Sensor 1)



b) Specimen LGV1 (Sensor 2)



c) Specimen LGV2 (Sensor 1)



d) Specimen LHV (Sensor 1)

Figure 4.38: Amplitude Superimposed with Cumulative Signal Strength vs. Load (Normalized)

4.2.2.2 Full-Scale Specimen Results

Both specimens failed by tensile fracture of the bottom flange, as intended. Figures 4.39 and 4.40 show the tensile fracture of the bottom flange and of the web at the top and bottom of the circular hole in FGI beam, respectively. Figure 4.41 is a picture of beam FGV at failure.

Figures 4.42a and 4.42b show the load-deflection curves of both beams. The approximate elastic modulus of beam FGI based on the computed moment at the reduced section was 3,425 ksi. Beam FGV had a higher elastic modulus of 4,255 ksi. The ultimate strain of the bottom flange was 9,100 microstrain for beam FGI, and 14,000 microstrain for beam FGV.

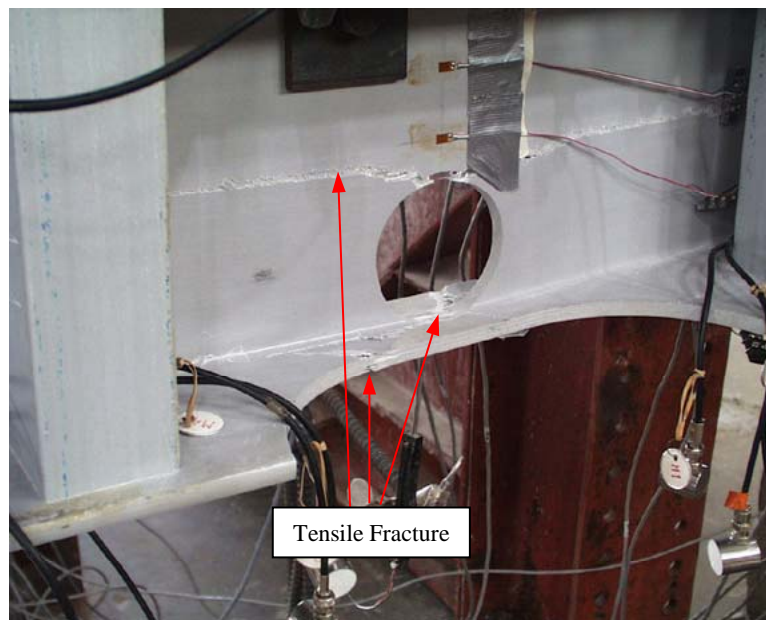


Figure 4.39: Beam FGI at Failure

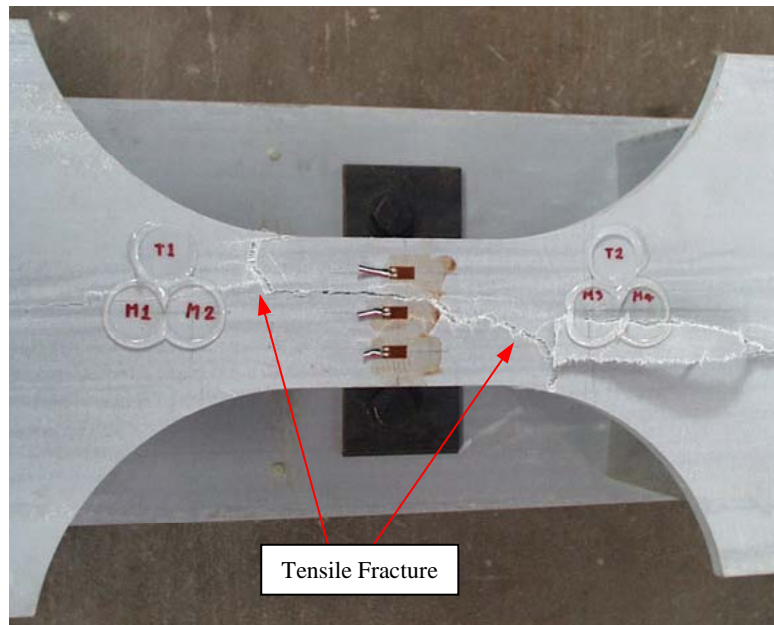


Figure 4.40: Bottom Flange at Failure of Beam FGI

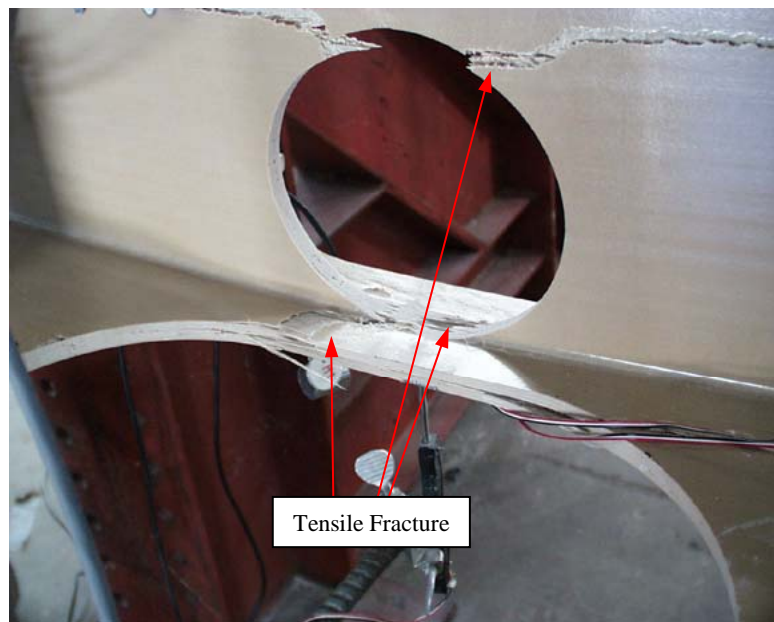
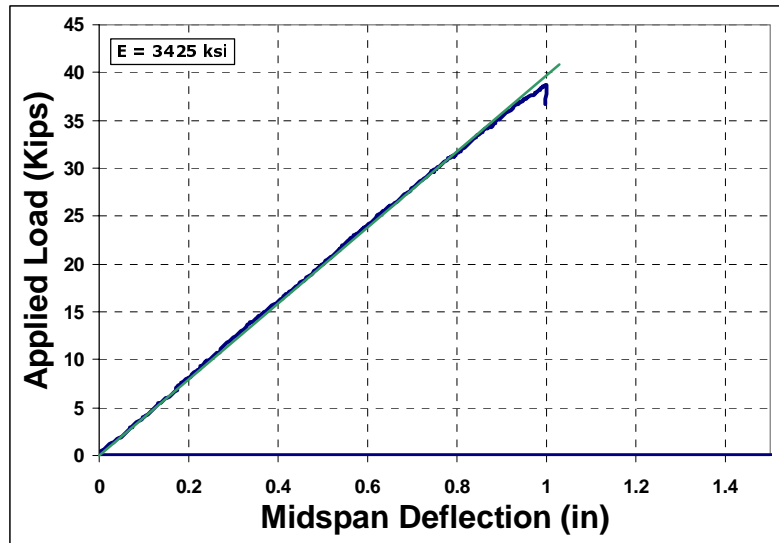
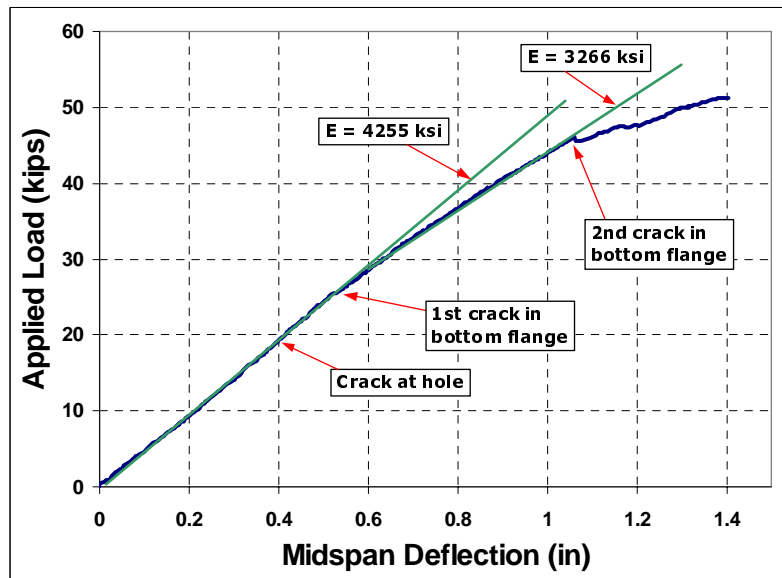


Figure 4.41: Beam FGV at Failure



a) Beam FGI



b) Beam FGV

Figure 4.42: Load Deflection Response at Midspan (Adapted from Ulloa, 2002)

The AE data was focused only on the four sensors located on the bottom flange of both specimens because the bottom flange was subjected to the tensile stress. The total AE hits from both beams are summarized in Table 4.6.

Table 4.6: Summary of Total AE Hits

Beam	Average AE hits per sensor
FGI	110,029
FGV	117,409

The damage evolution of both specimens was recorded. Only the damage evolution of beam FGV is described in this section:

1. No damage was observed during the initial loading (0-19.8 kips). This corresponded with low amplitude AE hits detected from the test.
2. At a load of 19.8 kips, a small crack was noticed at the bottom of the circular hole (see Fig. 4.43). This corresponded with the onset of high amplitude hits, as well as a rise of cumulative signal strength.
3. At a load of 25 kips, a crack on the side of the bottom flange was observed (see Fig. 4.44). This corresponds to the departure from linearity of the load vs. deflection curve. High amplitude hits continued to occur.
4. At a load of 45 kips, another crack occurred on the bottom flange (see Fig. 4.45). Here, there is a significant discontinuity in the load vs. deflection curve with the load dropping. The cumulative signal strength curve has a pronounced knee at this point.
5. At a load of 51 kips, the beam failed due to the tensile fracture of the bottom flange. No AE could be recorded after this point since all the AE sensors became detached from the beam (see Fig. 4.41).

6. After failure, the load was held constant, and a longitudinal shear crack propagated from the center of the beam to the north end. The failure appeared to be caused by shear transfer due to the reduced cross section (see Fig. 4.46).

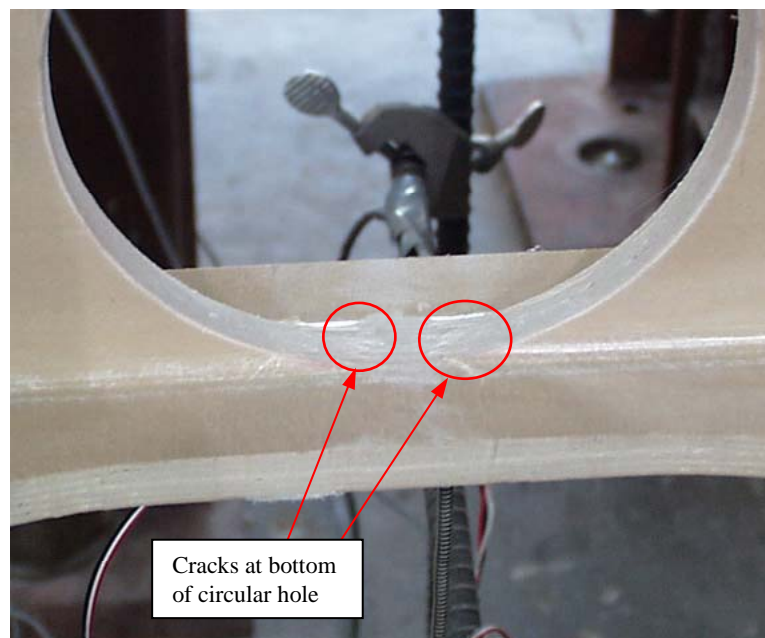


Figure 4.43: First Observed Crack at the Circular Hole

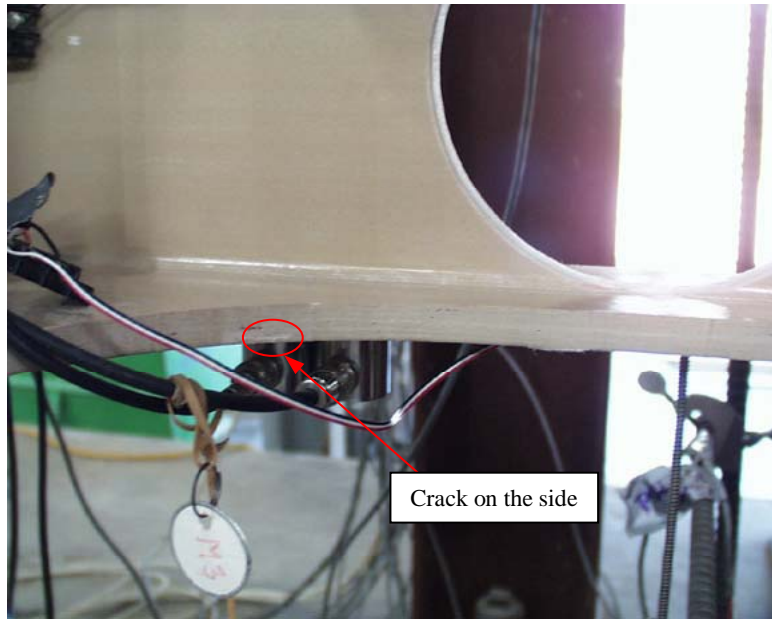


Figure 4.44: Crack on Side of Bottom Flange



Figure 4.45: Additional Crack at Bottom Flange

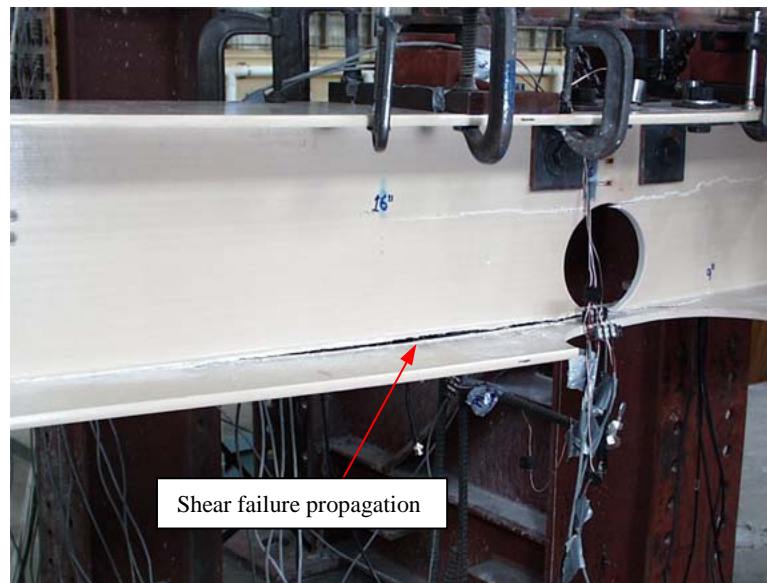


Figure 4.46: Shear Failure (During the Load Hold)

Figure 4.47 shows the AE response (amplitude/cumulative signal strength vs. normalized load) of beam FGV. Figure 4.48 shows the same plot but with a smaller signal strength range. This plot shows a knee of the signal strength curve corresponding with the crack at the hole. For beam FGI, the damage evolution occurred almost identically to that observed in beam FGV. The one exception was that there was no shear failure propagation. Figure 4.49 shows the amplitude/cumulative signal strength vs. normalized load plot of beam FGI. As was the case with FGV, it was noticed in beam FGI that the start of high amplitude hits was associated with the first crack found at the bottom of the circular hole.

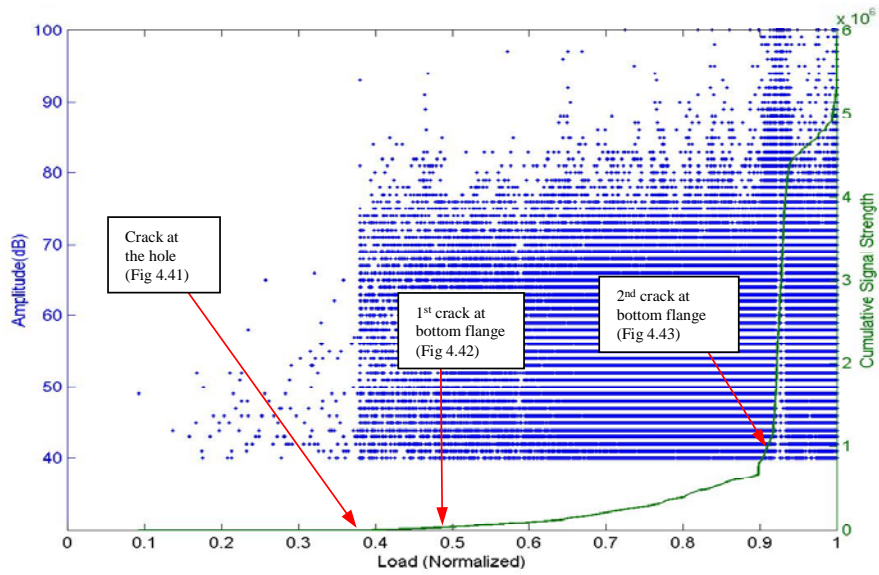


Figure 4.47: Amplitude Superimposed with Cumulative Signal Strength vs. Load of Beam FGV

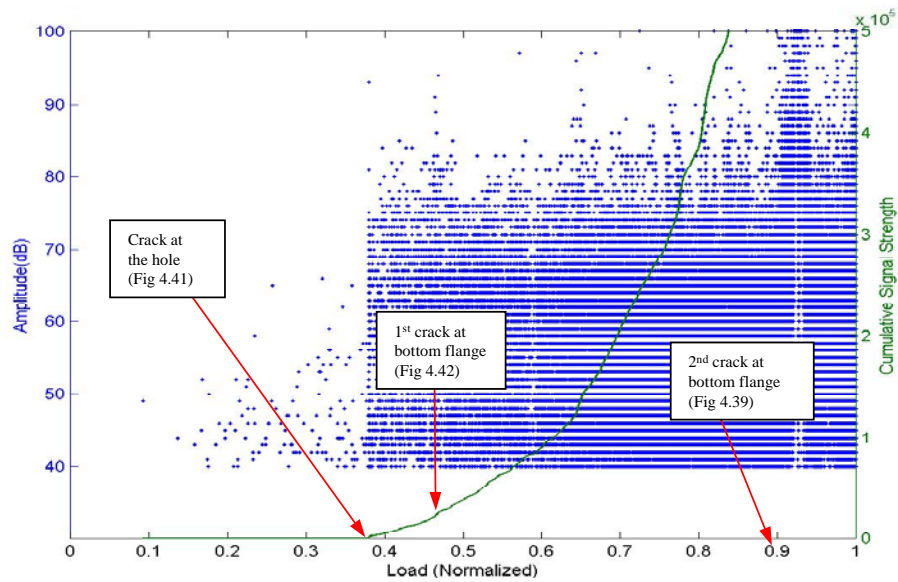


Figure 4.48: Amplitude Superimposed with Cumulative Signal Strength (with a Smaller Range) vs. Load of Beam FGV

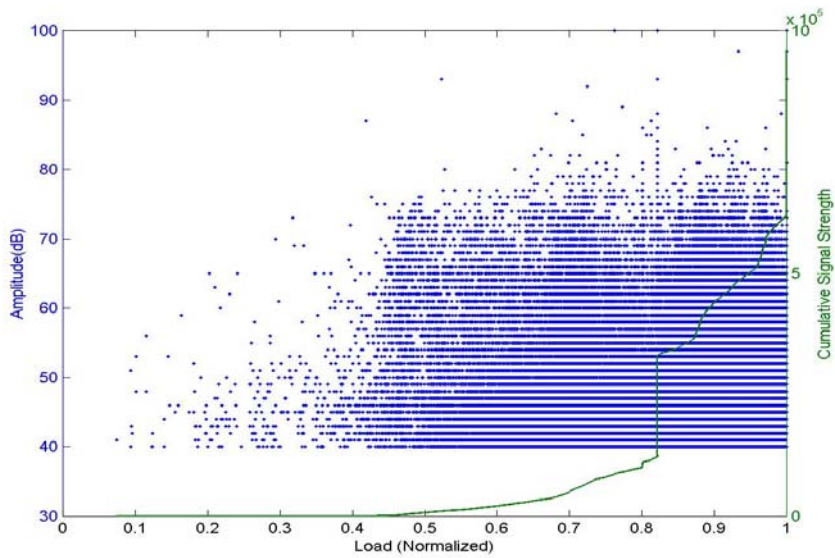


Figure 4.49: Amplitude Superimposed with Cumulative Signal Strength vs. Load of Beam FGI

4.2.3 Discussion

General

The amplitude vs. load plots of all specimens in this section (4.2) can be divided into two portions. The first portion mainly consists of low amplitude AE hits, which occur in the beginning of the test. The study from Section 4.1 found that the only mechanism that occurs before the first fiber break takes place (or before the appearance of the first high amplitude hit) is matrix cracking. As a result, it is concluded that the first portion of the test was associated with matrix cracking only.

The second portion involves both low and high amplitude hits. This portion started later during the test. Generally, it began when the first crack was

observed. The cumulative signal strength curve also began to increase at this point. The findings from Section 4.1 explain that this portion involved fiber breakage and other failure mechanisms such as matrix cracking, fiber/matrix debonding, and delamination.

Low Amplitude Filtering

The low amplitude filtering, which is a tool used to estimate the borderline between fiber breakage and non-fiber breakage hits, was also performed. The results are shown in Table 4.7. As expected, the borderline amplitudes of all but specimens LHV are in a high range (above 75 dB). Specimen LHV, which was made of glass and carbon fibers, exhibited relatively low borderline amplitude when fiber broke. This agrees with the result from Valentin’s work (Valentin, et al., 1983), which was attributed to the effect of the small diameter of the carbon fibers. Figure 4.50 shows the representative plot of an amplitude/cumulative signal strength vs. load (from specimen LGV1) with a superposed failure mechanism summary.

Table 4.7: Summary of Low Amplitude Filtering Results

Specimen	Material	Average borderline amplitude
LGI1	Glass/Isophthalic Polyester	76
LGI2	Glass/Isophthalic Polyester	76
FGI	Glass/Isophthalic Polyester	76
LGV1	Glass/Vinyl Ester	80
LGV2	Glass/Vinyl Ester	81
FGV	Glass/Vinyl Ester	81
LHV	Hybrid/Vinyl Ester	68

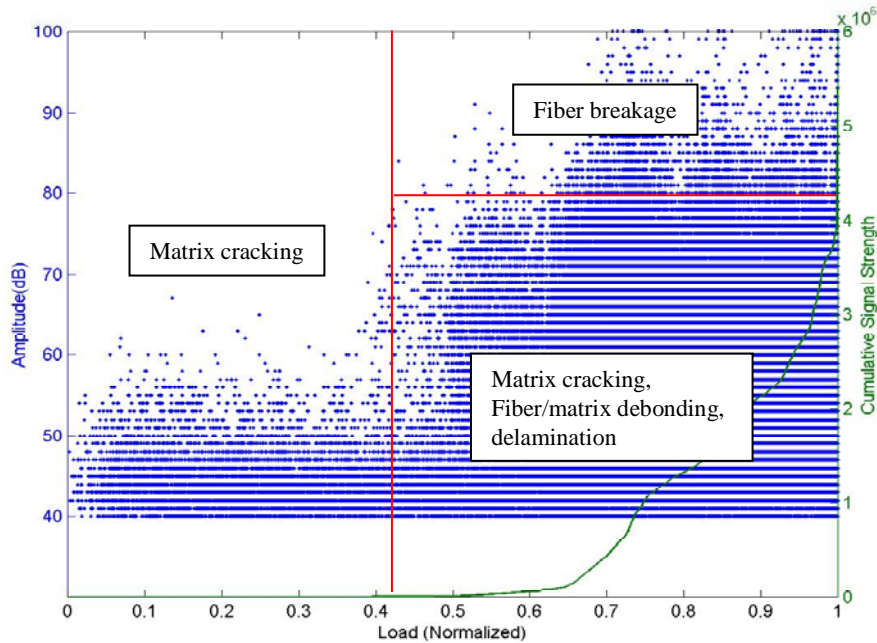
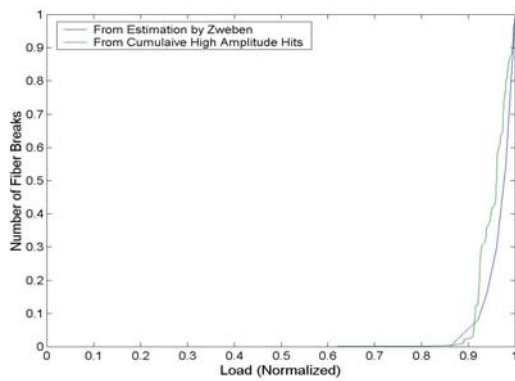


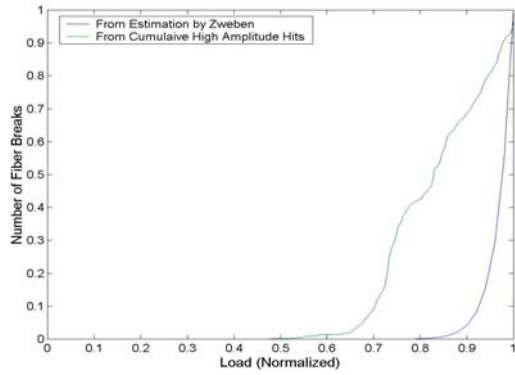
Figure 4.50: Summary of Failure Mechanisms of Specimen LGV

Comparison Cumulative High Amplitude Hits with Zweben's Theory

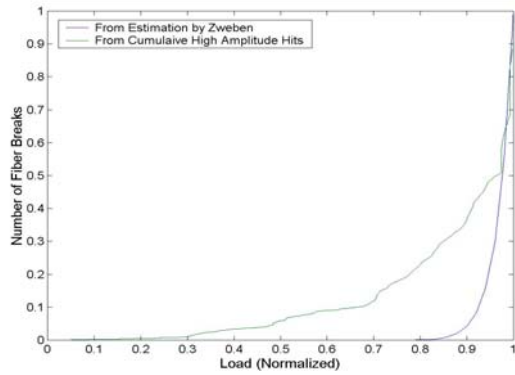
The number of fiber breaks calculated by Zweben theory is plotted against the cumulative high amplitude hits vs. load plot of three coupon specimens LGI1, LGV1, and LHV (Fig. 4.51). The Weibull parameters for fiber strength distribution used here are the same as those used with specimen T5. It is shown that the numbers of fiber break plot based on Zweben study has a good correlation with cumulative high amplitude hits vs. load plot of specimen LGI1 (Fig. 4.51a). However, the estimation based on Zweben study has a poor and bad correlation with the cumulative high amplitude hits vs. load plots of specimens LGV1 and LHV, respectively (Fig. 4.51b and 4.51c).



a) Specimen LGII



b) Specimen LGVI



c) Specimen LHV

Figure 4.51: Number of Fiber Breaks Plots from Zweben's Study and from Cumulative High Amplitude Hits

The reason of a bad correlation between Zweben's estimation and the plot of cumulative high amplitude hits vs. load of specimen LHV can be attributed to the carbon fibers. Carbon fibers should have different values of Weibull parameters than those of glass, which is used in the plots. Carbon fibers are more brittle than glass fibers and, thus, are more susceptible to be damaged during the fabrication process. Therefore, it is believed that carbon fibers should have a lower β value than glass.

The reason of a poor correlation between Zweben's estimation and the plot of cumulative high amplitude hits vs. load of specimen LGV1 can be attributed to the combination effects of high ductility of vinyl ester resin and the presence of chopped strand fibers in the specimen. Specimen LGV1 consists of some chopped strand mats. These chopped strand mats have to undergo more strain to pick up load as fibers are strengthened. Vinyl ester in this specimen is very flexible and, therefore, allows chopped strand mat to be more effective. This is the reason that specimens with the same glass content are stronger (higher ultimate load) if parts of the specimens are chopped strand mats (see stress vs. strain plots of specimens LGV1 and LGI1 in Fig. 4.33). Thus, it can be concluded that chopped strand mats have a greater influence on ultimate stress for the specimen made of flexible resin and Zweben estimation cannot be applied to this specimen.

The poor correlation of Zweben's estimation can also be attributed to the Zweben's theory itself. In his paper, the derivation of the calculation method is based on modeling only one layer of glass fibers. The specimens tested in this research consist of many fiber layers leading to a different pattern of stress redistribution when a fiber is broken. However, it is noted that the Zweben's estimation fits very well with the cumulative high amplitude hits vs. load of

specimen LGV1. Thus, his theory works well with specimens that have a less flexible resin.

4.3 SUMMARY

In Section 4.1, five unidirectional glass FRP coupons were tested and monitored with AE. The tensile stress was applied parallel to the fiber direction to ensure fiber breakage. The fiber breakage is proven by SEM observation to be associated with the high amplitude AE hits. The shape of the plot of cumulative signal strength vs. load was also proven to be closely related to the plot of the cumulative number of fiber breaks vs. load. As a result, a method to separate the fiber break AE hits from the entire AE data, the low amplitude filtering technique, was developed.

In Section 4.2, five FRP coupons and two full-scale beams were also subjected to tensile stress. These specimens were made of different resins, and fibers. In addition to the unidirectional fibers, the specimens also had some random chopped strand fibers to provide strength in the transverse direction. Therefore, the AE data from the tests are more complex, but on the other hand, they are more realistic than the unidirectional specimens in Section 4.1. The experience from Section 4.1 showed that the first part of the tests, which exhibited only low amplitude hits, was associated with matrix cracking. Also, the remaining part of the tests, which included high amplitude hits, corresponded with fiber breakage, matrix cracking, debonding, and delamination.

The AE data and failure mechanism information provide an important documented database for training neural networks. These networks are used for pattern recognition analysis as discussed in Chapter 8.

CHAPTER 5

Matrix Cracking and Debonding

This chapter focuses on matrix cracking and fiber/matrix debonding (debonding) of FRP structures. The first section presents a study of both mechanisms on a microscopic scale. This study includes a bending test of three FRP specimens. By placing the fibers perpendicular to the longitudinal axis, tensile stress causes the specimen to fracture. The microscopic failure mechanisms observed are mainly matrix cracking and debonding. The second section presents the testing of additional specimens experiencing matrix cracking and debonding for the AE database. These specimens are fabricated from a more complex variety of materials. Accordingly, the AE database from the second test is more realistic. The observations from the first section are applied to the data from the second section in order to identify the failure mechanisms. The AE database and failure mechanism information are used as a training set for pattern recognition methods in the later chapters.

5.1 SEM STUDY

When applying tensile stress to a pure resin specimen, the specimen fails suddenly. This sudden type of failure is not representative of the growth of matrix-cracking that occurs in FRP over a period of time. As a result, a specimen reinforced with fibers is preferred to model matrix cracking. The specimen is tested such that a flexural stress is applied perpendicular to the fiber direction. This orientation has been found to yield the best AE data even though the main failure mechanisms observed during the test are a combination of matrix cracking and debonding.

The objective of this study is use the SEM to confirm the failure mechanisms in this type of the FRP specimen. The SEM is used to observe different stages of the load to determine the evolution of the failure mechanisms. These mechanisms are correlated with the AE data to establish the AE signature.

5.1.1 Experimental Program

Three FRP coupon specimens were subjected to bending. The specimens, which were made of a vinyl ester resin (Derakane 411-100) reinforced with glass fibers, were cut from the same plates as the specimens detailed in Section 4.1.2. All fibers were perpendicular to the longitudinal axis. Accordingly, when the specimen was tested, the applied stress was perpendicular to the fiber direction. The size of the specimens was 11 in. long, 0.75 in. wide, and 0.1 in. thick. A dog-bone was cut in each specimen to produce a constant 0.5 in. width in the middle. A strain gage was attached to the center of the dog-bone to monitor strains. A representative specimen is shown in Fig. 5.1. The wavy white lines running along the length of the specimen are the stitching holding the unidirectional fibers together.

The specimens were tested using a small-scale testing frame. Each specimen was loaded monotonically to different load levels. After unloading, the specimens were scanned by SEM. The SEM was performed only on the tension side or the smooth side of the specimens. A summary of the load level for each specimen is presented in Table 5.1.



Figure 5.1: Coupon Specimen

Table 5.1: Summary of the Test Program

Specimen	Maximum Load (% of ultimate strain)
T1	50
T2	85
T3	100

AE was monitored during the tests using the Mistras data acquisition system. The space for mounting an AE sensor was limited due to the size of the specimen. Thus, an R15 sensor was used. The test setup and loading geometry are shown in Figs. 5.2 and 5.3, respectively.

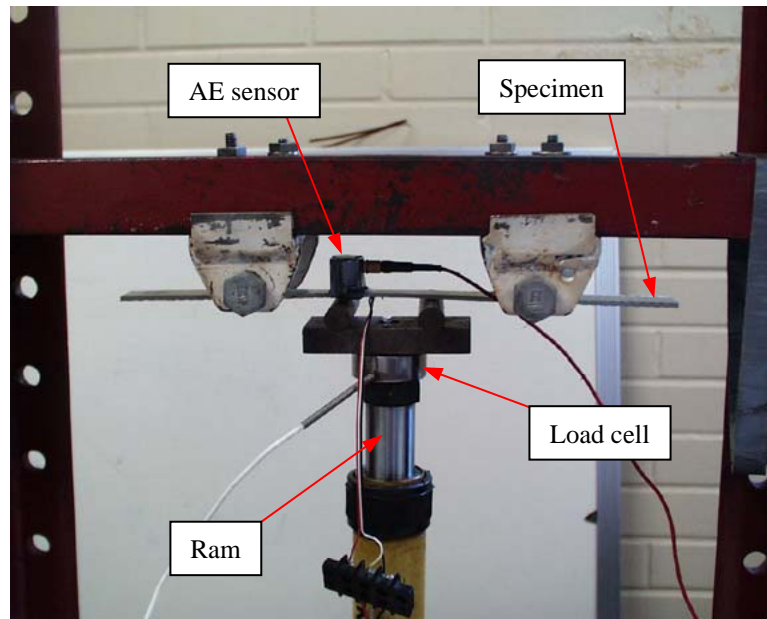


Figure 5.2: Test Setup of Coupon Specimen

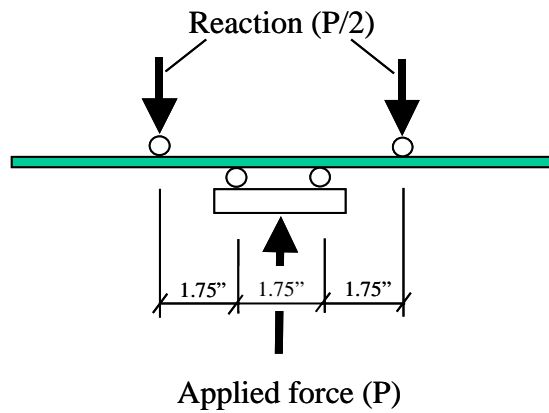


Figure 5.3: Loading Geometry of Coupon Specimen

5.1.2 Physical Results

The maximum stress based on calculated moment and maximum strain recorded for each specimen is reported in Table 5.2. No visual damage was

observed during the test except at the ultimate load. At the ultimate load, the specimen exhibited a transverse crack over the entire cross section. This crack is located under a point where the load was applied and is shown in Fig. 5.4.

Table 5.2: Summary of the Test Results

Specimen	Maximum Stress (ksi)	Maximum strain (microstrain)
T1	6.6	3,000
T2	12.1	5,050
T3	12.6	6,000

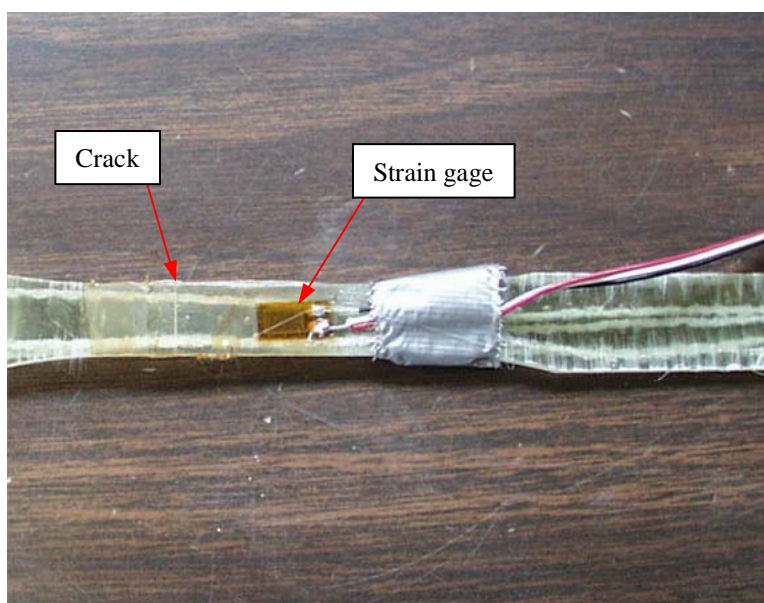


Figure 5.4: Crack at Ultimate Load

5.1.3 SEM Results

Microscopic damage was observed by SEM even though two out of three specimens appeared to be in good conditions from the naked eye. The condition

of the specimens prior to testing was as detailed in Section 4.1.4 for the specimens with longitudinal fibers. The microscopic damage of each specimen is described in the following sections:

Specimen T1 (50% of the Ultimate Strain)

Only a few cracks associated with matrix cracking were observed. These cracks were parallel to the orientation of the fibers and were located at the edge of the specimen initiating from the fractures caused by previous machining (Fig. 5.5). These previous fractures were produced during specimen fabrication. Breaking of the matrix shells, which covered the fibers, was also observed (Fig. 5.6). This damage was believed to be associated with matrix cracking and debonding (Fig. 5.7).

The sides of the specimen were also scanned. No damage development was observed.

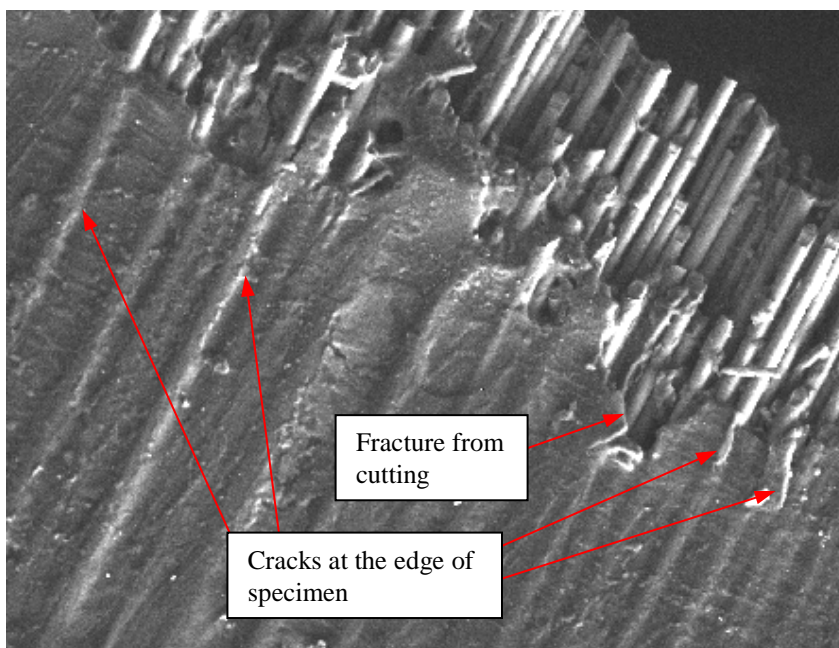


Figure 5.5: Cracks at the Edge of Specimen T1 (100x Magnification)

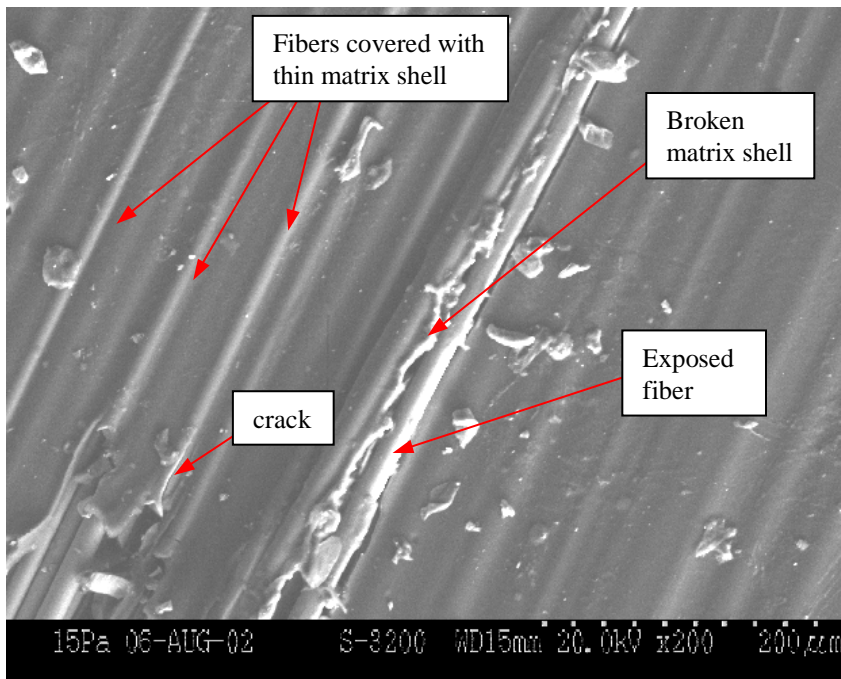


Figure 5.6: Broken Matrix Shell (200x Magnification)

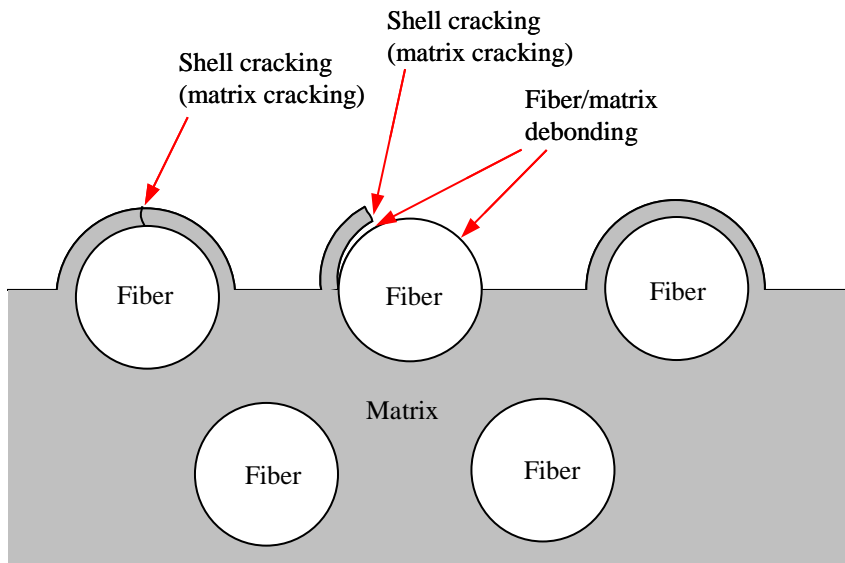


Figure 5.7: Illustration of Cross Section Showing Failure Mechanisms Associated with Matrix Shells

Specimen T2 (85% of the Ultimate Strain)

The same type of cracks that occurred in specimen T1 were found more frequently in specimen T2. Most of the cracks were longer than in specimen T2, indicating that they had propagated. The cracks observed in this specimen are shown in Fig. 5.8. Figure 5.9 is a zoom picture of one of the cracks in Fig. 5.8, which shows typical shell cracking. Additionally, the sides of the specimen showed no damage development.

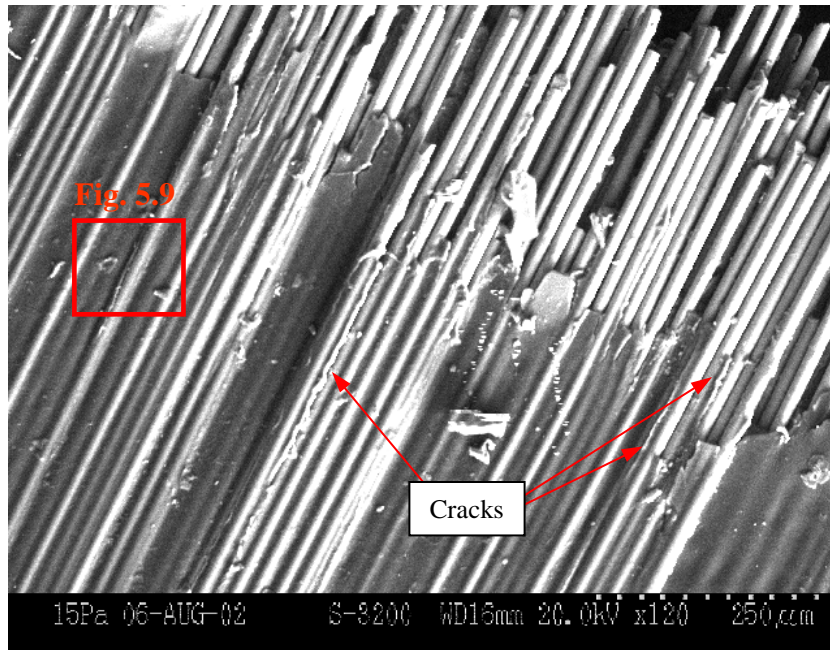


Figure 5.8: Cracks at the Edge of Specimen T2 (120x Magnification)

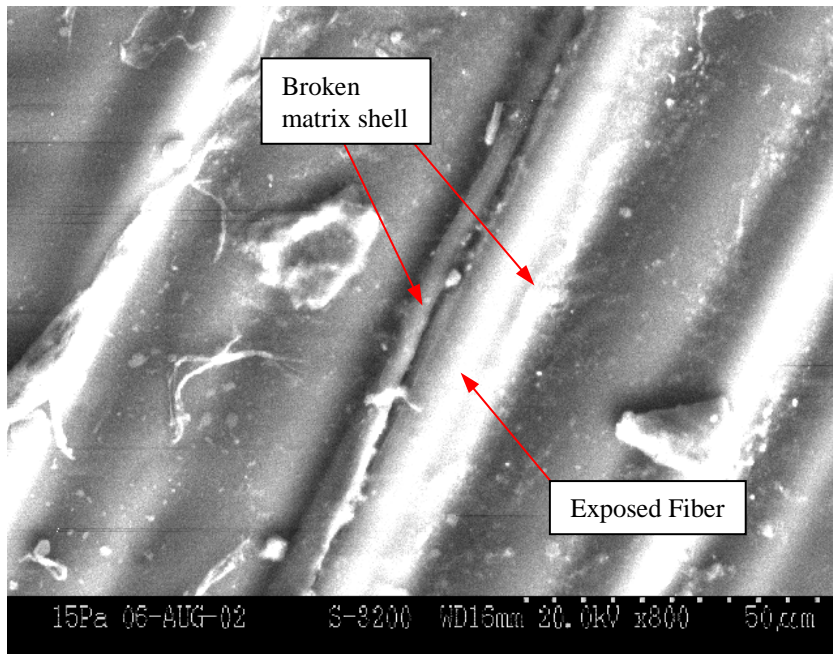


Figure 5.9: Broken Matrix Shell (800x Magnification)

Specimen T3 (100% of Ultimate Strain)

A transverse crack over the entire cross section was visible to the naked eye. Figures 5.10, and 5.11 are SEM pictures of the top and side of the crack. The specimen was clearly broken into two parts with fracture of the matrix. However, some of the fibers remained intact as fibers bridging the two pieces were observed. Some fiber breaks were found (Fig. 5.12).

The specimen was then broken manually in order to inspect the cross section of the specimen. Figure 5.13 shows a view of the cross section showing the texture of matrix cracking caused by the test. The pictures also show several groups of fiber breaks, which based on the type of break, are believed to be the result of manually breaking the specimen.

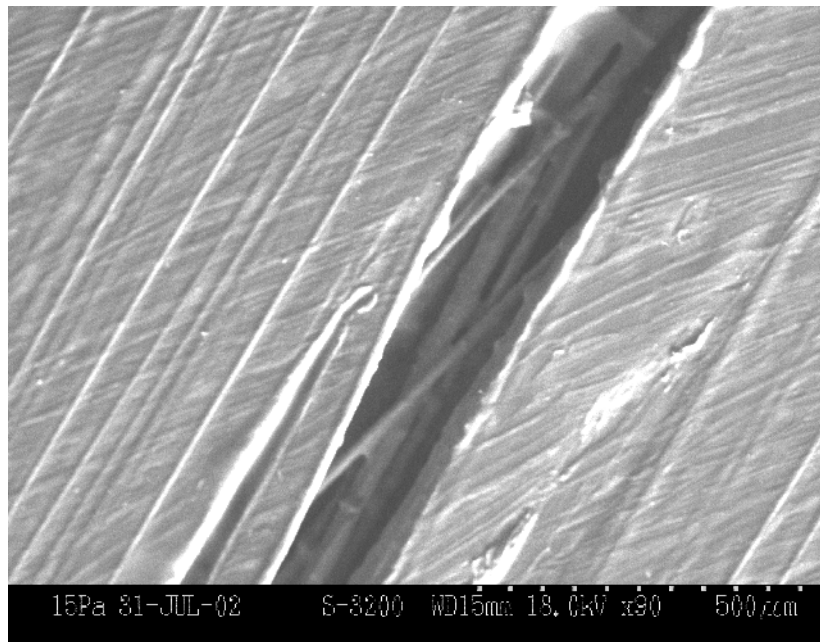


Figure 5.10: Crack Opening of Specimen T3 (90x Magnification)

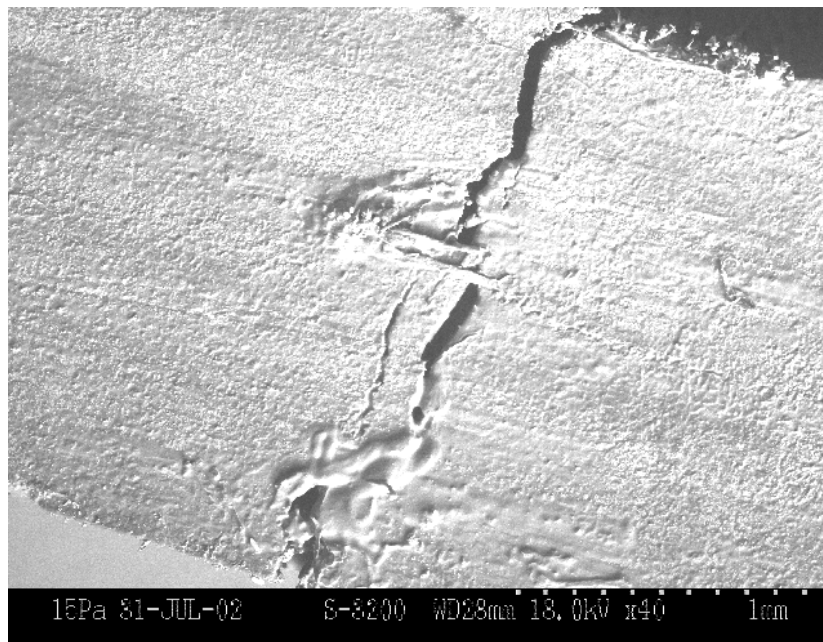


Figure 5.11: Crack from the Side View of Specimen T3 (40x Magnification)

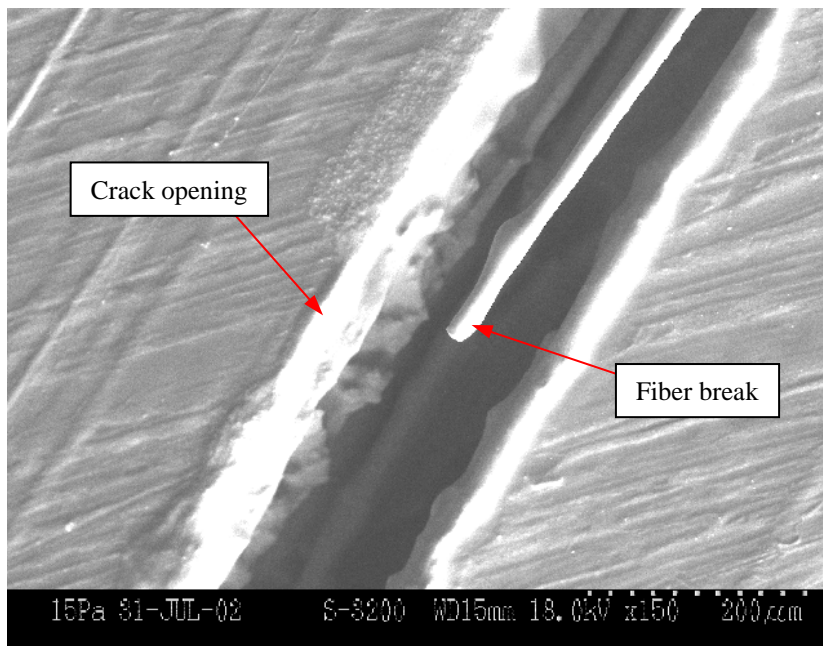


Figure 5.12: Fiber Break inside Crack of Specimen T3 (150x Magnification)

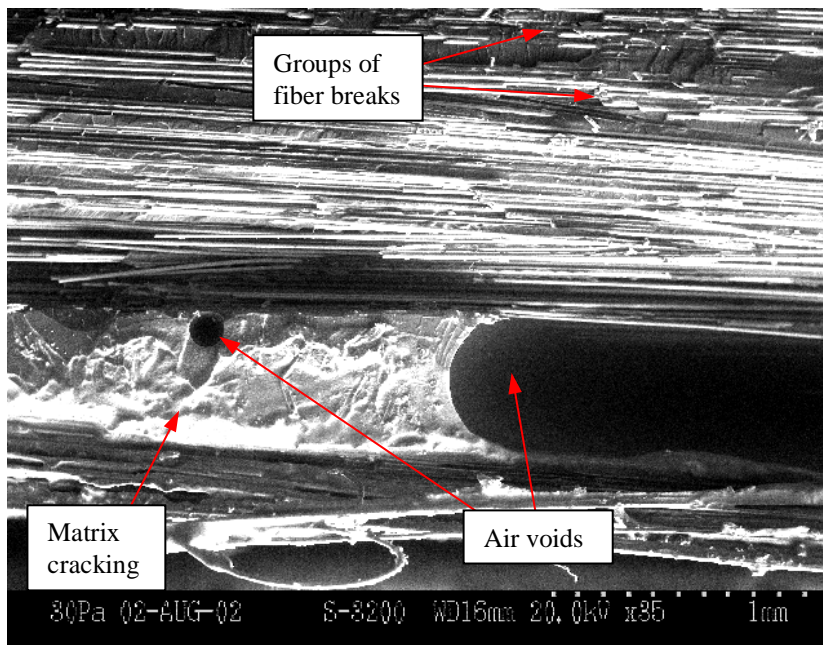


Figure 5.13: View of Cross Section Showing Matrix Cracking and Air Voids (35x Magnification)

The body of the specimen was also inspected for failures. Figure 5.14 shows the characteristic wide opening of a pure matrix crack. A fine crack, located at the shell of a fiber, was found nearby. This fine crack is associated with matrix cracking and debonding.

Several fine, short cracks were also observed at the edge of the specimen. Figure 5.15 shows an example of this type of crack, which is associated with matrix cracking. The picture also shows the elevated surface, which is a surface discontinuity that occurred during fabrication.

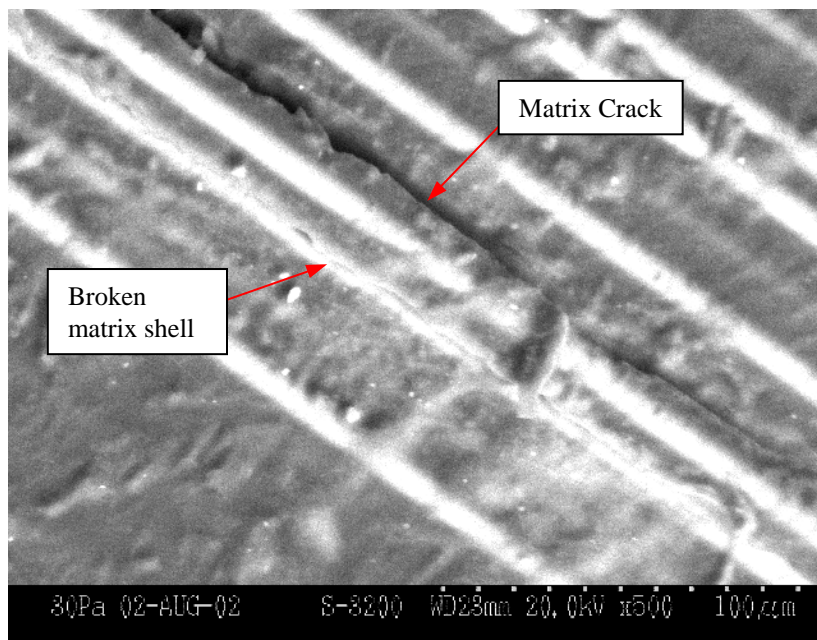


Figure 5.14: Pure Matrix and Shell Cracks (500x Magnification)

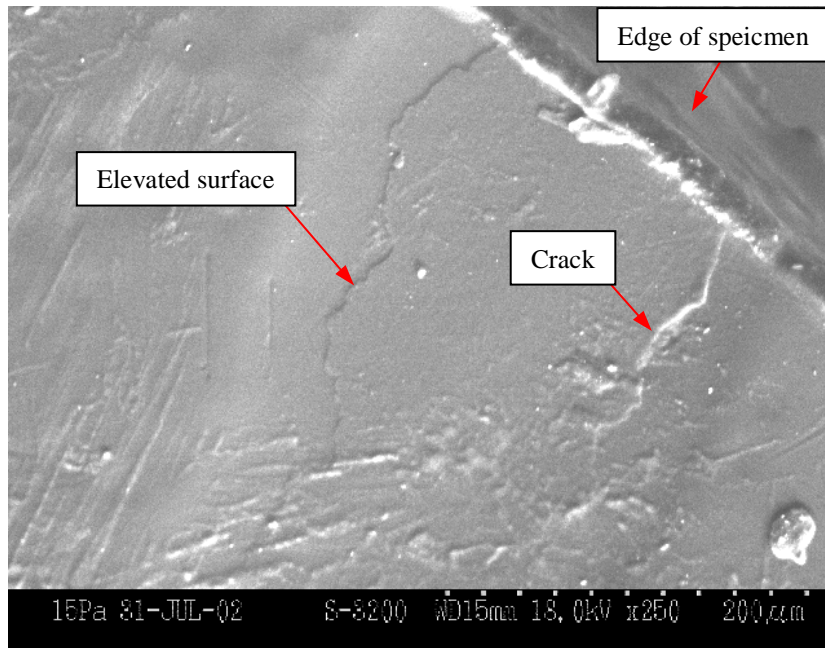


Figure 5.15: Fine Crack Near Edge of Specimen T3 (250x Magnification)

5.1.4 AE Results

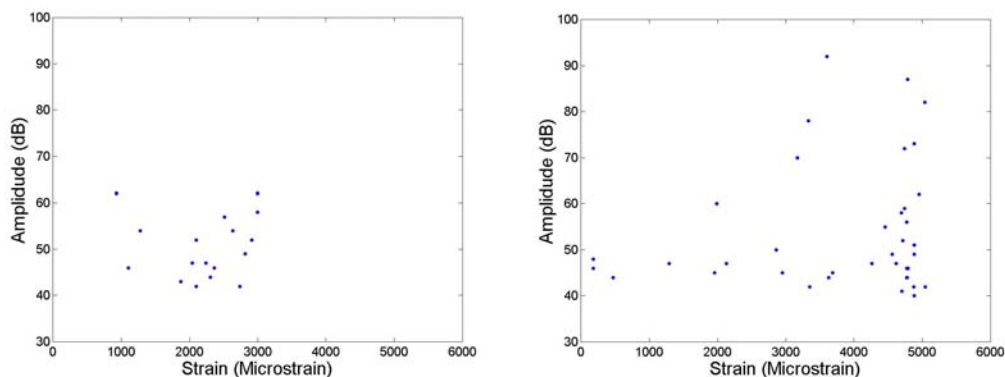
Presented in Table 5.3 is a summary of the total number of AE hits of all the specimens. From the results, it is clear that these specimens emitted fewer hits than the specimens tested in tension parallel to the direction of the fibers.

Table 5.3: Summary of Total Number of AE Hits of Each Specimen

Specimen	Total number of AE hits
T1	17
T2	38
T3	155

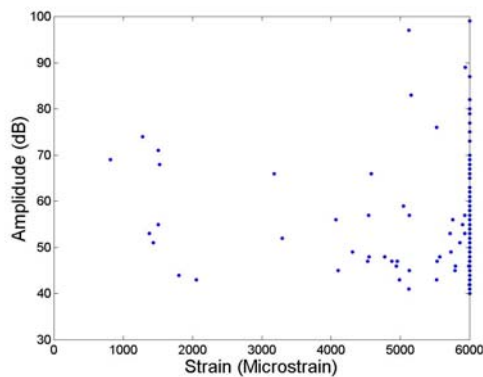
The amplitude vs. strain plots of all specimens are shown in Fig. 5.16. It was noticed that there were no high amplitude hits (≥ 80 db) from specimen T1,

while there were four high amplitude hits from specimen T2. Specimen T3 emitted 12 high amplitude hits near the end of the test.



a) T1

b) T2



c) T3

Figure 5.16: Hit Amplitude vs. Strain Plot

5.1.5 Discussion

From the SEM, three failure mechanisms were identified in these specimens: matrix cracking, debonding, and fiber breakage. The matrix cracking and debonding were found simultaneously. These two failure mechanisms were

characterized by cracking of the thin matrix shells in conjunction with exposing of the fiber. The matrix cracking and debonding were found at all three strain levels. The fiber breakage was observed only when the crack opening was wide enough to allow inspection inside.

Experience from Chapter 4 showed that high amplitude hits are associated with fiber breaks. Specimen T1 exhibited no high amplitude hits, which indicates that no fiber breaks should be observed in the specimen. This agreed with the SEM result that only matrix cracking and debonding were observed in specimen T1. Specimen T2 exhibited four high amplitude hits, which indicates that a few fiber breaks occurred during the test. The SEM scanning of the surface of the specimen showed no evidence of fiber breakage. It is probable that a few fiber breaks are located beneath the surface of the specimen and thus could not be scanned by the SEM. Twelve high amplitude hits were recorded for specimen T3. The SEM photos confirmed two to three fiber breaks inside the crack opening. Several more fiber breaks, which the SEM could not detect, are expected to be beneath the surface of the specimen. Comparison of these test data with the data from the tests on specimens with longitudinal fibers reported in Chapter 4 shows that the number of high amplitude hits is two to three orders of magnitude less for these specimens.

Thus, it is concluded that the AE data from the beginning of the test, before the first occurrence of the high amplitude hit, are associated with the matrix cracking and debonding. For this type of material, these low amplitude hits range from the beginning of the test up to approximately 55% of the ultimate strain. The AE data after the occurrence of the high amplitude hits corresponds to matrix cracking, debonding, and fiber breakage. This occurs between 55% to 100% of the ultimate strain.

5.2 EXPERIMENTAL PROGRAM FOR FIBER BREAKAGE DATABASE

The objective of this experiment is to compile an AE database of FRP coupons tested in tension transverse to the fiber direction. The FRP coupons were cut from the original beams FG and IKG. The structure of the coupons consisted of unidirectional fiber layers alternated with chopped strand mat layers. As a result, the AE data obtained in this section are more realistic than that from the first section and cover two types of resin: isophthalic polyester and vinyl ester. The findings from the first section of this chapter are then applied to these AE data to identify failure mechanisms of the specimens. These AE data and the failure mechanism information are used as a database for pattern recognition techniques in the later chapters.

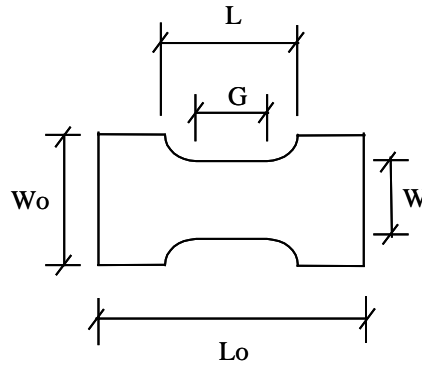
5.2.1 Experimental Program

Three coupons were cut from the web of beams FG and IKG (see Chapter 3). The coupons were fabricated into dog-bone shapes. The dimensions and the material information are given in Table 5.4. The representative coupons from each beam are shown in Figure 5.17.

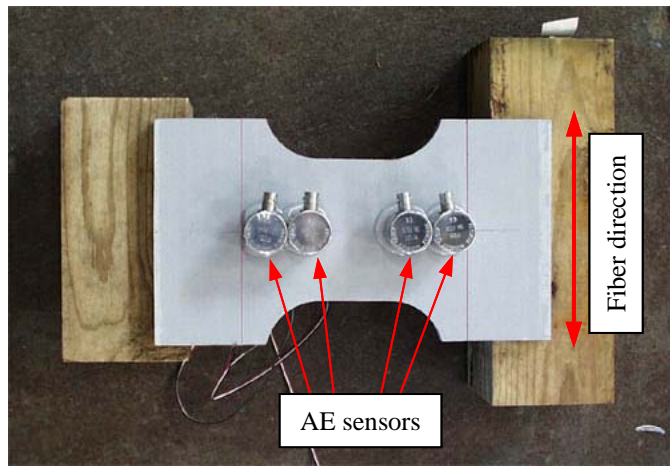
The tensile loading was applied to the longitudinal axis of the specimens. The load was applied monotonically up to failure. The testing machine used was the Universal Testing Machine 600HVL. Three strain gages were attached on each specimen to monitor longitudinal strains during the test.

AE was monitored during testing. The AE data acquisition system used was the Mistras system. Four R15I sensors were mounted on the specimens. The sensors were arranged in two pairs located at both ends of the reduced section, as shown in Figure 5.18. With this sensor arrangement, source location of damage sites could be performed if needed.

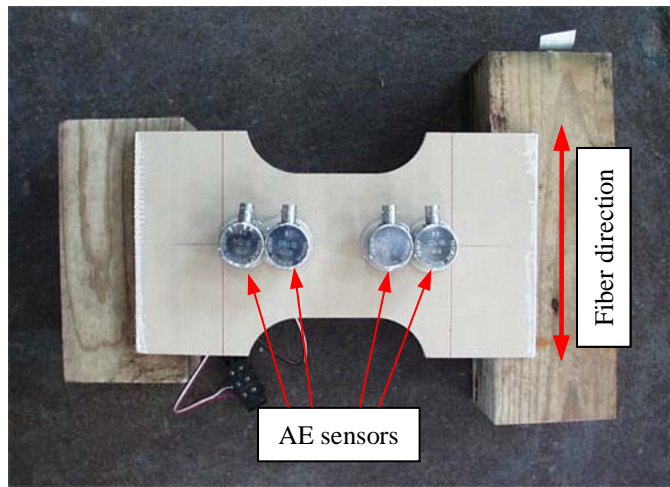
Table 5.4: Material Information and Specimen Dimensions (inches)



Specimen	TGI1	TGI2	TGV
Girder the specimen was cut from	FG	FG	IKG
Material	Glass fiber/ isophthalic polyester	Glass fiber/ isophthalic polyester	Glass fiber/ vinyl ester
Overall length (L_o)	10.75	10.75	10.75
Overall width (W_o)	6	6	6
Dog-bone length (L)	5	4.75	4.75
Length of narrow section (G)	1	2	2
Width of narrow section (W)	3.75	3.75	3.75
Thickness	0.5	0.5	0.5



a) Specimen TGI2



b) Specimen TGV

Figure 5.17: Representative Samples for Coupon Tension Test

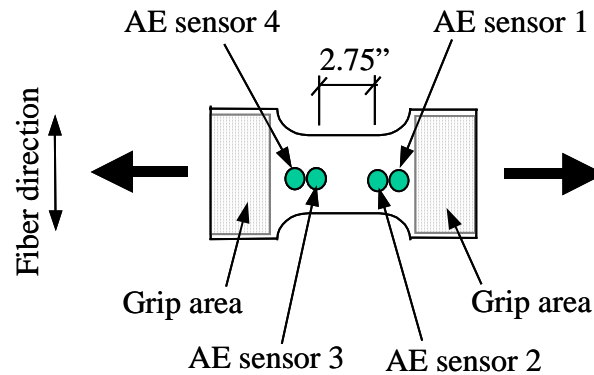
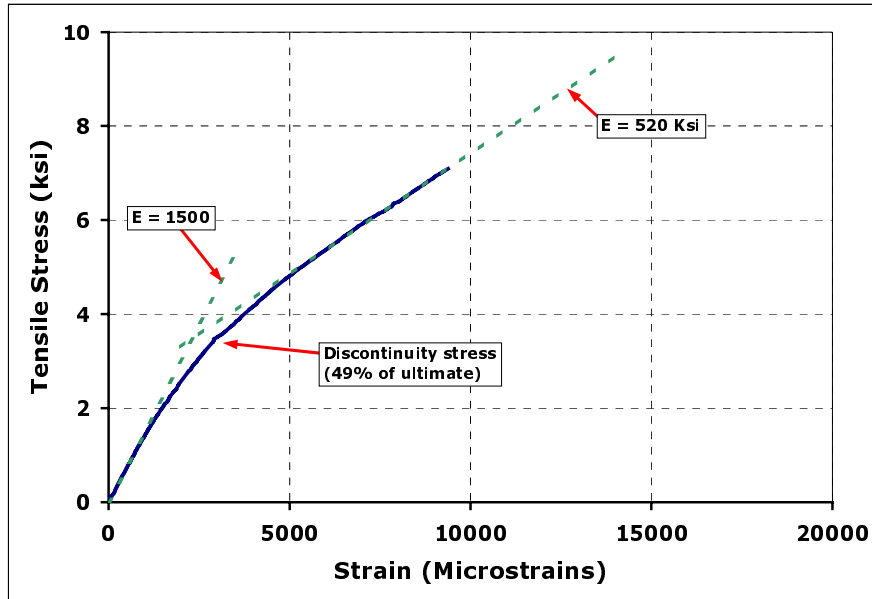


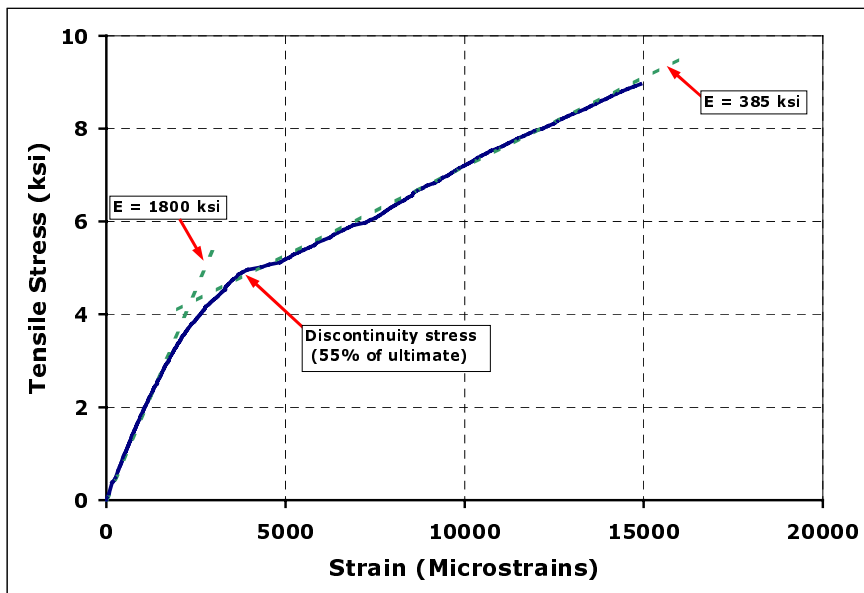
Figure 5.18: Sensor Location on the Specimen

5.2.2 Results

Stress-strain curves of specimens TGI2 and TGV are shown in Fig. 5.19. Specimen TGV had the higher ultimate stress and strain, which were 9.0 ksi and 15,000 microstrains, respectively. Specimen TGI2 had an ultimate stress of 7.0 ksi and an ultimate strain of 9,500 microstrains. Both specimens had non-linear stress-strain plots. The plot of specimen TGV appears to be bilinear (Fig. 5.19b). The initial elastic modulus of specimen TGV is higher than that of specimen TGI2.



a) Specimen TGI2



b) Specimen TGV

Figure 5.19: Stress-Strain Curves of Tension Tests

Visual inspections were performed during the tests. The visual damage evolution in both materials was observed to be very different.

Specimens TGI1 and TGI2 gave no visual indication of damage until the ultimate stress was reached. At the ultimate stress, the entire cross section at the end of the narrow section fractured in both specimens. Figure 5.20 shows the fracture of specimen TGI2.

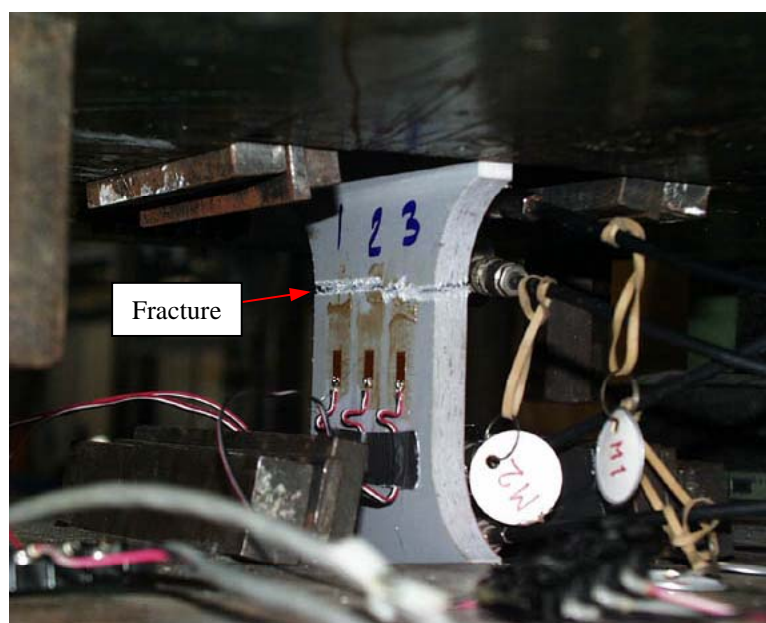


Figure 5.20: Tensile Failure on Specimen TGI2

Specimen TGV did not exhibit any sign of damage at the beginning of the test. At the stress of 4.98 ksi (55% of ultimate), a cracking noise was heard. As the load increased, more noise was constantly emitted, and numerous white crazing lines were observed over the entire dog-bone area on the front and back of the specimen. At the stress of 6.89 ksi (76% of ultimate), white lines were observed on the sides of the specimen. At the ultimate load (9.0 ksi), the entire

cross section at the end of the narrow section fractured. The specimen was subjected to a liquid dye penetrant method to help visualize the cracks. Figure 5.21 shows the fracture site. The multiple crazing lines are shown as red lines due to the red dye penetrant.

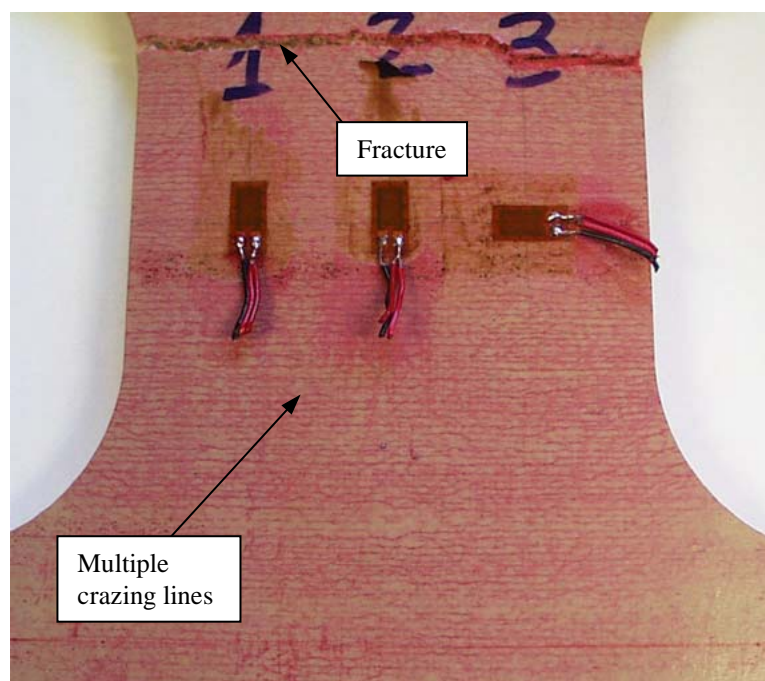


Figure 5.21: Tensile Fracture and Multiple Crazing of Specimen TGV

The fractures of all specimens were investigated. The SEM was performed on one representative specimen (TGI1). It was observed that the main failure mechanisms of the unidirectional fiber layers were matrix cracking and debonding. The main failure mechanism of the chopped strand fiber layers was fiber breakage, as shown in Figure 5.22.

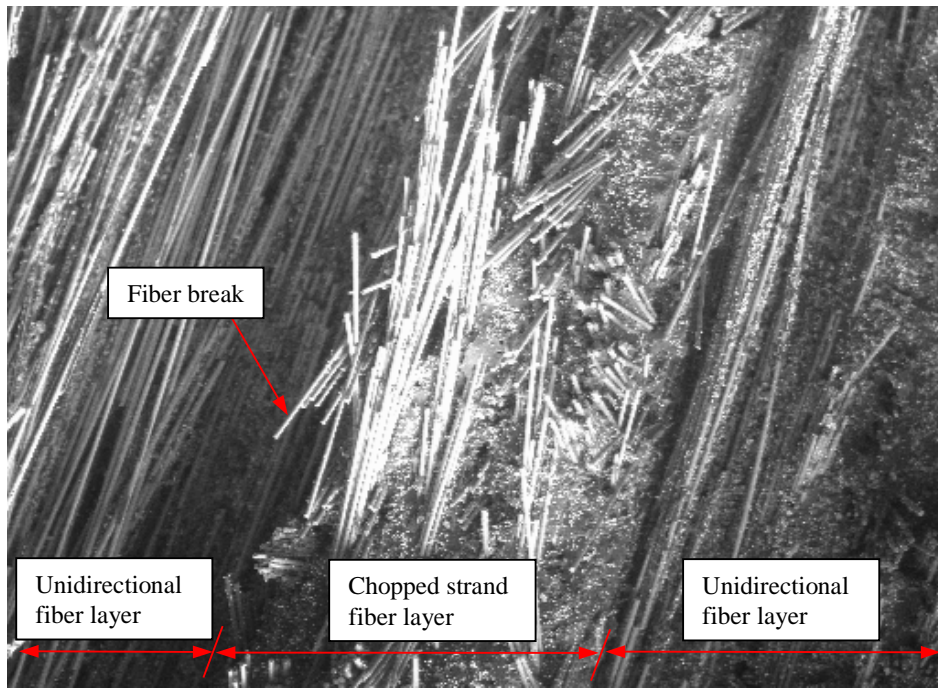


Figure 5.22: SEM View of the Fracture of Specimen TG11

A summary of the number of AE hits and high amplitude hits (based on criteria from Chapter 4) from all specimens is given in Table 5.5. It is noted that specimen TGV exhibited more hits than specimens TG11 and TG12. This is consistent with the results from the specimens discussed in Chapter 4 of specimens loaded parallel to the fibers. The more flexible vinyl ester redistributes load after damage occurs and results in a more controlled failure. The normalized plots of amplitude superimposed with cumulative signal strength vs. load of all specimens are shown in Fig. 5.23. It was observed that the plots of specimens TG11 and TG12 start with low amplitude hits (Fig. 5.23a and b). The amplitude then increases with the load and the rate of high amplitude hits is highest at ultimate. Specimen TGV has low amplitude hits at the start of the test (Fig. 5.23c). At a load of approximately 50% to 55% of ultimate, high amplitude hits

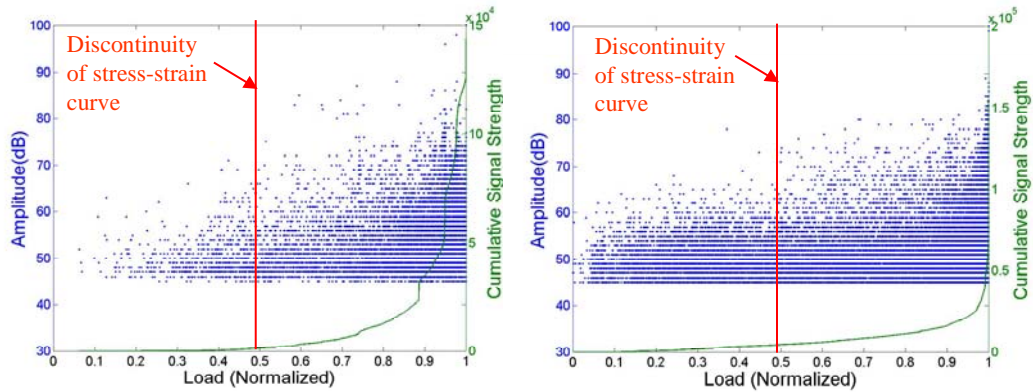
were first detected, and were thereafter constantly detected until failure. The number of high amplitude hits from specimen TGV was much greater than that from specimens TGI1 and TGI2. The high amplitude hits and the knee of the cumulative signal strength from this specimen appeared simultaneously with the observation of the white crazing lines.

5.2.3 Discussion

The failure mechanisms occurred in the specimens tested in this section are matrix cracking, debonding, fiber breakage. The fiber breakage occurred mainly in the chopped strand fiber layers. The purpose of these layers is to add strength to the direction perpendicular to the unidirectional fiber layers. However, fiber volume fraction is still very low in this direction.

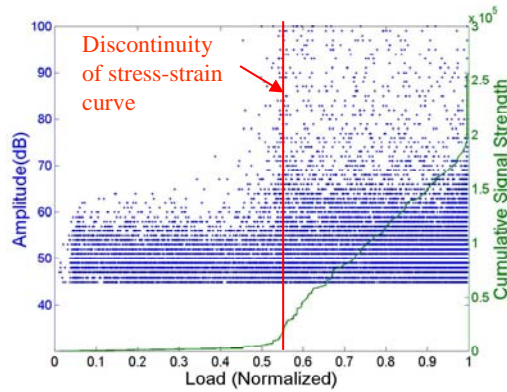
Table 5.5: Summary of AE Data

Specimen	Average AE hits per sensor	High amplitude hits per sensor
TGI1	15,791	65
TGI2	18,800	184
TGV	41,075	507



a) TG11 (Sensor2)

b) TG12 (Sensor 1)



c) TGV (Sensor1)

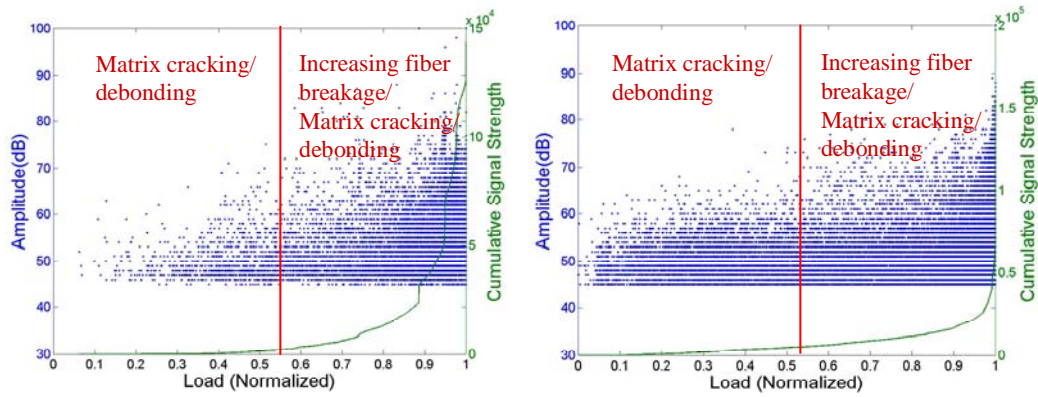
Figure 5.23: Amplitude Superimposed with Cumulative Signal Strength vs. Load (Normalized)

The results of Chapter 4 and Section 5.1 indicate that fiber breakage is associated with high amplitude hits. Specimens TGI1 and TGI2 did not exhibit many high amplitude hits before failure. This is because these specimens were made of isophthalic polyester resin, which has a low ultimate strain. This behavior is due to the brittle resin and low fiber volume, which causes the single fracture (McGowan, 1983). On the other hand, specimen FGV was made of ductile vinyl

ester matrix. The ductile matrix combined with low fiber volume fraction results in multiple fiber fractures before complete failure. Thus, numerous high amplitude hits are observed long before the ultimate load is reached.

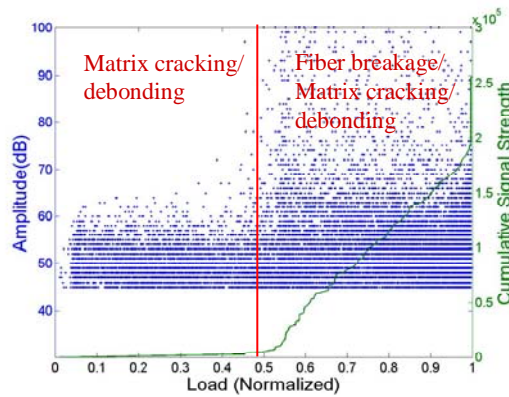
High amplitude hits from specimen TGV were detected at the same time as the appearance of the white crazing lines. Thus, the white crazing lines are determined to be associated with fiber breakage in the chopped strand fiber layers.

In Section 5.1, only matrix cracking and debonding mechanisms were detected at the start of the AE data collection before the first occurrence of a high amplitude hit. Accordingly, the start of the AE data collection in specimens TGI1, TGI2, and TGV are identified as matrix cracking and debonding mechanisms. The remaining stages of the test following the first high amplitude hit involve matrix cracking, debonding, and fiber breakage mechanisms. Figure 5.24 shows the plots of amplitude/cumulative signal strength vs. load for all specimens, with the failure mechanism information provided.



a) TGI1

b) TGI2



c) TGV

Figure 5.24: Summary of Failure Mechanisms

5.3 SUMMARY

In the first section, three unidirectional glass FRP coupons were tested and monitored using AE. The bending test applied a tensile stress perpendicular to the fiber direction in the specimen. This was done to minimize the amount of fiber breakage. The SEM confirmed that the main failure mechanisms were matrix cracking and debonding; however, a few fiber breaks were also observed at failure. As discussed in Chapter 4, the fiber breaks in these specimens are related

to the high amplitude hits. The high amplitude hits recorded from this specimen began shortly before the ultimate load was reached.

In the second section, three FRP dog-bone specimens were tested in pure tension. The loading direction was also perpendicular to the fiber direction. These specimens were made of two different resins; isophthalic polyester and vinyl ester. The specimens also had random chopped strand fibers, in addition to the unidirectional fibers. Therefore, the AE data from these tests are more complex, but are more realistic than the purely unidirectional specimens tested in the first section. The findings from the first section were applied to the AE data obtained in the second section. Thus, the first portion of the AE data, which consists of low amplitude hits, was identified as matrix cracking and debonding. The remaining portion of the data, which includes low to high amplitude hits, was identified as fiber breaks as well as matrix cracking and debonding. The high amplitude hits in this portion were found to be caused by fiber breaks in the chopped strand fiber layers.

The AE data and failure mechanism information are used as a database for pattern recognition techniques developed in the later chapters. Compared to specimens TGI1 and TGI2, specimen TGV had many more fiber breaks before the ultimate load was reached. This was attributed to the ductile matrix of specimen TGV, which allowed for the multiple fiber breaks. These fiber breaks were observed visually during testing as multiple white crazing lines on the surface of specimen TGV.

CHAPTER 6

Delamination and Additional Specimens with Unknown Failure Mechanisms

This chapter is divided into two parts. The first part focuses the AE characteristics of the delamination mechanism. Two types of tests are reported in the research program. The first type of test is a four-point bending test of a short beam. The high shear stress in the shear span of the specimen causes failure at the weak bond of layers. This type of test is usually called “short beam shear” and its results are reported in Section 6.1. The second type of test involves a tension test of a pair of “T” sections bonded together with a resin. To ensure failure originating at the center without sudden failure, a Teflon strip was placed at the center of the bond line acting as a crack initiator. This test is a tension test of a resin rich layer and is similar to the condition present in many secondary FRP joints. The details and results of this test are reported in Section 6.2. The objective of this chapter is to replicate the delamination and other mechanisms that occur in field FRP applications. The AE data are used as a database for neural network performing pattern recognition analysis in Chapter 8.

The second part describes test setups and results of four additional experiments. This includes double-web specimens subjected to a compression test, a full-scale hybrid specimen subjected to a four-point bending test, a chopped strand FRP specimen subjected to a direct tension test, and a woven roving FRP specimen subjected to a direct tension test. The SEM scan was not performed to observe failure mechanisms of these specimens during testing. Accordingly, the

neural network performing pattern recognition in Chapter 8 will be used to identify failure mechanisms of these specimens instead.

6.1 DELAMINATION

Two types of tests, short beam shear and direct tension of “T” sections, are reported below.

6.1.1 Short Beam Shear Test

This section presents details of the experimental program, results, and discussion of the AE characteristics of the specimens subjected to a short beam shear.

6.1.1.1 Experimental Program

Ten coupons were cut from the original full-scale beams. The dimensions and the material information are described in Table 6.1. The coupons were made of three different materials. A representative sample of glass fiber/vinyl ester material is shown in Fig. 6.1.

The specimens were subjected to a bending test using a small-scale testing frame. Each specimen was loaded monotonically to failure. AE was monitored during the test using the Mistras data acquisition system. Two R15I sensors were mounted at each end of the specimen. A dial gage was used to measure deflections at the midspan. On specimens SGI3, SGV3, and SHV3, a strain gage replaced the dial gage so as to obtain strain information instead of deflections. The test setup and loading geometry are shown in Fig. 6.2 and 6.3, respectively.

Table 6.1: Material Information and Specimen Dimensions (inches)

Specimen	Width	Length	Thickness	Material	Girder the specimen was cut from
SGI1	1	6	0.5	Glass fiber/Isophthalic polyester	FG1
SGI2	1	6	0.5	Glass fiber/Isophthalic polyester	FG1
SGI3	1	6	0.5	Glass fiber/Isophthalic polyester	FG1
SGI4	1	6	0.5	Glass fiber/Isophthalic polyester	FG1
SGV1	1	6	0.5	Glass fiber/vinyl ester	IKG1
SGV2	1	6	0.5	Glass fiber/vinyl ester	IKG1
SGV3	1	6	0.5	Glass fiber/vinyl ester	IKG1
SHV1	1	6	0.6	Hybrid/vinyl ester	SW2
SHV2	1	6	0.6	Hybrid/vinyl ester	SW2
SHV3	1	6	0.6	Hybrid/vinyl ester	SW2

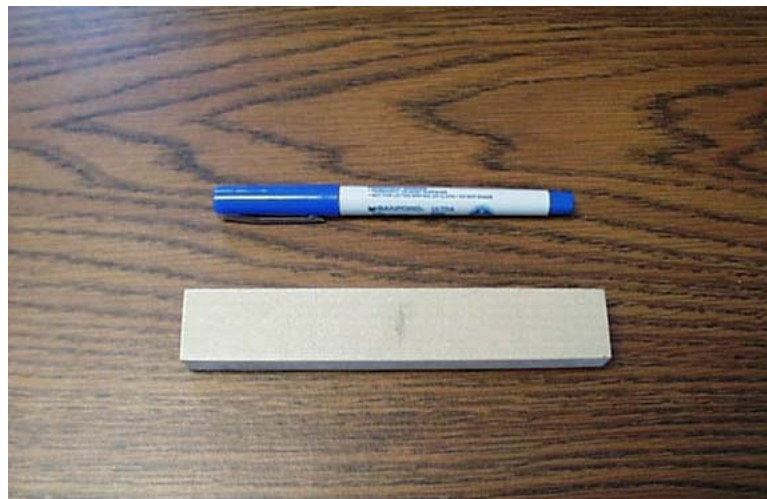


Figure 6.1: Glass Fiber/Vinyl Ester Specimen

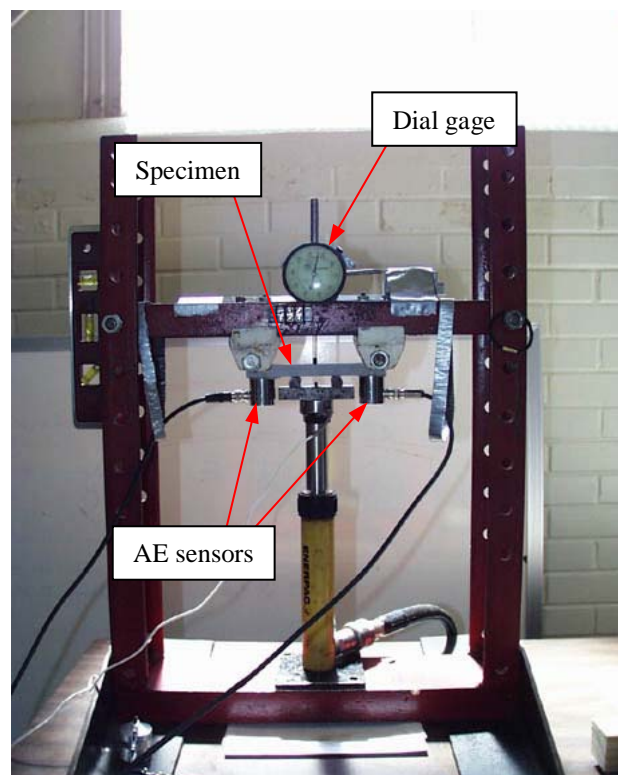


Figure 6.2: Short Beam Shear Test Setup of Specimen SG11

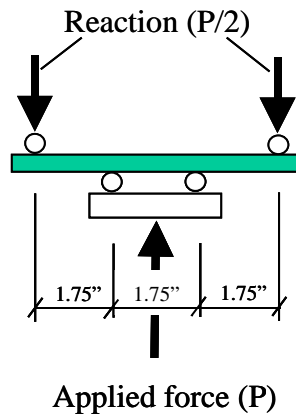


Figure 6.3: Loading Geometry of Short Beam Shear Test

6.1.1.2 Physical Results

Pictures of representative specimens at failure are shown in Fig. 6.4, 6.5, and 6.6. The delamination crack typically occurred at one end of the specimen and propagated approximately to midspan. The stress-strain responses of representative specimens are shown in Fig. 6.7, 6.8, and 6.9. For the specimens that were made from glass fibers exhibited only one delamination at failure. This corresponds to the linearity from the beginning to the failure of the stress-strain curve of these specimens (Fig. 6.7 and 6.8). For hybrid specimens, i.e. specimen SHV3, multiple delaminations were observed. The first delamination was observed at approximately 71% of the ultimate load, after which a small drop in load was observed. The second and the final delaminations occurred at 91% and 100% of the ultimate load, respectively (Fig. 6.9).

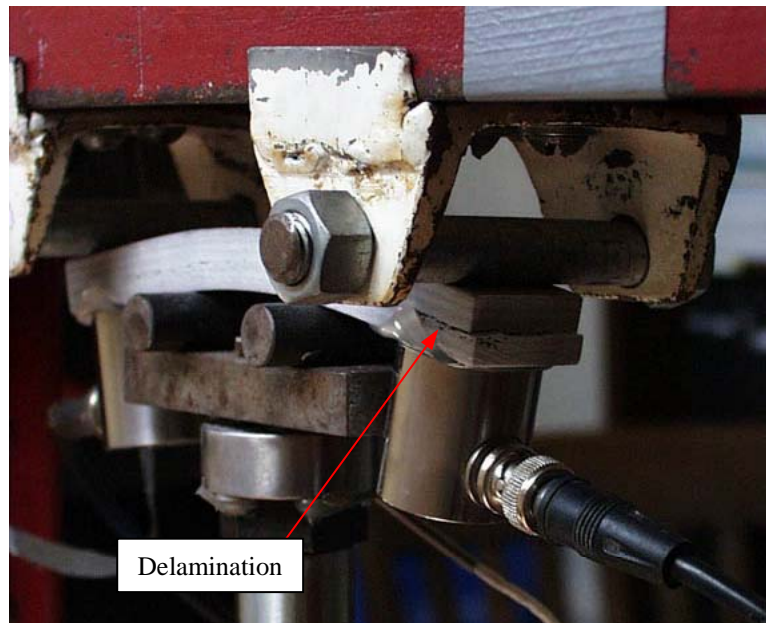


Figure 6.4: Glass/Isophthalic Polyester Specimen at Failure



Figure 6.5: Glass/Vinyl Ester Specimen at Failure

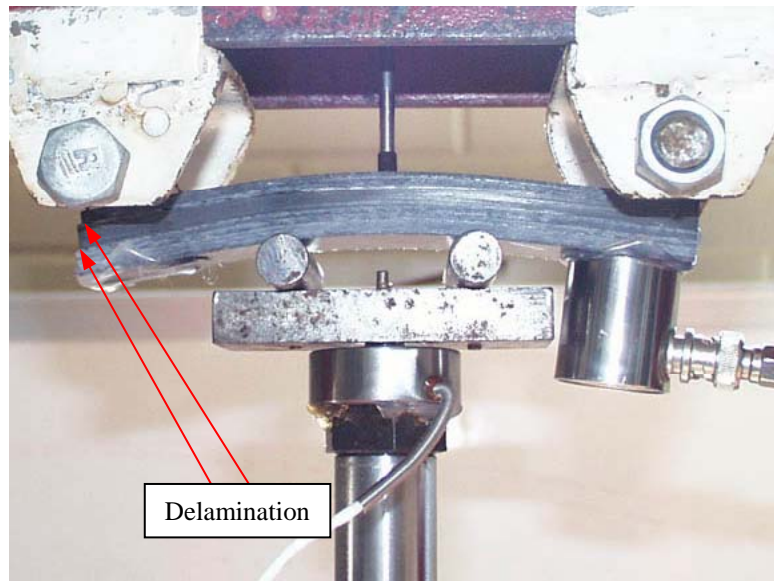


Figure 6.6: Hybrid/Vinyl Ester Specimen at Failure

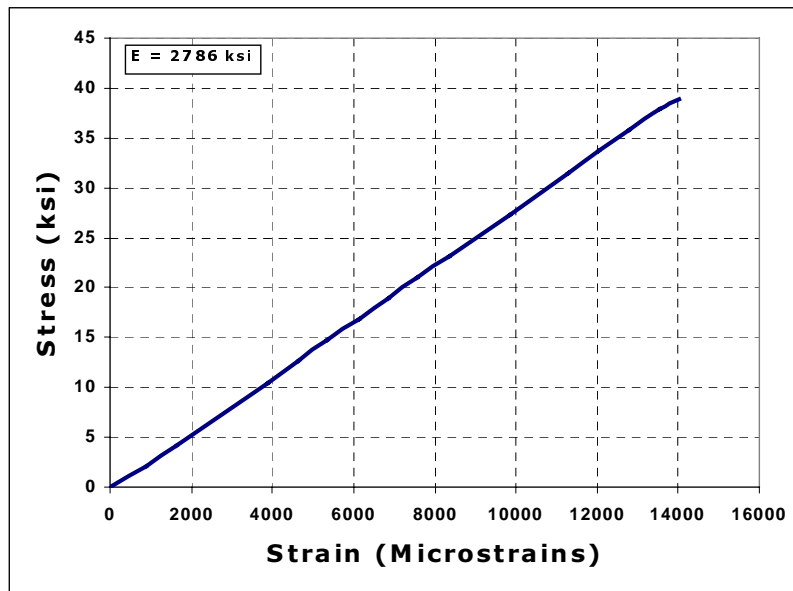


Figure 6.7: Stress vs. Strain Relationship of Representative Glass Fiber/Isophthalic Polyester Specimen (Specimen SGI3)

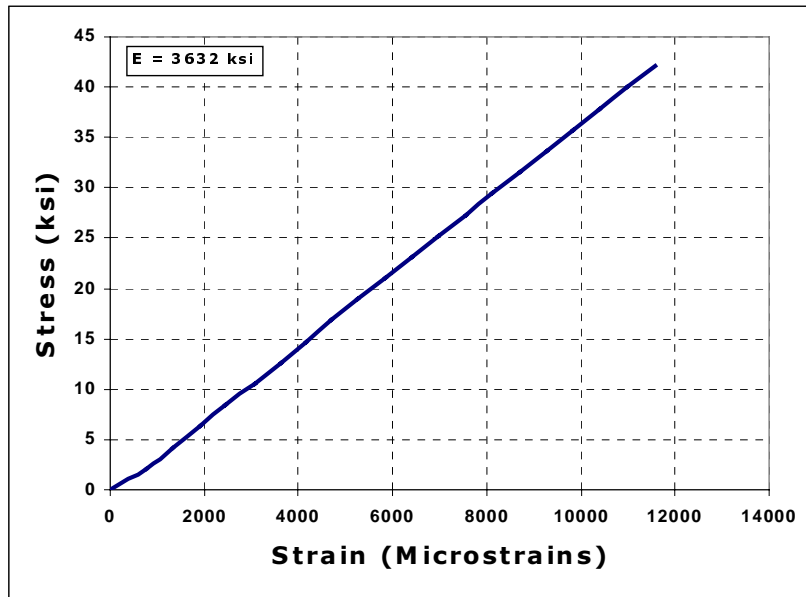


Figure 6.8: Stress vs. Strain Relationship of Representative Glass Fiber/Vinyl Ester Specimen (Specimen SGV3)

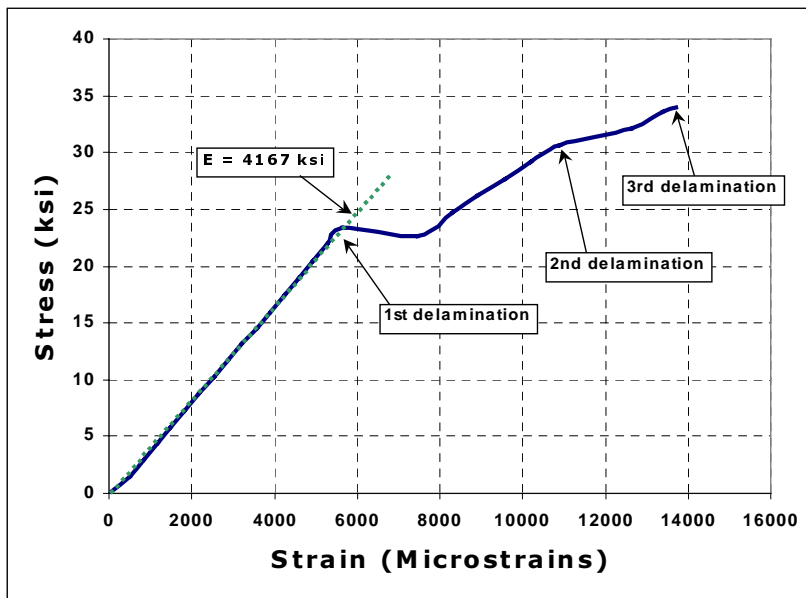


Figure 6.9: Stress vs. Strain Relationship of Representative Hybrid/Vinyl Ester Specimen (Specimen SHV3)

Table 6.2 is a summary of the bending tests showing maximum loads, maximum stress at the top surface, maximum strains at the top surface, and maximum deflections. It is noted that the maximum loads (maximum stresses) within the same group of material are consistent.

Table 6.2: Summary of Short Beam Shear Test Results

Specimen	Material	Max. load (lbs)	Max. Stress (ksi)	Max. Strain (microstrains)	Max. Deflection (x10³ in.)
SGI1	Glass Iso	1,600	33.6	N.A.	198
SGI2	Glass /Iso	1,550	32.6	N.A.	175
SGI3	Glass /Iso	1,869	39.3	14,008	N.A.
SGI4	Glass /Iso	1,621	34.1	N.A.	230
SGV1	Glass /vinyl ester	1,995	42.0	N.A.	212
SGV2	Glass /vinyl ester	2,000	42.1	N.A.	221
SGV3	Glass /vinyl ester	2,000	42.1	11,582	N.A.
SHV1	Hybrid/vinyl ester	2,300	33.5	N.A.	295
SHV2	Hybrid/vinyl ester	2,320	33.8	N.A.	238
SHV3	Hybrid/vinyl ester	2,330	34.0	13,708	N.A.

6.1.1.3 Visual and SEM Observation

The delamination of specimen SGI1 was manually broken open to inspect the failure surface (Fig. 6.10). It was observed that the failure plane is located within a chopped strand mat layer. Also, in some areas, it extended into an interface between chopped strand mat and unidirectional fiber layers. Within the chopped strand mat layer, a significant number of air voids between fiber strands were observed. This generates a weak plane for the shear stress.

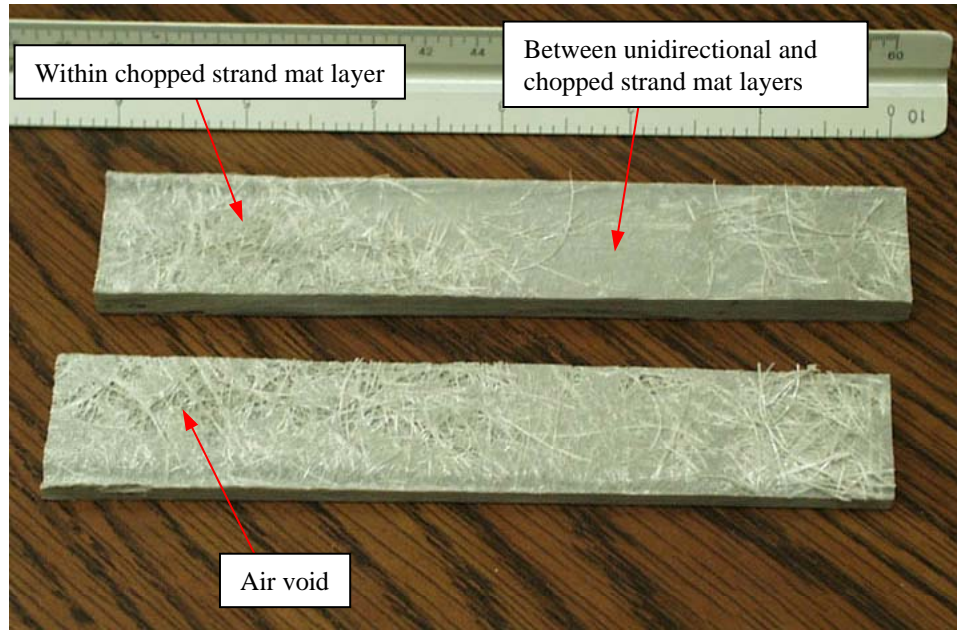


Figure 6.10: Failure Surface of Specimen SG11 After Breaking Off

The primary failure mechanisms observed by visual inspection are matrix cracking and fiber/matrix debonding (debonding). A few fiber breaks were also observed. Figure 6.11 shows a picture of fiber breaks of a strand. The picture is a magnified image, but was not from the SEM.

SEM observation confirms the mechanisms discussed above. Figure 6.12 shows fiber imprint, which is an indication of debonding. Also, fiber breaks were found from the SEM as shown in Fig. 6.13.

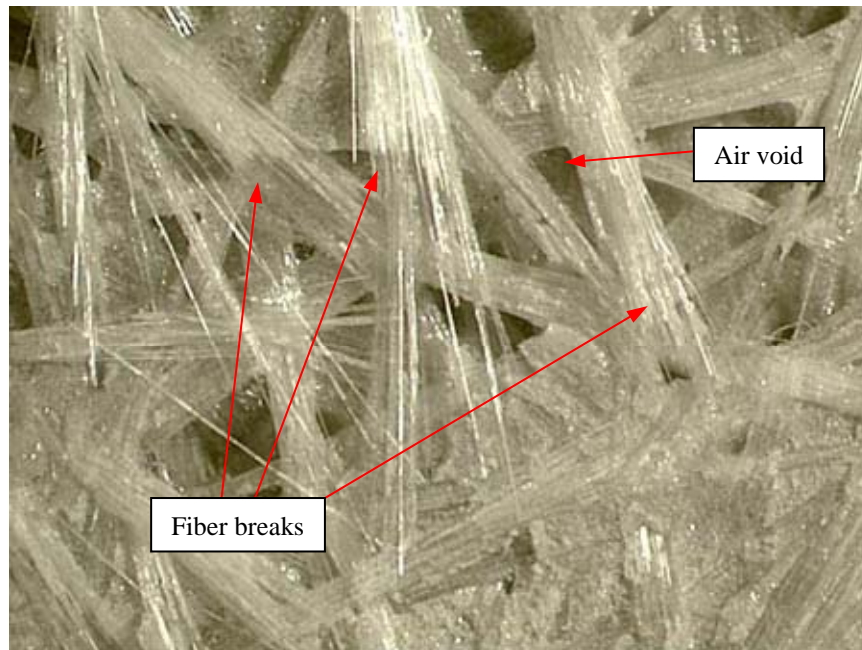


Figure 6.11: Fiber Breaks in Specimen SG11

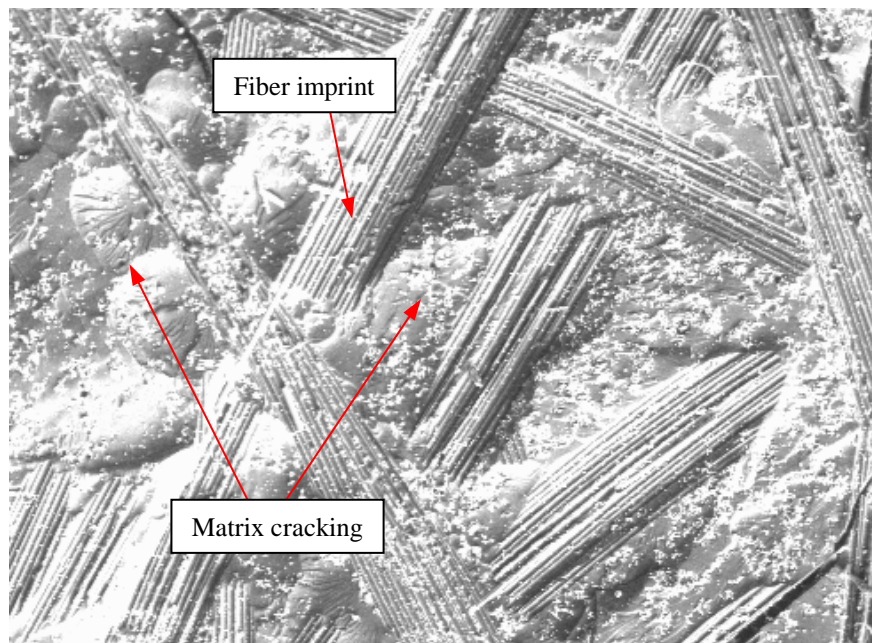
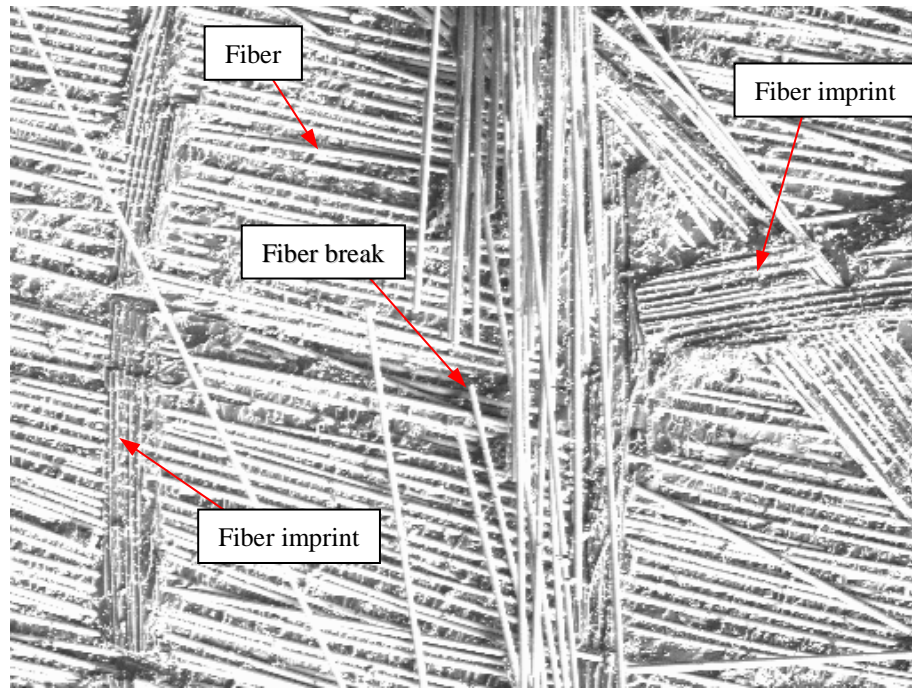


Figure 6.12: SEM Photo Showing Fiber Imprint (Debonding) and Matrix Cracking of Specimen SG11 (Approximately 40x Magnification)



**Figure 6.13: SEM Photo Showing Fiber breaks of Specimen SG11
(Approximately 60x Magnification)**

6.1.1.4 AE Results

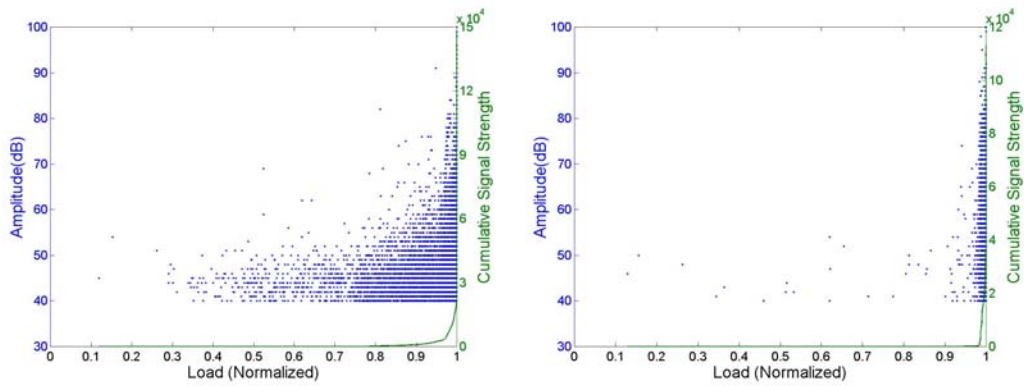
A summary of the number of AE hits from all specimens is given in Table 6.3. It is noted that many more hits were detected from the hybrid specimens than from the glass specimens. One of the reasons is the multiple delaminations, which occurred in the hybrid specimens.

Normalized plots of amplitude superimposed with cumulative signal strength vs. load of representative specimens (SG11, SGV1, and SHV1) are shown in Fig. 6.14. It was observed that the plot of specimen SG11 starts with low amplitude hits (Fig. 6.14a). The onset of high amplitude hits occurred at 92% of the ultimate load. For specimen SGV1, low amplitude hits were dominant up to 97% of the ultimate load, at which point the high amplitude hits became dominant

(Fig. 6.14b). The plot of specimen SHV1 shows high amplitude hits at the early stage of the test (10% of the ultimate load). At 60% of the ultimate load, an increase of high amplitude hits is observed and the cumulative signal strength curve starts to rise (Fig. 6.14c). At 74% of the ultimate load, an increase in high amplitude hits and a sharp rise in the signal strength curve are observed. This corresponds to the first observed crack. Other jumps in high amplitude hits also occur at 86%, 92%, and 100% of the ultimate load corresponding to observed crack formations at those loads (Fig. 6.14c).

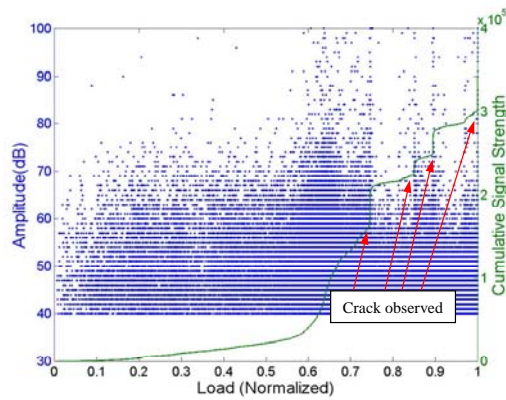
Table 6.3: Summary of AE Data

Specimen	Material	Average AE hits per sensor	
SGI1	Glass Iso	10,045	Average 10,177
SGI2	Glass /Iso	9,846	
SGI3	Glass /Iso	9,527	
SGI4	Glass /Iso	11,289	
SGV1	Glass /vinyl ester	4,024	Average 4,175
SGV2	Glass /vinyl ester	4,859	
SGV3	Glass /vinyl ester	3,642	
SHV1	Hybrid/vinyl ester	87,383	Average 82,967
SHV2	Hybrid/vinyl ester	47,131	
SHV3	Hybrid/vinyl ester	114,395	



a) SGII (Glass/Iso)

b) SGVI (Glass/Vinyl Ester)



c) SHVI (Hybrid/Vinyl Ester)

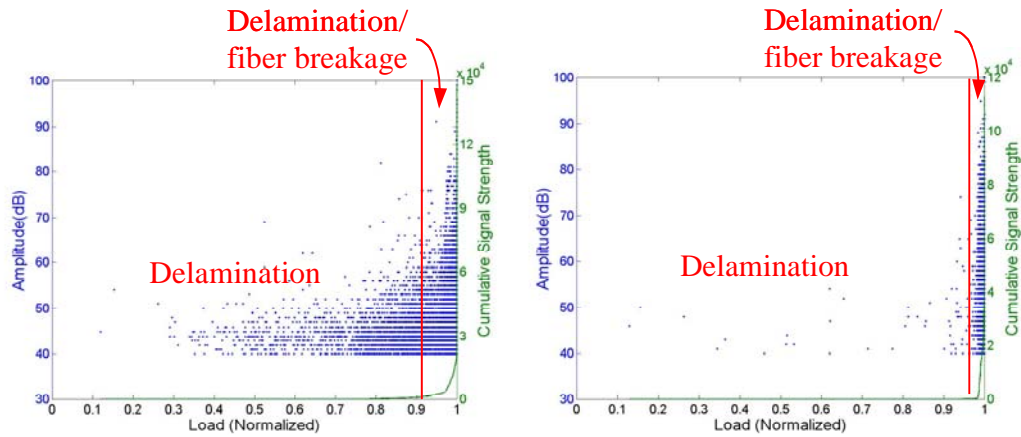
Figure 6.14: Amplitude Superimposed with Cumulative Signal Strength vs. Load of Representative Specimens

6.1.1.5 Discussion

The failure mechanisms observed from this type of specimen are delamination and fiber breakage. The delamination is associated with matrix cracking and debonding. The failure plane is parallel to the layers, whereas the failure plane of the specimens in Chapters 4 and 5 is perpendicular to the layers.

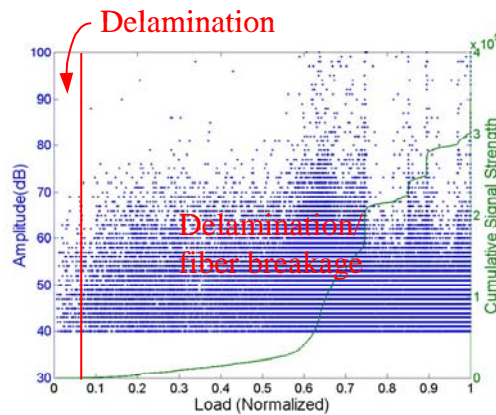
Accordingly, AE characteristics from matrix cracking and debonding of the specimens in this section are believed to be different from those of specimens in Chapter 4 and 5. An example of this is ratio of the AE hits from matrix cracking to the AE hits from debonding. Therefore, AE data from the beginning of the test until the onset of high amplitude hits is identified as delamination rather than matrix cracking and debonding. The AE data after the onset of high amplitude hits, as discussed previously, is identified as delamination as well as fiber breakage. Figure 6.15 shows the plot of amplitude/cumulative signal strength vs. load for representative specimens, with the failure mechanism information incorporated.

Carbon fibers, which were included in the hybrid specimens, generally are more susceptible to damage during fabrication than glass fibers. As a result, fabrication damage of the carbon fibers can cause premature fiber breaks, which show as high amplitude hits at a very early stage of the test. This agrees with the results from the tension test of a hybrid specimen with the fibers parallel to the direction of the applied stress (specimen LHV), which also exhibited fiber breaks at the early stage.



a) SG11 (Glass/Iso)

b) SGV1 (Glass/Vinyl Ester)



c) SHV1 (Hybrid/Vinyl Ester)

Figure 6.15: Summary of Failure Mechanisms on Amplitude Superimposed with Cumulative Signal Strength vs. Load of Representative Specimens

6.1.2 Tension Test of “T” Specimens

This section presents details of a pure tension test of “T” specimens. The results, and discussion including AE characteristics of the test are provided in this section.

6.1.2.1 Experimental Program

This test was adapted from ASTM F 521. Three specimens (Tee1, Tee2, and Tee3) were supplied by Dow Chemical and fabricated by Proske Plastic Products, Inc. A typical specimen is shown in Fig. 6.16. The samples were fabricated from two FRP “T” sections bonded together with resin and a chopped strand glass fiber mat. A Teflon strip was placed at the center of the bond line, which acted as a crack initiator to ensure that the failure originated at the center and is not a sudden failure. Both upper “T” and lower “T” were made of vinyl ester resin that was reinforced with glass fibers. The dimensions of the entire specimens are given in Fig. 6.17.



Figure 6.16: “T” Sample

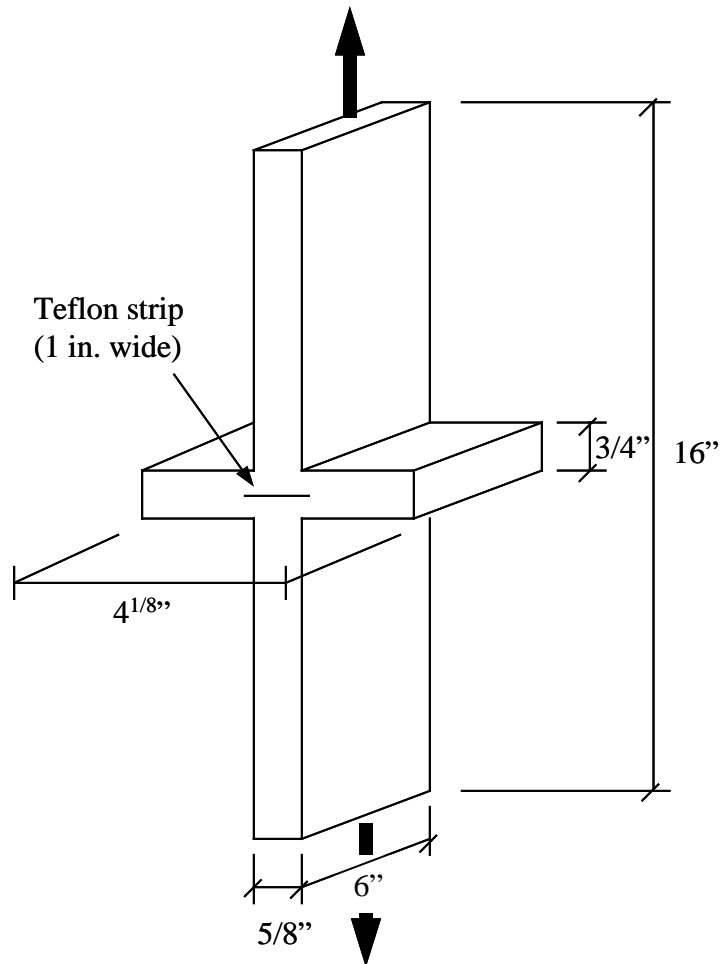


Figure 6.17: “T” Specimen Dimensions

Tensile loading was applied along the longitudinal axis of the specimens. The load was applied monotonically up to failure. The testing machine used was the Universal Testing Machine 600HVL.

AE was monitored during testing using the Mistras data acquisition system. Four R15I sensors were mounted on the specimens. The sensors were arranged in two pairs located at the top surface of both wings. The specimen test setup is shown in Fig. 6.18.

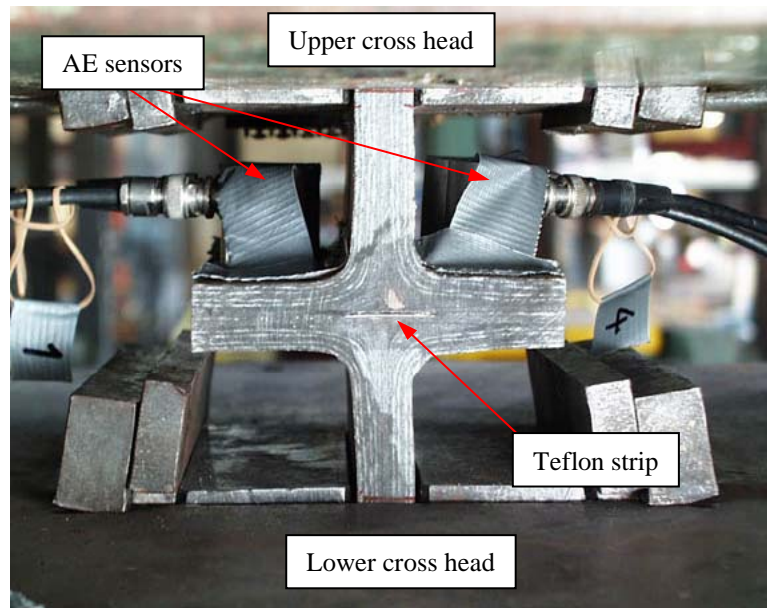


Figure 6.18: “T” Specimen Test Setup

6.1.2.2 Physical Results

Table 6.4 summarizes the maximum load and bond strength of all three specimens. It is noted that specimen Tee1 had a higher maximum load than the other specimens. This is attributed to the high rate of loading of the first specimen. Subsequent tests were loaded at a much slower rate.

Table 6.4: Summary of the Test Results

Specimen	Maximum Load (kips)	Maximum Bond Stress (psi)
Tee1	2,580	121.6
Tee2	2,070	94.4
Tee3	1,550	66.7

No specimens showed any sign of damage before the maximum load was reached. At the maximum load, a horizontal crack extending from the crack initiator was observed (Fig. 6.19). At this point, the load dropped slightly. As loading continued, the crack began to propagate (Fig. 6.20) until the entire bonding interface opened (Fig. 6.21). At this point, the fibers bridging between the upper portion and the low portion were clearly observed. As loading continued, more fiber breaks and debonding were observed in conjunction with a gradual decrease in load (Fig. 6.22). Until the load was reduced to zero, the upper and low portions were almost completely unattached. The bonding surface after the test is shown in Fig. 6.23.

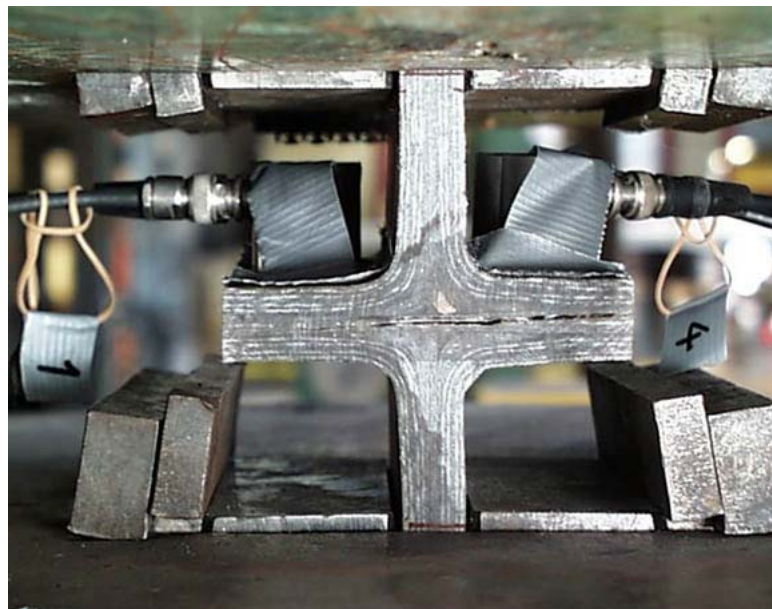


Figure 6.19: First Crack of Specimen Tee1

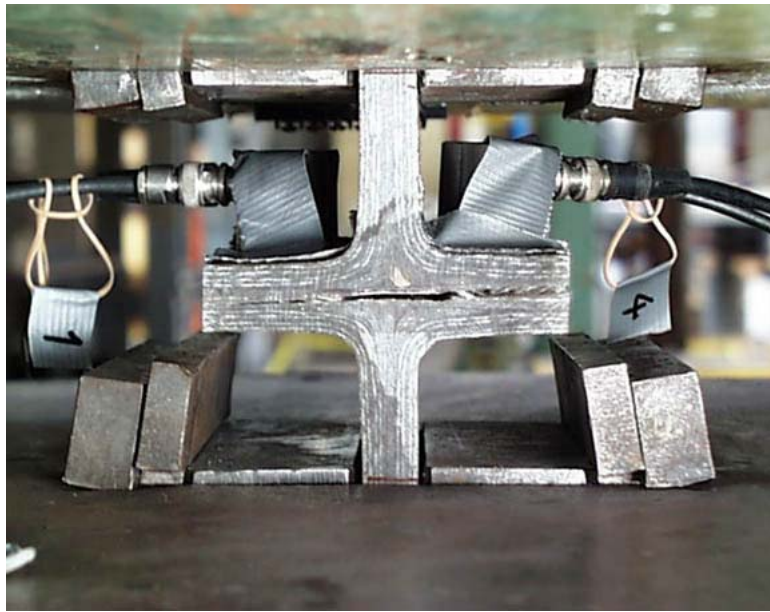


Figure 6.20: Crack Propagation of Specimen Tee1

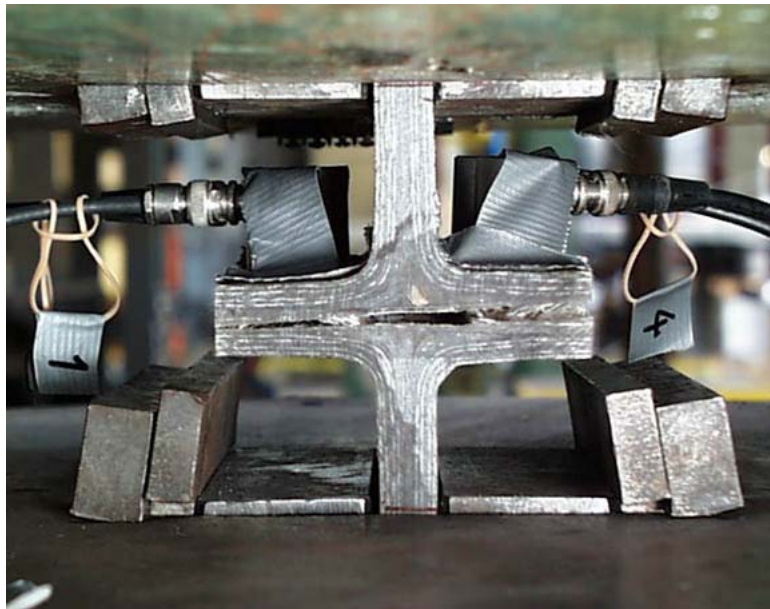


Figure 6.21: Opening of Entire Bonding Interface of Specimen Tee1



Figure 6.22: Wide Opening of the Interface Showing Fiber Bridging from Upper Portion to Lower Portion of Specimen Tee1

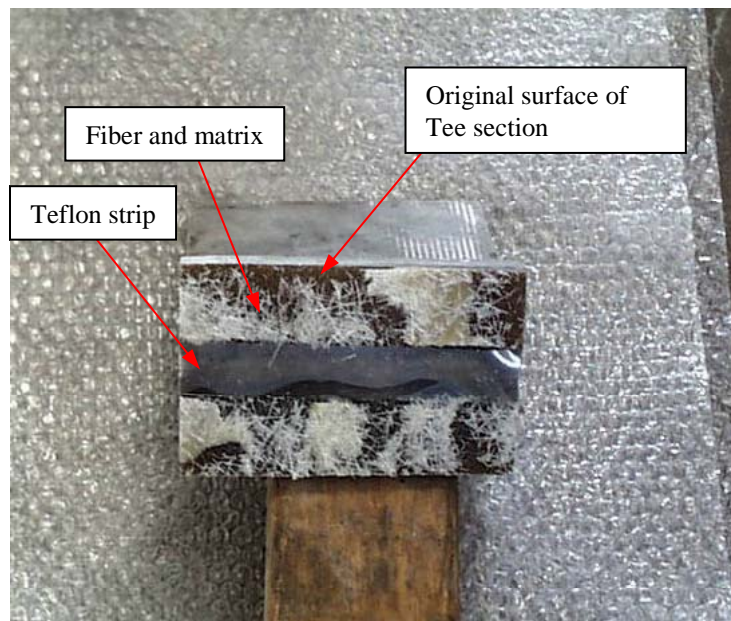


Figure 6.23: Bonding Surface After the Test of Specimen Tee1

6.1.2.3 AE Results

Table 6.5 is a summary of the AE hits from all specimens. For specimen Tee1, AE was recorded only until crack initiation. Thus, the total number of hits is much less than those of specimens Tee2 and Tee3. The table also provides the number of hits immediately before the crack started, which shows that the numbers of hits from all specimens are in the same range.

Table 6.5: Summary of Total AE Hits

Specimen	Total number of hits per sensor	Number of hits before crack started per sensor
Tee1	5,976	506
Tee2	81,638	382
Tee3	54,350	678

The plot of amplitude superimposed with load vs. time of a representative specimen, Tee3, is shown in Fig. 6.24. The plot shows high amplitude hits occurring at the beginning of the test. At the maximum load or when the crack began, significant numbers of high amplitude hits were detected. These high amplitude hits continued to occur during the load decrease as the high density of hits shows in the plot.

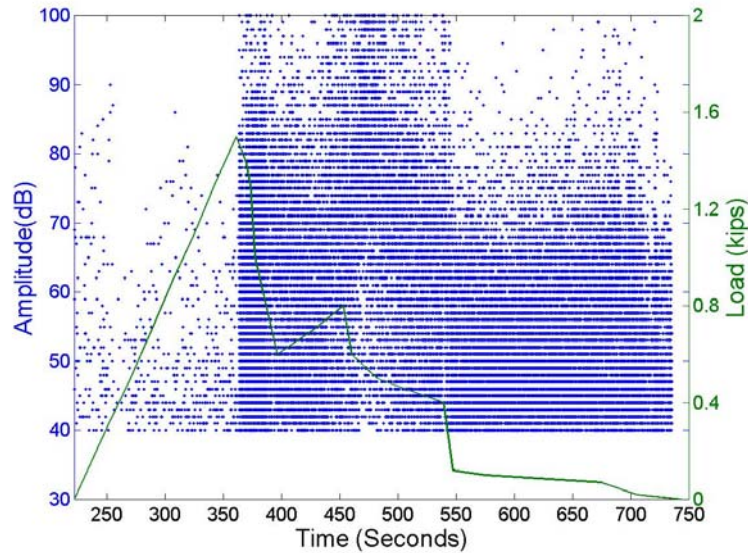


Figure 6.24: Amplitude Superimposed with Load vs. Time

6.1.2.4 Discussion

The primary failure mechanism that occurred from the beginning of the test to the maximum load was delamination. In addition to the delamination, fiber breaks, in the form of high amplitude AE hits, also occurred during the early stage. During crack propagation, delamination was still in progress until the entire bonding surface became unattached. It was observed that after the crack started, a significant number of high amplitude hits were detected. This was found to correspond with many fiber breaks. The visual inspection of the fracture surface confirmed that this process consisted primarily of fiber breaks and debonding.

Only AE data from the beginning of the test until immediately after crack initiation (maximum load) will be used as a database for pattern recognition analysis in the later chapters. The AE data after the crack started is beyond nondestructive inspection practice. Figure 6.25 is the plot of amplitude

superimposed with cumulative signal strength vs. load of a representative specimen, Tee1, plotted to the maximum load with the failure mechanism information provided.

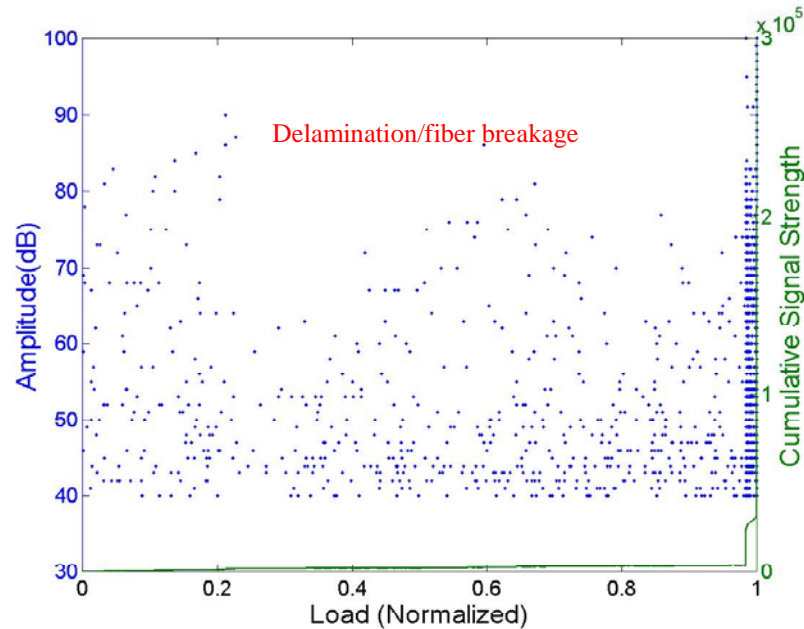


Figure 6.25: Summary of Failure Mechanisms of Representative Tee specimen

6.2 ADDITIONAL SPECIMENS WITH UNKNOWN FAILURE MECHANISM EVOLUTION

This section describes specimens that were tested in order to identify additional failure mechanism combinations. The evolution of failure mechanisms with SEM was not observed for these specimens. Therefore, these failure mechanisms will be identified by the preliminary networks instead. The AE information from these tests and the identified failure mechanisms will be added to the networks in order to extend the FRP database.

6.2.1 Specimens Subjected to a Compression Loading

Three specimens (BHV1, BHV2, and BHV3) were cut from beam SW. Figure 6.26 shows the dimensions and test setup for the three specimens. This test is intended to determine the buckling capacity of the double web cross section.

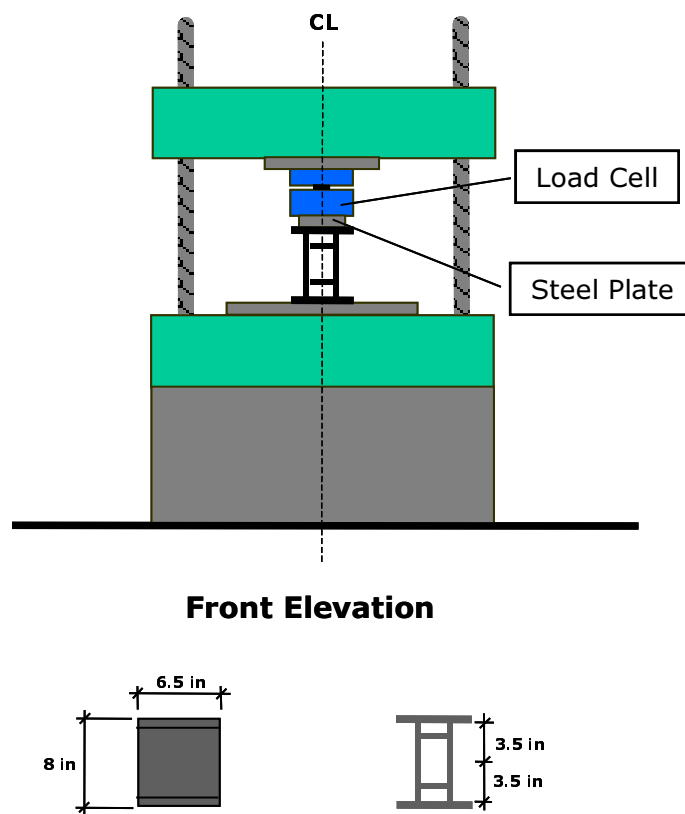


*Figure 6.26: Compression Buckling Specimen, Dimension and Test Setup
(Ulloa, 2002)*

The loading was applied stepwise to the specimen up to failure. The testing machine used was the Universal Testing Machine 600HVL. AE was

monitored by an R15I sensor mounted on a web of the specimen. The AE data acquisition system used was the Transportation Instrument.

No damage was visually observed during the test until failure. At failure, delamination of the web could be seen as shown in Fig. 6.27. This behavior is believed to be caused by the low transverse strength between lamina, particularly in the web where the reinforcement is mainly glass (Ulloa, 2002). In addition to the delamination, fiber breaks are also observed.

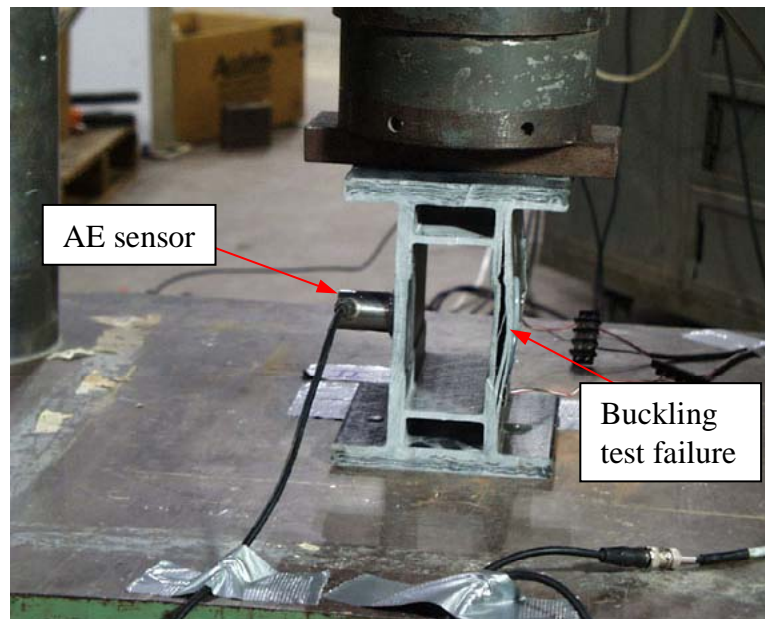


Figure 6.27: Specimen BHV2 Showing Web Buckling Test Failure

A summary of total AE hits from all specimens and their ultimate loads is shown in Table 6.6. It is noticed that for specimen BHV1 the ultimate load is much higher and the total number of hits is much low than for the other specimens.

Table 6.6: Summary of Ultimate Load and AE Data

Specimen	Ultimate load (kips)	Number of AE hits
BHV1	94.5	9,508
BHV2	76.1	36,102
BHV3	69.4	39,306

The plot of amplitude superimposed with normalized load vs. time of specimen BHV1 is shown in Figure 6.28. High amplitude hits (amplitude ≥ 68 dB), which are an indication of fiber breaks, occurred at 40% of the ultimate load. Also, the high amplitude hits continued to occur and the number of high amplitude hits increase with load.

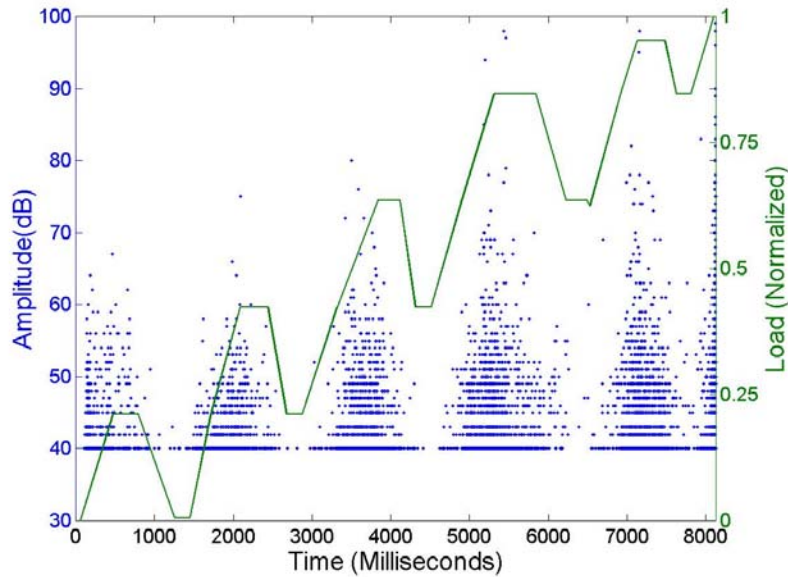


Figure 6.28: Amplitude Superimposed with Normalized Load vs. Time of Specimen BHV1

6.2.1.1 Specimen SW2 Subjected to a Four-Point Bending Test

Specimen SW2 was subjected to a four point bending test with a clear span of 28.5 feet and a constant moment span of 58 inches. The test set up and the specimen dimension are shown in Fig. 6.29. The strains and deformations at midspan of the specimen were measured and AE was monitored during testing. The AE data acquisition system used was the Transportation Instrument. Twenty R15I sensors were mounted on the specimens as shown in Figures 6.30 and 6.31.

A stepwise loading was applied to the specimen. The specimen failed at 12.8 kips. As seen in Fig. 6.32, specimen SW2 experienced large deflections prior to failure, yet the specimen behaved linear-elastically from the beginning of the test up to 10 kips (78% of the ultimate load). The load-deflection curve of specimen SW2 at midspan is shown in Fig. 6.33. The strain information at midspan was used to determine the longitudinal elastic modulus, which was calculated as 6,460 ksi.

Delamination occurred in the top flange at the ultimate load of 12.8 kips. The maximum compressive strain at the top flange for this load was 4,260 microstrains. Figure 6.34 shows initial delamination on the top flange of the beam near the midspan. Figures 6.35 and 6.36 show the top flange of the beam at midspan after failure. The failure type was similar to that observed in the compression-buckling tests (specimen BHV1, BHV2, and BHV3), in which delamination-induced buckling occurred.

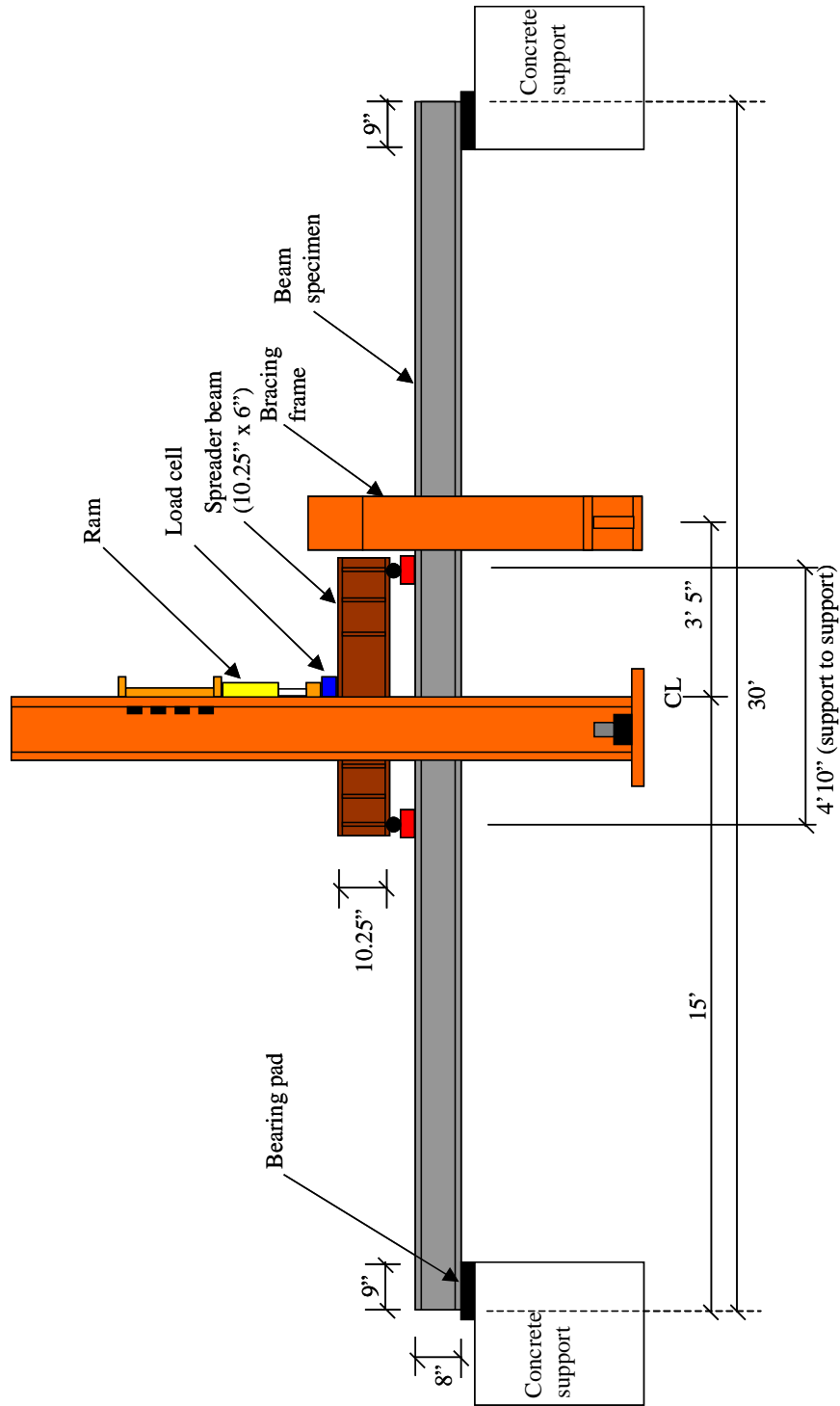


Figure 6.29 Four-Point Bending Test Setup and Dimensions of Specimen SW2

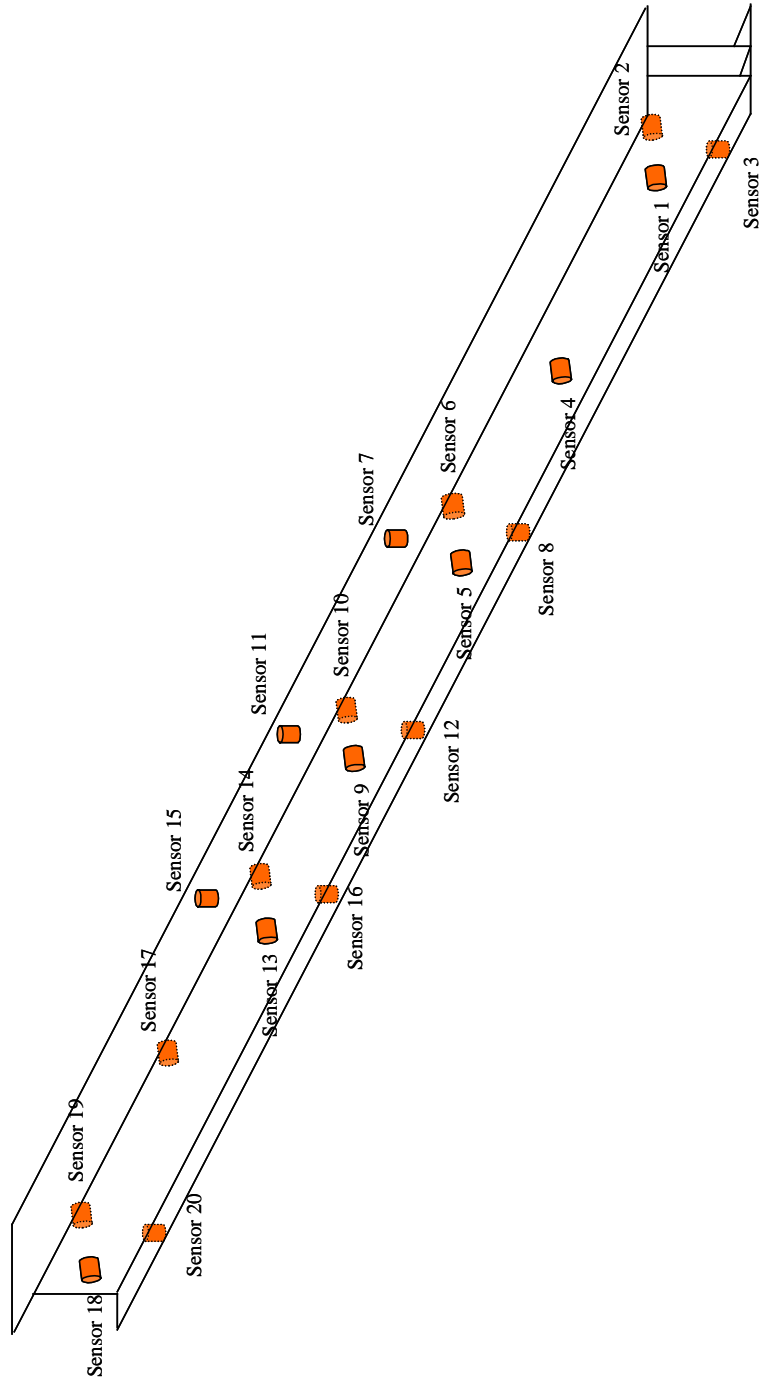


Figure 6.30: AE Sensor Locations on Specimen SW2

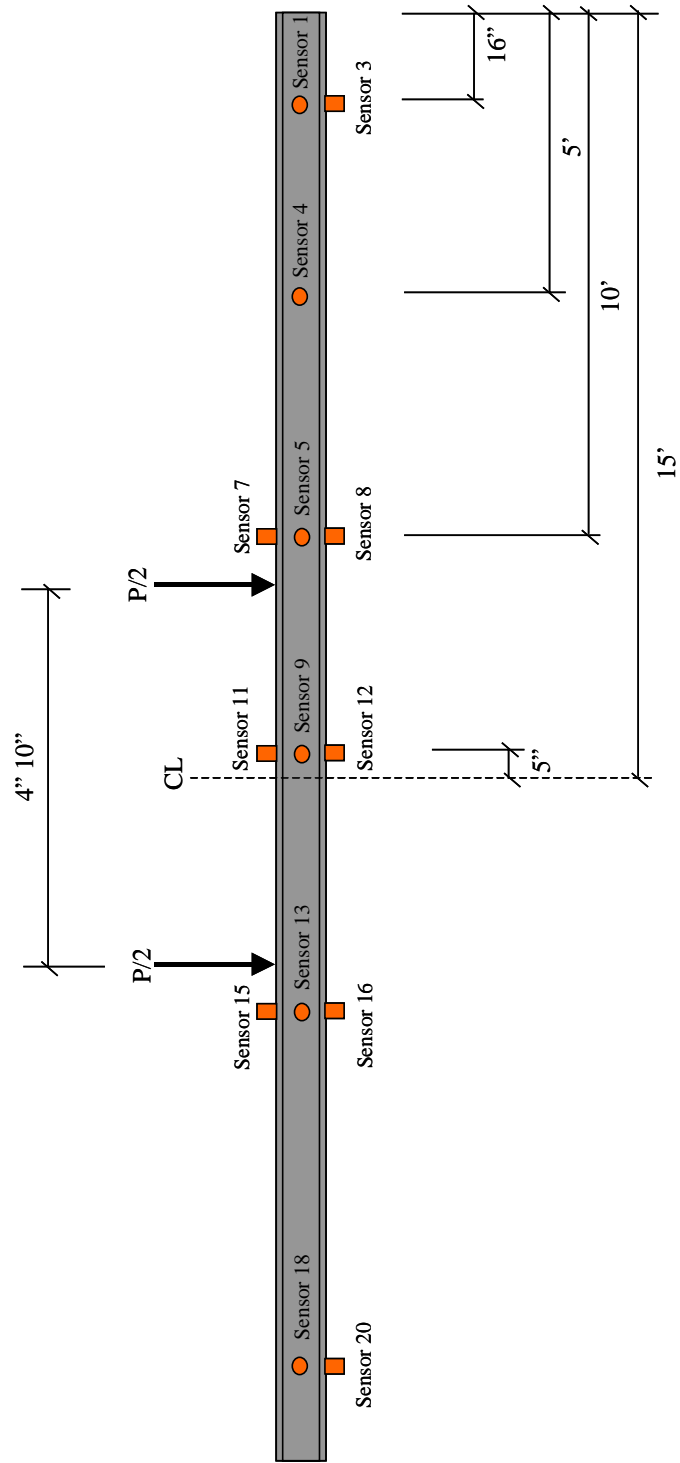


Figure 6.31: AE Sensor Locations on Specimen SW2



Figure 6.32: Specimen SW2 During Testing

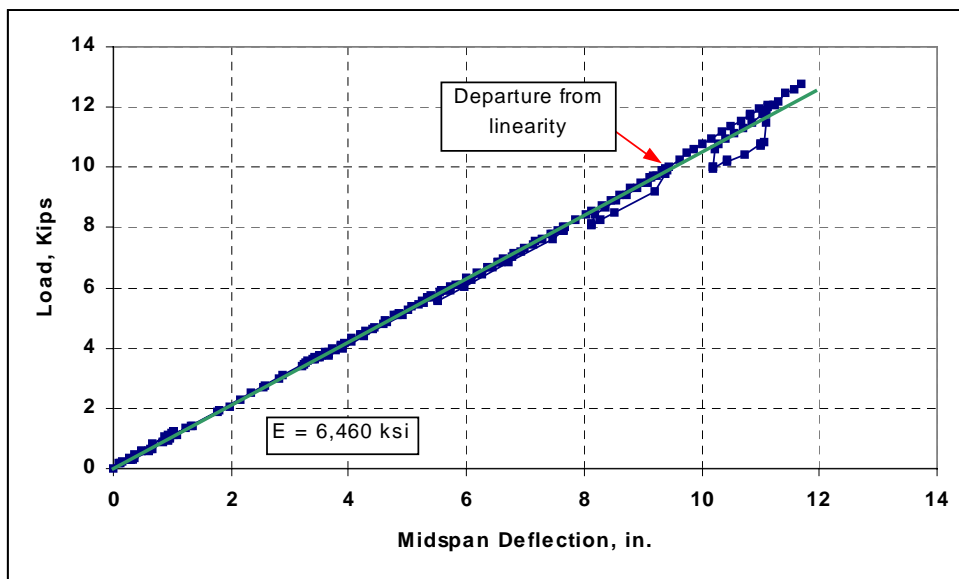


Figure 6.33: Specimen SW2 Load-Deflection Relationship



Figure 6.34: Specimen SW2 Top Flange Early Delamination (Ulloa, 2002)

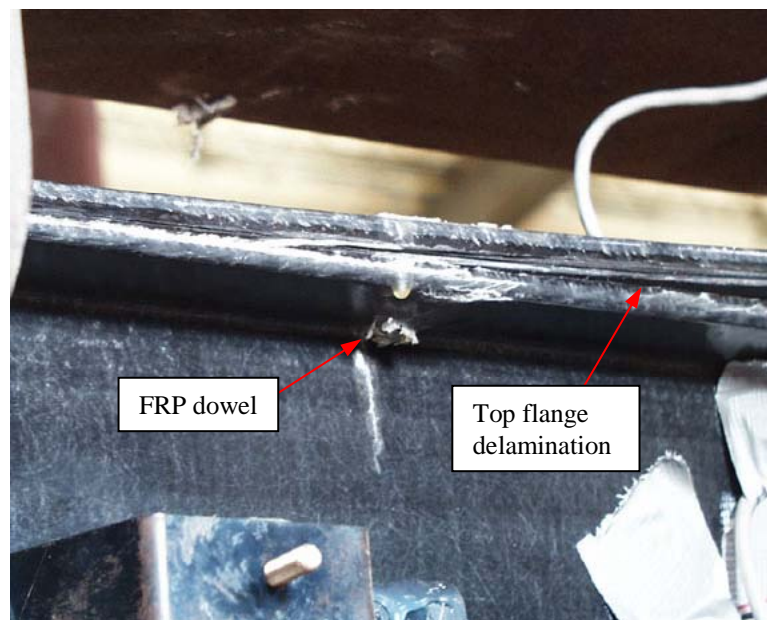


Figure 6.35: Delamination at Top Flange of Specimen SW2 (Ulloa, 2002)

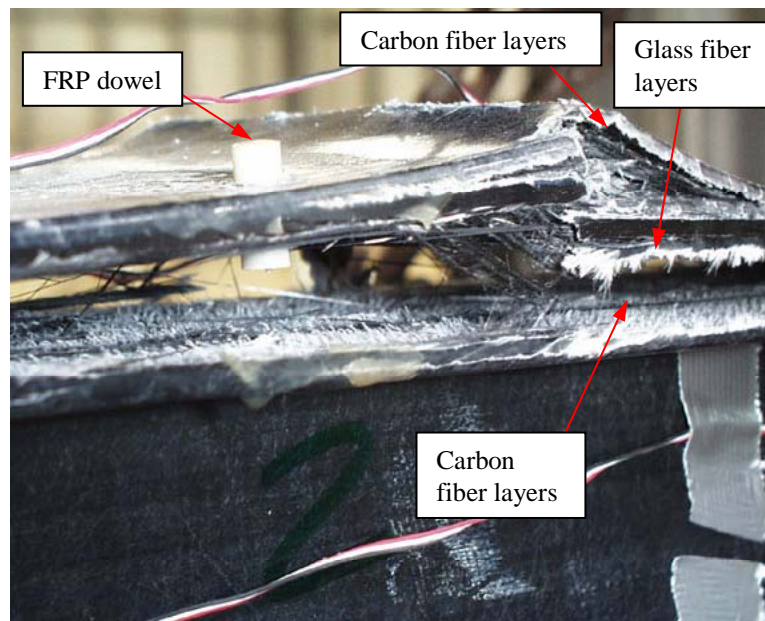


Figure 6.36: Delamination at Top Flange of Specimen SW2 Where Buckling Occurred (Ulloa, 2002)

The damage is clearly seen at the top flange of the specimen. Accordingly, the area of top flange at midspan is the area to be focused on for AE. Only AE data from R15I sensors 7, 11, and 15 are used for AE analysis and for failure mechanism determination by the neural networks. A summary of the number of AE hits from these three sensors is presented in Table 6.7. The number of hits on sensor 11 is higher than on the others because sensor 11 was located at midspan where the buckling occurred. Figure 6.37 shows the amplitude superimposed with normalized load vs. time of sensor 11. The plot shows that high amplitude hits (amplitude of 68 dB and higher) occurring at the beginning of the test (while the load increase from zero to 30% of the ultimate load). The number of high amplitude hits increased at every load step and high amplitude hits started to occur during the load hold at 62% of the ultimate load (third loading step).

Table 6.7: Number of AE Hits of Sensors 7, 11, and 15 of Specimen SW2

Sensor	Number of AE hits
7	5,823
11	12,441
15	7,019

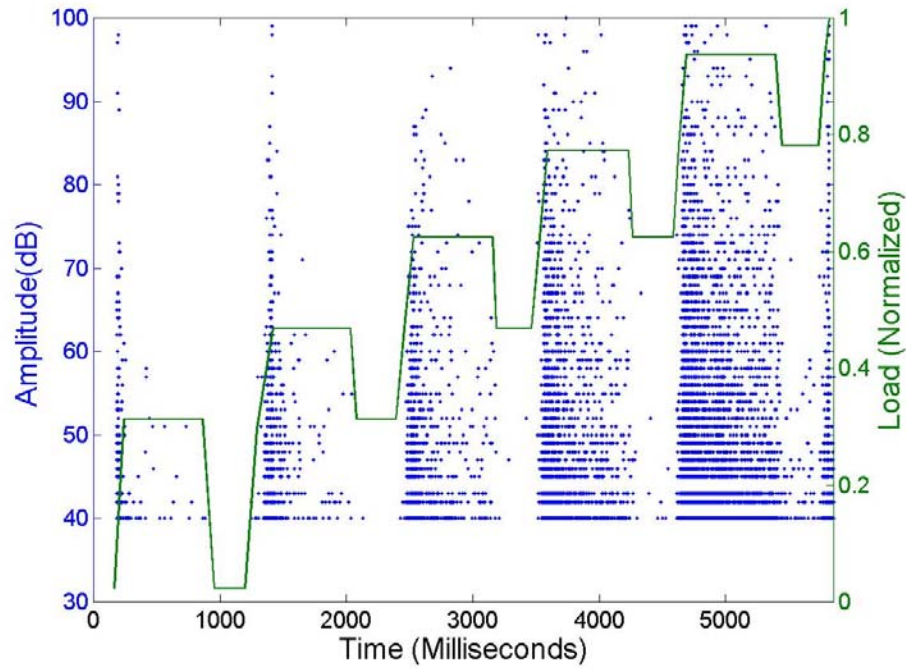


Figure 6.37: Amplitude Superimposed with Normalized Load vs. Time of Specimen SW2 (Sensor 11)

6.2.1.2 Chopped Strand Fiber and Woven Roving FRP Coupons Subjected to Direct Tension Test

Two ¼ in.-thick FRP plates were fabricated by Industrial Pipe and Plastics of Texas, Inc. (IPP). The first plate was made of vinyl ester, Derakane 8084, reinforced with chopped strand glass fiber, and the second plate was made of vinyl ester reinforced with woven roving glass fiber layers alternating with chopped strand fiber layers. Dog-bone coupons, Chop and Wov, were cut from each plate by water jet cutting. The dimensions for the coupons are given in Fig. 6.38. Figures 6.39 and 6.40 shows pictures of each specimen.

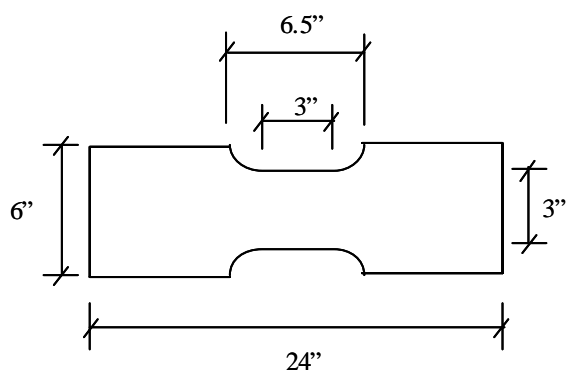


Figure 6.38: Dimensions of Specimens Chop and Wov



Figure 6.39: Specimen Chop (Chopped Strand Fiber Structure)

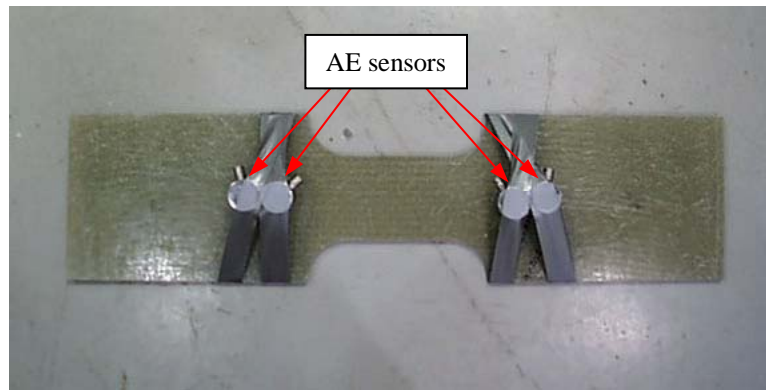


Figure 6.40: Specimen Wov (Woven Roving Fiber Structure)

Load was applied monotonically to the longitudinal axis of the specimens and until failure. The testing machine used was an MTS machine at the Texas Department of Transportation, Cedar Park Campus.

AE was monitored during testing. The data acquisition system used to collect AE was the Mistras system. Four R15I sensors were mounted on the specimens. The sensors were arranged in two pairs located at both ends of the reduced section (Fig. 6.40).

Specimen Chop failed at an ultimate tensile stress of 15.7 ksi, while specimen Wov failed at a tensile stress of 19.5 ksi. Stress vs. displacement plots of both specimens are shown in Figures 6.41 and 6.42. Note that the displacement was measured from the top to the bottom grips of the testing machine, which may include slippage between the specimen and the grips in the displacement measurement. The plots of both specimens start with a linear portion from 0 ksi to approximately 4 ksi. The curves become non-linear until failure. Near the failure of specimen Wov, a sharp increase in slope can be seen. This is attributed to the straightening of the fiber bundles in the woven roving mats.

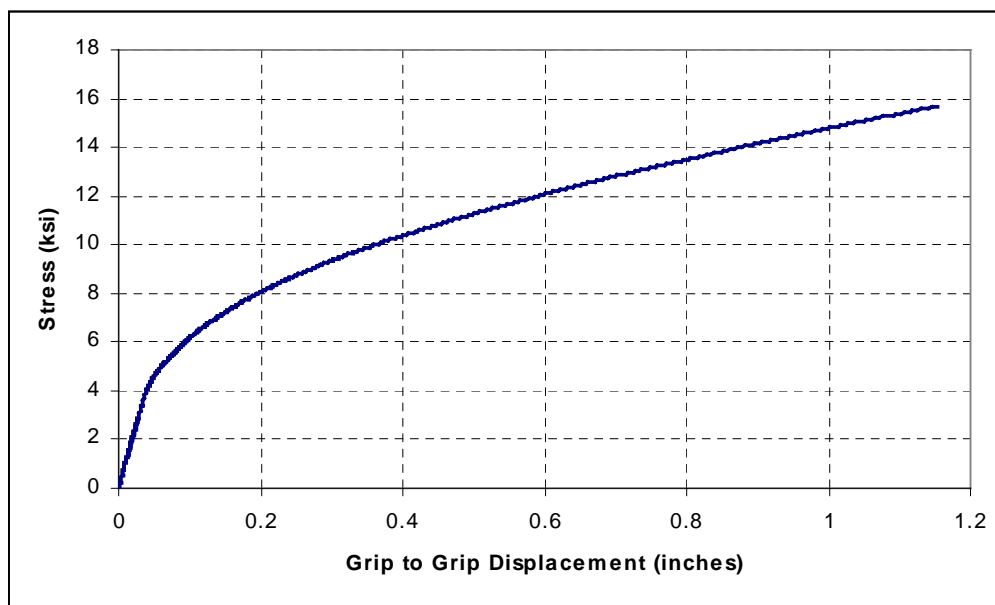


Figure 6.41: Stress vs. Displacement Plot of Specimen Chop

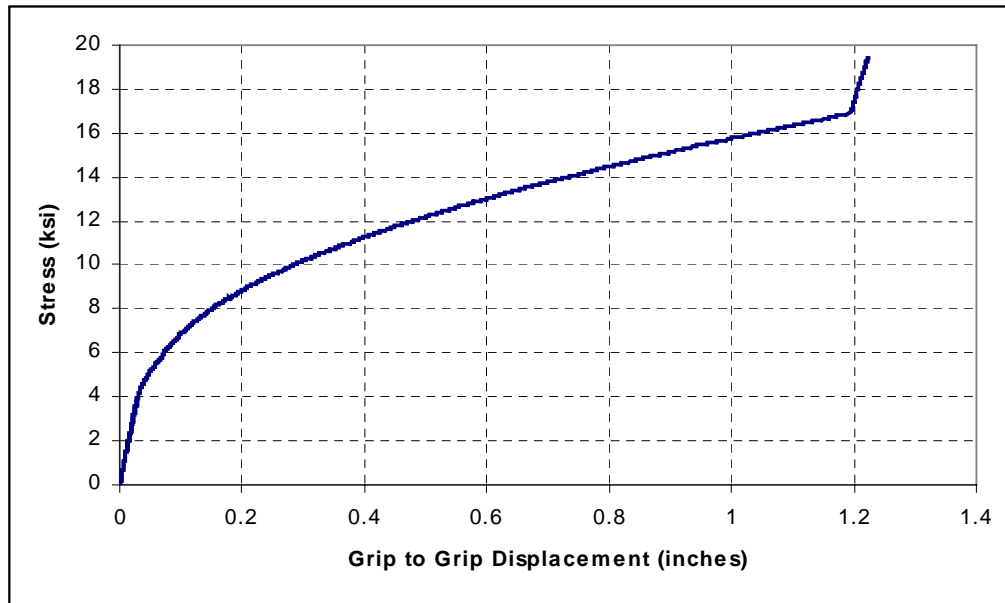


Figure 6.42: Stress vs. Displacement Plot of Specimen Wov

Failure of specimen Chop after the test was completed is shown in Fig. 6.43. The specimen had a complete fracture of the cross section at failure. Figure 6.44 shows the fracture plane of the specimen. In addition to the observed fiber breaks, delamination occurred near the fracture plane of the specimen. This is indicated by a color lighter than the surrounding areas. Several fine matrix cracks were also observed at the area near the fracture (Fig. 6.44). At the other end of the narrow section, two small delaminations incorporated with matrix cracks were observed as shown in Fig. 6.45. Also, at the curve of the dog-bone section, a white area was observed indicating initial delamination. Therefore, it can be concluded that delamination occurred during the test before the specimen fractured.



Figure 6.43: Tensile Failure of Specimen Chop

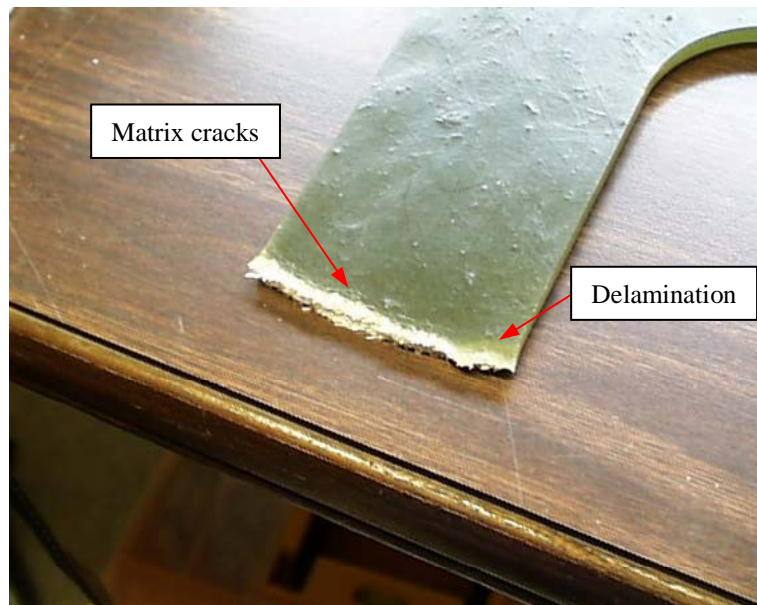


Figure 6.44: Fracture of Specimen Chop Showing Delamination and Surrounding Matrix Cracking



***Figure 6.45: Delamination at Other End of Narrowed Section of Specimen
Chop***

Figure 6.45 shows the failure of specimen Wov after the test was completed. The specimen did not have a complete fracture of the cross section at failure. Broken longitudinal fibers were observed at the fracture area, while unbroken fibers also could be observed. Additionally, delamination in the longitudinal direction was clearly observed as shown in Fig. 6.47.



Figure 6.46: Tensile Failure of Specimen Wov

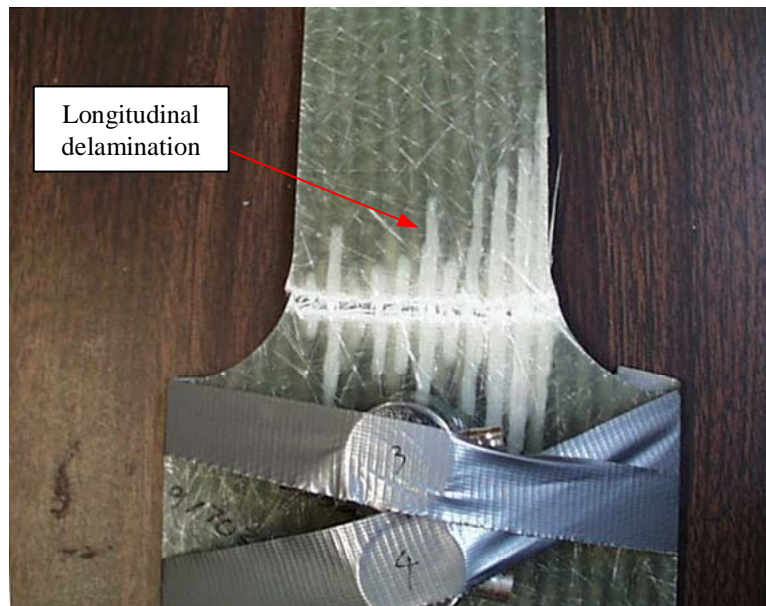


Figure 6.47: Fracture and Longitudinal Delamination of Specimen Wov

The total number of AE hits from specimen Chop was 30,064 hits, while it was 70,461 hits from specimen Wov. The normalized plots of amplitude superimposed with cumulative signal strength vs. load of specimen Chop and Wov are shown in Fig. 6.48 and 6.49, respectively. It was noticed that AE hits with low amplitude occurred constantly at the beginning of the test for both specimens. High amplitude hits (for vinyl ester FRP, high amplitude hits are amplitude of 80 dB or higher), which are an indication of fiber breaks, occurred in specimen Chop from approximately 90% of the ultimate load, while they occurred from 62% of the ultimate load for specimen Wov.

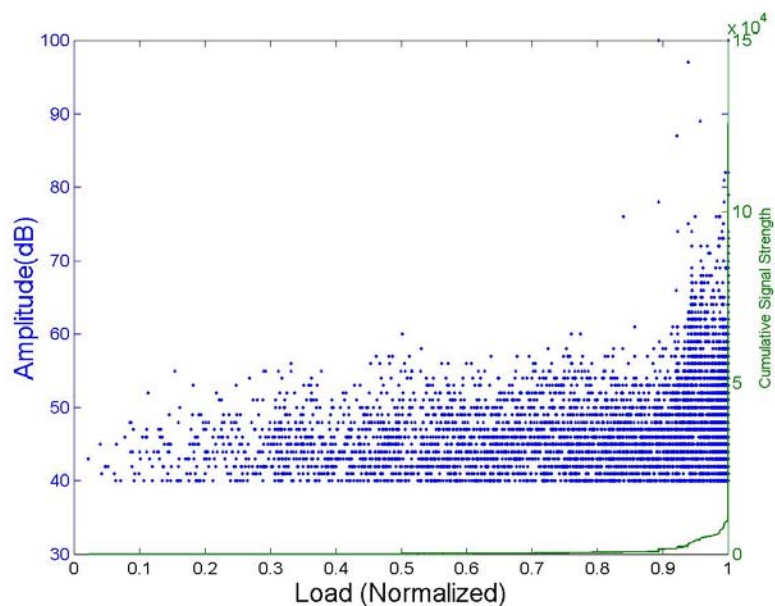


Figure 6.48: Amplitude Superimposed with Cumulative Signal Strength vs. Load of Specimen Chop

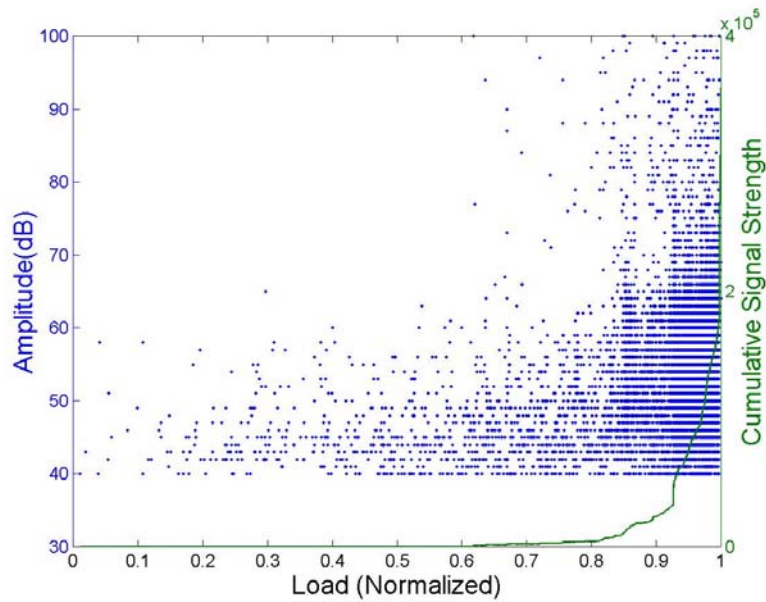


Figure 6.49: Amplitude Superimposed with Cumulative Signal Strength vs. Load of Specimen Wov

6.3 SUMMARY

In the first section, ten pultruded FRP specimens were subjected to a short beam shear test and monitored using AE. The specimens failed by delamination, which occurred within the chopped strand mat layer. Visual and SEM observation found that the failure mechanisms that occurred were primarily matrix cracking and debonding. These two mechanisms are believed to be a unique combination and may give different AE characteristics. Accordingly, the AE data from the start of the test to 92%-97% of the ultimate load for the glass specimens and the AE data from the start to 7% of the ultimate load for hybrid specimens are determined as delamination rather than matrix cracking and

debonding. The failure mechanisms involved after that are delamination and fiber breakage.

The first section also reports a study of bonded “T” sections subjected to tension. The tensile load was applied perpendicular to the bonding plane. The specimens failed by delamination of the bond surface. The delamination is essentially tension failure of the resin. The failure originated from the Teflon sheet placed at the center of the bonding plane and propagate to the end of the specimen without a sudden failure. The visual inspection and AE data showed that the failure mechanisms included delamination and fiber breakage, which occurred from the beginning of the test until failure.

The AE data and failure mechanism information provide an important documented database for pattern recognition analysis. Visual pattern recognition analysis and neural networks are discussed in Chapters 7 and 8.

The second section describes test setups and results of four additional experiments. This includes double-web specimens subjected to a compression test, a full-scale hybrid specimen subjected to a four-point bending test, a chopped strand FRP specimen subjected to a direct tension test, and a woven roving FRP specimen subjected to a direct tension test. The neural networks developed in Chapter 8 will be used to identify failure mechanisms of these specimens. After that, the AE data and the failure mechanism information of these specimens will be added to the AE database and be used to develop the final neural networks.

CHAPTER 7

Visual Pattern Recognition

Visual pattern recognition is a basic method of identifying an AE signature. For different types of damage mechanisms, there may be differences in the AE plots. Accordingly, putting AE plots from all tests together in one place helps visualize the dissimilarity in AE patterns.

AE plots and the test results from representative specimens are summarized in this chapter. The plots are arranged such that the same plots of all representative damage mechanisms are shown together. Evaluations of each type of plot are provided.

7.1 ORGANIZATION

Table 7.1 is a summary of all specimens tested for the database of failure mechanisms. Type of resin, type of fiber, number of AE sensors used, and loading description are included. The fiber structure of all specimens except specimens Chop and Wov are mainly unidirectional fibers. Specimen Chop is made of chopped strand fibers and specimen Wov is made of woven roving fibers.

Some of the tests are repeated. Thus, only representative specimens are presented in this chapter. These twelve representative specimens are marked by the “*” sign in Table 7.1. Note that the priority in selecting the representative specimens is given to specimens that are made of vinyl ester resin. However, two representative isophthalic polyester samples are included for comparison. This is because the flexibility property of the vinyl ester resin is found to give a better FRP performance than isophthalic polyester resin. Thus FRP made with vinyl ester resin has more potential for use in real applications (Ziehl, 2000).

Table 7.1 Specimen Summary for Research Program Database

Name	Fiber type	Resin type	No. of sensors	Loading Description
TGI1	Glass	Isophthalic polyester	4	Transverse tension
TGI2*	Glass	Isophthalic polyester	4	Transverse tension
TGV*	Glass	Vinyl ester	4	Transverse tension
LGI1*	Glass	Isophthalic polyester	4	Longitudinal tension
LGI2	Glass	Isophthalic polyester	4	Longitudinal tension
LGV1*	Glass	Vinyl ester	4	Longitudinal tension
LGV2	Glass	Vinyl ester	4	Longitudinal tension
LHV*	Carbon	Vinyl ester	4	Longitudinal tension
FGI	Glass	Isophthalic polyester	4	Longitudinal tension (full scale)
FGV*	Glass	Vinyl ester	4	Longitudinal tension (full scale)
SGI1	Glass	Isophthalic polyester	2	Short beam shear
SGI2	Glass	Isophthalic polyester	2	Short beam shear
SGI3	Glass	Isophthalic polyester	2	Short beam shear
SGI4	Glass	Isophthalic polyester	2	Short beam shear
SGV1*	Glass	Vinyl ester	2	Short beam shear
SGV2	Glass	Vinyl ester	2	Short beam shear
SGV3	Glass	Vinyl ester	2	Short beam shear
SHV1*	Hybrid	Vinyl ester	2	Short beam shear
SHV2	Hybrid	Vinyl ester	2	Short beam shear
SHV3	Hybrid	Vinyl ester	2	Short beam shear
Tee1*	Glass	Vinyl ester	4	Bond test
Tee2	Glass	Vinyl ester	4	Bond test
Tee3	Glass	Vinyl ester	4	Bond test
BHV1*	Hybrid	Vinyl ester	2	Compression on both flanges
BHV2	Hybrid	Vinyl ester	2	Compression on both flanges
BHV3	Hybrid	Vinyl ester	2	Compression on both flanges
FHV	Hybrid	Vinyl ester	3	4-point bending
Chop*	Chopped glass	Vinyl ester	4	Longitudinal tension
Wov*	Woven roving glass	Vinyl ester	4	Longitudinal tension

* Specimens that are representative of a group of tests

Plots of the same AE correlation for all representative specimens are displayed together in one set. Each set consists of 12 plots representing 12 specimens. Each set is arranged to fit on to two pages. The page layout is shown in Fig. 7.1.

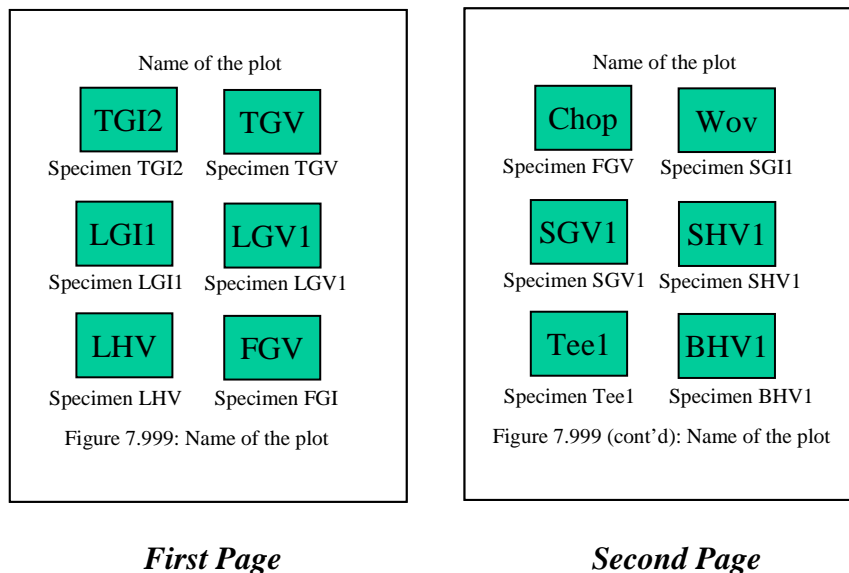


Figure 7.1: Display of a Series of One Correlation Plots

It is noted that the name of the specimen begins with a three-letter sequence. The first letter in the sequence describes the loading geometry. The letter T designates that the tensile load is applied in the transverse direction to the fiber orientation (90 degrees). The letter L designates that the tensile load is applied in the longitudinal direction to the fiber orientation (0 degrees). The letter F designates the full-scale test. The letter S designates the short beam shear test, and the letter B the buckling test. The second letter represents the fiber material, where G stands for glass and H stands for glass/carbon hybrid. The third letter represents the resin materials. The letter I stands for isophthalic polyester, and the

letter V stands for vinyl ester. If the three-letter sequence is followed by a number, it indicates that the same type of material and test was repeated and that number is the number of the specimen of that group. Note that this lettering system does not include specimens Tee 1, Tee2, Tee3, Chop, and Wov.

To avoid confusion, the plot of each specimen is assigned to a specific location on the page. For example, any plot of specimen SGV1 is always located at the first column and the second row on the second page. If a correlation cannot be plotted for that specimen, the assigned location is displayed as “N.A.”.

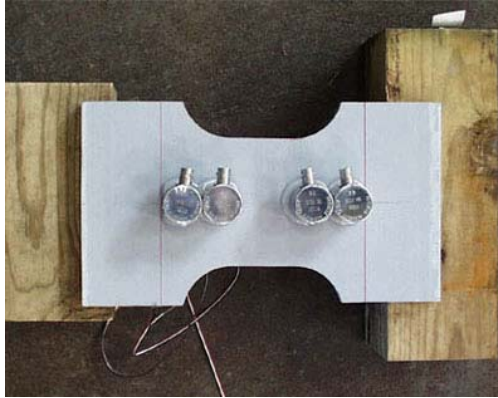
7.2 THE PLOTS FOR VISUAL PATTERN RECOGNITION

The summary of total AE hits, maximum stress, and maximum strain of all representative specimens is given in Table 7.2. The series of plots are shown in Figs. 7.2 to 7.17.

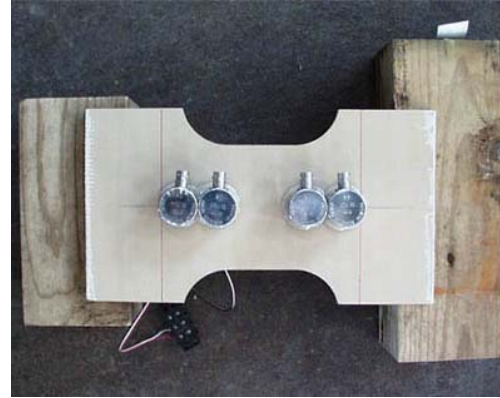
Table 7.2: Summary of Representative Specimens and Basic Properties

Specimen	Total AE hits (per sensor)	Max. stress (ksi)	Max. strain (microstrains)
TGI2	18,800	7.03	9,500
TGV	41,075	9.01	15,000
LGI1	32,494	24.36	7,547
LGV1	171,476	39.53	11,492
LHV	244,238	61.0	9,600
FGV	117,409	N.A.	13,344
SGV1	4,024	42.0	11,582
SHV1	87,383	33.5	13,708
Teel	5,976	0.12 (bond stress)	N.A.
BHV1	9,508	N.A.	N.A.
Chop	7,516	15.7	N.A.
Wov	17,615	19.5	N.A.

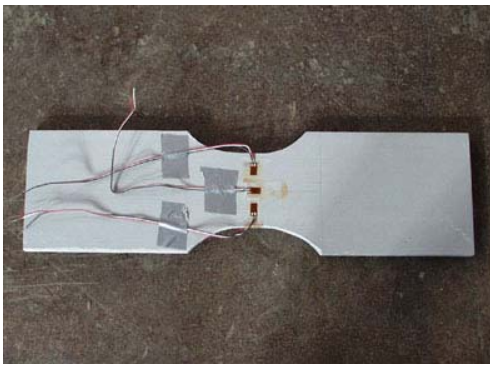
Pictures of Test Specimens



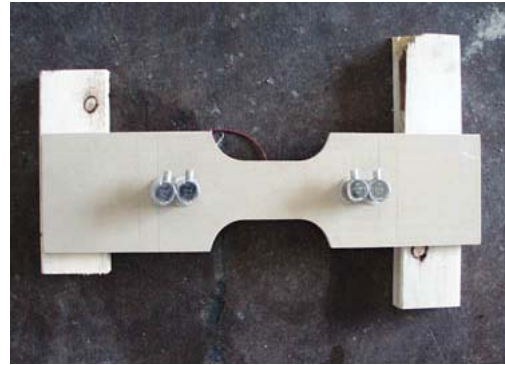
TGI2 (Transverse/Glass/Isophthalic)



TGV (Transverse/Glass/Vinyl Ester)



LGI1 (Longitudinal/Glass/Isophthalic)



LGV1 (Longitudinal/Glass/Vinyl Ester)



LHV (Longitudinal/Hybrid/Vinyl Ester)



FGV (Full-Scale/Glass/Vinyl Ester)

Figure 7.2: Pictures of Test Specimens

Pictures of Test Specimens



Chop (Chopped Glass/Vinyl Ester)



Wov (Woven Roving Glass/Vinyl Ester)



SGVI (Shear/Glass/Vinyl Ester)



SHVI (Shear/Hybrid/Vinyl Ester)



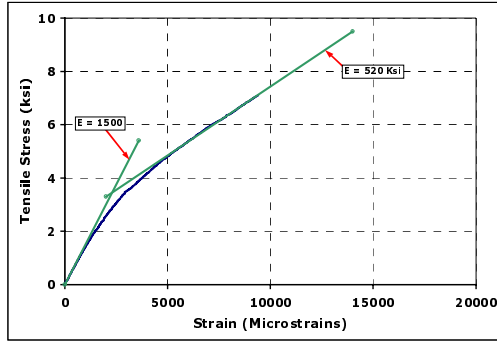
Tee1 (Bond/Glass/Vinyl Ester)



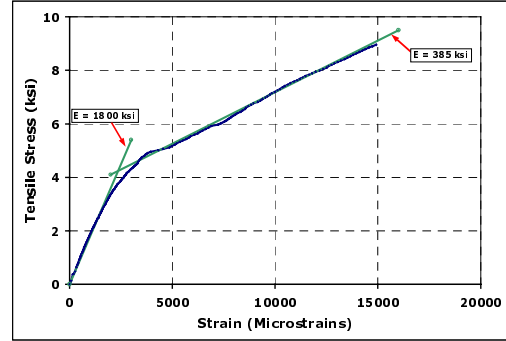
BHVI (Buckling/Hybrid/Vinyl Ester)

Figure 7.2 (cont'd): Pictures of Test Specimens

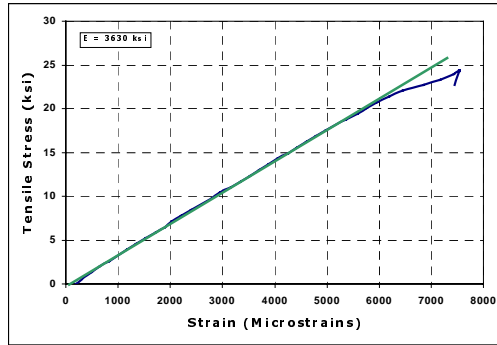
Stress vs. Strain



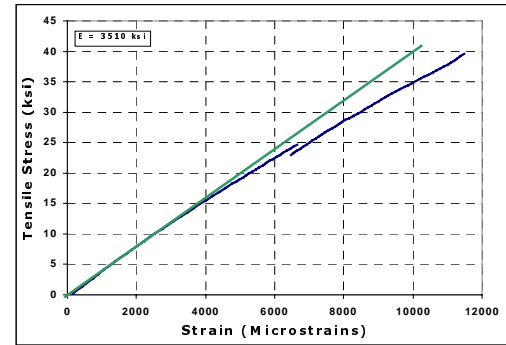
TGI2 (Transverse/Glass/Isophthalic)



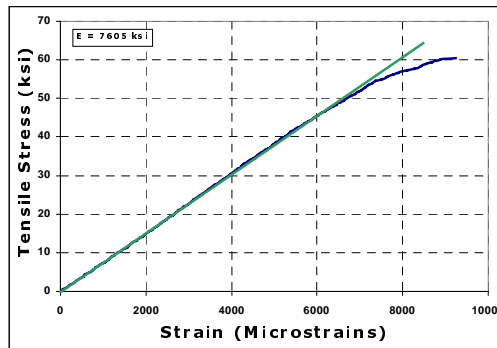
TGV (Transverse/Glass/Vinyl Ester)



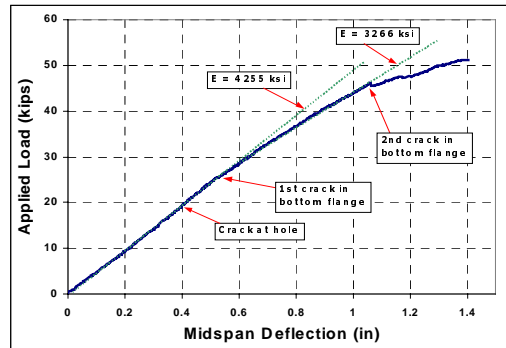
LGI1 (Longitudinal/Glass/Isophthalic)



LGV1 (Longitudinal/Glass/Vinyl Ester)



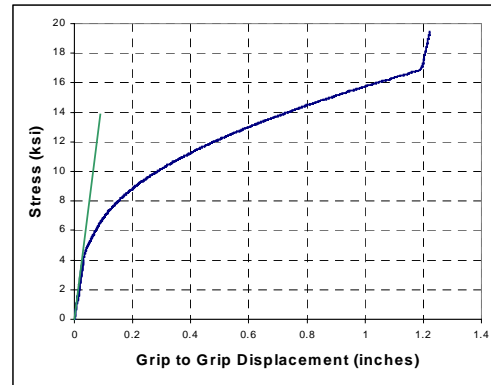
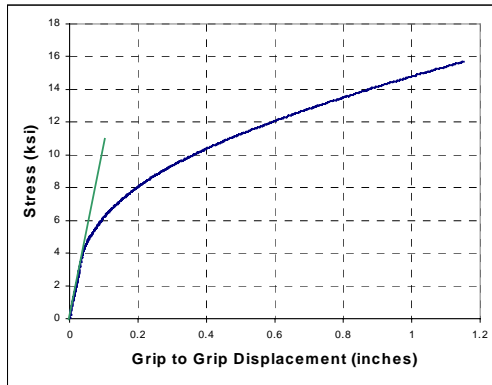
LHV (Longitudinal/Hybrid/Vinyl Ester)



FGV (Full-Scale/Glass/Vinyl Ester)

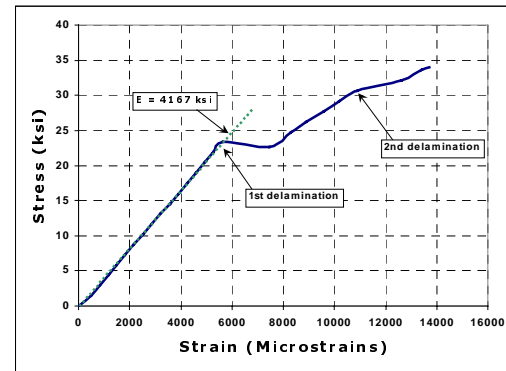
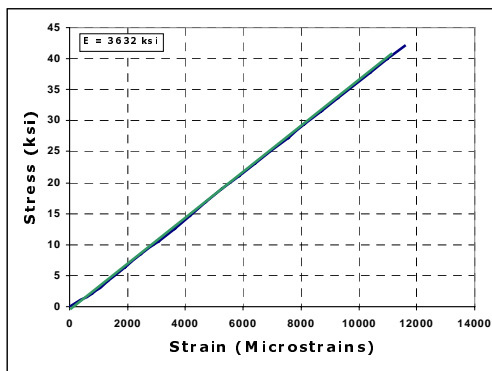
Figure 7.3: Stress vs. Strain of Representative Specimens

Stress vs. Strain



Chop (Chopped Glass/Vinyl Ester)

Wov (Woven Roving Glass/Vinyl Ester)



SGVI (Shear/Glass/Vinyl Ester)

SHVI (Shear/Hybrid/Vinyl Ester)

N.A.

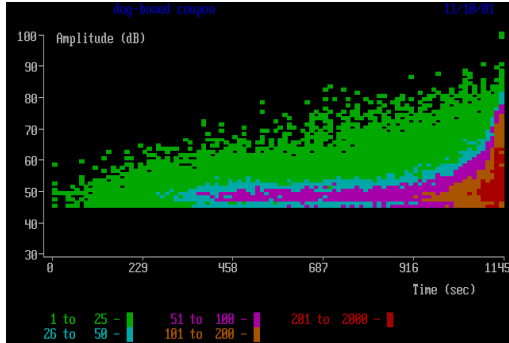
N.A.

Tee1 (Bond/Glass/Vinyl Ester)

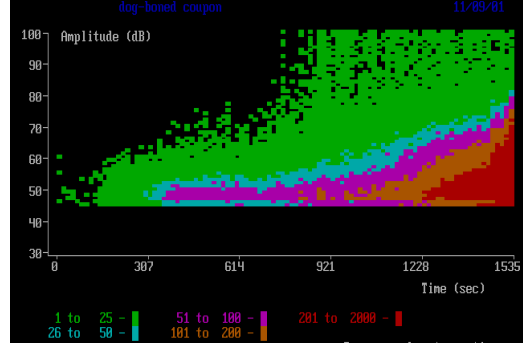
BHV1 (Buckling/Hybrid/Vinyl Ester)

Figure 7.3 (cont'd): Stress vs. Strain of Representative Specimens

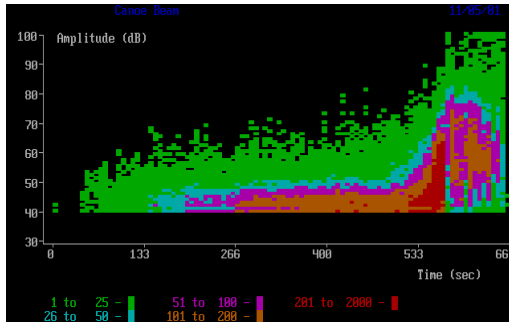
Amplitude vs. Time (or Load)



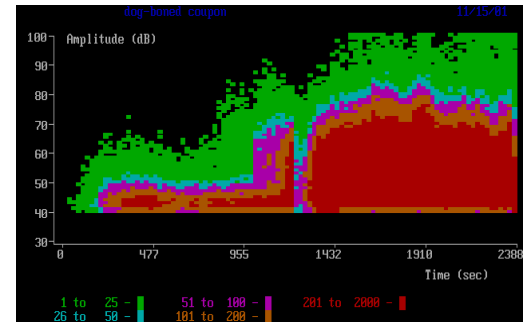
TGI2 (Transverse/Glass/Isophthalic)



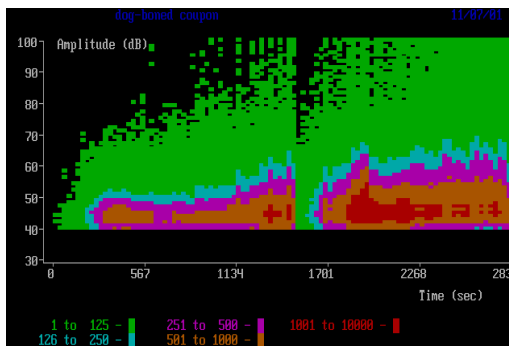
TGV (Transverse/Glass/Vinyl Ester)



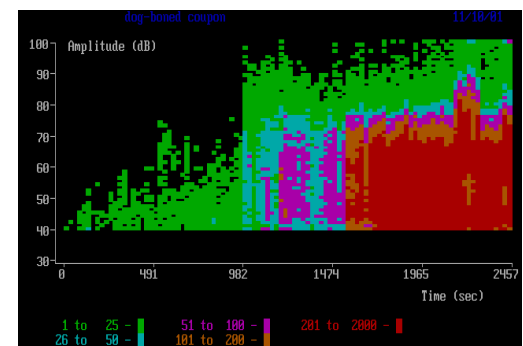
LGI1 (Longitudinal/Glass/Isophthalic)



LGV1 (Longitudinal/Glass/Vinyl Ester)



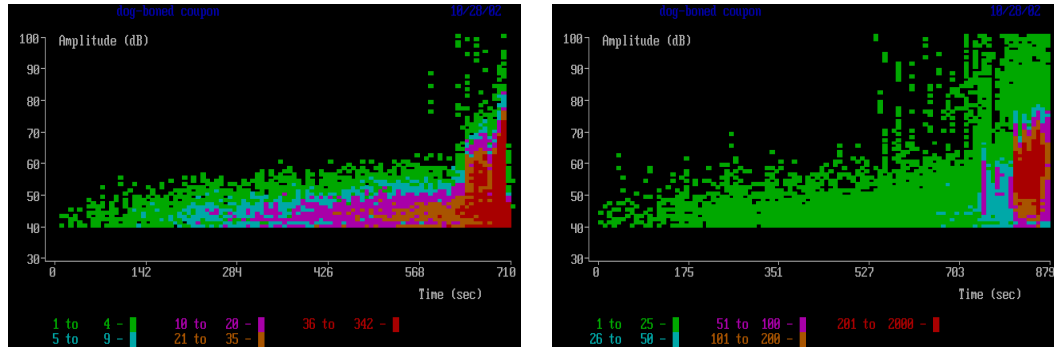
LHV (Longitudinal/Hybrid/Vinyl Ester)



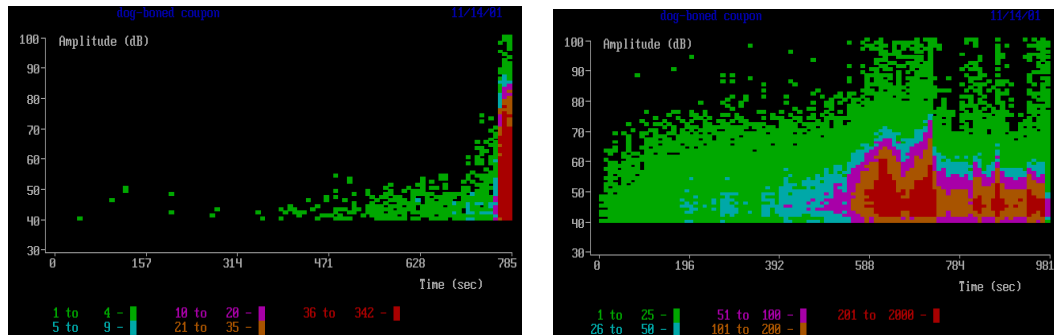
FGV (Full-Scale/Glass/Vinyl Ester)

Figure 7.4: Amplitude vs. Time (or Load) of Representative Specimens

Amplitude vs. Time (or Load)

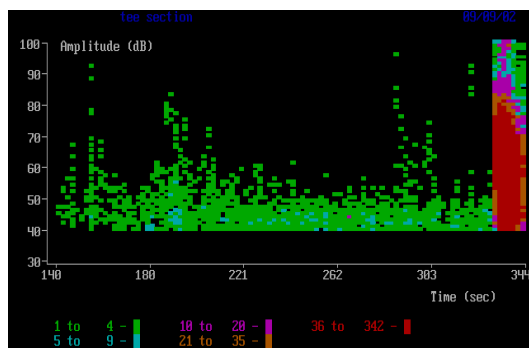


Chop (Chopped Glass/Vinyl Ester) Wov (Woven Roving Glass/Vinyl Ester)

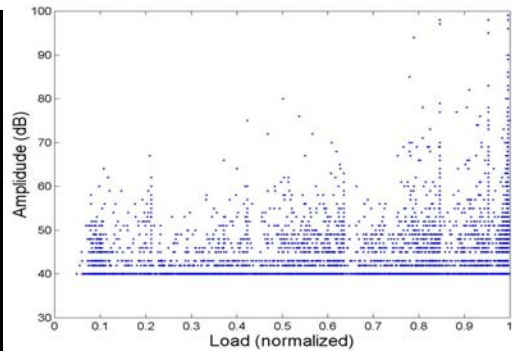


SGVI (Shear/Glass/Vinyl Ester)

SHVI (Shear/Hybrid/Vinyl Ester)



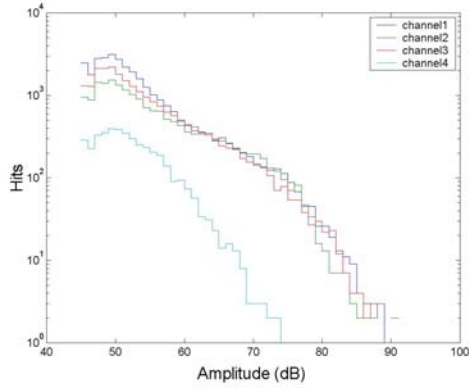
Tee1 (Bond/Glass/Vinyl Ester)



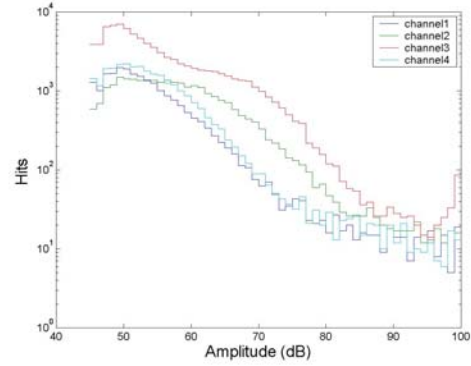
BHV1 (Buckling/Hybrid/Vinyl Ester)

Figure 7.4 (cont'd): Amplitude vs. Time (or Load) of Representative Specimens

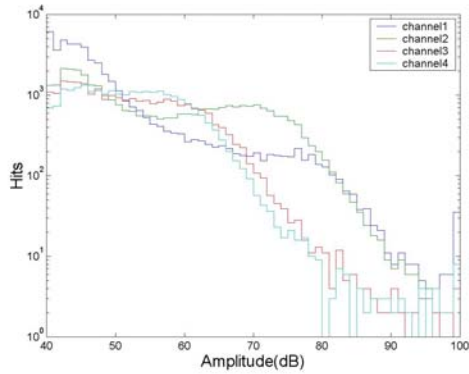
Amplitude Distribution



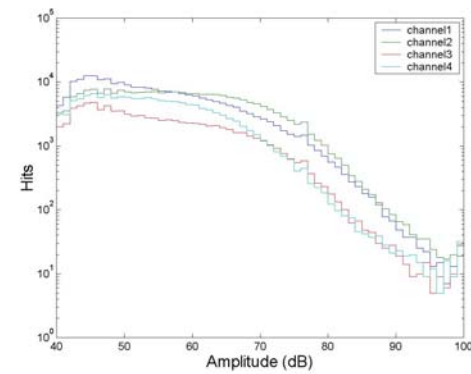
TGI2 (Transverse/Glass/Isophthalic)



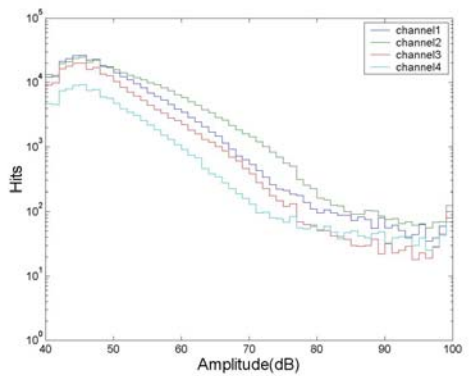
TGV (Transverse/Glass/Vinyl Ester)



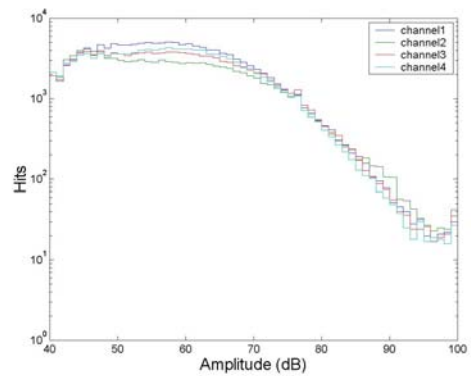
LGI1 (Longitudinal/Glass/Isophthalic)



LGV1 (Longitudinal/Glass/Vinyl Ester)



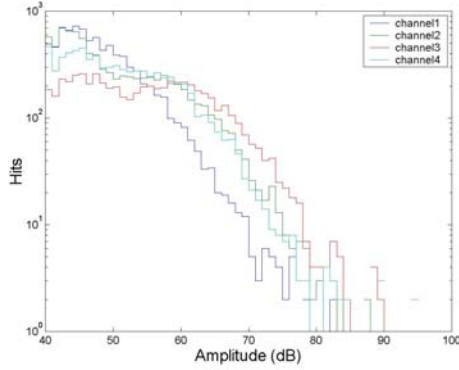
LHV (Longitudinal/Hybrid/Vinyl Ester)



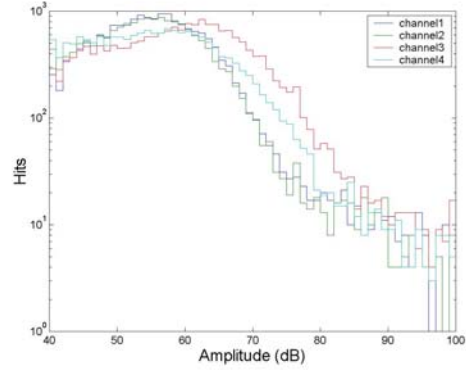
FGV (Full-Scale/Glass/Vinyl Ester)

Figure 7.5: Amplitude Distribution of Representative Specimens

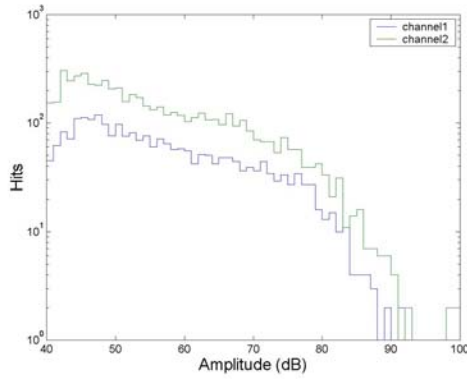
Amplitude Distribution



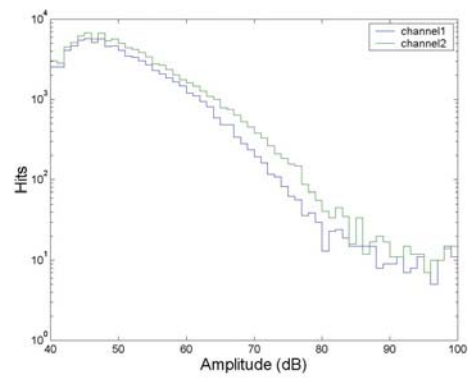
Chop (Chopped Glass/Vinyl Ester)



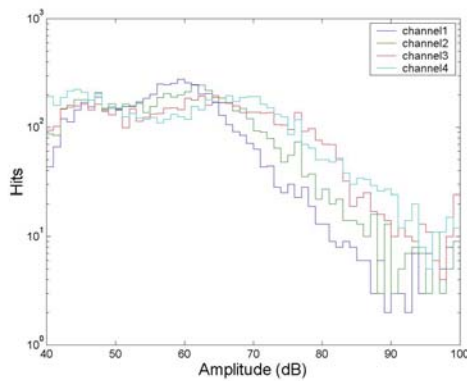
Wov (Woven Roving Glass/Vinyl Ester)



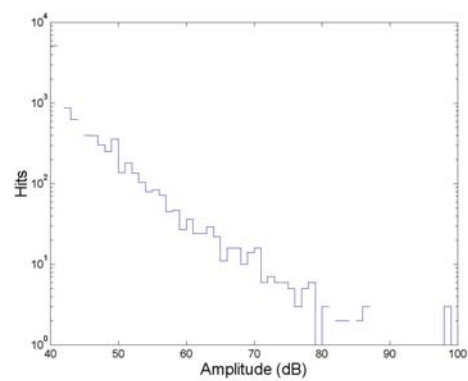
SGV1 (Shear/Glass/Vinyl Ester)



SHV1 (Shear/Hybrid/Vinyl Ester)



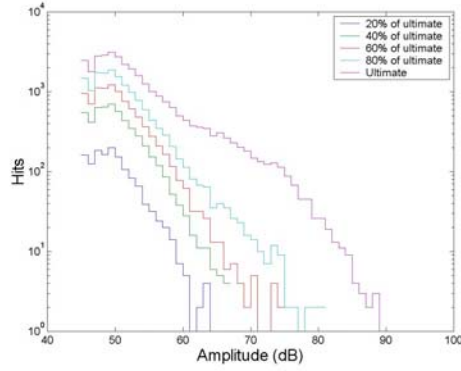
Tee1 (Bond/Glass/Vinyl Ester)



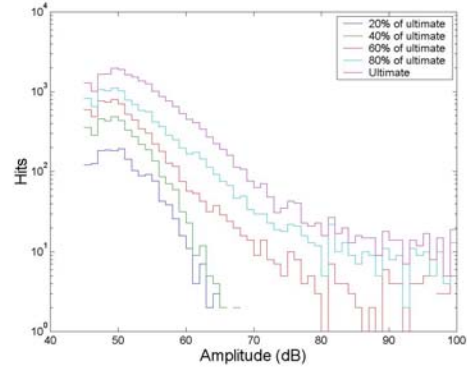
BHV1 (Buckling/Hybrid/Vinyl Ester)

Figure 7.5 (cont'd): Amplitude Distribution of Representative Specimens

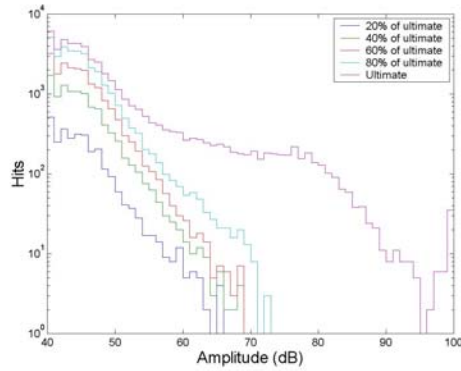
Progression of Amplitude Distribution



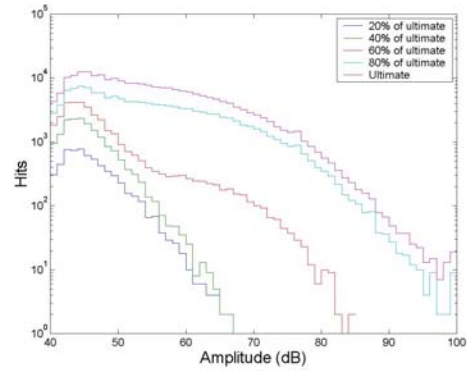
TGI2 (Transverse/Glass/Isophthalic)



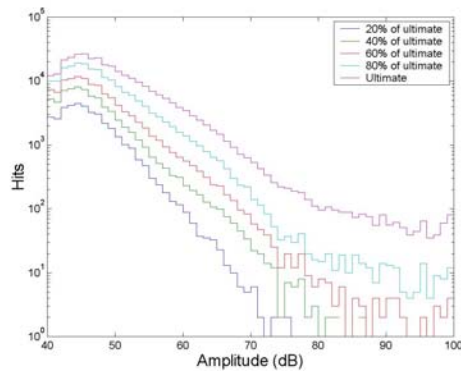
TGV (Transverse/Glass/Vinyl Ester)



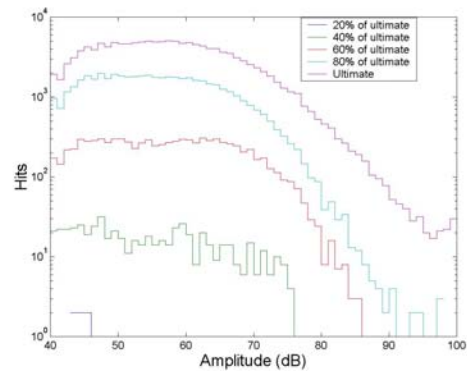
LGI1 (Longitudinal/Glass/Isophthalic)



LGV1 (Longitudinal/Glass/Vinyl Ester)



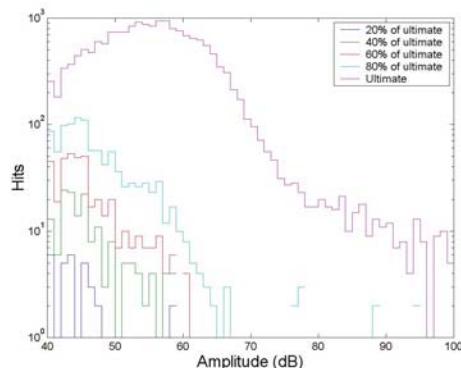
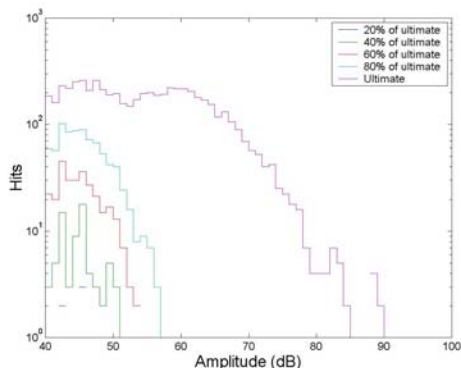
LHV (Longitudinal/Hybrid/Vinyl Ester)



FGV (Full-Scale/Glass/Vinyl Ester)

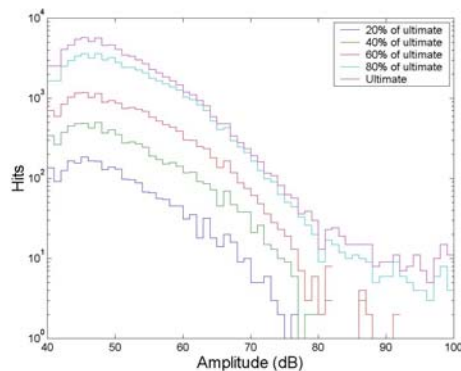
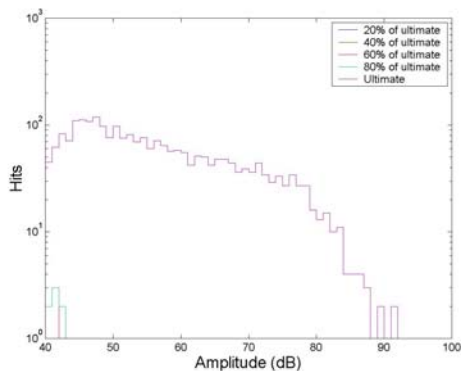
Figure 7.6: Progression of Amplitude Distribution of Representative Specimens

Progression of Cumulative Amplitude Distribution



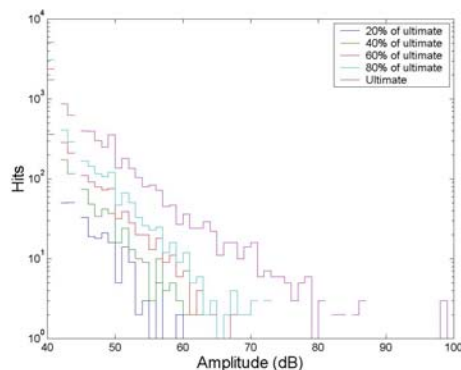
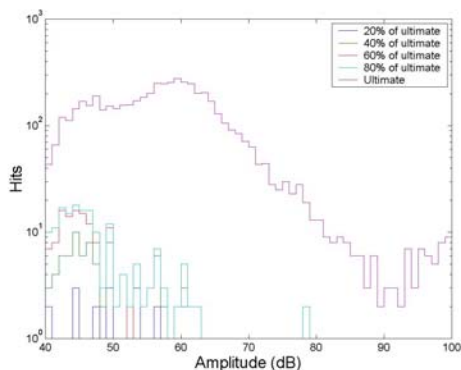
Chop (Chopped Glass/Vinyl Ester)

Wov (Woven Roving Glass/Vinyl Ester)



SGV1 (Shear/Glass/Vinyl Ester)

SHV1 (Shear/Hybrid/Vinyl Ester)



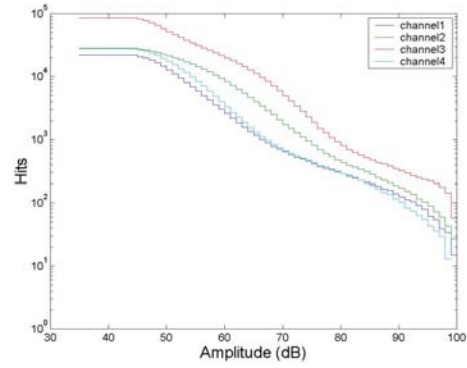
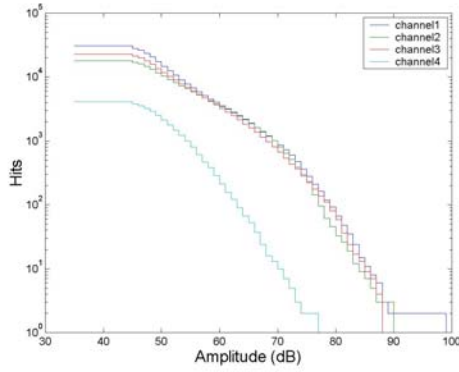
Tee1 (Bond/Glass/Vinyl Ester)

BHV1 (Buckling/Hybrid/Vinyl Ester)

Figure 7.6 (cont'd): Progression of Amplitude Distribution of Representative

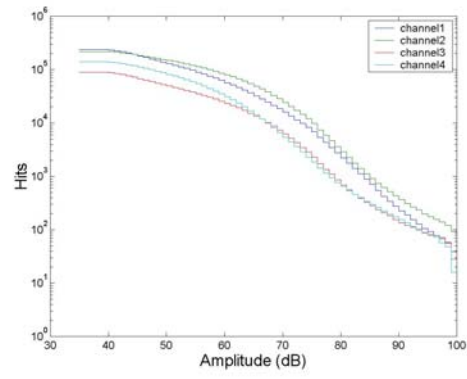
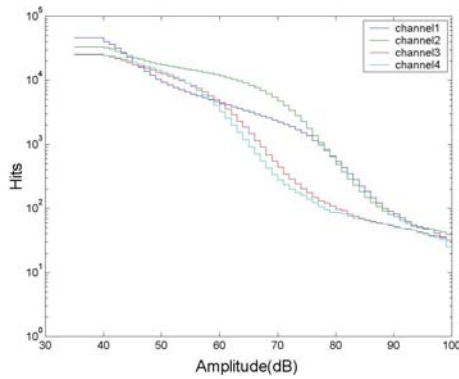
Specimens

Cumulative Amplitude Distribution



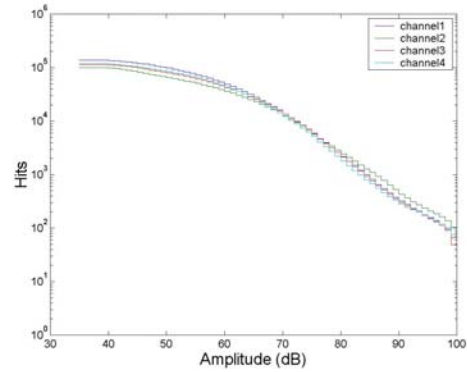
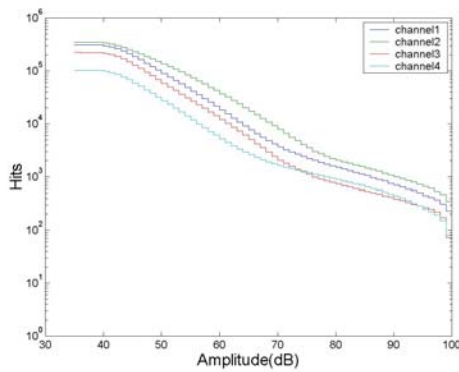
TGI2 (Transverse/Glass/Isopthalic)

TGV (Transverse/Glass/Vinyl Ester)



LGI1 (Longitudinal/Glass/Isopthalic)

LGV1 (Longitudinal/Glass/Vinyl Ester)

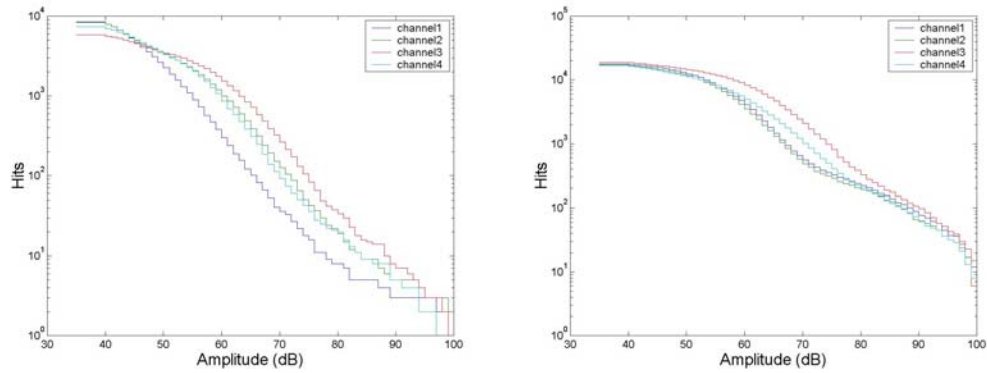


LHV (Longitudinal/Hybrid/Vinyl Ester)

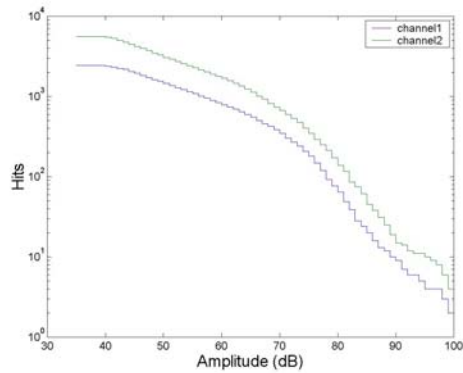
FGV (Full-Scale/Glass/Vinyl Ester)

Figure 7.7: Cumulative Amplitude Distribution of Representative Specimens

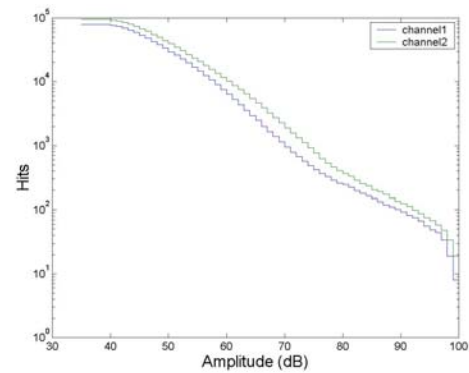
Cumulative Amplitude Distribution



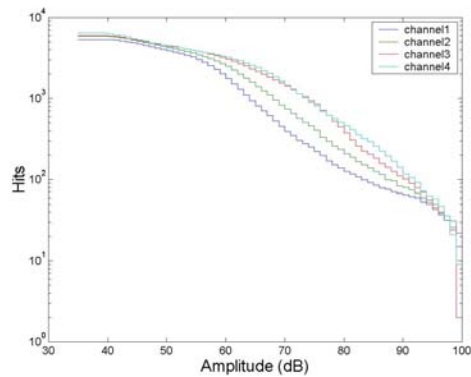
Chop (Chopped Glass/Vinyl Ester)



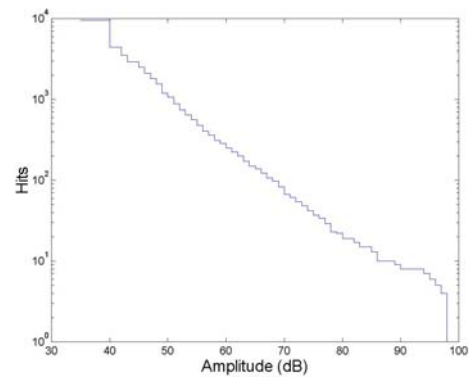
Wov (Woven Roving Glass/Vinyl Ester)



SGV1 (Shear/Glass/Vinyl Ester)



SHV1 (Shear/Hybrid/Vinyl Ester)

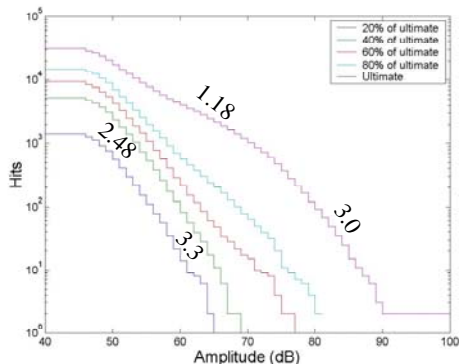


Tee1 (Bond/Glass/Vinyl Ester)

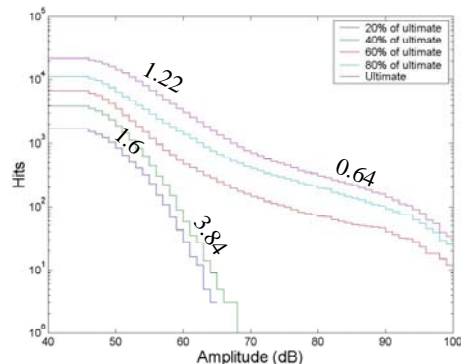
BHV1 (Buckling/Hybrid/Vinyl Ester)

Figure 7.7 (Cont'd): Cumulative Amplitude Distribution of Representative Specimens

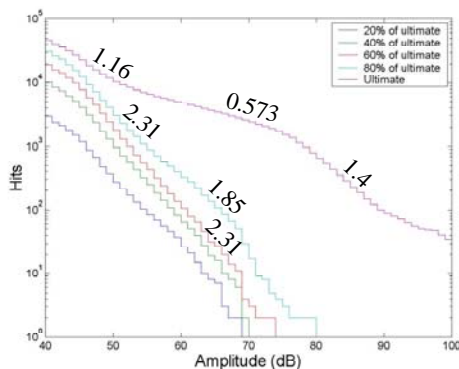
Progression of Cumulative Amplitude Distribution



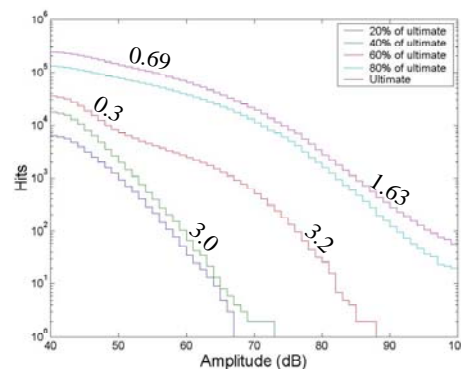
TGI2 (Transverse/Glass/Isophthalic)



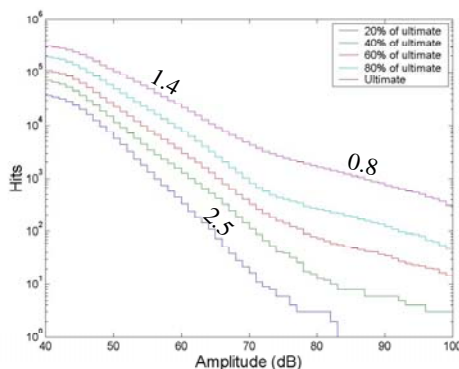
TGV (Transverse/Glass/Vinyl Ester)



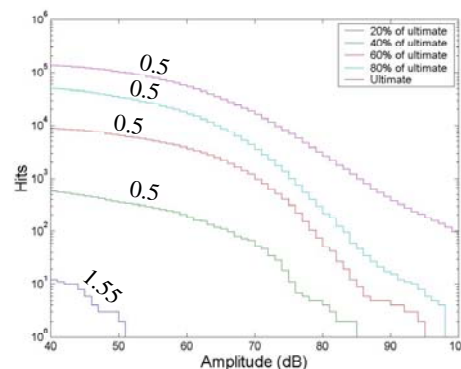
LGI1 (Longitudinal/Glass/Isophthalic)



LGV1 (Longitudinal/Glass/Vinyl Ester)



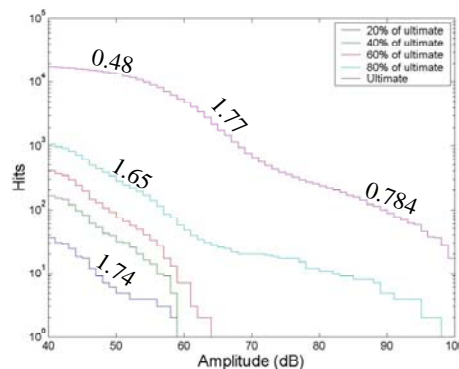
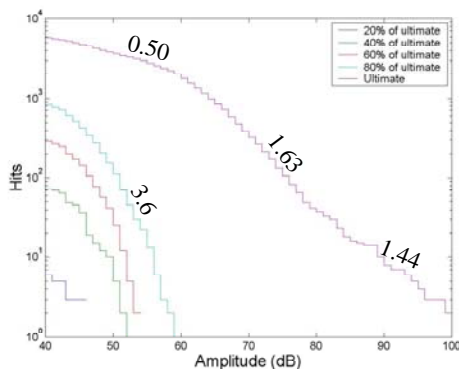
LHV (Longitudinal/Hybrid/Vinyl Ester)



FGV (Full-Scale/Glass/Vinyl Ester)

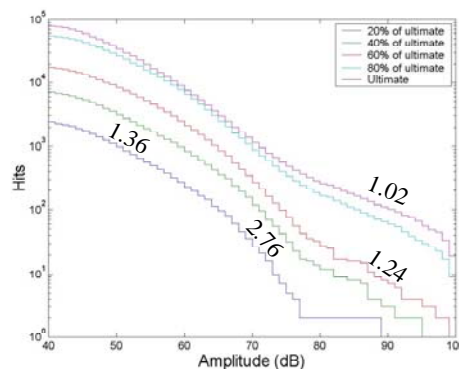
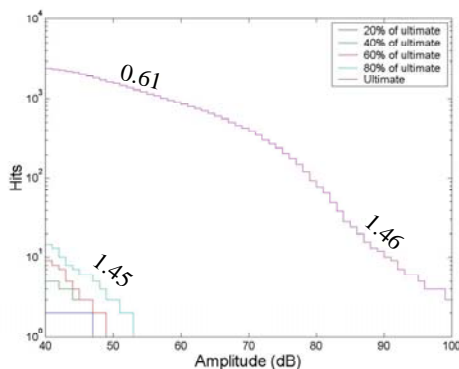
Figure 7.8: Progression of Cumulative Amplitude Distribution of Representative Specimens

Progression of Cumulative Amplitude Distribution



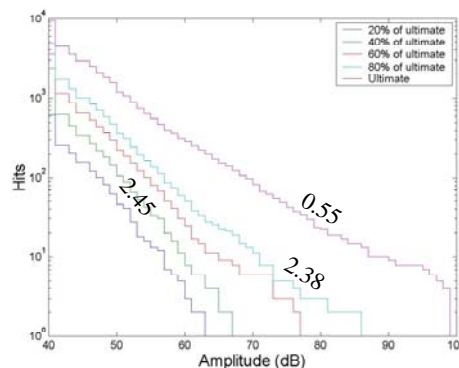
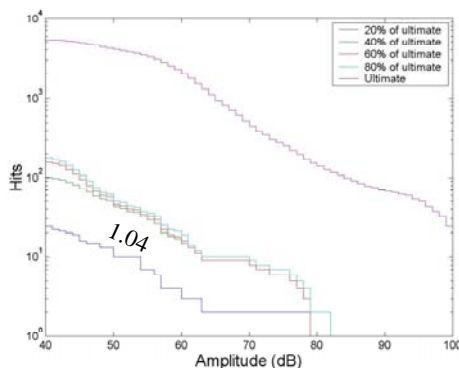
Chop (Chopped Glass/Vinyl Ester)

Wov (Woven Roving Glass/Vinyl Ester)



SGV1 (Shear/Glass/Vinyl Ester)

SHV1 (Shear/Hybrid/Vinyl Ester)

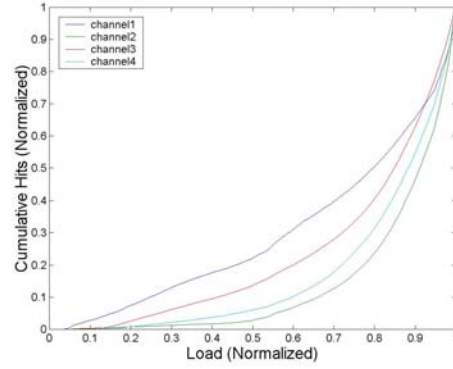
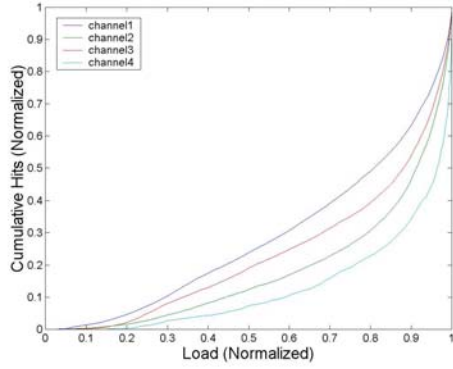


Tee1 (Bond/Glass/Vinyl Ester)

BHV1 (Buckling/Hybrid/Vinyl Ester)

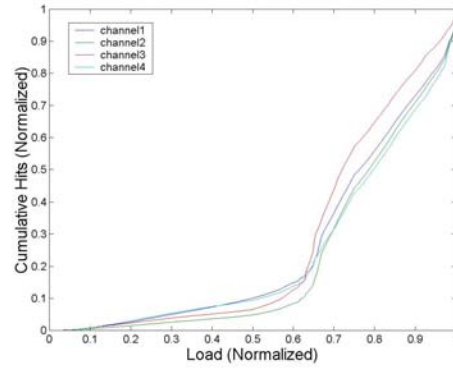
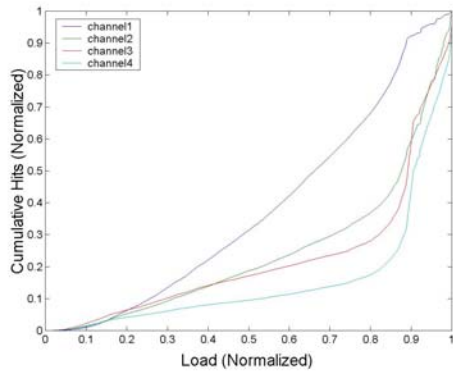
Figure 7.8 (cont'd): Progression of Cumulative Amplitude Distribution of Representative Specimens

Cumulative Hits vs. Load



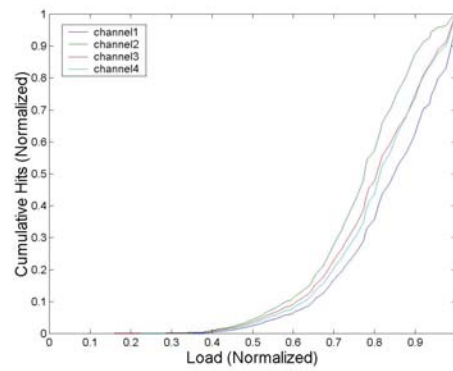
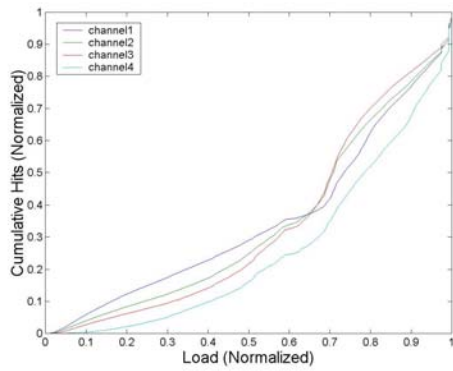
TGI2 (Transverse/Glass/Isophthalic)

TGV (Transverse/Glass/Vinyl Ester)



LGI1 (Longitudinal/Glass/Isophthalic)

LGV1 (Longitudinal/Glass/Vinyl Ester)

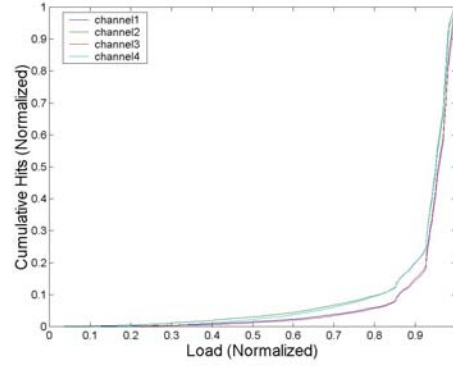
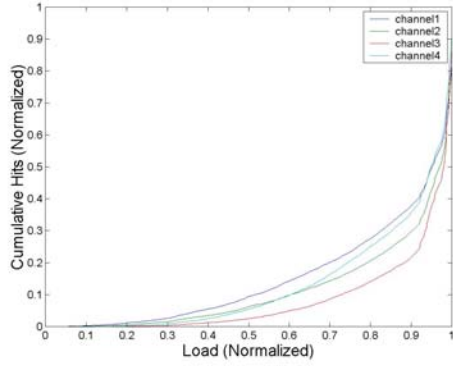


LHV (Longitudinal/Hybrid/Vinyl Ester)

FGV (Full-Scale/Glass/Vinyl Ester)

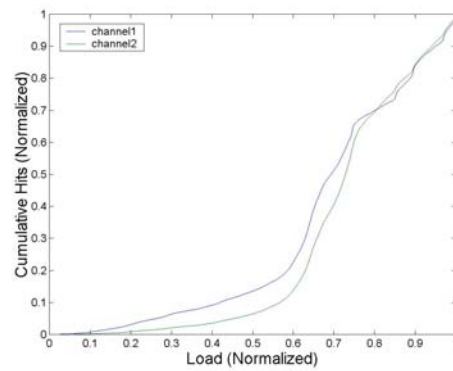
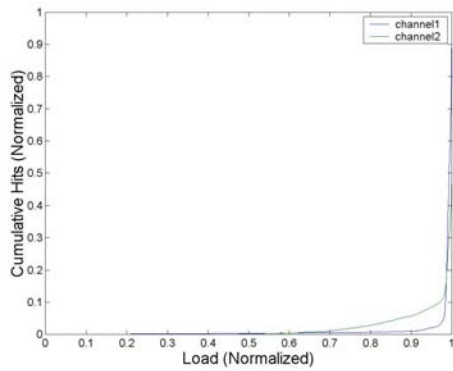
Figure 7.9: Cumulative Hits vs. Load of Representative Specimens

Cumulative Hits vs. Load



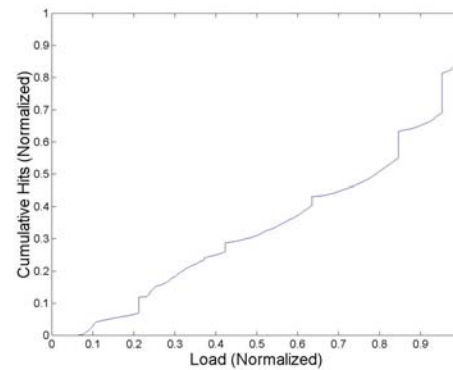
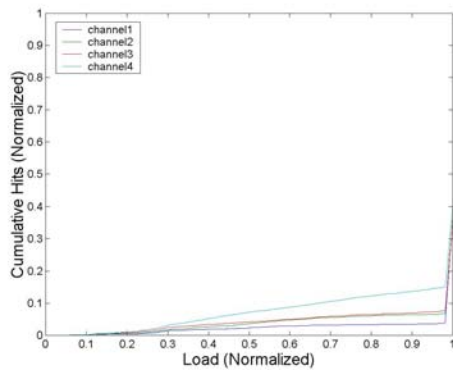
Chop (Chopped Glass/Vinyl Ester)

Wov (Woven Roving Glass/Vinyl Ester)



SGV1 (Shear/Glass/Vinyl Ester)

SHV1 (Shear/Hybrid/Vinyl Ester)

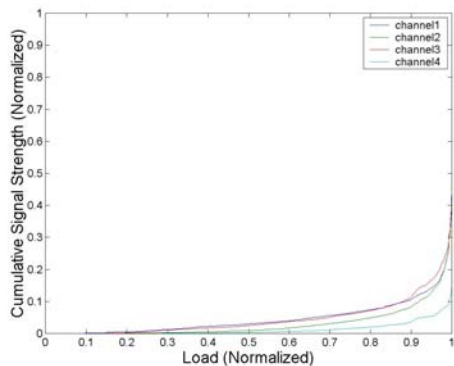


Tee1 (Bond/Glass/Vinyl Ester)

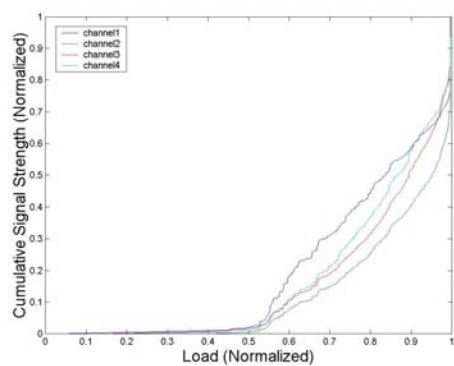
BHV1 (Buckling/Hybrid/Vinyl Ester)

Figure 7.9 (cont'd): Cumulative Hits vs. Load of Representative Specimens

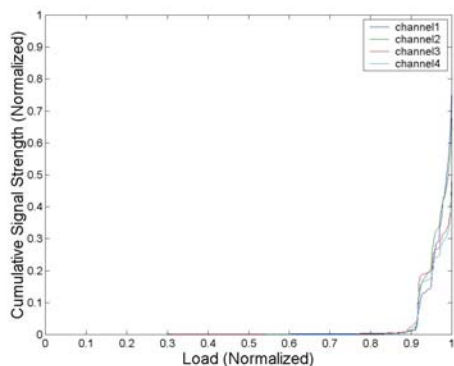
Cumulative Signal Strength vs. Load



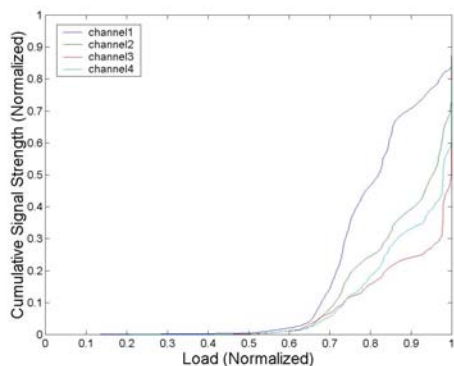
TGI2 (Transverse/Glass/Isophthalic)



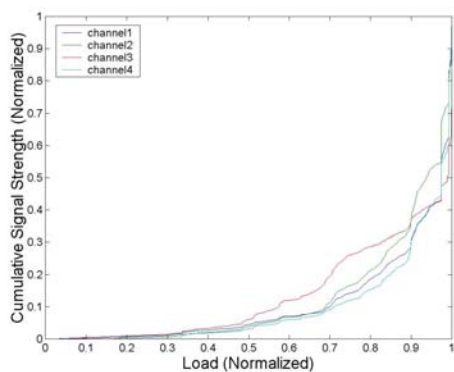
TGV (Transverse/Glass/Vinyl Ester)



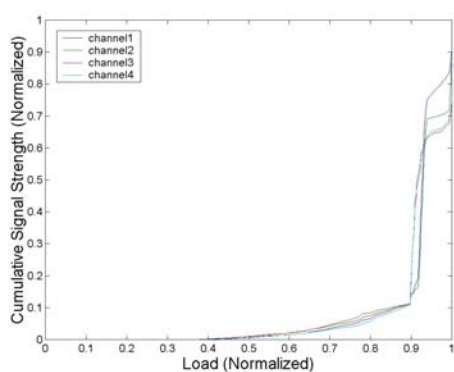
LGI1 (Longitudinal/Glass/Isophthalic)



LGV1 (Longitudinal/Glass/Vinyl Ester)



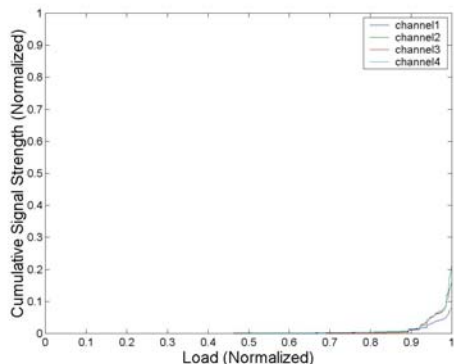
LHV (Longitudinal/Hybrid/Vinyl Ester)



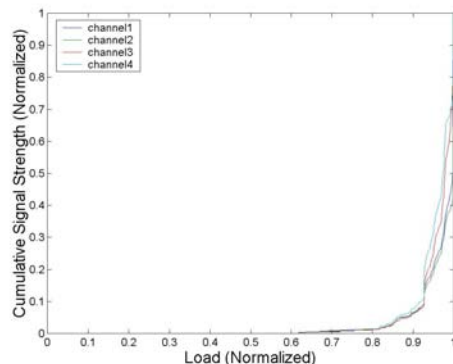
FGV (Full-Scale/Glass/Vinyl Ester)

Figure 7.10: Cumulative Signal Strength vs. Load of Representative Specimens

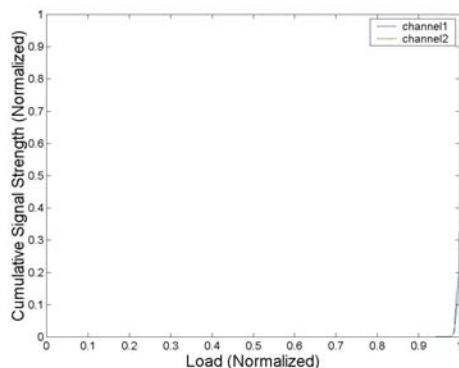
Cumulative Signal Strength vs. Load



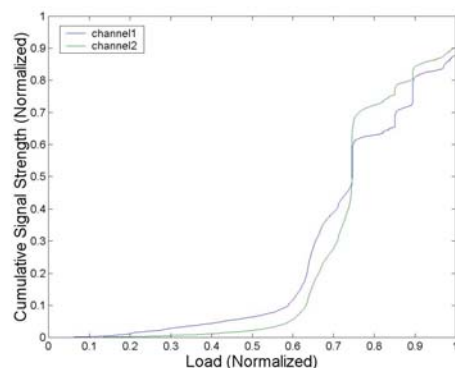
Chop (Chopped Glass/Vinyl Ester)



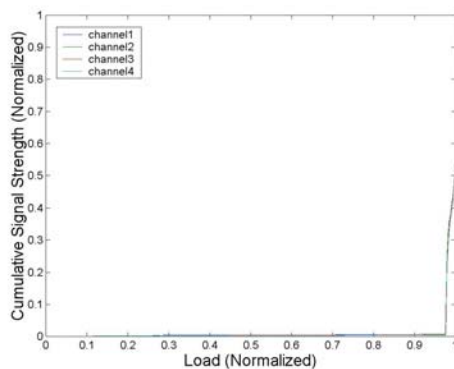
Wov (Woven Roving Glass/Vinyl Ester)



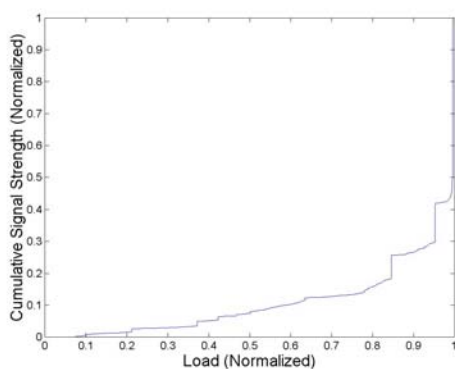
SGV1 (Shear/Glass/Vinyl Ester)



SHV1 (Shear/Hybrid/Vinyl Ester)



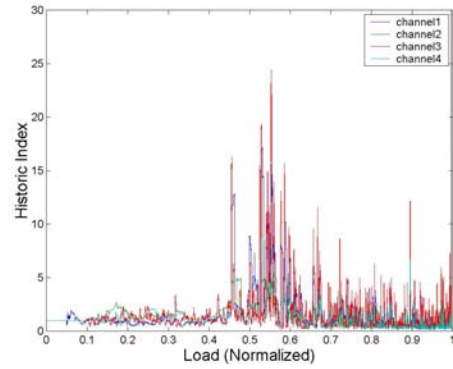
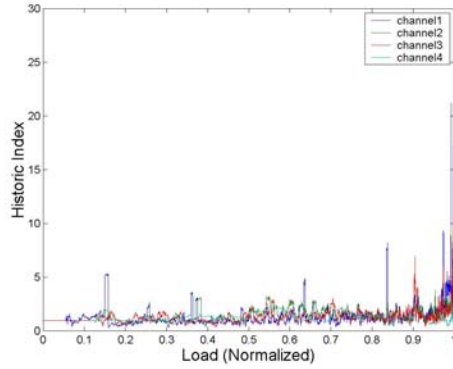
Tee1 (Bond/Glass/Vinyl Ester)



BHV1 (Buckling/Hybrid/Vinyl Ester)

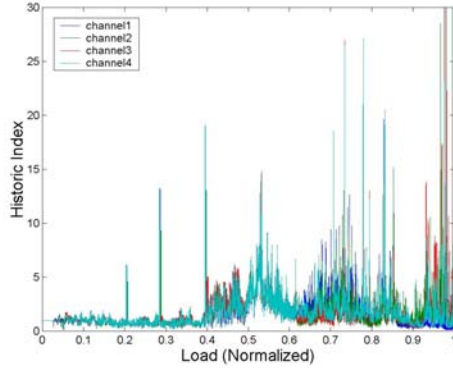
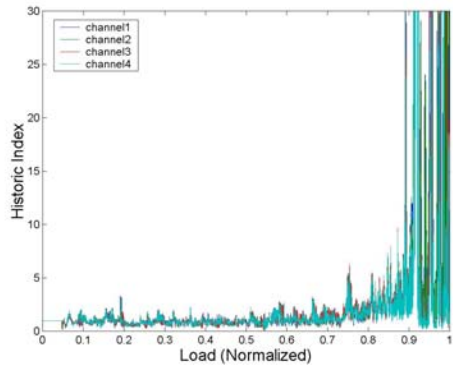
Figure 7.10 (cont'd): Cumulative Signal Strength vs. Load of Representative Specimens

Historic Index vs. Load



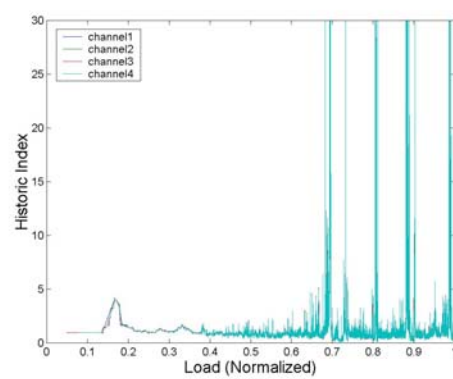
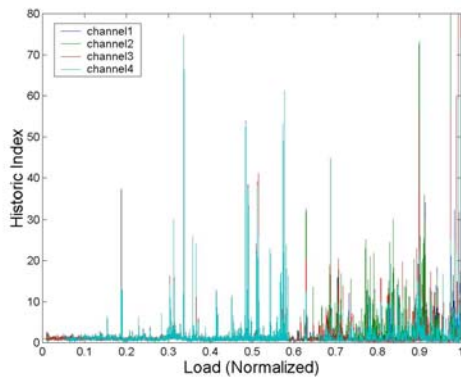
TGI2 (Transverse/Glass/Isophthalic)

TGV (Transverse/Glass/Vinyl Ester)



LGI1 (Longitudinal/Glass/Isophthalic)

LGV1 (Longitudinal/Glass/Vinyl Ester)

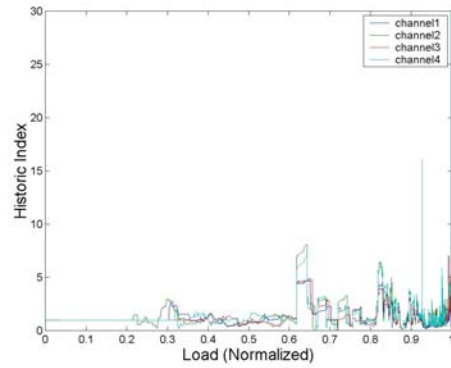
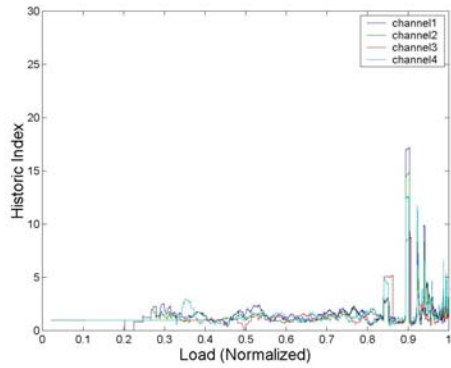


LHV (Longitudinal/Hybrid/Vinyl Ester)

FGV (Full-Scale/Glass/Vinyl Ester)

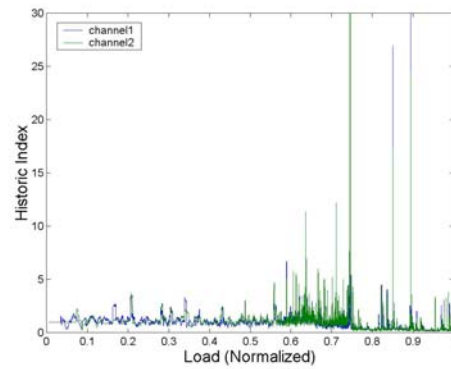
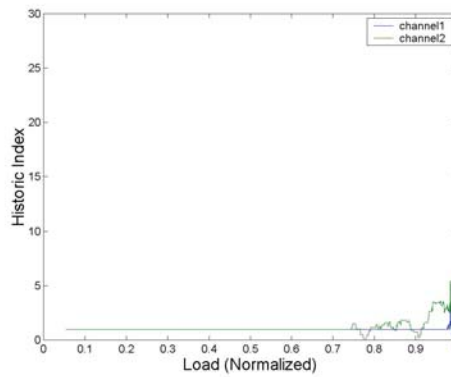
Figure 7.11: Historic Index vs. Load of Representative Specimens

Historic Index vs. Load



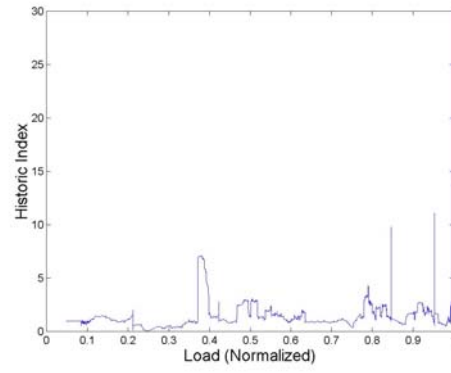
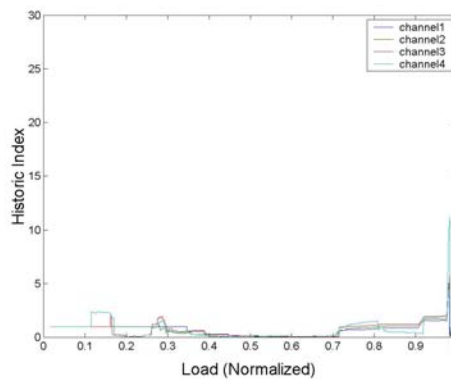
Chop (Chopped Glass/Vinyl Ester)

Wov (Woven Roving Glass/Vinyl Ester)



SGVI (Shear/Glass/Vinyl Ester)

SHVI (Shear/Hybrid/Vinyl Ester)

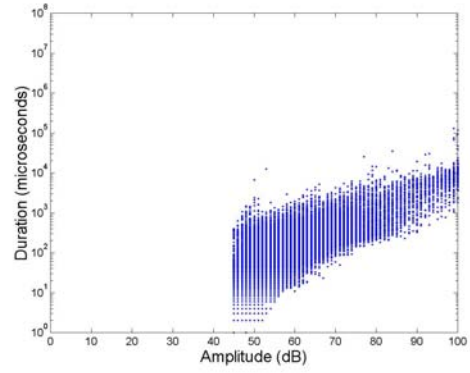
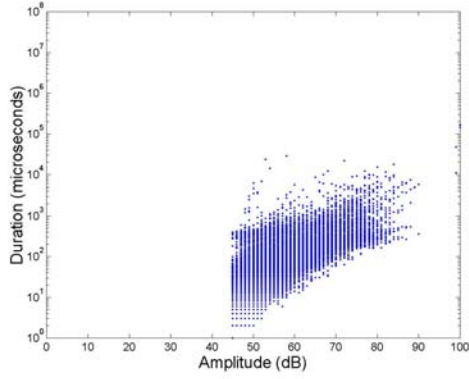


Tee1 (Bond/Glass/Vinyl Ester)

BHVI (Buckling/Hybrid/Vinyl Ester)

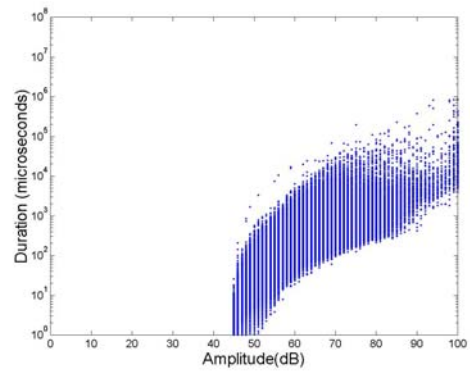
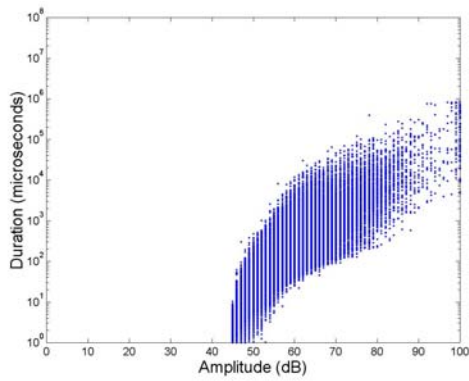
Figure 7.11 (cont'd): Historic Index vs. Load of Representative Specimens

Amplitude vs. Duration



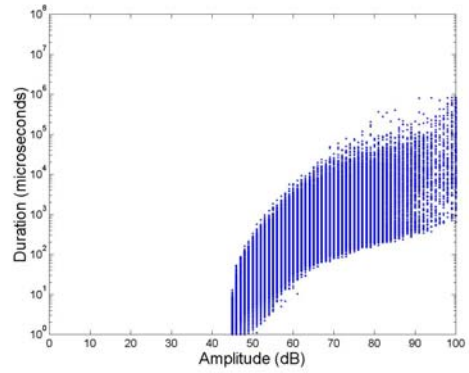
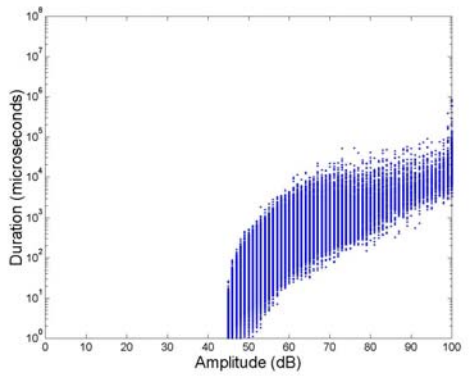
TGI2 (Transverse/Glass/Isophthalic)

TGV (Transverse/Glass/Vinyl Ester)



LGI1 (Longitudinal/Glass/Isophthalic)

LGV1 (Longitudinal/Glass/Vinyl Ester)

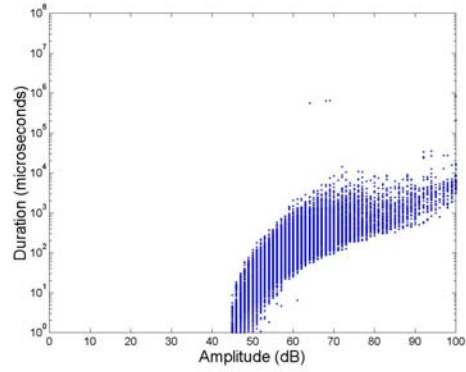
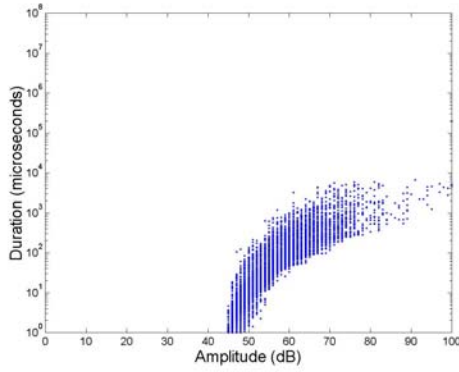


LHV (Longitudinal/Hybrid/Vinyl Ester)

FGV (Full-Scale/Glass/Vinyl Ester)

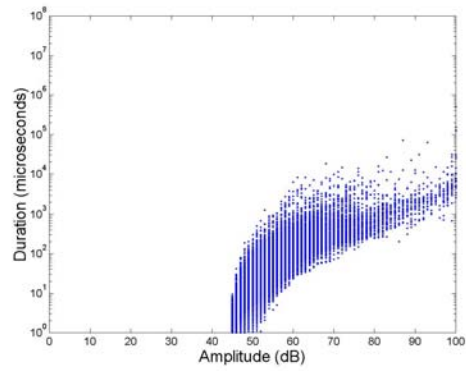
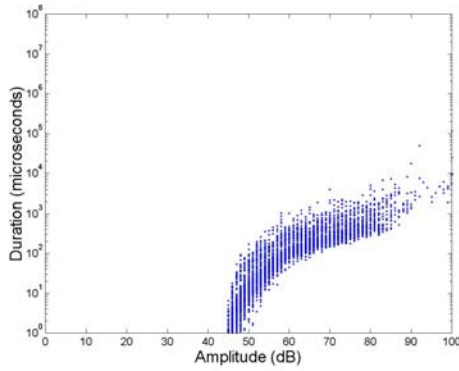
Figure 7.12: Amplitude vs. Duration of Representative Specimens

Amplitude vs. Duration



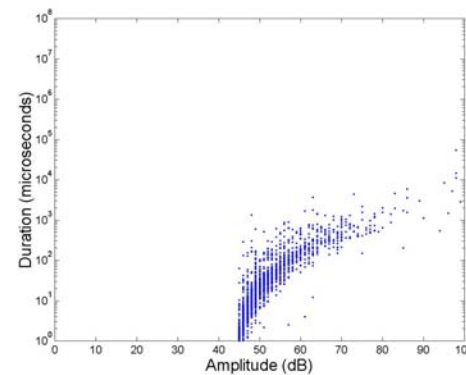
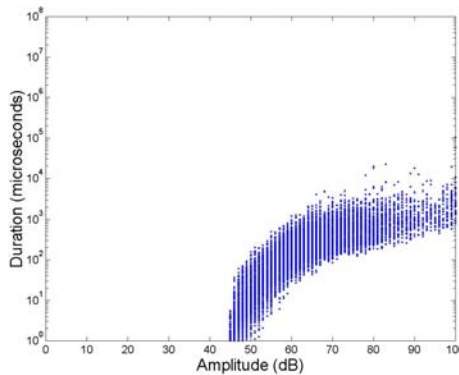
Chop (Chopped Glass/Vinyl Ester)

Wov (Woven Roving Glass/Vinyl Ester)



SGV1 (Shear/Glass/Vinyl Ester)

SHV1 (Shear/Hybrid/Vinyl Ester)

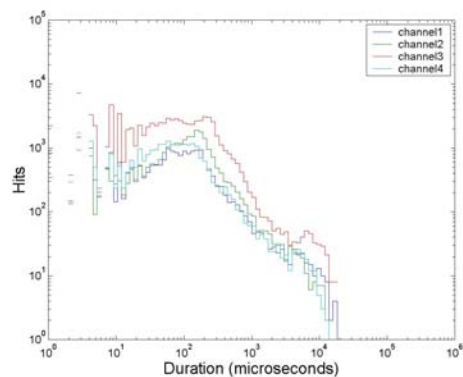
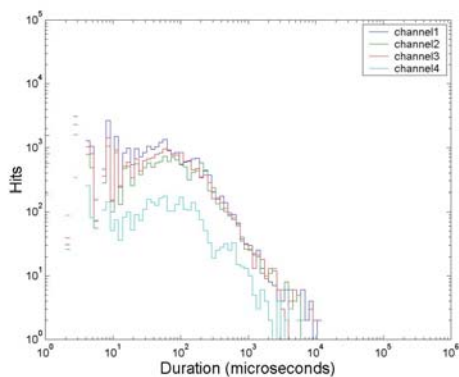


Tee1 (Bond/Glass/Vinyl Ester)

BHV1 (Buckling/Hybrid/Vinyl Ester)

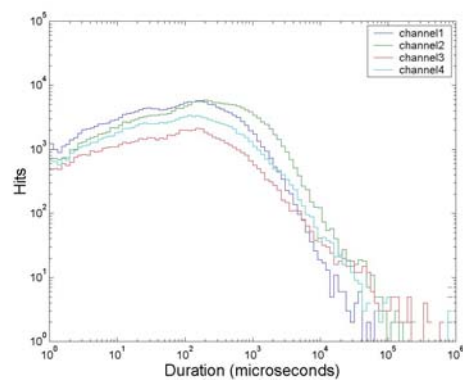
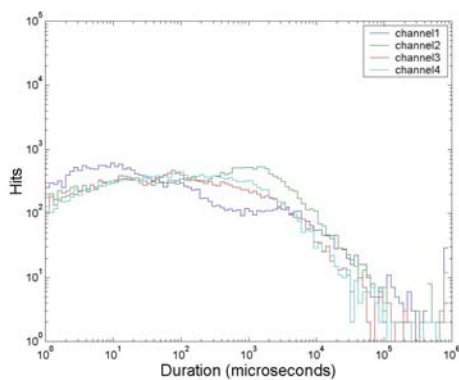
Figure 7.12 (cont'd): Amplitude vs. Duration of Representative Specimens

Duration Distribution



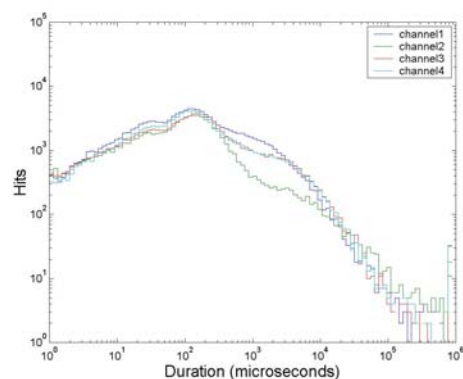
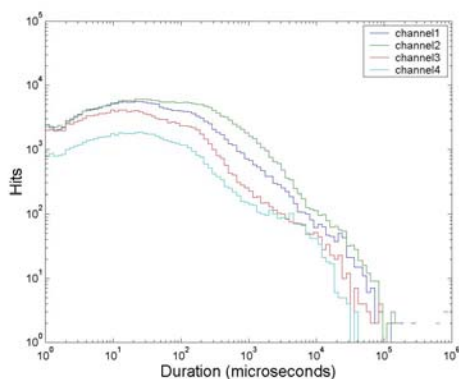
TGI2 (Transverse/Glass/Isopthalic)

TGV (Transverse/Glass/Vinyl Ester)



LGI1 (Longitudinal/Glass/Isopthalic)

LGV1 (Longitudinal/Glass/Vinyl Ester)

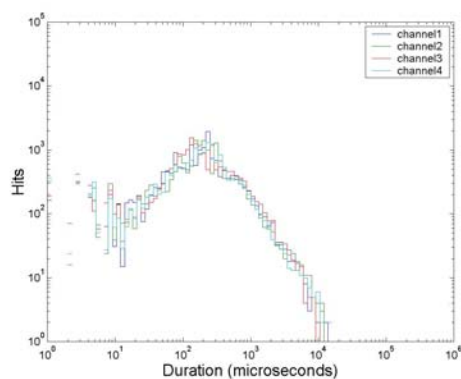
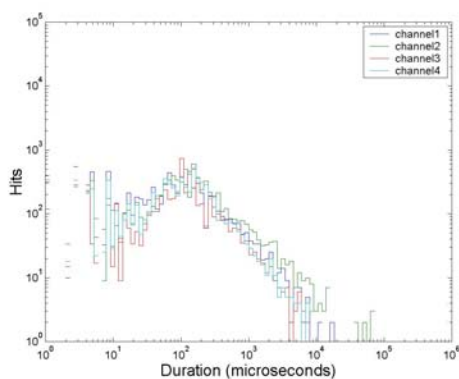


LHV (Longitudinal/Hybrid/Vinyl Ester)

FGV (Full-Scale/Glass/Vinyl Ester)

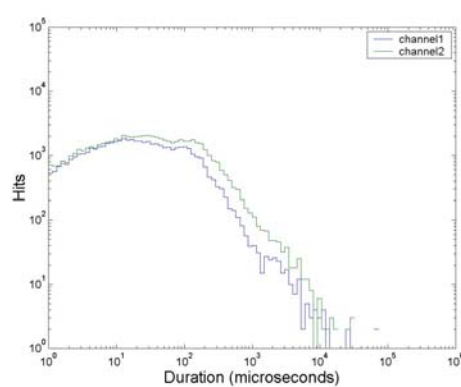
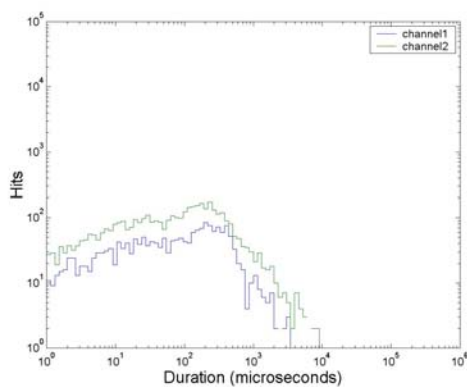
Figure 7.13: Duration Distribution of Representative Specimens

Duration Distribution



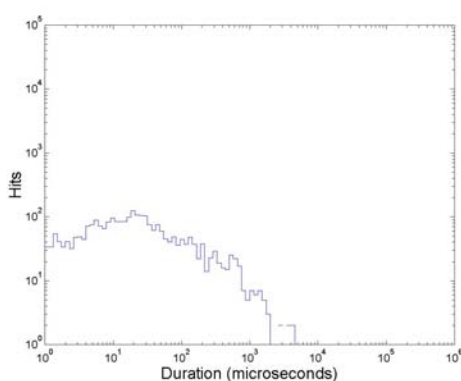
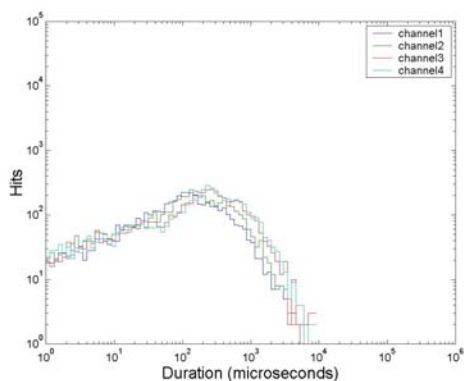
Chop (Chopped Glass/Vinyl Ester)

Wov (Woven Roving Glass/Vinyl Ester)



SGV1 (Shear/Glass/Vinyl Ester)

SHV1 (Shear/Hybrid/Vinyl Ester)

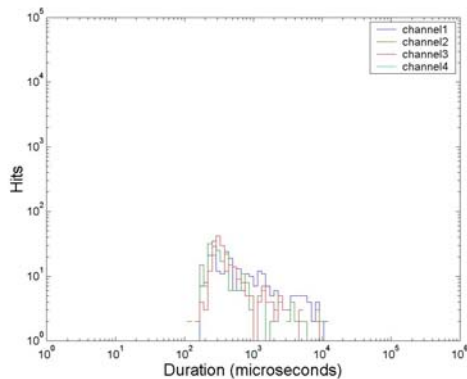


Tee1 (Bond/Glass/Vinyl Ester)

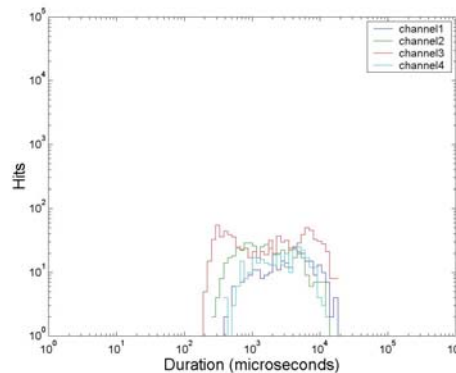
BHV1 (Buckling/Hybrid/Vinyl Ester)

Figure 7.13 (cont'd): Duration Distribution of Representative Specimens

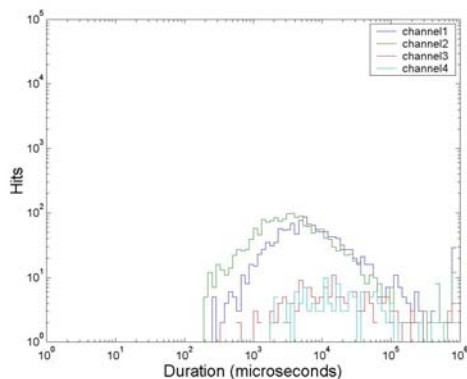
Duration Distribution of High Amplitude Hits



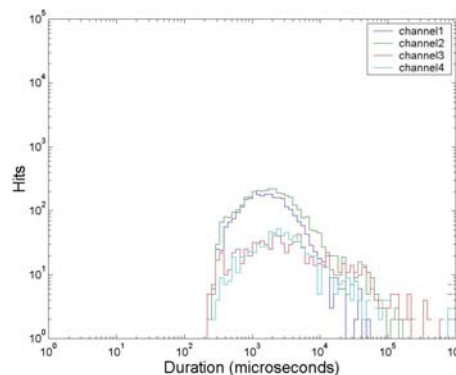
TGI2 (Transverse/Glass/Isopthalic)



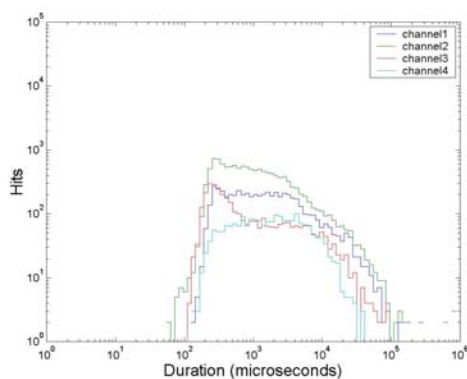
TGV (Transverse/Glass/Vinyl Ester)



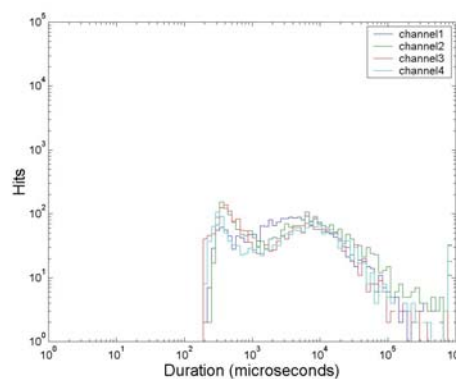
LGI1 (Longitudinal/Glass/Isopthalic)



LGV1 (Longitudinal/Glass/Vinyl Ester)



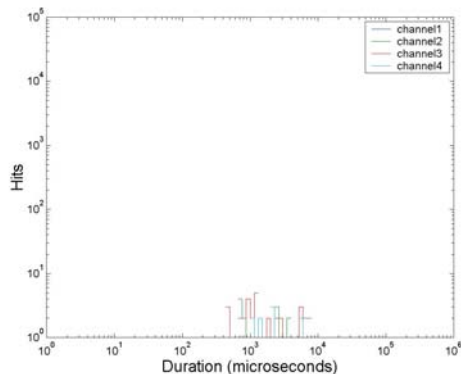
LHV (Longitudinal/Hybrid/Vinyl Ester)



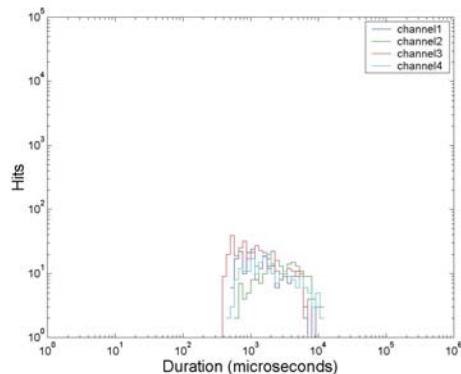
FGV (Full-Scale/Glass/Vinyl Ester)

Figure 7.14: Duration Distribution of High Amplitude Hits of Representative Specimens

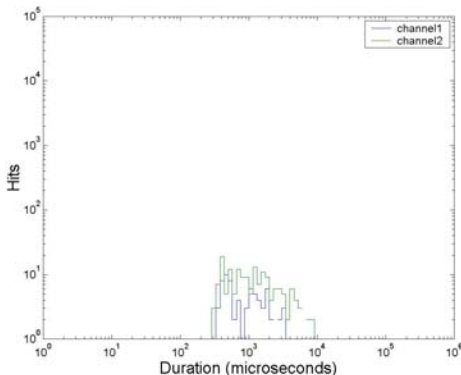
Duration Distribution of High Amplitude Hits



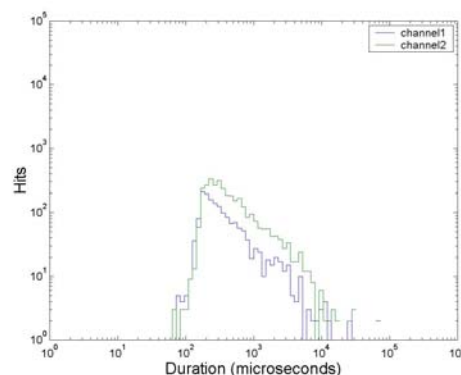
Chop (Chopped Glass/Vinyl Ester)



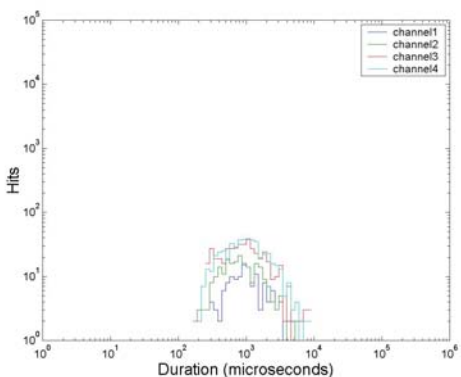
Wov (Woven Roving Glass/Vinyl Ester)



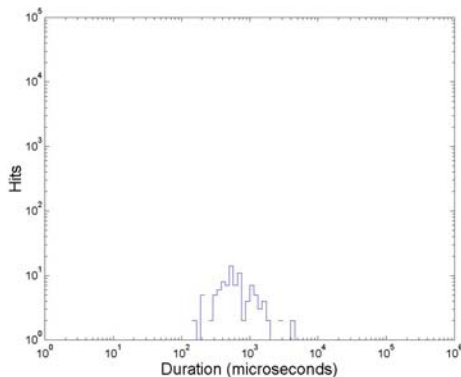
SGV1 (Shear/Glass/Vinyl Ester)



SHV1 (Shear/Hybrid/Vinyl Ester)



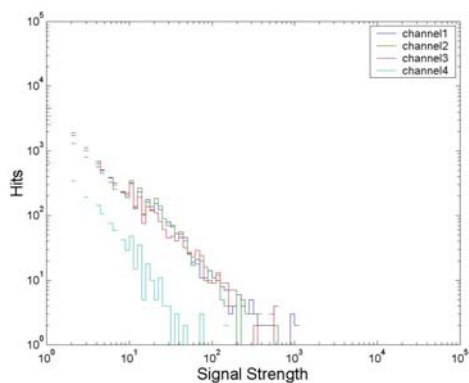
Tee1 (Bond/Glass/Vinyl Ester)



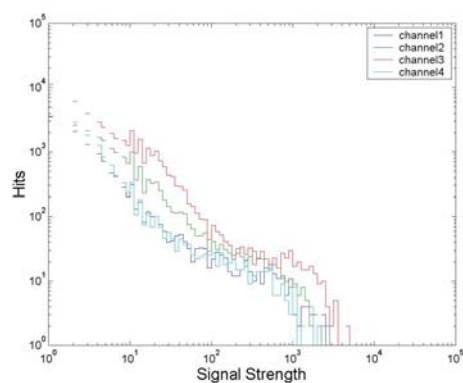
BHV1 (Buckling/Hybrid/Vinyl Ester)

Figure 7.14 (cont'd): Duration Distribution of High Amplitude Hits of Representative Specimens

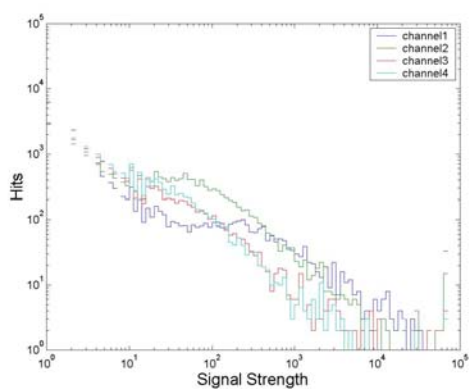
Signal Strength Distribution



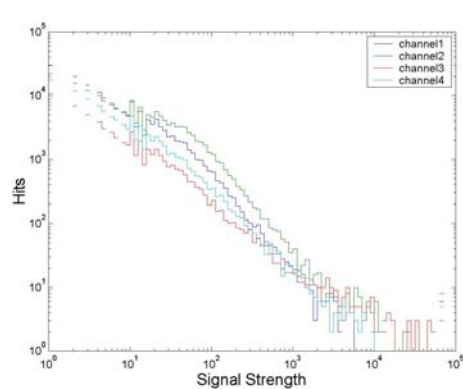
TGI2 (Transverse/Glass/Isophthalic)



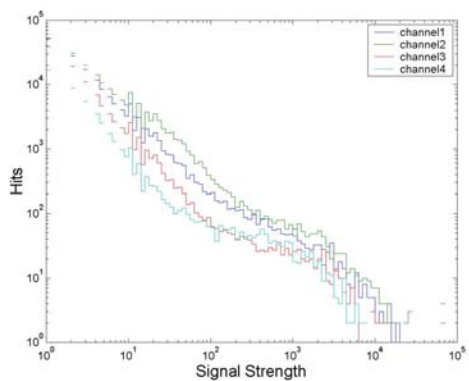
TGV (Transverse/Glass/Vinyl Ester)



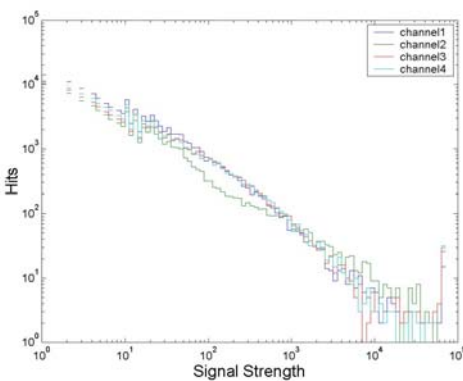
LGI1 (Longitudinal/Glass/Isophthalic)



LGV1 (Longitudinal/Glass/Vinyl Ester)



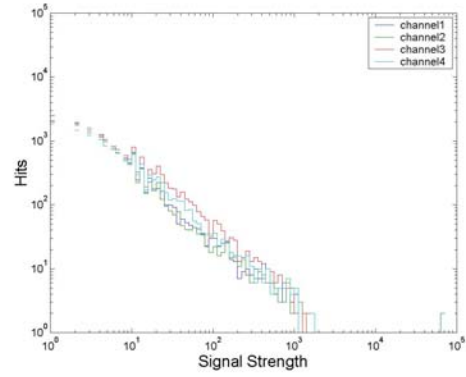
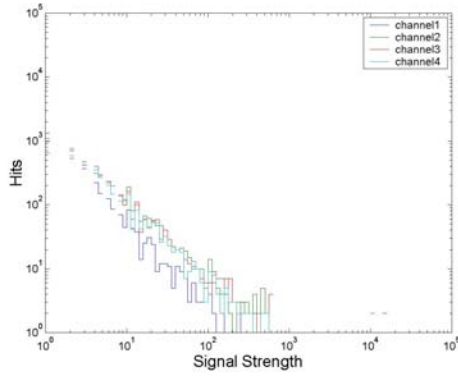
LHV (Longitudinal/Hybrid/Vinyl Ester)



FGV (Full-Scale/Glass/Vinyl Ester)

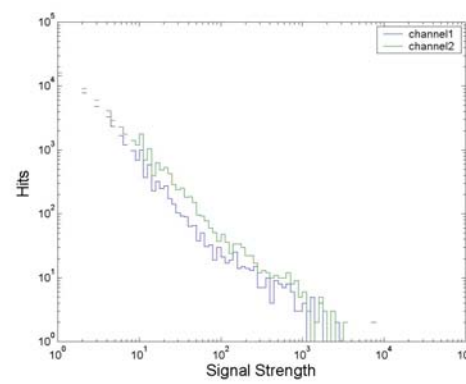
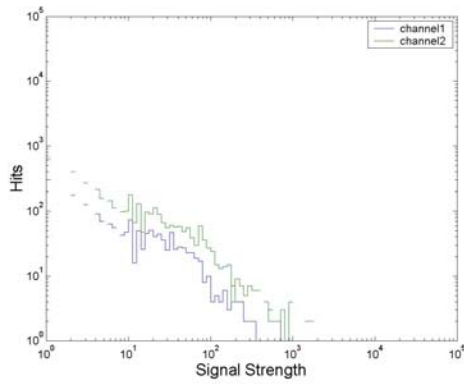
Figure 7.15: Signal Strength Distribution of Representative Specimens

Signal Strength Distribution



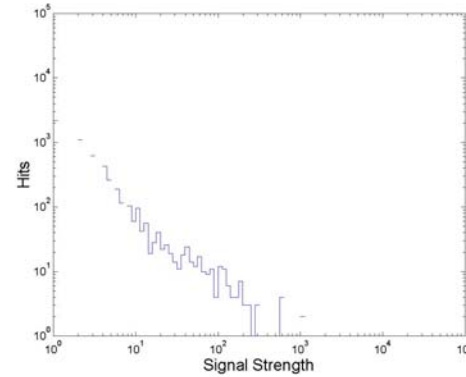
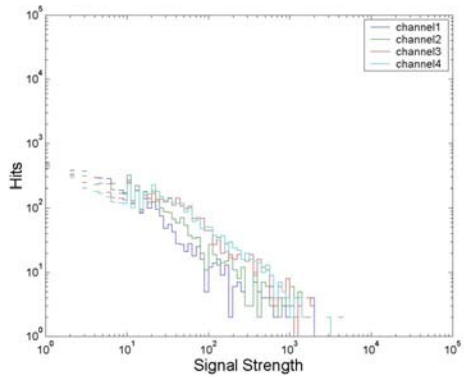
Chop (Chopped Glass/Vinyl Ester)

Wov (Woven Roving Glass/Vinyl Ester)



SGV1 (Shear/Glass/Vinyl Ester)

SHV1 (Shear/Hybrid/Vinyl Ester)

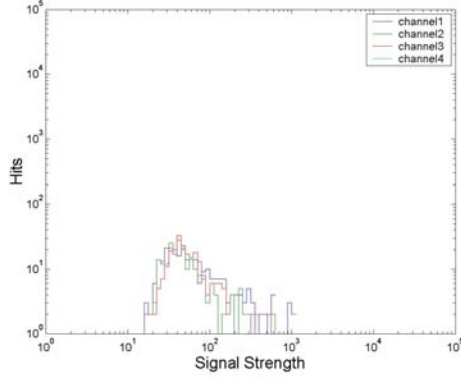


Tee1 (Bond/Glass/Vinyl Ester)

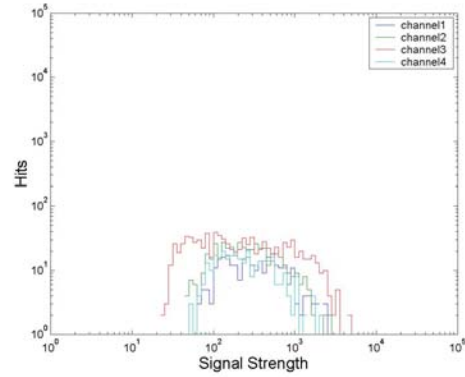
BHV1 (Buckling/Hybrid/Vinyl Ester)

Figure 7.15 (cont'd): Signal Strength Distribution of Representative Specimens

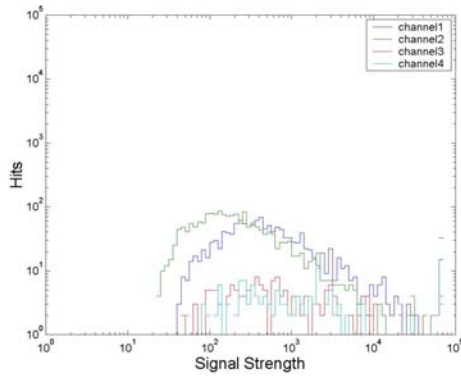
Signal Strength Distribution of High Amplitude Hits



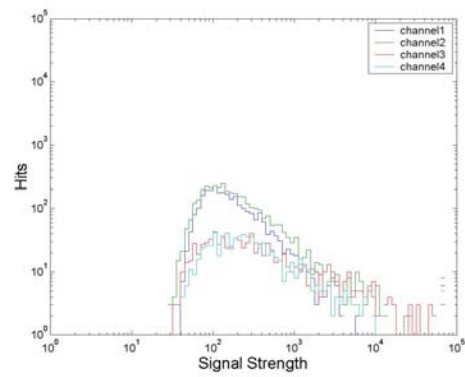
TGI2 (Transverse/Glass/Isopthalic)



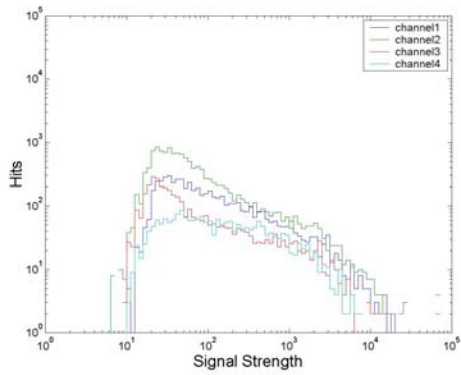
TGV (Transverse/Glass/Vinyl Ester)



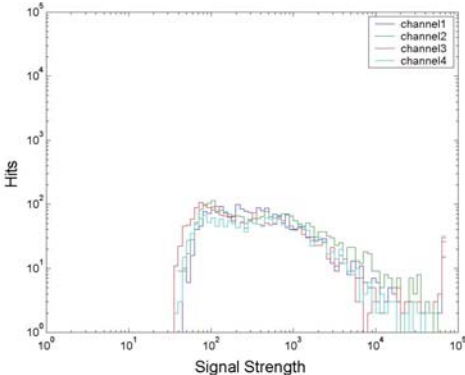
LGI1 (Longitudinal/Glass/Isopthalic)



LGV1 (Longitudinal/Glass/Vinyl Ester)



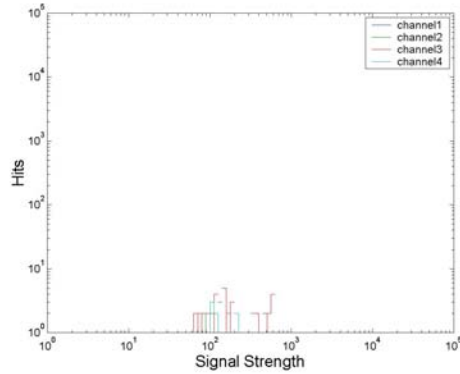
LHV (Longitudinal/Hybrid/Vinyl Ester)



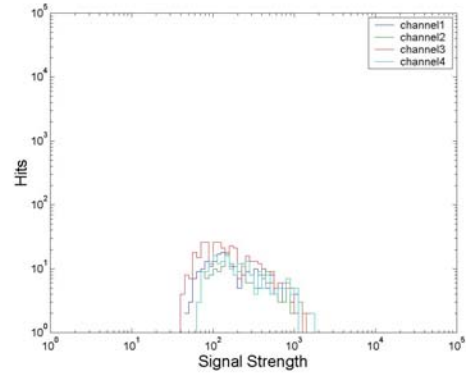
FGV (Full-Scale/Glass/Vinyl Ester)

Figure 7.16: Signal Strength Distribution of High Amplitude Hits of Representative Specimens

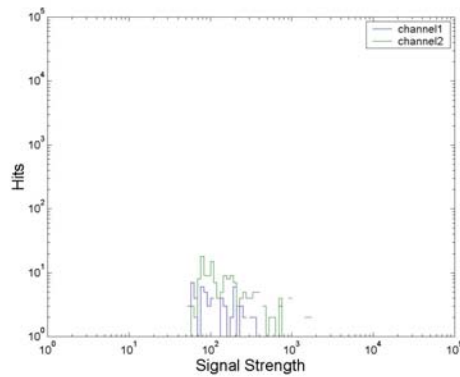
Signal Strength Distribution of High Amplitude Hits



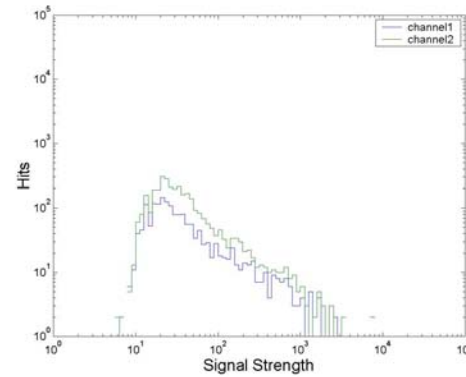
Chop (Chopped Glass/Vinyl Ester)



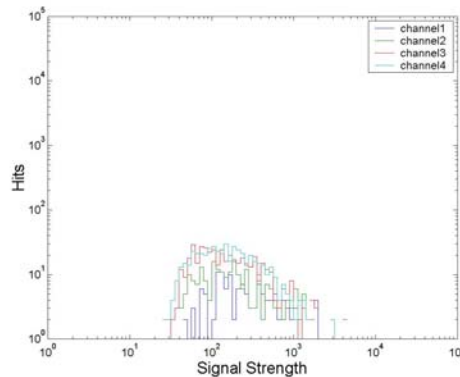
Wov (Woven Roving Glass/Vinyl Ester)



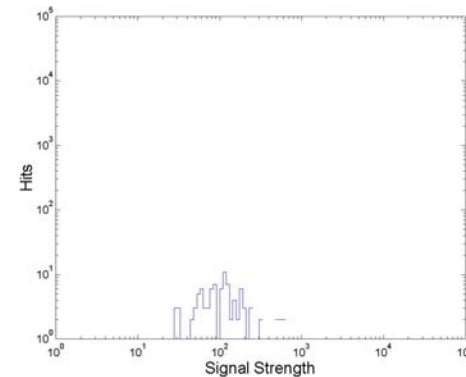
SGV1 (Shear/Glass/Vinyl Ester)



SHV1 (Shear/Hybrid/Vinyl Ester)



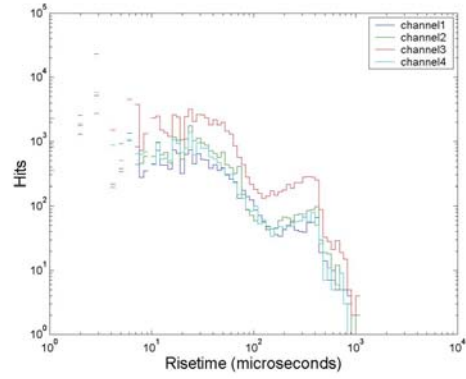
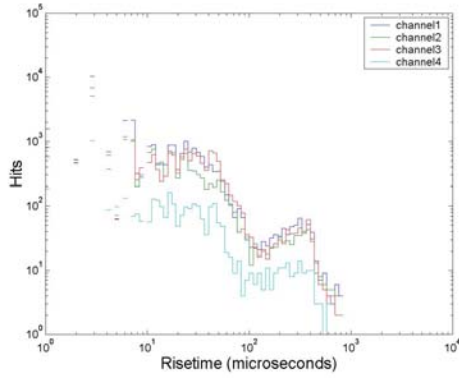
Tee1 (Bond/Glass/Vinyl Ester)



BHV1 (Buckling/Hybrid/Vinyl Ester)

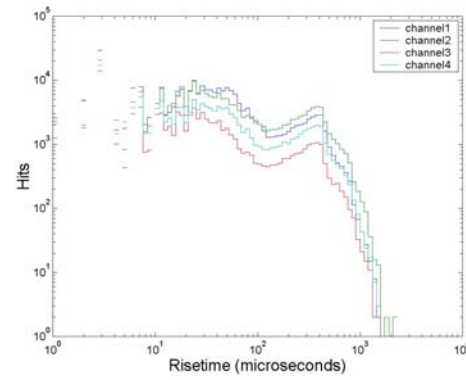
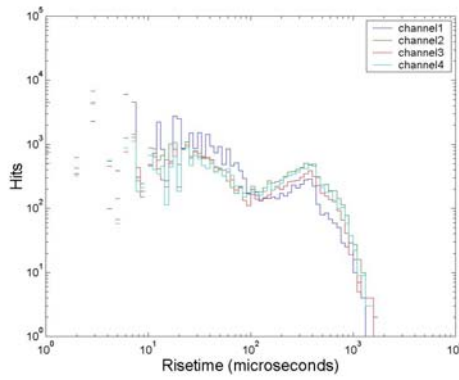
Figure 7.16 (cont'd): Signal Strength Distribution of High Amplitude Hits of Representative Specimens

Rise Time Distribution



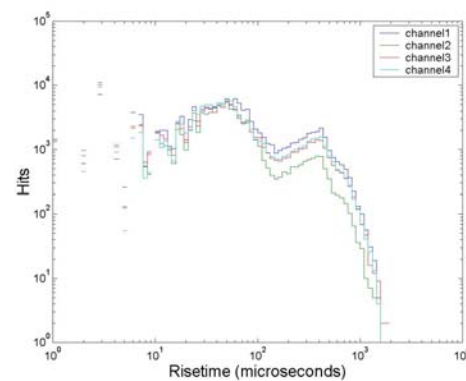
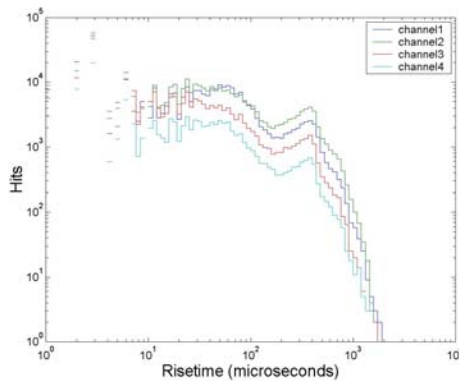
TGI2 (Transverse/Glass/Isopthalic)

TGV (Transverse/Glass/Vinyl Ester)



LGI1 (Longitudinal/Glass/Isopthalic)

LGVI (Longitudinal/Glass/Vinyl Ester)

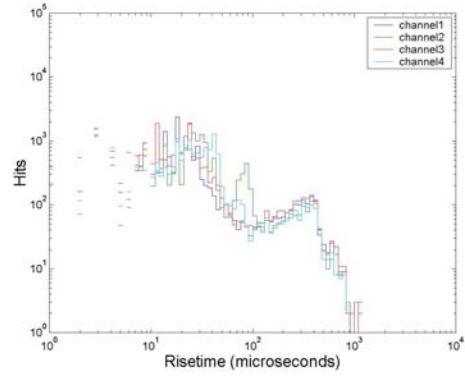
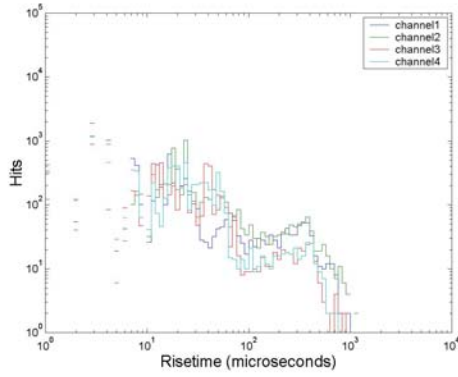


LHV (Longitudinal/Hybrid/Vinyl Ester)

FGV (Full-Scale/Glass/Vinyl Ester)

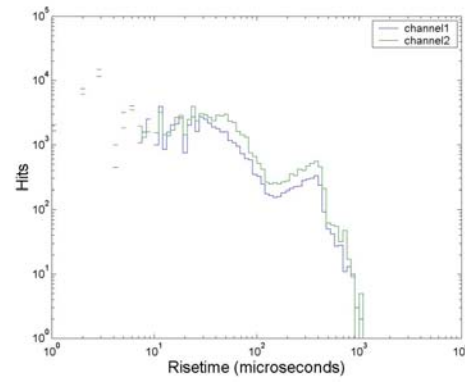
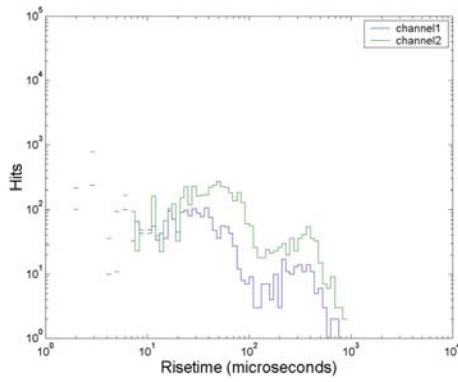
Figure 7.17: Rise Time Distribution of Representative Specimens

Rise Time Distribution



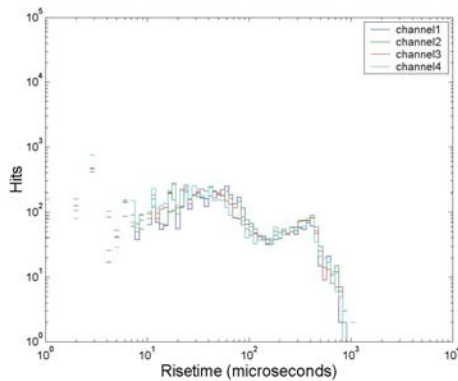
Chop (Chopped Glass/Vinyl Ester)

Wov (Woven Roving Glass/Vinyl Ester)



SGV1 (Shear/Glass/Vinyl Ester)

SHV1 (Shear/Hybrid/Vinyl Ester)



N.A.

Tee1 (Bond/Glass/Vinyl Ester)

BHV1 (Buckling/Hybrid/Vinyl Ester)

Figure 7.17 (cont'd): Rise Time Distribution of Representative Specimens

7.3 DISCUSSION

The details of each type of plot are presented in this section starting from the stress vs. strain plots of representative specimens.

7.3.1 Stress vs. Strain (Fig. 7.3)

Undamaged FRP generally is associated with a linear stress vs. strain relationship. Departure from linearity is an indication of an onset of damage during the test.

Specimens TGI2 (trasverse/glass/iso) and TGV (transverse/glass/vinyl ester) have a bilinear curve. The first portion of the curve has a higher modulus than the second portion. The departure from the linearity of the first portion of specimen TGI2 is at 28% of the ultimate load, while it is at 33% of the ultimate load for specimen TGV. The departure from the linearity of these two specimens is believed to be caused by matrix cracking and debonding of the unidirectional fiber layers, which were stressed perpendicular to the fiber direction. This leaves only chopped strand fiber layers to carry the entire load.

For tension specimens, subjected to applied stress parallel to the fiber direction, the stress vs. strain curves are close to linear. This is because when a fiber is broken, the stress can be redistributed to the adjacent fibers or matrix causing less damage propagation. The plot of specimen LGI1 (longitudinal/glass/iso) exhibits a departure from linearity at 80% of the ultimate load. This characteristic is similar to specimen FGI, which is a full-scale version of this type of test. Specimens LGV1 (longitudinal/glass/vinyl ester) and FGV (full scale/glass/vinyl ester) exhibit a departure from linearity at a lower range of 30% to 50% of the ultimate load. The lower departure points of these vinyl ester

specimens compared to that of specimen LGI1 is referred to the resin type of the specimen. Vinyl ester resin in specimens LGV1 and FGV is more flexible, allowing more fiber to break before failure. For specimen LHV, its linearity departure is at 75% of the ultimate load, whereas the fiber breaks are found to occur from 30% of the ultimate load (see Chapter 4). This is because the specimen is partly made of carbon fibers, which have much smaller diameter than glass fibers. As a result, there is a higher number of fibers per unit area in the cross section of hybrid specimen than in a glass specimen. This cross section area does not decrease much compared to a glass specimen with the same number of fiber breaks.

Specimen SGV, in which delamination plays an important role during the test, shows linearity of the plot until 98% to 100% of the ultimate load or until the delamination is observed. This characteristic is similar to that of specimen SGI1 (not shown in the figure). Also, specimen SHV1 (hybrid) maintains the linearity of the plot until the first delamination is observed. A unique characteristic of this hybrid specimen is that the specimen can carry more stress with a slightly lower stiffness after the first delamination occurs. It can even carry more stress after the second delamination occurs in some specimens.

The stress vs. strain plot of specimen Chop is linear at the beginning and becomes nonlinear after 30% of the ultimate load. Specimen Wov behaves in the same manner, except its departure from linearity is at 22% of the ultimate load. This is because the wavy fibers in woven roving are ineffective to take much of the initial stress. This allows chopped strand fiber layers in the specimen to take the major portion of the stress. At the end of the test, when the woven roving fibers are straightened up, the specimen becomes stiffer and the stress is transferred from chopped strand fibers to the woven roving fibers. This is indicated by the sharp rise at the end of the plot of specimen Wov.

The strains are not measured during the test of specimens Tee1 and BHV1. This is because the nature of the test setups is too complicated. Also, the strains are not related to the failure plane of the specimens.

Within the same type of testing (e.g. longitudinal, transverse or short beam shear), hybrid specimens always exhibit higher elastic modulus than glass specimens. This is attributed to the carbon fibers in the specimen, which have much higher elastic modulus than that of glass fibers.

7.3.2 Amplitude vs. Time or Load (Fig. 7.4)

This type of plot generally tells the rates of AE hits of different amplitudes during the test. The rates of hits are shown by the color of the plot, which range from a lowest (green) to the highest (red) rate emission. All the plots except the plot of specimen BHV1 are generated by Vtrnsmon software. A stepwise loading is applied to specimen BHV1. Therefore, a plot of amplitude vs. load is generated for this specimen so that the visual observation of the plot can be done more easily.

Specimen TGI2 (transverse/glass/iso) has a gradually increasing rate and amplitude hits. This is referred to the characteristics of matrix cracking/debonding mechanisms of this type of specimen. Specimen TGV, which has the same stress orientation but is made from vinyl ester resin, exhibits the same behavior until 45% of the ultimate load. Then, the plot is observed as a superposition of the plot of specimen TGI2 and a consistent rate of high amplitude hits. This is due to the effect of flexible vinyl ester resin, which allows the specimen to elongate more leading to more breaking of the brittle fibers.

As discussed in Chapter 4, the plots of specimens LGI1, LGV1, LHV, and FGV consist of two parts. The first part involves low amplitude with an

increasing rate of hits. This part is found to be associated with matrix cracking. The second part involves high amplitude hits and is proved to be related to matrix cracking/ debonding/ delamination/ fiber breakage. This part is also associated with the observed cracks at the end of the narrow section of the dog-bone specimens. High amplitude hits in specimen LGV1 occur earlier than those of specimen LGI1. This is also due to the effect of flexible vinyl ester resin, which permits a higher strain in the specimen leading to more breaking of the brittle fibers. High amplitude hits in specimen LHV begin even earlier than in specimen LGV1. This is due to the carbon fibers in specimen LHV. The carbon fibers are very brittle and susceptible to having imperfections introduced during the fabrication process. This causes premature fiber breaks during the test.

When comparing the low-amplitude part of specimens LGV1 and FGV plots, it is found that number of hits from coupon specimen LGV1 is higher than full-scale specimen FGV. This is because the coupon specimens are smaller and can increase the chance of detecting reflected signals. The full-scale specimens permit signals to travel further so that they are attenuated before being reflected back to the AE sensor.

Specimens SGV1, SHV1, and Tee1 are subjected to delamination failures. The glass specimens in this series yield lower numbers of AE hits compared to the specimens made of the same materials but dominated by different failure mechanisms. Also, the glass specimens (SGV1 and Tee1) have a very sudden failure, which involves a high number of hits from low to high amplitudes. The hybrid specimen subjected to the delamination failure shows many more hits than the glass specimens. This is shown in the plot as a band of green area from 0 to approximately 500 seconds. This band covers a range of amplitudes from 40 dB to approximately 75 dB. Near the time of the first delamination crack, a rapid increase of high amplitude (up to 100 dB) and low amplitude hits can be seen

(shown as the red and orange band in the plot). This band continues through the second and the third occurrences of the delamination cracks.

Specimen Chop has a gradually increasing rate and amplitude of hits. However, the hit amplitudes are below 60 dB until approaching failure. At this point, the high amplitude hits, as well as a significant number of low amplitude hits, occur suddenly. When compared with specimen LGV1 (made of the same resin but with unidirectional fibers), specimen Chop begins to exhibit high amplitude hits when the load is closer to failure than specimen LGV1. This is because the chopped fibers in specimen Chop are much shorter than the unidirectional fibers in specimen LGV1 causing less friction between the fiber-matrix interface. Therefore, the fibers are less likely to break by tension but rather experience the fiber pullout mechanism. Also, the chopped fibers in specimen Chop are randomly oriented. The fibers are less likely to undergo axial tension and, therefore, are less likely to break.

Specimen Wov also has a gradually increasing rate and amplitude of hits as similar to specimen Chop. This is because the main part of specimen Wov consists of chopped strand fibers. However, high amplitude hits of specimen Wov start earlier than those of specimen Chop. This is because specimen Wov also consists of some continuous fibers oriented longitudinally to the applied stress. This can cause some fiber breaks even though the fibers are wavy. Near the end of the test, these continuous-but-wavy fibers are straightened up and a great portion of the load is redistributed to these fibers. This leads to more fiber breaks at failure.

7.3.3 Amplitude Distribution (Fig. 7.5)

Many researchers have used this type of plot for AE signature analysis. The plot may show one or more “humps”, each of which is believed to be

representative of a certain failure mechanism. The amplitude at the peak of the hump is the criteria for the AE signature.

The figure shows that the plots of a specimen show a constant profile for all sensors, which means that attenuation does not have a big effect on the slopes of the plot. However, the peaks of the plot of different sensors sometimes are located at different amplitude levels. This shows that the slopes of the amplitude distribution are a good indicator of a particular failure mechanism, regardless of the distance of the sensor from the source, a feature that can be used by the neural network analysis. An example of this is the plot of specimen LGI1. The first peak of this specimen is located at approximately 45 dB to 50 dB for all sensors. The second peak is located at 60 dB for sensors 3 and 4, while it is approximately at 70 dB to 80 dB for sensors 1 and 2. The visual inspection found that the failure site of this specimen is located much closer to sensors 1 and 2 than to sensors 3 and 4. It is possible that the differing amplitude of the peaks is due to the effect of attenuation, reflecting the different distances of the sensors from the source. This may affect the accuracy of using only the peak amplitude of these plots as the criteria for AE signature.

It is shown from the plot of specimen TGI2 that sensor 4 has a different shape than the rest of the sensors. This is due to the low sensitivity of sensor 4, which may be from a poor mounting on the specimen.

7.3.4 Progression of Amplitude Distribution (Figure 7.6)

These plots are a series of amplitude distribution plots of the representative specimens from 20% to the ultimate load (at a 20% load interval). Sensor 1 is selected to use for all specimens except specimen Chop. This is because sensor 1 of specimen Chop is located too far away from the failure site.

For specimens TGI2 (transverse/ glass/ iso) and TGV (transverse/ glass/ vinyl ester), the plot is quite linear at the beginning and starts to have a deviation from linearity in the range of mid to high amplitudes at a higher load. The deviation from linearity is speculated to be associated with the fiber break mechanism. This is because of two reasons.

1. The deviation from linearity covers the mid to high amplitude range of the plot. High amplitude hits are found to be an indication of fiber breaks.
2. The deviation from linearity of the amplitude distribution plot starts to occur at the same load level as the onset of high amplitude hits from the amplitude vs. load plot

Specimens LGI1, LGV1, and LHV, which are tension specimens tested parallel to the fiber direction, exhibit linear plots at the beginning of the test as well. The deviation from linearity occurs at the higher load, which covers the range of mid to high amplitudes. After comparing with the amplitude vs. load plot, this deviation from linearity of the amplitude distribution plot is also proven to be associated with the fiber break mechanism.

For specimens Chop and Wov, the beginning of the plots are not quite linear, but the shape of the plots are almost the same once the load is increased. The abrupt change in the shape of the plot is also a contribution of the fiber break mechanism (as compared with amplitude vs. load plots). This abrupt change occurs at almost the ultimate load of specimen Chop, while it starts to occur at 80% of the ultimate load of specimen Wov.

Specimen BHV1 (buckling/hybrid/vinyl ester) exhibits a linear plot at the beginning of the test until 80% of the ultimate load. At the ultimate load, the shape of the plot is observed as bilinear. This can be also a contribution of the fiber break mechanism.

It is also interesting to compare the plots of specimen LGV1 with specimen FGV. Both specimens are made of the same materials, but the sizes of the specimens are different. The plots of the full-scale specimen (FGV) from 40 dB to 70 dB are flat at the beginning of the test (20% and 40% of the ultimate load), while the plots of the coupon specimen (LGV1) at the same amplitude range and the same load levels are inclined. This is due to the contribution of reflected signals in the coupon specimen. The reflected signals travel in shorter distances in the coupon specimen, experiencing less attenuation. The amplitude of the reflected signal is low due to some attenuation in the coupon, but enough to pass the amplitude threshold of the AE instrument. This results in a higher number of the low amplitude hits than the high amplitude hits, making the plot inclined. In contrast, the reflected signals traveling in the full-scale specimen experience more attenuation. The attenuation reduces the amplitude of the reflected signals until the signals cannot be detected by the AE instrument.

7.3.5 Cumulative Amplitude Distribution (Figure 7.7)

Many researchers have used the slope of the cumulative amplitude distribution plot (b-value) for AE signature analysis. It is believed that the plot of a single failure mechanism should be linear and the slope of the plot should be different than that of other failure mechanisms. In addition, a bi-linear plot is an indication of two failure mechanisms occurring during the test.

It is noticed from the plots that the slopes of the plots are very consistent for all sensors. An example of this consistency is the plot of specimen LHV. The plots of this specimen basically are bi-linear. The slopes of each linear portion are similar for all sensors. This proves that the slope of the plot is independent of the source-to-sensor distance (attenuation), and also proves that the slope of the plot can be a suitable parameter for AE signature analysis.

Unlike the slope of the plot, the changing points from the first linear portion to another are located at different amplitudes for different sensors (see also the plot of specimen LHV). Therefore, it is concluded that the changing point is dependent to the source-to-sensor distance (attenuation), and should not be used for AE signature analysis.

The plots in this figure represent cumulative amplitude distributions at the ultimate load of the representative specimens. It is observed with SEM that there are many failure mechanisms occurring in the specimens when the load is approaching failure. This is the reason the plot is made up of more than one line in all cases. Accordingly, it is more convenient to observe the slope (b-value) at a lower load level, where the number of failure mechanisms is limited to only one or two.

The plots in Figure 7.8 show the progression of the cumulative amplitude distributions from 20% to the ultimate load. These plots at low load levels (e.g. 20% and 40%) will be focused on for the AE signature analysis. The discussion of the slope (b-value) at these load levels will be provided in the next section.

7.3.6 Progression of Cumulative Amplitude Distribution (Figure 7.8)

The slope value, or b-value, is provided above each plot. An example of how this number is calculated is shown in Fig. 7.18, which is the plot of specimen TGV.

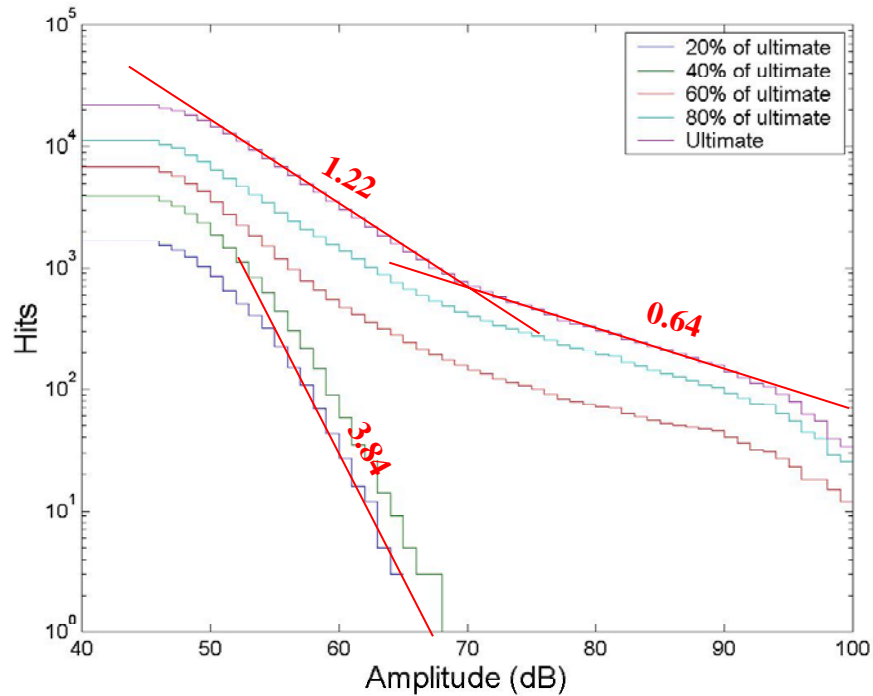


Figure 7.18 : Example of How to Calculate the *b*-Value, or Slope, of the Cumulative Amplitude Distribution Plot

As discussed in Chapter 4, the AE hits from the beginning of the tension test perpendicular to the fiber direction are found to be associated with matrix cracking. This covers the range from 0% to the first occurrence of high amplitude hits. The cumulative amplitude distributions during this period respond as straight lines (see the plots of 0% to 60% of the ultimate load for specimen LG11, 0% to 40% of the ultimate for specimen LGV1, and 0% to 20% of the ultimate load for specimen LHV). The slopes of the lines fall between 2.31 to 3.0. To be specific, the slope is 2.31 for the isophthalic polyester specimen, while it is 2.5 to 3.0 for the vinyl ester specimen.

The full-scale specimen FGV and the coupon specimen LGV are made of the same material, and are subjected to the same stress orientation. However, it is observed that the plots of both specimens are quite different. As discussed earlier, this difference is due to the contribution of the reflected signals in the coupon specimen. For the purpose of this analysis, only plots of the coupon specimens will be focused upon. This is because the majority of the specimens tested in the research program are coupon specimens.

As discussed in Chapter 5, the AE hits from the beginning of the tension test perpendicular to the fiber direction are found to be associated with matrix cracking/ debonding. This dominates the data from 0% to the first occurrence of high amplitude hits. The cumulative amplitude distributions during this period also exhibit as straight lines (see the plots of 20% to 40% of the ultimate load for specimens TGI2 and TGV). The slopes of the lines vary from 3.3 for isophthalic polyester resin to 3.84 for vinyl ester resin.

For delamination specimens SGV1 and Tee1 (glass fibers), the slope of the 20% to 80% plots ranges consistently from 1.04 to 1.50. Specimen SHV1 experiences carbon fiber breaks at the very beginning of the test (see Chapter 5). The plot of this specimen corresponds with a bi-linear plot. The slopes of the first and second linear portions are 1.36 and 2.76, respectively.

Fiber breaks are found to be involved in all specimens. The fiber breaks usually occur in the later stage of the test and are associated with high amplitude hits. When the fiber breaks occur, the cumulative amplitude distribution plots generally correspond with the reduction of the slope at the high amplitude range. This slope is found to be lower than 1.24.

Table 7.3 summarized the slope or b-value of the cumulative amplitude distribution plot and its corresponding failure mechanisms. The value is based on the results of only coupon specimen testing. It is interesting that the table shows

the different range of b-value for different type of failure mechanism with almost no overlap.

Table 7.3: Summary of b-Values of Failure Mechanisms Found in Research Program

Failure mechanism	b-value
Matrix cracking	2.3-3.0
Matrix cracking/ debonding	3.3-3.84
Delamination (only for glass fibers)	1.04-1.50
Fiber breakage involvement	< 1.24 in high amplitude zone

7.3.7 Cumulative Hits vs. Load, Cumulative Signal Strength vs. Load, and Historic Index vs. Load (Figures 7.9, 7.10, and 7.11)

These three plots have been used by many researchers for finding the “knee” or the onset of significant damage during testing. The knee can also be an AE signature since the knee of different types of testing can occur at different load level.

As discussed in Chapter 2, historic index is the measurement of the change of the slope in the cumulative signal strength vs. load plot. A sudden change in the slope is referred to as the “knee”, which usually is associated with a rapid rise of historic index. For the purposes of this study, a value of historic index equal to 6.0 is used as an indication of the knee. A summary of the knee of each representative specimen by all three plots is presented in Table 7.4.

Table 7.4: Summary of Knee from Cumulative Hits vs. Load, Cumulative Signal Strength vs. Load, and Historic Index Plots

Specimen	Knee location (% of ultimate load)		
	Cumulative hits vs. load	Cumulative signal strength vs. load	Historic index vs. load
TGI2	86	90	83
TGV	54	52	46
LGI1	81	90	75
LGV1	62	50	29
LHV	96	90	18
FGV	57	40	69
Chop	91	88	89
Wov	84	84	62
SGV1	96	98	100
SHV1	58	55	59
Tee1	98	98	98
BHV1	94	93	38

It is found that the knees estimated from the cumulative hits vs. load and cumulative signal strength vs. load plots are fairly similar for all cases. Some of the knee values given by the historic index plot are different than those from the other two plots. Examples of these are the knees of specimens LGV1, LHV, Wov, and BHV1. This can be attributed to the fact that the historic index is normally used with the subsequent loading (CARP, 1999). The data presented is from the first loading and is thus different than data that has been repeated elsewhere (Fowler, 1992).

For the direct tensile specimens, the knees of the curves are located at higher loads for isophthalic polyester specimens (TGI2 and LGI1) than vinyl ester specimens (TGV and LGV1). This is due to the higher flexibility of vinyl ester

resin that can redistribute the stress to the adjacent area when fiber break occurs. Isophthalic polyester resin, in opposite, is brittle and does not allow redistribution after fiber breaks. This causes a rapid crack propagation in the specimen leading to a more rapid failure in isophthalic polyester specimens.

For specimen LHV (longitudinal/hybrid/vinyl ester), the knee appears to be beyond 90% of the ultimate load but it is found previously that carbon fiber breaks occur much earlier in this specimen. This conflict is explained by the fact that the carbon fibers have a very small diameter. Therefore, with a small number of fiber breaks, the reduction in the specimen's cross-section is not high enough to cause significant damage.

It is concluded for specimens SGV1 and Tee1 that delamination in the glass specimens occurs very suddenly since the knees of the plots are located almost at the ultimate load. This is significant information for design of structures that are made from this material.

7.3.8 Amplitude vs. Duration (Fig. 7.12)

The amplitude vs. duration plot has been used as a key to evaluate the quality of the data (CARP, 1999). Therefore, with this technology, it is clearly seen from the plots that the AE data recorded is very "clean", meaning well banded. There is no EMI (very short duration, high amplitude) and no external sliding noise (low amplitude, long duration), which may come from grips. Also, there are few overlapping events (long duration, medium amplitude). This suggests very good instrumentation and test setup.

Most of AE data is recorded by a Mistras data acquisition system. This system is newly developed and has better hardware that can reduce the chance of recording overlapping events. Also, the Mistras system can record AE hits that have duration longer than 10^5 microseconds.

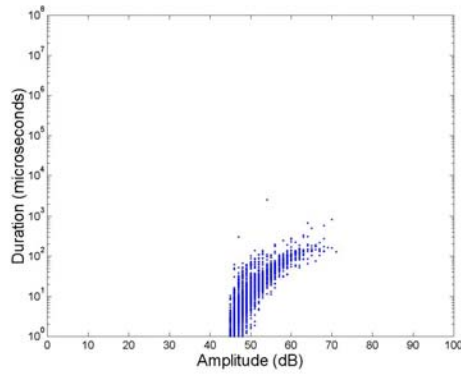
The data of specimen BHV1 is recorded by the Transportation Instrument. This system was manufactured many years ago with old computer technology. The data recorded from this system, therefore, has some scattering, which indicates non-genuine AE hits. Also, the hits having duration longer than 65,535 microseconds are recorded with these value (see Chapter 3).

The specimens with fibers in the direction longitudinal to the tensile stress show high duration hits (>30,000 microseconds) on the plots. These long duration hits are associated with high amplitude, which were found in Chapter 4 to be fiber breaks. Figure 7.19 is the progression of amplitude vs. duration relationship of specimen LGI1. It is observed that these high amplitude/long duration hits do not appear until after 90% of the ultimate load.

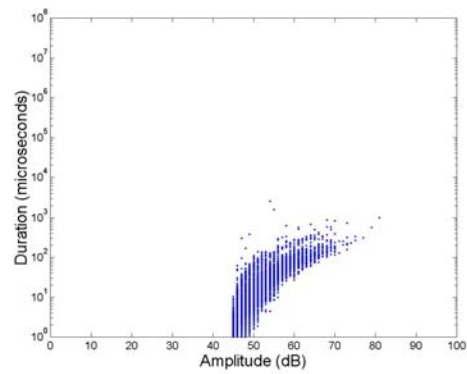
Other specimens also show the occurrence of fiber breaks or high amplitude hits. However, these high amplitude hits are associated with a duration of lower than 30,000 microseconds.

The detection of high amplitude, very long duration hits has been observed by several researchers. They believe that this long duration characteristic is a continuation of more than one failure mechanism. In this case, fiber breakage should be one of the failure mechanisms since the long duration hits have high amplitude.

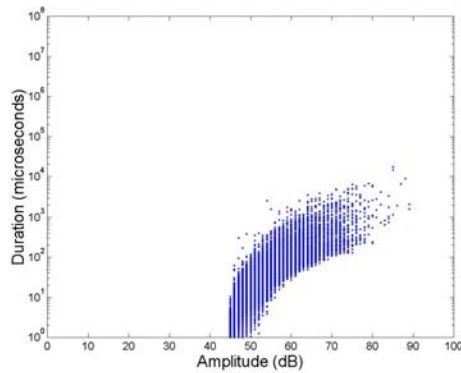
The SEM study in the previous chapters has shown that the specimens with fibers in the direction of the tensile stress produce fiber breaks in conjunction with fiber pullout in the later stage of the test. The fiber breaks occurring at the earlier stage are found in conjunction with other mechanisms such as matrix cracking or debonding. In addition, the fiber breaks in the other specimens are never found to be associated with fiber pullout. Thus, it is concluded that a single fiber break is related to high amplitude/short duration hits, whereas fiber break/pullout is related to high amplitude/long duration.



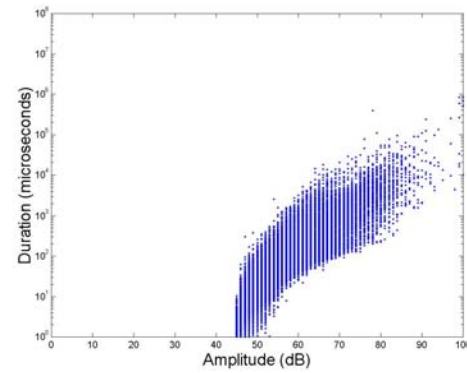
a) At 50% of Ultimate



b) At 80% of Ultimate



c) At 90% of Ultimate



d) At 95% of Ultimate

Figure 7.19: Progression of Amplitude vs. Duration Plot for Specimen LG11 at Different Loads

The other possible cause of this event is that the long duration hits are a continuation of more than one fiber break. This is due to the high number of fiber breaks during failure. The fiber breaks occur almost simultaneously, such that the AE data acquisition system cannot separate the signal from each break.

7.3.9 Duration Distribution (Fig. 7.13)

These plots are log-log plots of duration and the number of hits that fall into different duration intervals. Duration distribution essentially confirms the occurrence of long duration hits from the specimens that have fibers in the direction of the tensile stress. Table 7.5 is a summary of the duration range of each type of the specimens.

Table 7.5: Summary of Duration Range of Each Type of Specimens

Loading description	Duration range (microseconds)
Transverse tension of unidirectional specimens	0 – 20,000
Longitudinal tension of unidirectional specimens	0 – 1,000,000
Short beam shear and bond	0 – 30,000
Buckling	0 – 5,000

The AE duration of the hits from the specimens with fibers in the direction of the applied tensile stress (longitudinal) is between 0 and 1,000,000 microseconds. The duration of specimens having fibers in the direction transverse to the tensile stress ranges from 0 to 20,000 microseconds. The specimens subjected to the short beam shear and bond tests have a duration range of 0 to 30,000 microseconds. The specimen that failed by buckling yields a duration range of 0 to 5,000 microseconds.

7.3.10 Duration Distribution of High Amplitude Hits (Fig. 7.14)

These plots are primarily duration distribution plots of the fiber break hits in the specimens. The borderline amplitude used to filter out the low amplitude hits follows the results from Table 4.7.

Table 7.6 is a summary of the duration range of the high amplitude hits from each type of specimen. The duration of fiber breaks in the specimens with fibers in the direction transverse to the tensile stress ranges from 10 to 20,000 microseconds. The duration of fiber breaks in the specimens with fibers in the direction longitudinal to the tensile stress ranges between 100 to 1,000,000 microseconds. The specimens subjected to the short beam shear and bond tests produce fiber break hits with a duration between 200 and 30,000 microseconds. The specimen that failed by buckling produces fiber break hits with duration between 100 and 5,000 microseconds.

Table 7.6: Summary of Duration Range of High Amplitude Hits from Each Type of Specimens

Loading description	Duration range (microseconds)
Transverse tension of unidirectional specimens	10 – 20,000
Longitudinal tension of unidirectional specimens	100 – 1,000,000
Short beam shear and bond	200 – 30,000
Buckling	100 – 5,000

The duration ranges shown in Tables 7.5 and 7.6 are essentially the same. Table 7.6 is for fiber break data only. The difference is the absence of very short duration hits associated with high amplitude suggesting that the observed phenomena is associated with fiber break.

7.3.11 Signal Strength Distribution (Fig. 7.15)

This plot is a log-log plot between signal strength and the number of hits that fall into different signal strength intervals. Table 7.7 gives a summary of the range of signal strength from each type of specimen. Like the duration distribution plot, the plot of the specimen with fibers in the direction longitudinal to the tensile stress shows a broader and higher range of signal strength, ranging between 0 and 100,000. Other specimens have a signal strength ranging from 0 to less than 5,000. This supports the theory that the long duration hits are multiple fiber breaks occurring at approximately the same time. As discussed previously, the principal sources of energy (represented by signal strength) are the fiber breaks. Therefore, the large values of signal strength associated with longitudinal fibers suggest multiple breaks. A single fiber break and fiber pullout would likely have signal strength values closer to the hits from other mechanisms.

Table 7.7: Summary of Range of Signal Strength from Each Type of Specimens

Loading description	Signal Strength range (microseconds)
Transverse tension of unidirectional specimens	0 – 5,000
Longitudinal tension of unidirectional specimens	0 – 100,000
Short beam shear and bond	0 – 4,000
Buckling	0 – 1,000

7.3.12 Signal Strength Distribution of High Amplitude Hits (Fig. 7.16)

These plots are primarily signal strength distribution plots of fiber break hits from the specimens. The borderline amplitude used to filter out the low amplitude hits follows the results from Table 4.7.

Table 7.8 is a summary of the signal strength range of high amplitude hits. The fiber breaks of the specimen with fibers in the direction longitudinal to the applied stress appear to have a broader and higher range, ranging between 60 and 100,000. The fiber breaks of the specimen with fibers in the direction transverse to the applied stress ranges from 10 to 5,000. The range of the specimen subjected to the short beam shear and bond tests is between 6 and 2,000. Again, this confirms that the long duration phenomena is associated with fiber breakage.

Table 7.8: Summary of Signal Strength Range of High Amplitude Hits from Each Type of Specimen

Loading description	Signal Strength range (microseconds)
Transverse tension of unidirectional specimens	10 – 5,000
Longitudinal tension of unidirectional specimens	60 – 10,000
Short beam shear and bond	6 – 4,000
Buckling	20 – 700

7.3.13 Rise Time Distribution (Fig. 7.17)

These plots are log-log plots between rise time and the number of hits that fall into different rise time intervals. It is noted that the data from specimen BHV1 was recorded by the Transportation Instrument data acquisition system, which does not record rise time information.

In all cases, the plots of rise time distribution consist of two peaks. The first peak occurs between 20 and 60 microseconds. The second peak occurs between 200 and 400 microseconds. Figure 7.20 shows an example of the progression of the rise time distribution according to load for specimen LG11,

sensor 1. It can be observed that both peaks grow at the same time (or the left peak may start to grow slightly before the right peak). Also, the peaks start to grow at the early stage of the test and before fiber breaks begin to occur. This explains that fiber breaks are not associated with the peaks.

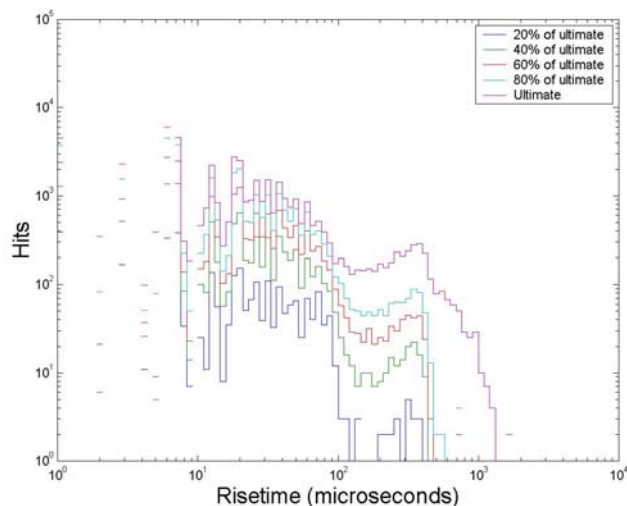


Figure 7.20: Progression of Rise Time Distribution of Specimen LG11, Sensor 1

Figures 7.21, 7.22, and 7.23 show the correlation plot between rise time vs. amplitude, rise time vs. duration, and rise time vs. signal strength of specimen LG11. It can be seen from the plots that there is a small concentration of the data into two clusters. One cluster is located between rise times of 10 to 100 microseconds, while the other cluster is located above a rise time of 100 microseconds. However, these clusters are not clearly seen and do not show any relationship between rise time and these AE parameters. The sharp boundary in Fig. 7.22 is rise time equal to duration. Obviously, the rise time cannot be longer than the duration.

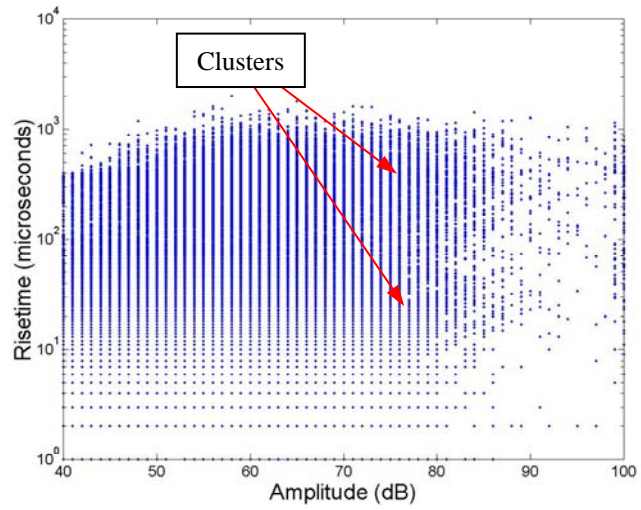


Figure 7.21: Rise Time vs. Amplitude Plot of Specimen LG11

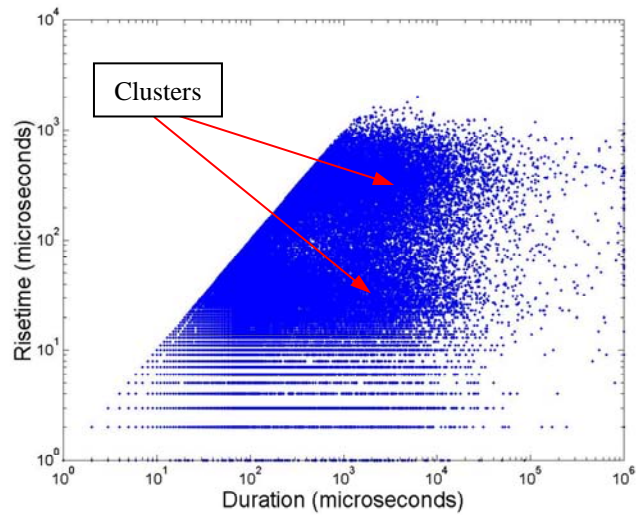


Figure 7.22: Rise Time vs. Duration Plot of Specimen LG11

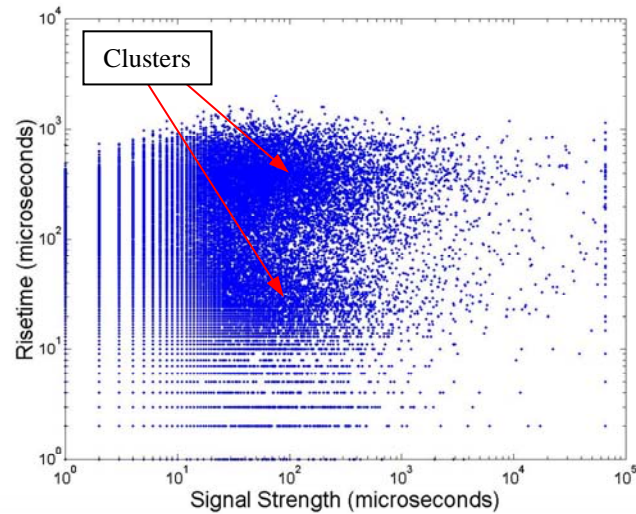


Figure 7.23: Rise Time vs. Signal Strength of Specimen LGII

When comparing the coupon specimen to the full-scale specimen (specimens LGV1 and FGV), the plots of both specimens shows similar peaks. This indicated that these two peaks are not associated with the reflected signals.

Thus, there is no conclusion at this point to explain the association of these two peaks with any failure mechanisms. Also, it is concluded that the measurement of rise time is unlikely to be able to categorize failure mechanisms since there is so little distinction between plots of the specimens.

7.4 SUMMARY

In this chapter, the material properties and AE plots of all representative specimens are shown. The dissimilarities among the plots represent many aspects of material and failure mechanism characteristics. The significant findings from this chapter are summarized below:

1. Vinyl ester resin is more flexible and elongates more than isophthalic polyester resin. This allows more fibers in the vinyl ester FRP to break before final

failure than isophthalic polyester FRP when the tensile stress is applied longitudinally to the fibers. This is observed from the earlier presence of high amplitude hits (beginning at 40% of the ultimate load) in the vinyl ester specimens tested in tension parallel to the unidirectional fiber direction.

2. Vinyl ester resin is flexible and allows the tensile stress to redistribute to the adjacent fibers or matrix after a fiber is broken. For this reason, the departure from linearity of the stress vs. strain curve appears long before failure for the vinyl ester FRP tested in tension parallel to the fibers.
3. When a tension load is applied parallel to the fibers, the onset of AE is at a higher load for the glass/isophthalic polyester FRP than for the glass/vinyl ester FRP. Onset of copious emission (knee in the curve) is also at a higher load for the glass/isophthalic polyester FRP. When a tension load is applied perpendicular to the fibers, the onset of AE is at a higher load for the glass/vinyl ester FRP than the glass/isophthalic polyester FRP. This is because the vinyl ester is more flexible than the isophthalic polyester (Ziehl, 2000). However, onset of copious emission is at a higher load for the glass/isophthalic polyester FRP.
4. Isophthalic polyester resin is brittle and does not allow redistribution as much as vinyl ester resin after a fiber is broken. This explains why the departure from linearity of the stress vs. strain curve appears close to failure for isophthalic polyester FRP. Also, the glass/isophthalic polyester FRP shows the onset of significant AE at the load higher than glass/vinyl ester FRP. This does not allow much warning before failure.
5. Carbon fibers tend to break more easily than glass fibers. It is shown by the very early fiber breaks during the test of most hybrid specimens. This is due to the brittle property of the carbon fibers, which are susceptible to damage during the fabrication process, leading to premature breaking.

6. Under axial tensile stress, carbon fiber breaks have less effect on the stiffness of the structure than the same number of glass fiber breaks. This is because a carbon fiber has a smaller size cross section than a glass fiber. When it is broken, a carbon fiber break will not reduce the area of the specimen's cross section as much as a glass fiber break does.
7. Fiber breaks, as evidenced by high amplitude hits, do not occur in the chopped strand FRP until 90% of the ultimate load in tension. Two factors contribute to this behavior. The first is the short length of the fibers, which permits them to pull out of the resin matrix rather than break. The second is that there are fewer fibers in the direction of maximum stress than with a unidirectional fabric loaded parallel to the fibers. When fibers start to break, the strength of the FRP starts to degrade rapidly.
8. The fibers in woven roving FRP are usually wavy. Accordingly, the fibers are ineffective to carry a low tensile stress. This is why the woven roving FRP does not show fiber breaks at a lower load compared to unidirectional FRP. At a higher load, the woven roving fibers are straightened up and can take tensile stress. This explains the reason that fiber breaks in woven roving FRP occur at a load of 60% of the ultimate, which is higher than the unidirectional FRP but lower than the chopped strand FRP with the same material.
9. The stress vs. strain relationship of woven roving FRP shows a sharp rise near failure. This is also because of the fiber straightening, which increases the stiffness of the FRP considerably.
10. The slope of the amplitude distribution plot and cumulative amplitude distribution plot is independent of the sensor-to-source distance. In contrast, the peak amplitude of the amplitude distribution plot is dependent on the sensor-to-source distance. Also, the amplitude where the plot changes the slope is dependent on the sensor-to-source distance.

11. b-values and the corresponding failure mechanisms are determined and presented in table 7.3.
12. The slope of the amplitude distribution plot for a coupon specimen is likely to be different than that of a full-scale specimen of the same material, due to the reflection effect. The difference in the size of the specimen also yields the different shapes of the cumulative amplitude distribution plots.
13. Delamination failure of glass FRP occurs very suddenly. Only a few AE hits can be detected before the delamination occurs. Also, it is shown that the onset of significant AE occurs almost at failure.
14. The stress vs. strain relationship of specimen associated with delamination remains linear until the delamination occurs. This applies to both glass and carbon FRP.
15. High amplitude/long duration hits (duration of 30,000 microseconds and higher) are found only in the tension specimens tested parallel to the unidirectional fiber direction. Also they occur when the load is approaching failure. A high amplitude/long duration hit is attributed to a fiber break followed immediately by another failure mechanism, which may be fiber pullout or more likely simultaneous fiber breaks. The signal strengths of these hits are higher than 5,000.

CHAPTER 8

Neural Networks for AE Pattern Recognition

An AE database has been collected throughout the research program and the failure mechanisms of each test are known. In this chapter, this AE database will be used to develop neural networks in order to perform AE pattern recognition. The objective of this chapter is to develop two network systems: a network system that can determine failure mechanisms of damage in the structures, and another system that can determine damage severity. The chapter is divided into three sections. The first section covers the development of preliminary network systems. The second section discusses applying the preliminary network system to unknown failure mechanisms of additional specimens. The AE data and failure mechanism information of these specimens will be added to the AE database. The final network system will be developed from this database and is discussed in the third section of the chapter.

8.1 PRELIMINARY NEURAL NETWORK SYSTEM

The preliminary network system is developed in order to evaluate which type of network structure, data input, and training method give the best performance to the network system. The preliminary network system is trained only to perform failure the mechanism determination task and is organized into two levels. The network in the first level is called the primary network, while the network in the second level is called the secondary network.

The primary network receives data input that is arranged from the AE database. There are many ways to model the AE data to the network input. In

this research program, on AE database in the form of AE correlation plots are arranged into arrays of numbers and used as the primary network input. This is because it has been shown that AE correlation plots can help visualize dissimilarity of failure mechanism patterns (see details of basic AE correlation plots in Section 2.3.5 of Chapter 2). This way, the network will learn to recognize the dissimilarity from the AE plot of different failure mechanisms and is able to identify unknown failure mechanisms. Ten AE correlation plots are initially selected and, therefore, ten primary networks are constructed to receive the input from each type of plot. After training and testing, the performance of every primary network will be evaluated. The primary networks associated with a poor performance will be eliminated from the system.

Each selected primary network has strengths and weaknesses in determining each type of failure mechanism and the networks are complementary to one another. As a result, a secondary network is developed as a supplement to the primary networks. This secondary network is trained using outputs from the primary networks as its input. The mechanism of the secondary network combines the strengths of each primary network, leading to a higher performance of the network system. A flow chart of a network system including primary and secondary networks is shown in Fig. 8.1.

All of the networks in this analysis are generated and trained using NeuralWork® Professional II/PLUS software version 5.51. Only AE data from 45 dB to 100 dB are used for training. Two network systems, each with primary and secondary networks, are developed in parallel. The first network system is trained by the backpropagation training method, while the other system is trained by the PNN method (see backpropagation and PNN training methods in Section 2.4 of Chapter 2). The performance of the networks trained by each training

method will be compared, and the superior method will be used to train the networks in the next sections.

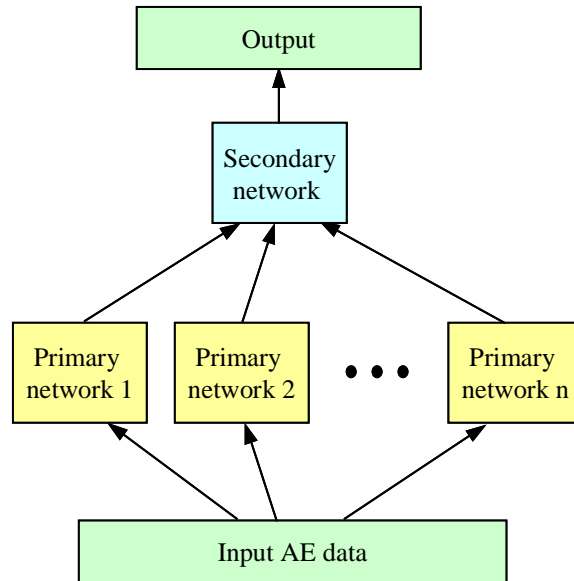


Figure 8.1: Flow Chart of Network System Consisting of Primary and Secondary Neural Networks

8.1.1 Primary Networks

Ten primary networks are developed based on ten AE correlation plots. The AE plots are chosen such that they cover a number of the important AE parameters, which are amplitude, duration, historic index, severity, and signal strength. A new AE parameter, the centroid of the waveform, is developed in this chapter and will also be used as a network input.

8.1.1.1 Primary Network Organization

The networks consist of three layers: input, output, and hidden layers (see Fig. 8.2). The input layer consists of a group of input neurons that represent the AE plots. The input layer also consists of three additional input neurons representing material information of a specimen: glass/isophthalic polyester, glass/vinyl ester, and hybrid/vinyl ester.

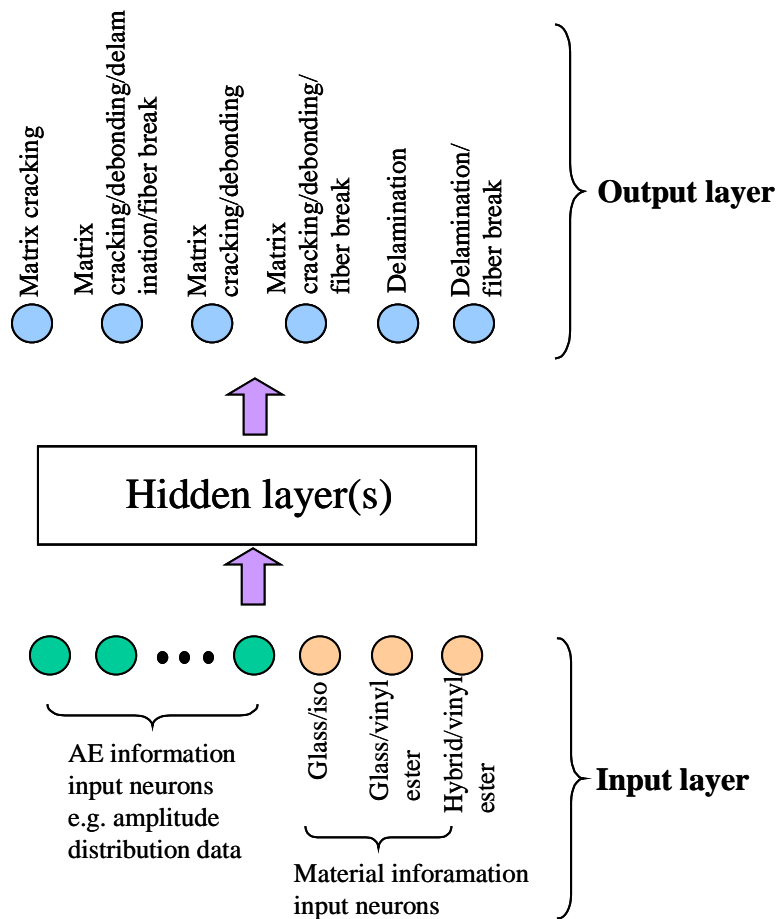


Figure 8.2: Typical Primary Neural Network Diagram

The output layer consists of six neurons. These output neurons represent the six failure mechanism combinations, which are

1. Matrix cracking
2. Matrix cracking/ debonding/ delamination/ fiber break
3. Matrix cracking/ debonding
4. Matrix cracking/ debonding/ fiber break
5. Delamination
6. Delamination/ fiber break

These combinations are chosen based on the failure mechanisms that were found in the specimens tested for the AE database.

The structure of the hidden layer of a primary network differs depending on the types of training methods used. For the backpropagation method, one hidden layer is used and the number of hidden neurons is varied. For the PNN training method, two hidden layers are used and the number of the neurons in each hidden layer is fixed (see Section 2.4.6 of Chapter 2 for details of PNN). The network performance can be optimized by adjusting the values of the network parameters until the best performance is obtained (trial and error method). For the backpropagation method, the parameters to be adjusted are the number of hidden neurons and the initial weights. For the PNN method, the smoothing parameter is the main parameter to be adjusted. NeuralWorks implementation uses a representation of the smoothing parameter defined by the equation below:

$$\sigma = \frac{S}{N^{E/M}}$$

Where,

σ = Smoothing parameter per NeuralWorks

M = number of input neurons

S = Sigma scale

E = Sigma exponent

N = Number of training data points or number of Pazen Windows

Another parameter to be adjusted in the software for the PNN training method is the radius of influence. The radius of influence *“is a simple clustering mechanism that assigns an input vector to a cluster if the cluster center is the nearest cluster center to the input vector and it is of the same class as the cluster and it is closer than the radius of influence. Otherwise the input vector is assigned as the center of a new cluster (if possible).”* (Neuralware, 2000).

A value of 0.5 for E is recommended by Neuralware. Therefore, this leaves only parameters S and radius of influence to be adjusted by the trial and error during the training process to obtain the most optimized network.

A summary of the specimens tested for the AE database is presented in Table 8.1. AE data from each sensor and specimen are plotted at every 10% of the ultimate load. AE is not generated at zero load. Accordingly, the first plot is for 10% of ultimate load. Each AE plot is arranged into an array of numbers. This gives the total of 720 data arrays for each type of AE plot (72 sensors x 10 levels of load = 720 data arrays). From these 720 data arrays, 550 data arrays or 76% are statistically selected as a training data set and the remaining data arrays become a testing data set. Figure 8.3 illustrates a process of preparing input data for a primary network. This figure uses an example of an amplitude distribution plot to model the network input. The details of how to transform each type of AE plot into an input array for each primary network are described below.

Table 8.1: Specimen Summary for Neural Network

Name	Fiber type	Resin type	No. of sensors	Loading Description
TGV	Glass	Vinyl ester	4	Transverse tension
TGI1	Glass	Isophthalic polyester	4	Transverse tension
TGI2	Glass	Isophthalic polyester	4	Transverse tension
LGI1	Glass	Isophthalic polyester	4	Longitudinal tension
LGI2	Glass	Isophthalic polyester	4	Longitudinal tension
LGV1	Glass	Vinyl ester	4	Longitudinal tension
LGV2	Glass	Vinyl ester	4	Longitudinal tension
LHV	Carbon	Vinyl ester	4	Longitudinal tension
FGI	Glass	Isophthalic polyester	4	Longitudinal tension (full scale)
FGV	Glass	Vinyl ester	4	Longitudinal tension (full scale)
SGI1	Glass	Isophthalic polyester	2	Short beam shear
SGI2	Glass	Isophthalic polyester	2	Short beam shear
SGI3	Glass	Isophthalic polyester	2	Short beam shear
SGI4	Glass	Isophthalic polyester	2	Short beam shear
SGV1	Glass	Vinyl ester	2	Short beam shear
SGV2	Glass	Vinyl ester	2	Short beam shear
SGV3	Glass	Vinyl ester	2	Short beam shear
SHV1	Hybrid	Vinyl ester	2	Short beam shear
SHV2	Hybrid	Vinyl ester	2	Short beam shear
SHV3	Hybrid	Vinyl ester	2	Short beam shear
Tee1	Glass	Vinyl ester	4	Bond test
Tee2	Glass	Vinyl ester	4	Bond test
Tee3	Glass	Vinyl ester	4	Bond test

Total sensors = 72 sensors

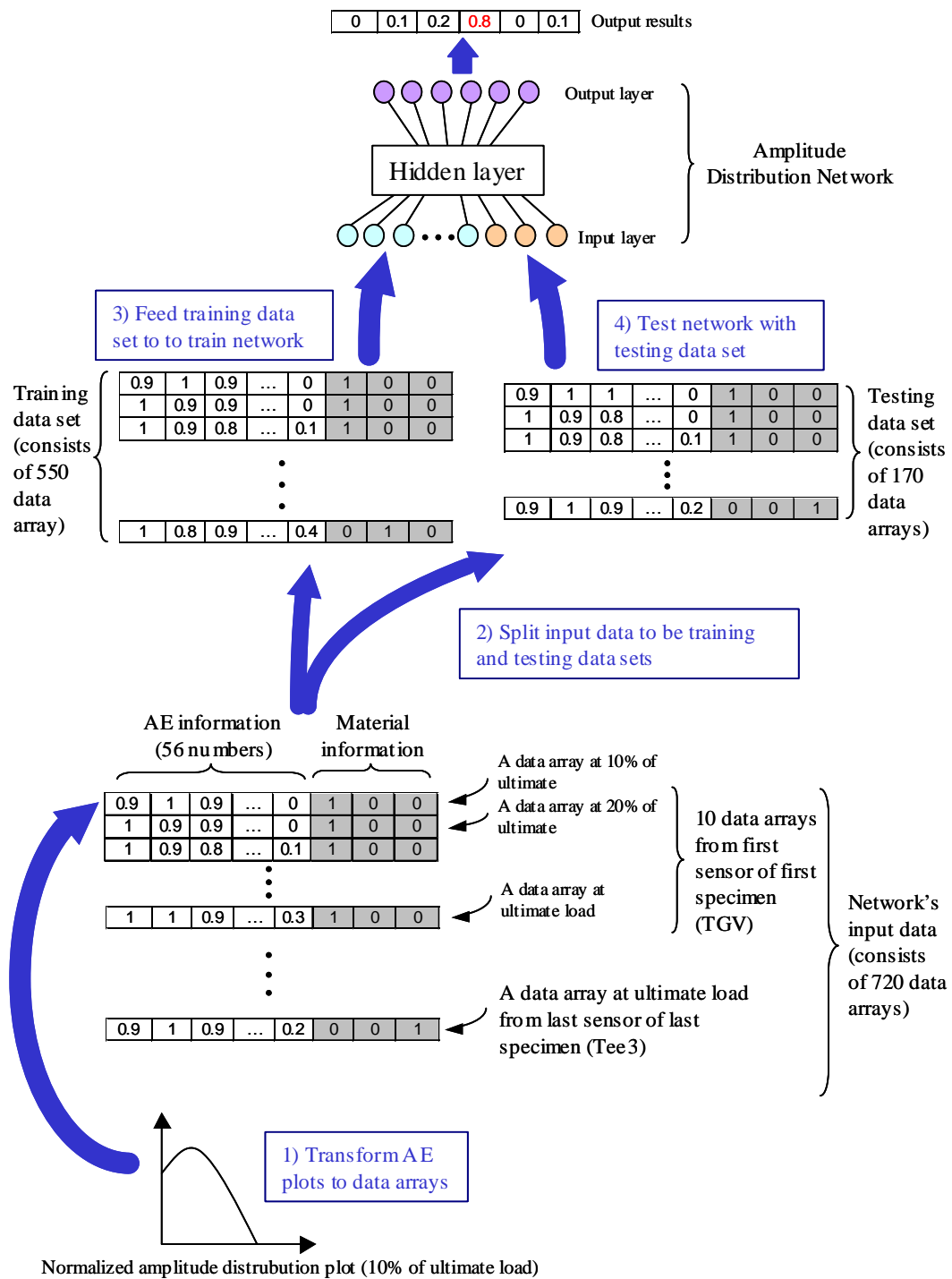


Figure 8.3: Process of Preparing Input Data for a Primary Network

Differential Amplitude Distribution Neural Networks

A differential amplitude distribution plot is a histogram of the number of hits at different levels of amplitude. The x-axis of the plot represents 56 amplitude points (from 45 dB to 100 dB) and the y-axis represents number of hits on a log scale. As described below, the y-axis of the plot is normalized to eliminate the effect of the total number of hits. The AE information from an individual plot is transformed into a data array. The numbers in the data array come from the values of the plot at different amplitude levels. The data array also consists of three additional numbers representing material information of the specimen. Figure 8.4 illustrates how to transform an amplitude distribution plot to be a data array. The plot in the figure is the amplitude distribution plot of specimen TGII at 50% of the ultimate load. The numbers in the unshaded area are AE information and the numbers in the shaded area represents material information of the specimen TGII (1,0,0 represents glass/isophthalic polyester).

As discussed above, the plot is normalized before transforming to an array. There are two methods used for normalizing amplitude distribution plots. The first method is to divide all the numbers of hits by their maximum number. This gives the value of the maximum number of hits of the plot equal to one. The second method is to divide all the numbers of hits by the summation of the numbers. This yields the area under the plot equal to one. Two amplitude distribution networks are developed to support both normalizations. The network that receives input based on the plot with the first normalization method is called Amplitude Distribution Network 1. The network that receives input based on the plot with the second normalization method is called Amplitude Distribution Network 2. Each network consists of 56 input neurons that receive arrays of numbers for input, and three other input neurons that receive material information.

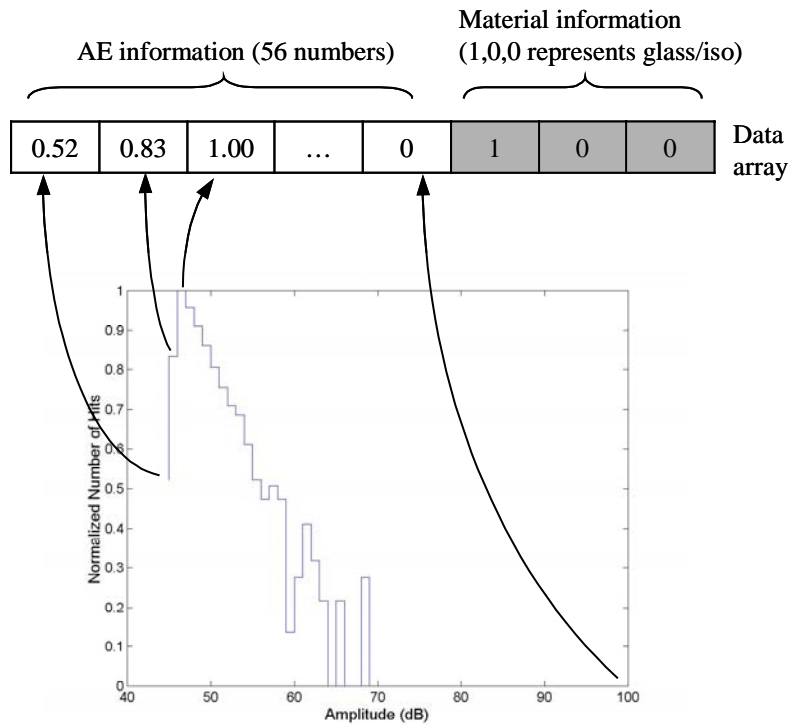


Figure 8.4: Transformation of Normalized Amplitude Distribution Plot to Data Array

Cumulative Amplitude Distribution Neural Networks

A cumulative amplitude distribution plot is a histogram of the number of hits at a specified amplitude and higher. The x-axis of the plot represents 56 amplitude points (45 dB to 100 dB) and the y-axis represents cumulative numbers of hits on a log scale. The y-axis of the plot is normalized to eliminate the effect of the total number of hits. An individual plot is transformed into a data array in the same manner to the amplitude distribution plot, with the values of the plot at different amplitude levels becoming the numbers in the data array. The data array also consists of three additional numbers representing material information of the specimen.

As discussed above, the plot is normalized before transforming to be an array. There are two methods used for normalizing cumulative amplitude distribution plots. These methods are the same two methods that are used in differential amplitude distribution networks. Two amplitude distribution networks are developed (one for each method of normalization). The network that receives input based on the plot with the first normalization method is called Cumulative Amplitude Distribution Network 1. The network that receives input based on the plot with the second normalization method is called Cumulative Amplitude Distribution Network 2. Each network consists of 56 input neurons that receive arrays of numbers for input, and three additional input neurons that receive material information.

Amplitude vs. Duration Neural Networks

Three primary networks are developed based on modeling the amplitude vs. duration plot as input data. These networks are:

1. Amplitude vs. Duration Network
2. Amplitude vs. Duration Network with Linear Conversion
3. Amplitude vs. Duration Network with Log Conversion

The details of each network are described below.

The AE data from the amplitude vs. duration plot, which ranges from 45 dB to 100 over a duration of 0 to 10^6 microseconds (log scale), are mapped into a 12 x 14 matrix of 168 cells (see Fig. 8.5). The cell of the matrix covers the equal interval of amplitude and duration. The number of each cell is the number of hits that fall into a specified amplitude and duration interval (Fig. 8.6). The number in each cell is then normalized using the total number of hits as a reference (Fig. 8.7).

														0.00
		0.00	0.00						0.00					0.00
	0.00						0.00	0.00	0.00	0.00	0.00			
0.00	0.00	0.00		0.00	0.00	0.00	0.00	0.00	0.00	0.00				
0.00	0.00	0.00	0.00	0.00	0.00	0.00	0.01	0.00	0.00	0.00				
0.00	0.01	0.02	0.03	0.03	0.03	0.01	0.01	0.00	0.00					
0.03	0.11	0.09	0.04	0.01	0.00	0.00	0.00							
0.04	0.14	0.04	0.01	0.00	0.00									
0.11	0.09	0.00	0.00											
0.11	0.00													

Figure 8.7: 12x14 Matrix Normalized by Total Number of Hits

Genuine AE hits usually do not fall into low amplitude/high duration or high amplitude/low duration areas. Accordingly, the 42 cells of the matrix representing these areas are removed (Fig. 8.8). The 126 remaining cells of the matrix are arranged into an array of numbers and introduced to 126 input neurons (Fig. 8.9). The data array also has three additional numbers representing material information of the specimen. Therefore, the network to receive this data input consists of 129 input neurons: 126 neurons receive AE information, and 3 additional neurons receive the material information. This network is called the original amplitude vs. duration network or Amplitude vs. Duration Network.

Normalization reduces the numbers in the cells to a range of 0 to 0.2. This range is believed to be too small and may confuse the network. It would be beneficial if these numbers were converted to be in a simpler range (i.e. 1 to 11). Two types of conversion tables are used for this conversion: linear and log. The linear conversion table is given in Table 8.2 and the corresponding plot in Fig. 8.10. The numbers in the matrix cells after conversion are arranged into an array of numbers and introduced to the input neurons of the network. The network that uses these linearly converted values is called the Amplitude vs. Duration Network with Linear Conversion.

A logarithmic conversion table is given in Table 8.3 and the corresponding plot is Fig. 8.11. The neural network that uses these transformed numbers is the Amplitude vs. Duration network with Log Conversion.

Table 8.2: Linear Conversion Table for Amplitude vs. Duration

Original value	Value used for neural network
0	0
0-0.02	1
0.02-0.04	2
0.04-0.06	3
0.06-0.08	4
0.08-0.10	5
0.10-0.12	6
0.12-0.14	7
0.14-0.16	8
0.16-0.18	9
0.18-0.20	10
>0.20	11

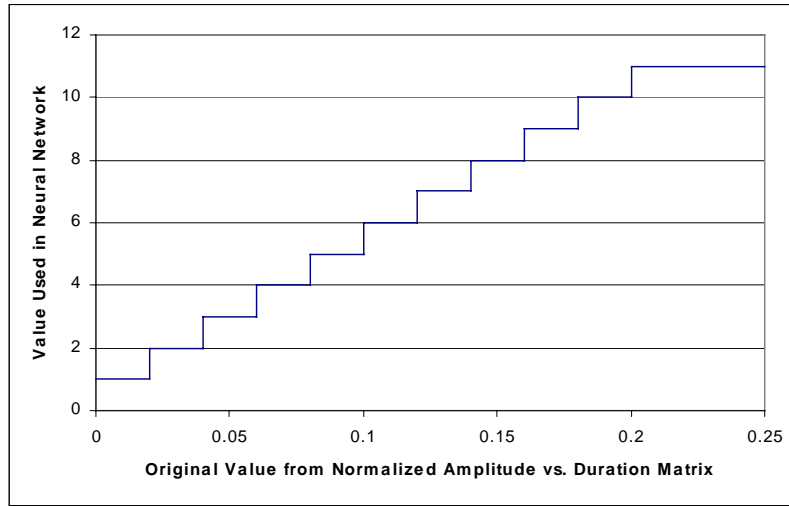


Figure 8.10: Original Values vs. Values Used in Amplitude vs. Duration Network with Linear Conversion

Table 8.3: Log Conversion Table for Amplitude vs. Duration

Original value	Value used for neural network
0	0
0-0.001167	1
0.001167-0.003016	2
0.003016-0.005950	3
0.005950-0.010601	4
0.010601-0.017974	5
0.017974-0.029664	6
0.029664-0.048197	7
0.048197-0.077578	8
0.077578-0.124158	9
0.124158-0.20	10
>0.20	11

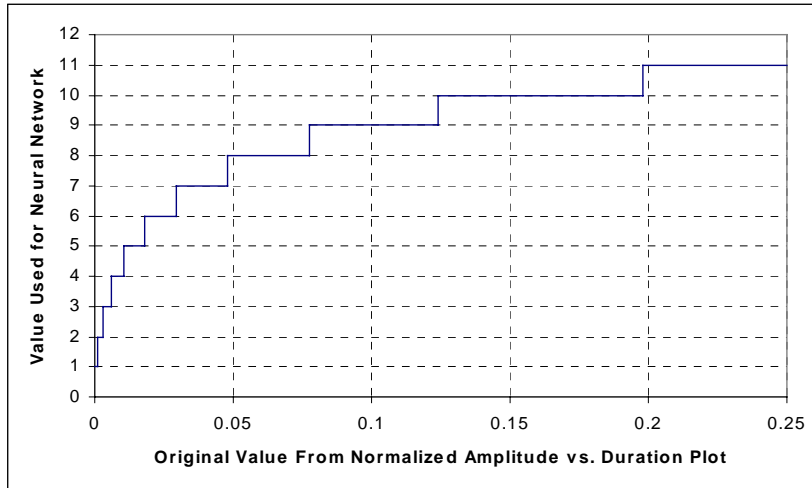


Figure 8.11: Original Values vs. Values Used in Amplitude vs. Duration Network with Log Conversion

Historic Index and Severity Network

A historic index vs. load and a severity vs. load for each sensor and specimen are plotted. Historic index and severity are independent of the total number of AE hits from the test and thus are not subjected to normalization. The maximum value of historic index vs. load plot from 0% to a specific level of load becomes the first number in the data array. The second number in the data array is the value of severity at that specific level of load. The data array also has three additional numbers representing the material information of the specimen. An example of how to transform the historic index vs. load and severity vs. load plots into a data array, for instance, at 70% of the ultimate load is shown in Fig. 8.12. The figure shows the plots of specimen TGI1, sensor 2. From the historic vs. load plot, the maximum value of historic index from 0% to 70% of the ultimate is found to be 1.65. This becomes the first number in the data array. From the

severity vs. load plot, the severity value at 70% of the ultimate is found to be 25.4. This value becomes the second number in the data array. The third, fourth, and fifth numbers in the data array represent the material information. In this case, specimen TG11 is made of glass/isophthalic polyester, which is represented by the numbers 1, 0, 0.

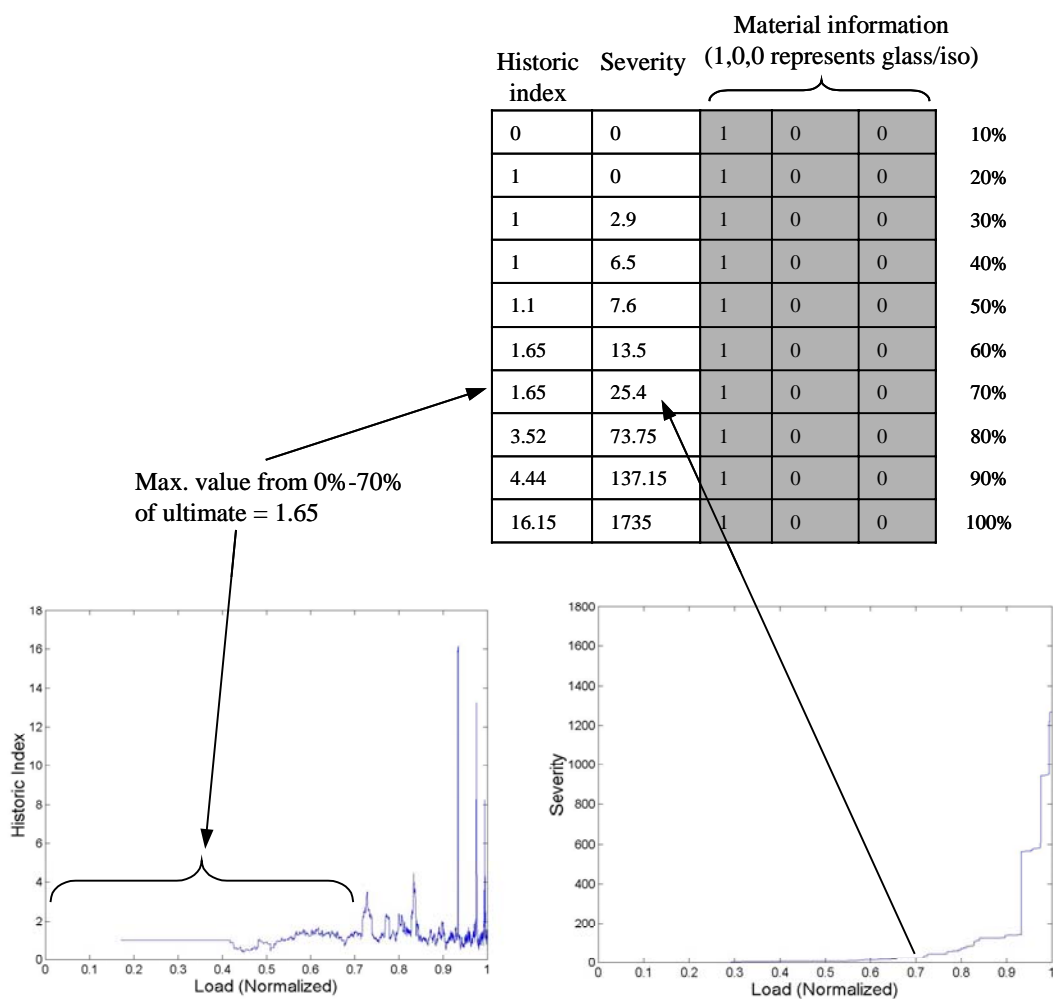


Figure 8.12: Transformation of Historic Index vs. Load and Severity vs. Load Plot into Data Arrays

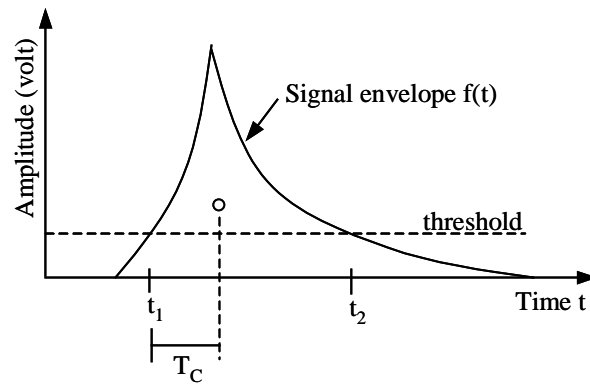
Cumulative Signal Strength Network

The cumulative signal strength plot displays cumulative signal strength on the y-axis and load on the x-axis. The plot is normalized using the maximum cumulative signal strength as a reference value. An array of numbers is created by taking the cumulative signal strength at every 5 % increment of the maximum load in the plot. Therefore, an input array consists of 20 numbers, which are fed to the 20 input neurons of the Cumulative Signal Strength Network. Three input neurons that receive material information are also used.

Waveform Centroid Distribution Neural Network

The new AE parameter, waveform centroid ratio, is developed for this analysis. The parameter is the ratio of time at the centroid of the area under the rectified waveform envelope (T_c) to the duration of the hit (see Fig. 8.13). This ratio represents the shape of an AE waveform. The hits that have a duration less than 30 microseconds are neglected. The ratios of all hits are plotted in the distribution histogram. The x-axis of the plot represents the waveform centroid ratio, which ranges from 0 to 1 (0.5 interval or 20 ratios). The y-axis of the plot represents the number of hits. The number of hits is normalized using the total number of hits as the reference. Figure 8.14 is an example of the waveform centroid distribution plot.

A distribution plot is transformed into a data array, with 20 numbers in the data array that come from the number of hits from the plot. The array also has three additional numbers representing the material information of the specimen. The network that receives these data arrays is called Waveform Centroid Distribution Network. This network has 23 input neurons to facilitate the numbers from the data array.



where,

t_1 = first threshold crossing of waveform envelope

t_2 = last threshold crossing of waveform envelope

$$T_c = \frac{\int_{t_1}^{t_2} f(t) t dt}{\int_{t_1}^{t_2} f(t) dt}$$

$$\text{Waveform centroid ratio} = T_c / (t_2 - t_1)$$

Figure 8.13: Waveform Centroid and Waveform Centroid Ratio Parameters

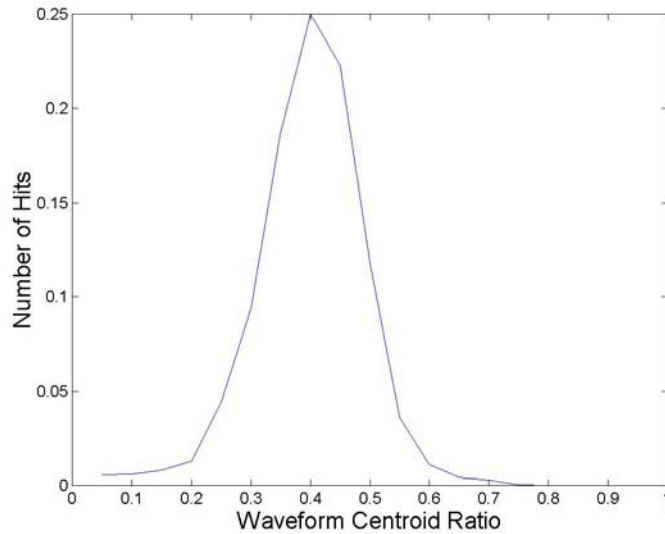


Figure 8.14: Example of a Waveform Centroid Distribution Plot

8.1.1.2 Results of Primary Neural Networks

After the primary networks are trained and all parameters (number of hidden neurons or smoothing parameter) are adjusted, the optimized network from each type of AE plot is obtained. The performance of each network is evaluated using the testing data set. The performance of the networks based on the backpropagation and PNN training methods is summarized in Table 8.4.

The performance by failure mechanism is calculated from the number of data arrays that are correctly classified in a failure mechanism combination divided by the total number of the data arrays in that failure mechanism combination. The overall performance is calculated from the number of data arrays of all failure mechanism categories divided by the total number of data arrays in the testing data set.

Table 8.4: Summary of Primary Neural Network Testing Performance

Neural networks type	Overall Performance (%)	Performance by failure mechanism (%)					
		1	2	3	4	5	6
Backpropagation							
Amplitude Distribution1	71.7	79.3	75.6	66.7	83.3	84.9	40.5
Amplitude Distribution2	49.7	69.0	70.7	0	33.3	84.9	40.5
Cumulative Amplitude Distribution1	52.9	75.9	70.7	0	50.0	66.7	54.1
Cumulative Amplitude Distribution2	51.5	75.9	65.9	0	50.0	60.6	56.8
Amplitude vs. Duration	78.6	75.9	87.8	83.3	91.7	54.6	78.4
Amplitude vs. Duration with Linear Conversion	83.7	65.5	85.4	88.9	100	75.8	86.5
Amplitude vs. Duration with Log Conversion	83.8	75.9	82.9	77.8	100	84.9	81.1
Historic Index and Severity	29.3	0	29.3	0	0	54.6	91.9
Cumulative Signal Strength	46.6	65.5	65.9	16.7	0	42.4	89.1
Waveform Centroid Distribution	37.9	75.0	66.7	0	80.0	5.9	0
PNN							
Amplitude Distribution1	61.4	79.3	80.5	44.4	58.3	27.3	78.4
Amplitude Distribution2	54.6	51.7	65.9	27.8	75.0	39.4	67.6
Cumulative Amplitude Distribution1	66.1	72.4	85.4	38.9	83.3	27.3	89.2
Cumulative Amplitude Distribution2	60.9	62.1	73.2	16.7	100	27.3	86.5
Amplitude vs. Duration	78.9	62.1	87.8	88.9	91.7	48.5	94.6
Amplitude vs. Duration with Linear Conversion	42.8	51.7	97.6	44.4	0	33.3	29.7
Amplitude vs. Duration with Log Conversion	49.6	75.9	95.1	61.1	25	24.2	16.2
Historic Index and Severity	40.5	69.0	22.0	44.4	83.3	0	24.3
Cumulative Signal Strength	61.6	79.3	58.5	22.2	75.0	42.4	91.9
Waveform Centroid Distribution	49.2	100	77.8	0	100	17.7	0

Note: Failure Mechanism combinations

1 = Matrix cracking

4 = Matrix cracking/ debonding/ fiber break

2 = Matrix cracking/ debonding/ delamination/ fiber break

5 = Delamination

3 = Matrix cracking/ debonding

6 = Delamination/ fiber break

There are some networks that determine certain failure mechanisms with a very high accuracy, but determine the rest of the failure mechanisms with a very low accuracy. These networks are considered of having a bias behavior, which means that the network tends to lump the results into one failure mechanism. An example of such a network is the Historic Index and Severity Network by the backpropagation training method. This network tends to determine all the failure mechanisms to be only the failure mechanism combinations 5 or 6. The network performance is 54% and 91% in failure mechanism combinations 5 and 6 respectively, while the performance is zero in three other failure mechanism combinations. Also, the Waveform Centroid Distribution Networks by both training methods tend to determine all the failure mechanisms to be only failure mechanism combinations 1, 2 or 4. This yields the lowest overall performance for the Historic Index and Severity Network and Waveform Centroid Distribution Network by both training methods.

The reason of the low performance and the bias behavior of Historic Index and Severity Network is that both historic index and severity are created for determining damage severity of the structure. Therefore, these two parameters are not meaningful for the network that performs the failure mechanism determination task. The Historic Index and Severity Network is eliminated from the network system at this point. However, in last section of this chapter, when the network system for determination of damage severity is developed, the Historic Index and Severity Network will be used.

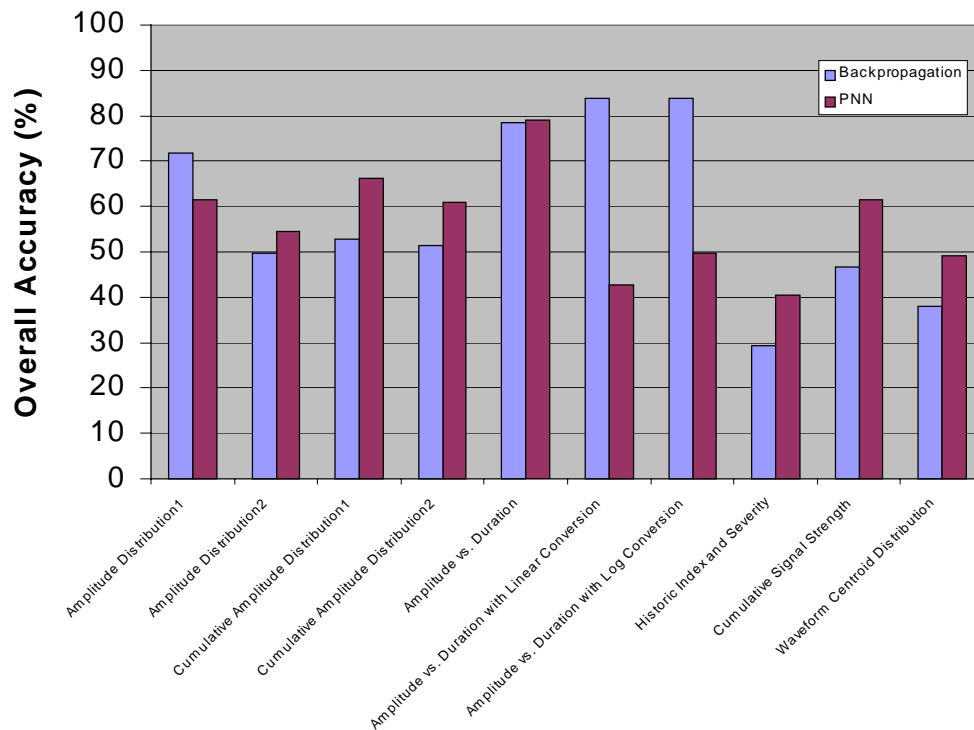
The reason of the low performance and the bias behavior of Waveform Centroid Distribution Network is that the AE data acquisition system cannot record waveforms of every hit that is emitted from the specimen. This can lead to a bias of the ratio distribution and a bias of the network determination. Also, the different failure mechanism may not be associated with differences in the shape of

the waveform, but may be associated with some other factors such as the distance of the sensor to the source. Therefore, Waveform Centroid Ratio Network is also eliminated at this point.

The 0% accuracy in other networks (e.g. Amplitude Distribution Network 2 by backpropagation method or Amplitude vs. Duration Network with Linear Conversion by PNN method) does not indicate the bias behavior of the network but is rather associated with the low capability in determining a specific failure mechanism. Therefore, the networks that have only one 0% accuracy in the performance table are acceptable and can be considered for using in the network system.

A comparison between the overall performance of the backpropagation and PNN training methods for each network is summarized in Fig. 8.15. It is interesting that Amplitude vs. Duration Network performs well by both training methods (>78% accuracy). However, Amplitude vs. Duration Networks with Linear and Log Conversions perform well only by the backpropagation method (> 83% accuracy). By PNN method, the performance of these networks drops below 50% accuracy. This shows that the simpler input has a bad effect on the PNN training method but, on the other hand, it has a good effect on the backpropagation training method.

Figure 8.15 also shows that seven out of ten networks trained by PNN perform better than those trained by backpropagation method. However, the highest performance of the network trained by backpropagation method reaches 84% accuracy, whereas the highest performance of the network trained by PNN is only 79%. Therefore, it cannot be concluded at this point which training method is superior to the other.

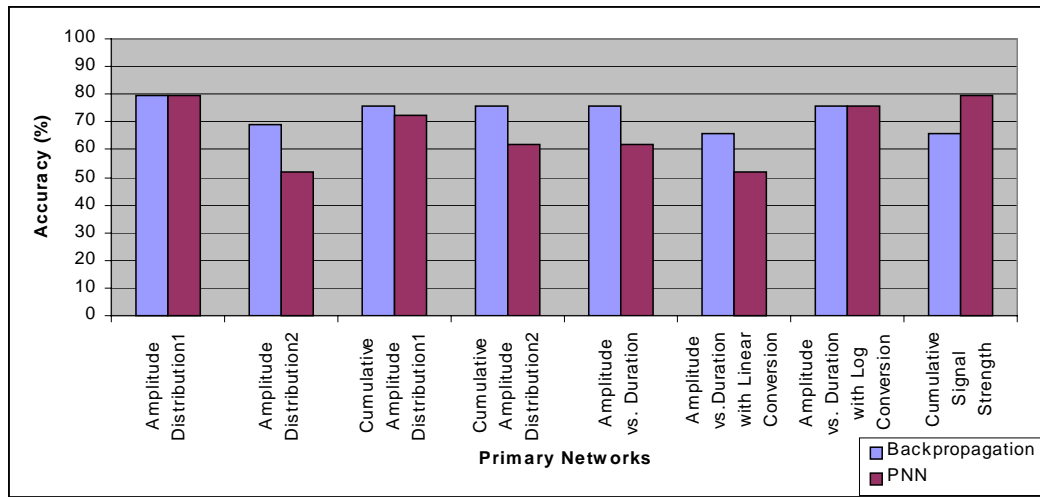


Neural Networks

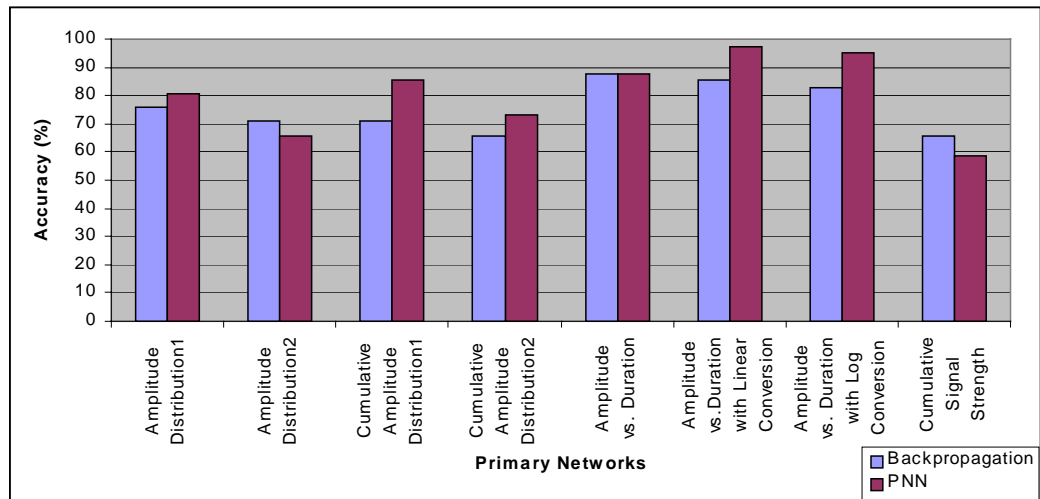
Figure 8.15: Overall Performance of Primary Neural Networks Trained by Backpropagation and PNN

Figure 8.16 presents a series of performance plots for each failure mechanism. To avoid confusion, the performance of Historic Index and Severity Network and Waveform Centroid Distribution Network are excluded. It is observed that each network has individual strengths and weakness and is complementary to one another for classifying failure mechanisms. For example, with the PNN method, the Cumulative Signal Strength Network performs the best in determining failure mechanism combination 1 (79.3% accuracy), while it performs poorly in determining failure mechanism combination 3 (22.2% accuracy). On the other hand, the Amplitude vs. Duration Network performs with

less accuracy in determining failure mechanism combination 1 (62.1% accuracy), while it performs with the highest accuracy in determining failure mechanism combination 3 (88.9% accuracy). Thus, by combining the strengths of each network, the performance of the network system may be optimized. This combination creates a secondary network.

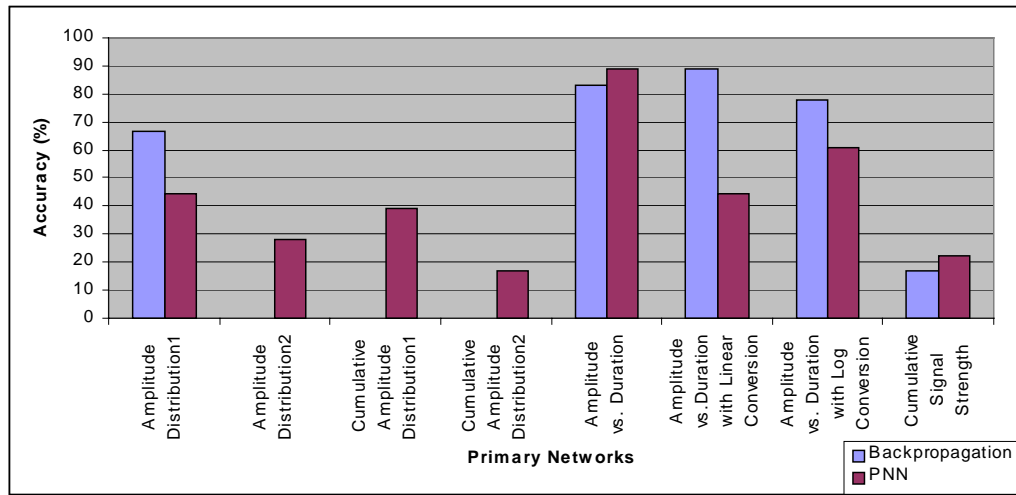


a) Failure Mechanism Combination 1 (Matrix Cracking)

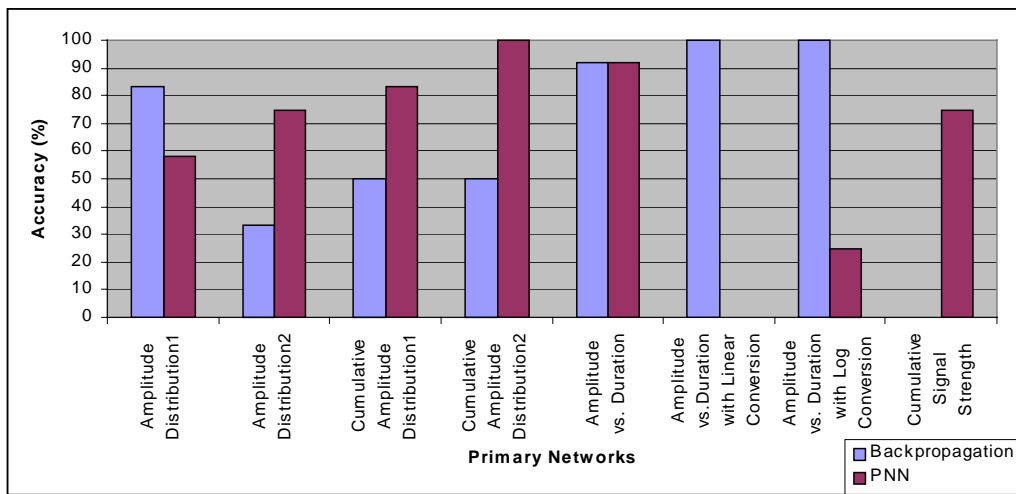


b) Failure Mechanism Combination 2 (Matrix Cracking/ Debonding/ Delamination/ Fiber Break)

Figure 8.16: Primary Network Performance for Each Failure Mechanism Combination

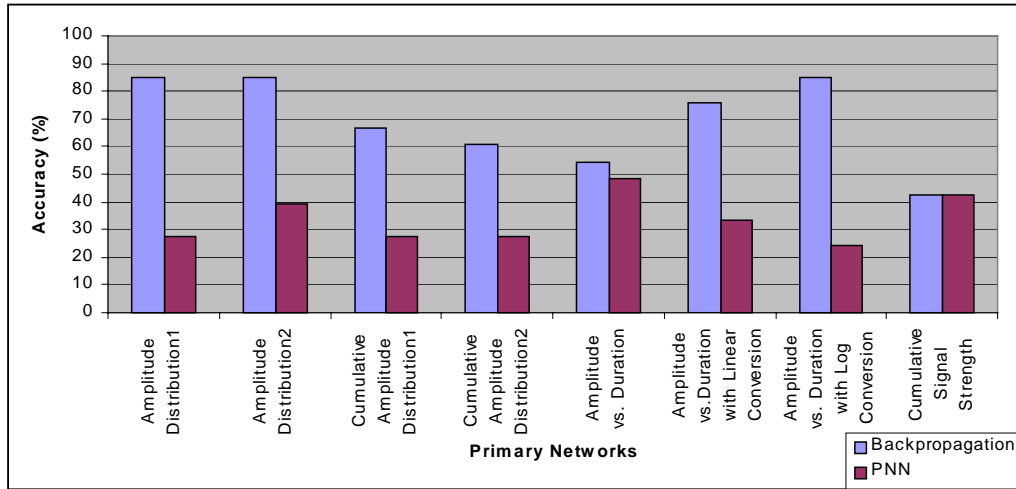


c) Failure Mechanism Combination 3 (Matrix Cracking/ Debonding)

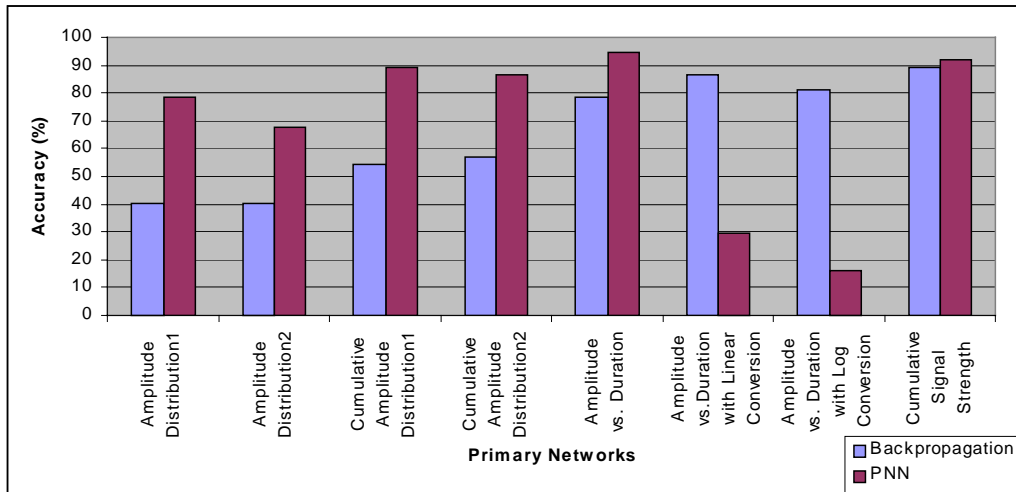


d) Failure Mechanism Combination 4 (Matrix Cracking/ Debonding/ Fiber Break)

Figure 8.16 (cont'd): Primary Network Performance for Each Failure Mechanism Combination



e) Failure Mechanism Combination 5 (Delamination)



f) Failure Mechanism Combination 6 (Delamination/ Fiber Break)

Figure 8.16 (cont'd): Primary Network Performance for Each Failure Mechanism Combination

8.1.2 Secondary Neural Network

Two secondary networks are developed. One is based on the backpropagation system and the other is based on the PNN system. The secondary networks receive output data from the appropriate corresponding primary network. The secondary networks are trained with changing parameters and/or number of hidden neurons, as was the case with the primary networks. Both training methods will be evaluated and the better method will be use for training the final network system.

8.1.2.1 Secondary Network Organization

Six failure mechanism outputs from the selected primary networks are used as input data for the secondary network. Therefore, the number in an input data array is different depending on what combination of the selected primary networks is used. The data arrays are introduced to the input neurons of the secondary network. There are a total of 170 data arrays (data points) used as a training set. These arrays are selected from the optimized primary networks (primary networks that have the optimum number of hidden neurons or smoothing parameter). The testing data set is another set of data, which is not used in the training data set. A typical data array and a secondary network diagram are illustrated in Fig. 8.17.

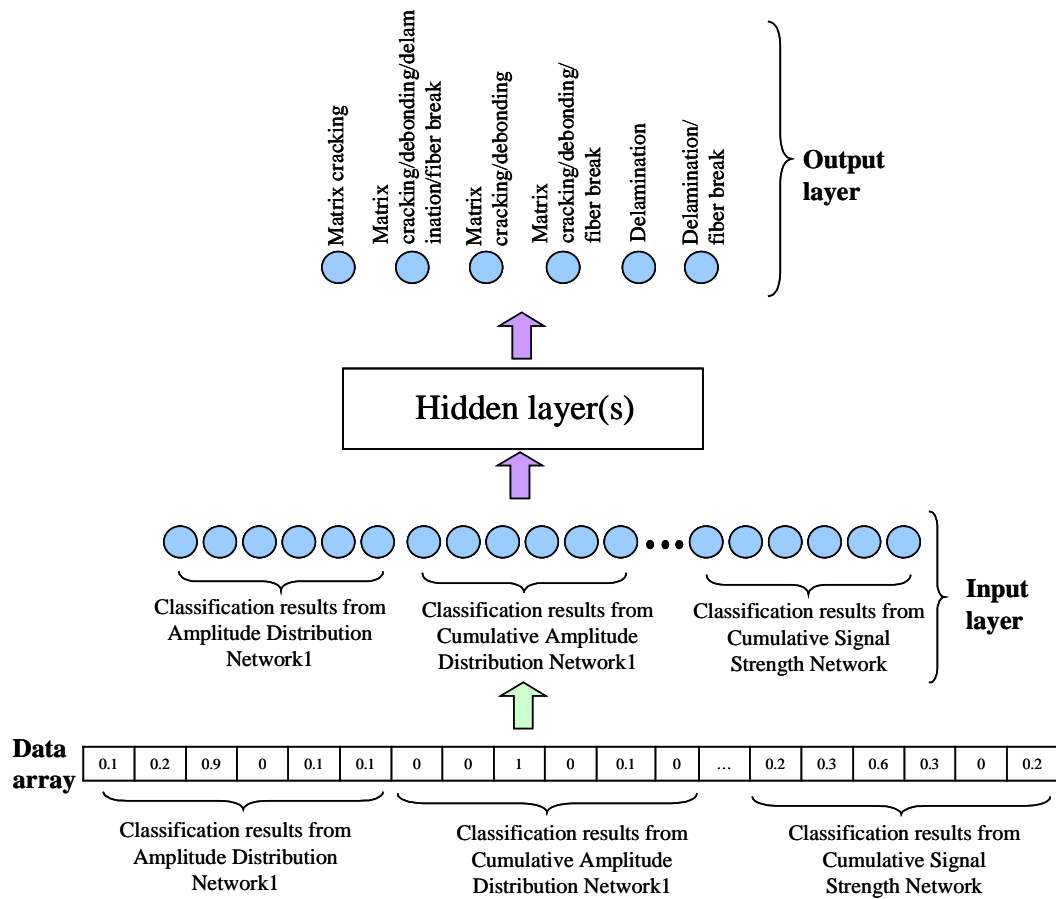


Figure 8.17: Secondary Neural Network Diagram

The outputs from different primary network combinations are used to train the secondary network. It is found that, for the backpropagation training method, the combination that yields the best secondary network performance consists of the output from:

1. Amplitude Distribution Network1
2. Cumulative Amplitude Distribution Network 1
3. Amplitude vs. Duration Network
4. Amplitude vs. Duration Network with Linear Conversion

5. Amplitude vs. Duration Network with Log Conversion
6. Cumulative Signal Strength Network

Also, with the PNN training method, the combination that yield the best secondary network performance consists of the output from:

1. Amplitude Distribution Network1
2. Amplitude Distribution Network2
3. Cumulative Amplitude Distribution Network 1
4. Cumulative Amplitude Distribution Network 2
5. Amplitude vs. Duration Network
6. Cumulative Signal Strength Network

The performance results of the above combination will be presented in the next section (8.1.2.2). It is noted that adding the output from Amplitude Distribution Network 2 and Cumulative Amplitude Distribution Network 2 to the secondary network almost has no effect to the performance of the network trained by the backpropagation method, while it increased the network performance by 2.3% if trained by PNN method. Also, removing the output from Amplitude vs. Duration Networks with Linear and Log Conversion from the PNN secondary network increases its performance by 5%.

8.1.2.2 Results of Secondary Networks

The performance of the secondary networks that use the best combination output from the primary networks is summarized in Table 8.5. It is noted that the output of the secondary network is the output of the network system and, therefore, the performance of the secondary network is the performance of the network system. The network trained by PNN can determine failure mechanism combination 1, 2, and 3 with a higher accuracy than the network trained by the backpropagation method. In contrast, the network trained by the backpropagation

method has more accuracy in determining failure mechanism combination 4, 5, and 6. For overall performance, the performance of the secondary network trained by the backpropagation method is 3.2% higher than the network trained by PNN. The lowest percent accuracy given by backpropagation is 93.1%, but drops to 84.9% if trained by PNN. Therefore, it is concluded that backpropagation is the better training method and will be selected to use for the rest of the network analysis for failure mechanism determination.

Table 8.5: Summary of Secondary Neural Network Testing Performance

Neural networks training method	Overall Performance (%)	Performance by failure mechanism (%)					
		1	2	3	4	5	6
Backpropagation	97.1	93.1	95.1	94.4	100	100	100
PNN	93.9	100	97.6	100	91.7	84.9	89.2

Note: Failure Mechanism combinations

1 = Matrix cracking

4 = Matrix cracking/ debonding/ fiber break

2 = Matrix cracking/ debonding/ delamination/ fiber break

5 = Delamination

3 = Matrix cracking/ debonding

6 = Delamination/ fiber break

8.2 FAILURE MECHANISM DETERMINATION OF ADDITIONAL SPECIMENS USING NEURAL NETWORK

There are tested specimens with unknown failure mechanisms in the research program. The preliminary network (backpropagation) developed in this chapter will be used to identify the failure mechanisms of these specimens. The AE data of these specimen and the corresponding failure mechanisms will be added to extend the existing AE database. The AE database will then be used to develop the final network system as will be discussed in Section 8.3.

As described in Chapter 6, several additional specimens were tested in the research program. These specimens are (see full descriptions, physical, and AE results in Chapter 6):

1. **BHV1, BHV2, and BHV3:** (box sections subjected to a compression loading)
2. **SW2:** (full scale girder subjected to a four-point bending test)
3. **Chop:** (Dogbone FRP coupon with chopped strand glass fibers subjected to a direct tension test)
4. **Wov:** (Dogbone FRP coupon with glass woven roving structure subjected to a direct tension test)

The failure mechanism of a specimen can vary from one to another during the test. Accordingly, failure mechanism determination by the preliminary network system is performed at every 10% of the ultimate load.

From visual observation, it was found that the failure mechanisms produced in specimens BHV1, BHV2, BHV3, and SW2 are similar. Thus the results of failure mechanism determination for these specimens are presented together in Table 8.6.

Most of the failure mechanism are identified as failure mechanism combination 2 (matrix cracking/ debonding/ delamination/ fiber break) or combination 6 (delamination/ fiber break). Thus, the results show a good agreement with the visual observation at failure, which are mainly associated with delamination. The network can pick up that delamination is present at an early stage in the test, well before the observation from the researchers. Nine out of 60 determination results are not combinations 2 or 6. This yields the network performance to be approximately 85% accuracy for this application. Out of the determination results that are not combinations 2 or 6, three are at very low load (10%) and two of these are delamination (combination 5), which is probably correct. Delamination may start without fiber breakage. The other six that are not combinations 2 or 6 are at the end of two of the flexural tests, when other mechanisms may be coming into play.

When compared among the results of specimens BHV1, BHV2, and BHV3, the results of specimen BHV1 consists mainly of combination 2, while the results of specimen BHV2 consists mainly of combination 6. The results of specimen BHV3 are mainly combination 6, but show some combination 2. This inconsistency of three specimens is attributed to bifurcation buckling, which leads to an uncertain failure mode and inconsistent failure evolution. Thus, the AE data from these specimens and specimen SW2 will not be added to the AE database nor used to re-train the network system.

Table 8.6: Failure Mechanism Determination of Specimens BHV1, BHV2, BHV3, and SW2

Load level	BHV1 Sensor 1	BHV2 sensor 1	BHV3 sensor 1	SW2 sensor 7	SW2 sensor 11	SW2 sensor 15
10%	2	5	4	5	6	6
20%	6	6	6	2	6	6
30%	6	6	6	2	6	6
40%	1	6	6	2	6	6
50%	2	6	6	2	6	6
60%	2	6	6	2	6	6
70%	2	6	6	6	6	6
80%	2	6	2	1	4	6
90%	2	6	6	1	4	6
100%	2	6	2	2	4	6

Note: Failure Mechanism combinations

1 = Matrix cracking

4 = Matrix cracking/ debonding/ fiber break

2 = Matrix cracking/ debonding/ delamination/ fiber break

5 = Delamination

3 = Matrix cracking/ debonding

6 = Delamination/ fiber break

The results from the failure mechanism determination of specimens Chop and Wov are presented in Table 8.7. The failure mechanism results are quite consistent for all sensors. The failure mechanism of specimen Chop was determined to be delamination for a range of 0% to between 30% and 40% of the ultimate load. The failure mechanism of matrix cracking becomes dominant from the end of the delamination range to greater than 90% of the ultimate load. For the final portion up to ultimate load, the failure mechanism includes matrix cracking/ debonding/ delamination/ fiber break.

Table 8.7: Failure Mechanism Determination of Specimen Chop and Wov

Load level	Chop sensor 1	Chop sensor 2	Chop sensor 3	Chop sensor 4	Wov sensor 1	Wov sensor 2	Wov sensor 3	Wov sensor 4
10%	5	5	5	5	5	5	5	5
20%	5	5	5	5	5	5	5	5
30%	5	5	5	1	5	5	5	5
40%	1	5	5	1	5	5	1	1
50%	1	1	1	1	5	1	1	1
60%	1	1	1	1	1	5	1	1
70%	1	1	1	1	1	1	1	1
80%	1	1	1	1	1	6	1	1
90%	1	1	1	1	2	2	2	2
100%	2	2	2	2	2	2	6	2

Note: Failure Mechanism combinations

1 = Matrix cracking

4 = Matrix cracking/ debonding/ fiber break

2 = Matrix cracking/ debonding/ delamination/ fiber break

5 = Delamination

3 = Matrix cracking/ debonding

6 = Delamination/ fiber break

The failure mechanism of specimen Wov also begins with delamination from a range of 0% to closer to 40% of the ultimate load. Also, from a range of 40% to 80% of the ultimate load, matrix cracking governs the failure mechanism.

Between 80 and 90% of the ultimate load and up to ultimate failure, the failure mechanisms are matrix cracking/ debonding/ delamination/ fiber break.

The failure mechanisms from Table 8.9 are checked with the amplitude superimposed with cumulative signal strength vs. load plot as shown in Fig. 8.18 and 8.19. It is found for specimen Chop that high amplitude hits (amplitude of 80 dB or higher), or indications of fiber breaks, appear beyond 90% of the ultimate load. This agrees with the fiber breakage mechanism determined by the preliminary network system (Fig. 8.18). For specimen Wov, high amplitude hits appear beyond 60% of the ultimate load. However, the network classifies this stage as matrix cracking rather than fiber break combination (Fig. 8.19). Therefore, these failure mechanisms are corrected prior to being used as an input data for the final networks.

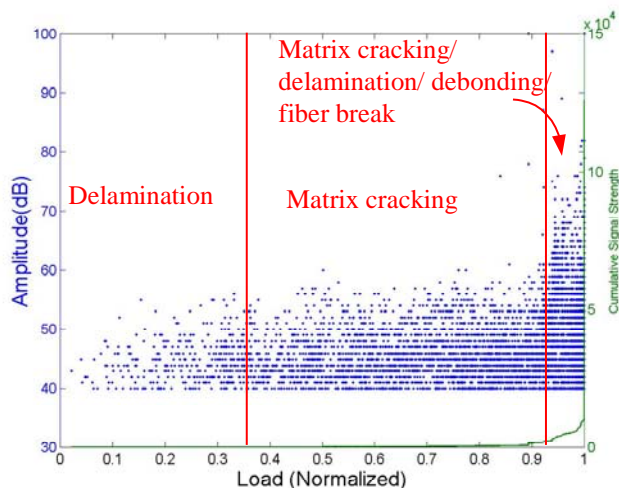


Figure 8.18: Amplitude Superimposed with Cumulative Signal Strength vs. Load Plot of Specimen Chop Showing Failure Mechanisms Determined by Neural Network

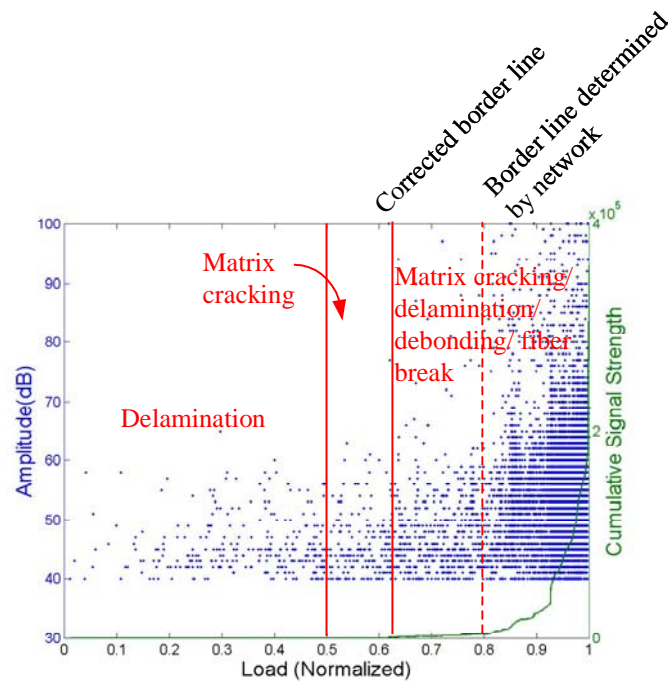


Figure 8.19: Amplitude Superimposed with Cumulative Signal Strength vs. Load Plot of Specimen Wov Showing Failure Mechanism Zones Determined by Neural Network and Its Correction

8.3 FINAL NETWORK SYSTEM

Like the preliminary network system, the input data of the final network system are from the AE database. At this point, the AE database includes AE data of specimens Chop and Wov as well as their failure mechanisms determined by the preliminary network system. The input data are arranged as training and testing data sets. Backpropagation is the only method for training the final network system.

In this section, two final network systems are developed. The first system is developed to perform the failure mechanism determination task, which is

similar to the preliminary network system. The second network system is trained to determine the level of load (in percent of the ultimate load) the specimen had reached. In other words, the network system is trained to determine the damage severity of the specimen.

8.3.1 Final Network System for Determination of Failure Mechanisms

With the additional AE data from specimens Chop and Wov, the number of the data arrays for the network input increases to 800 arrays. Out of 800 data arrays, 610 data arrays were selected to be in the training data set, and the remaining 190 data arrays become the testing data set for the final network system. The AE data are arranged to feed the final primary and secondary networks in the same manner as the primary networks discussed in Section 8.1.1.

The results of the final network system, primary and secondary networks, are summarized in Table 8.8. The overall performance of the final networks is slightly lower than the preliminary networks. This is due to the Correction in the network determination results of specimen Wov. The Amplitude vs. Duration Network with Log Conversion performs the best among the final primary networks with 85% accuracy, while the Cumulative Signal Strength Network has the lowest performance with only 44.5% accuracy. The final secondary network can classify all failure mechanism types with accuracy of approximately 92% and above.

Table 8.8: Testing Performance of Final Primary and Secondary Networks

Final neural networks type	Overall Performance (%)	Performance by failure mechanism (%)					
		1	2	3	4	5	6
Primary							
Amplitude distribution1	69.8	83.8	76.1	61.1	75.0	82.5	40.5
Cumulative amplitude distribution1	52.9	89.2	78.3	0	33.3	60.0	56.8
Amplitude vs. duration	76.0	59.5	78.3	77.8	91.7	65.0	83.8
Amplitude vs. duration with linear conversion	83.8	78.4	82.6	83.3	91.7	80.0	86.5
Amplitude vs. duration with log conversion	85.0	78.4	84.8	77.8	100	80.0	89.2
Cumulative signal strength	44.5	86.5	67.4	5.6	0	42.5	64.9
Secondary neural network	96.2	91.9	93.5	94.4	100	97.5	100

8.3.2 Final Network System for Determination of Damage Severity

This section discusses the organization of the primary and secondary networks of the final network system. The performance results of the primary and secondary networks are also included.

8.3.2.1 Primary and Secondary Network Organization of Final Network

Seven primary networks are used. This includes all primary networks that are used in the network system for determination of failure mechanism and the Historic Index and Severity Network. The input neurons of each network are organized by three schemes. All seven primary networks with these schemes are trained by backpropagation and the scheme that yields the best network performance will be selected. Then the secondary network is developed.

The first scheme uses two types of input: AE and material information. The AE information is arranged from the seven AE plots, and three material types, similar to the method used for the preliminary networks. The network consists of ten output neurons, which represent ten load levels (10% to 100% of

the ultimate load) or damage severity levels. Figure 8.20 shows the network diagram using the first scheme.

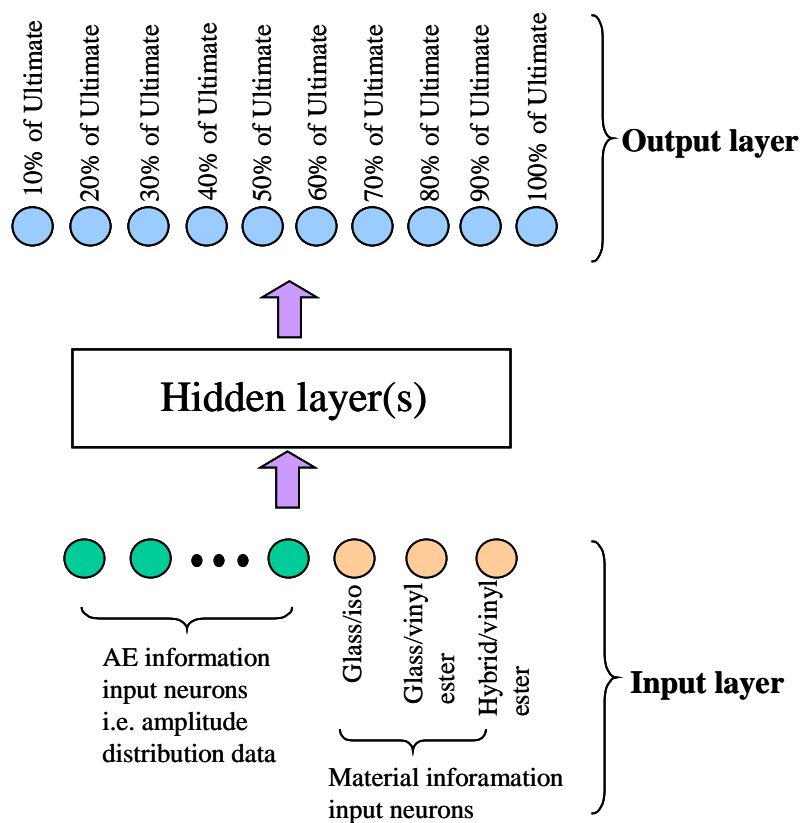


Figure 8.20: First Scheme of Primary Network Using AE data and Material Information as Network Input

The second scheme uses three types of input information: AE, material, and failure mechanism (Fig. 8.21). The network's output layer is organized similarly to the first scheme, which consists of ten output neurons representing ten damage severity levels. This second scheme is expected to provide a higher

performance than the first scheme since more information is used as the network input.

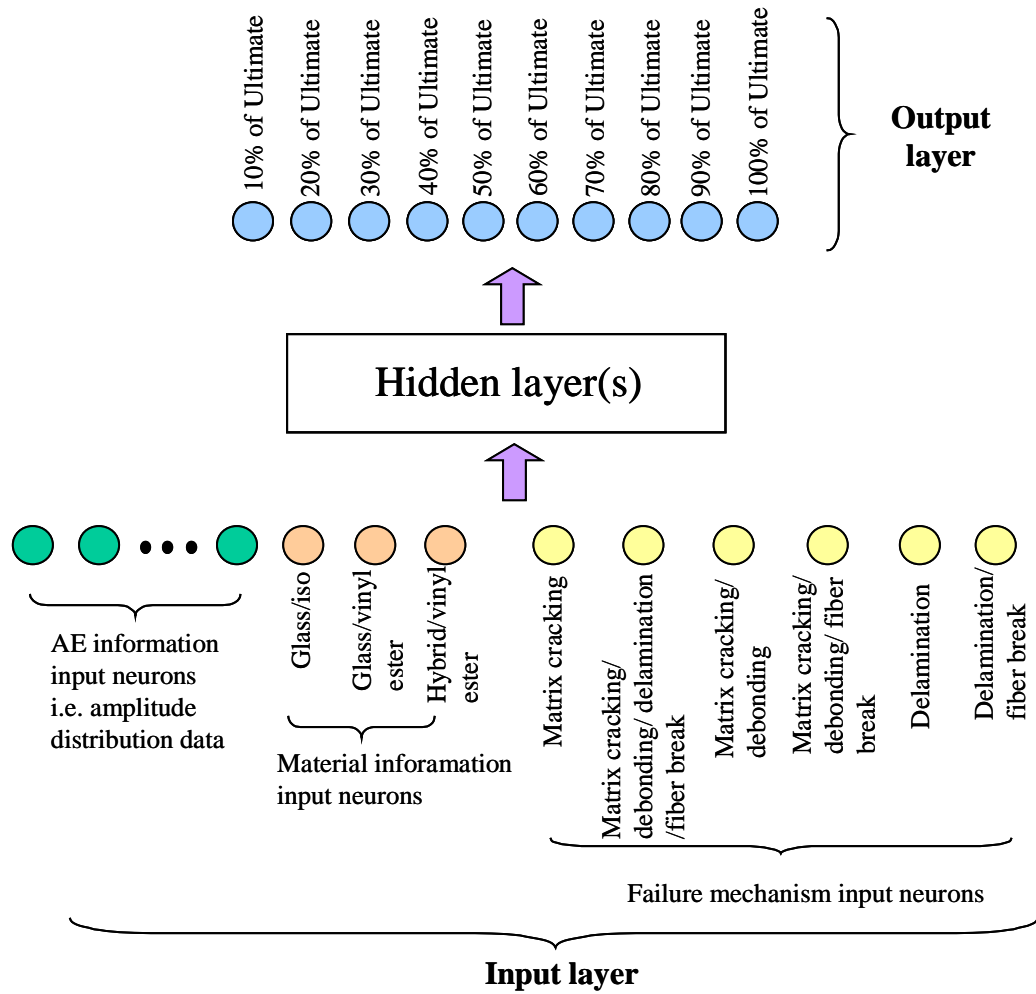


Figure 8.21: Second Scheme of Primary Network Using AE data, Material, and Failure Mechanism Information as Network Input

The network with the third scheme of input is trained by data only from 0% to 70% of the ultimate load. Accordingly, the output layer of the network consists of only seven neurons representing seven damage severity levels (Fig.

8.22). The input information will include failure mechanism information if the second scheme proves that by including failure mechanism information as input, a better testing performance is achieved. There are two reasons of using data only from 0% to 70% of the ultimate load, which are:

1. This very high load level is beyond non-destructive practice. This range is also beyond a design level that will be reached in the field testing.
2. The amount of AE data at higher load levels ($> 70\%$ of ultimate) can increase rapidly. This may bias the AE characteristics of the lower load levels.

Therefore, the networks trained with this scheme are expected to perform better than the first two schemes. The backpropagation training method is used to train these networks.

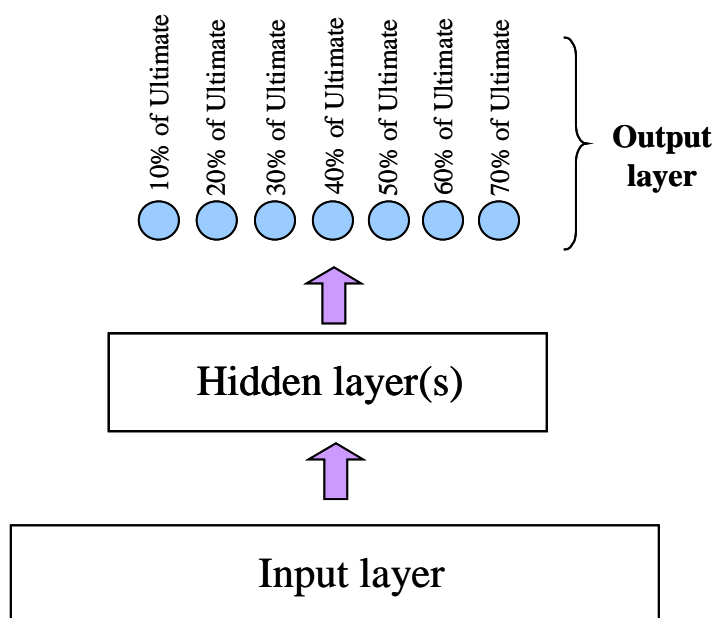


Figure 8.22: Third Scheme of Primary Network Only Using Data From 0% to 70% of Ultimate Load

8.3.2.2 Testing Results of Final Primary and Secondary Networks

As noted above, the networks for this task are trained by backpropagation. In addition, a set of networks is trained by PNN training method. The performance of the primary networks, which are tested with the testing data set, is summarized in Table 8.9. It is found that the second scheme, the network trained with failure mechanism information, performs slightly better than the first scheme. Thus, the third scheme networks are constructed based on the second scheme. As expected, the third scheme networks yield the best performance among all schemes.

With the third scheme, the performance of the primary network trained by backpropagation is below 40% accuracy. The performance of some of the primary networks trained by PNN is even below those trained by backpropagation, but three networks perform better. Out of these three networks, the Cumulative Signal Strength Network trained by PNN shows a performance of 61.7% accuracy, which is 23% higher than the best one trained by backpropagation.

Table 8.9: Summary of Testing Performance of Final Primary Neural Networks (with Load Level Determination)

Final primary neural networks type	Overall Performance (%)			
	1 st scheme (backprop)	2 nd scheme (backprop)	3 rd scheme (backprop)	3 rd scheme (PNN)
Amplitude Distribution1	30.5	34.7	34.6	23.3
Cumulative Amplitude Distribution 1	30.0	33.2	34.6	28.6
Amplitude vs. Duration	24.7	29.0	30.8	35.3
Amplitude vs. Duration with Linear Conversion	33.7	34.7	35.3	22.6
Amplitude vs. Duration with Log Conversion	31.6	36.8	36.8	30.1
Historic Index and Severity	19.5	23.7	24.6	31.6
Cumulative Signal Strength	29.5	33.2	38.4	61.7

The results from the third backpropagation scheme of the primary networks are used as an input for the secondary network. For this network system, the outputs from all seven primary networks are used. Therefore, the structure of the secondary network consists of 49 input neurons, which receive data from seven output categories from seven primary networks. Also, the output layer of the secondary network will consist of seven neurons representing seven levels of damage severity.

For the PNN network system, it is found that the primary network combination that yields the best secondary network performance consists of the output from:

1. Cumulative Amplitude Distribution Network 1
2. Amplitude vs. Duration Network
3. Historic Index and Severity Network
4. Cumulative Signal Strength Network

After being trained, the secondary network is tested. Table 8.10 presents the performance results of the secondary network.

Table 8.10: Testing Performance of Final Secondary Network

Training method	Overall Performance (%)	Performance by load (damage severity)						
		10%	20%	30%	40%	50%	60%	70%
Backprop	48.9	79.0	57.9	31.6	31.6	36.8	52.6	52.6
PNN	73.7	79.0	89.5	73.7	68.4	63.1	57.9	84.2

For backpropagation training method, the overall performance of the secondary network is 48.9% accuracy. This shows that the performance of the secondary network improves from the primary network by 10%. It is noted that

the network can determine loads at 10% of ultimate with the greatest accuracy, while it determines loads at 30% and 40% of ultimate with the least accuracy.

If the network prediction that falls within 10% of the actual severity is counted as a correct prediction, then the network performance improves to 81.2% accuracy. Also, if the network prediction that falls within 20% of the actual severity is counted as a correct prediction, the network performance improves to 89.5% accuracy. This improvement is because the network determines the range of severity results rather than exact results.

For the PNN training method, the overall performance of the secondary network is 74% accuracy, which is approximately 25% higher than that trained by backpropagation. Also, the performance in each damage severity level is higher than that trained by backpropagation. This explains that PNN is a more suitable training method for the damage severity determination task.

8.4 SUMMARY

The preliminary network systems are initially developed to determine failure mechanisms using AE data of known failure mechanisms. Two levels of neural networks in a system, primary and secondary, are organized in order to obtain the highest network performance. Two training methods, backpropagation and PNN, are also used. It is found that the network system trained by the backpropagation method yields performance 3.2% higher than the network system trained by the PNN method.

The preliminary network system (backpropagation) is then applied to additional AE data from additional test specimens to determine their failure mechanisms. The data from specimens Chop and Wov with their network

determined failure mechanisms are added to the AE database. At this point, the AE database covers the full range of FRP structures.

Two final network systems are developed and trained with the complete AE database. The first system is trained for the failure mechanism determination task, while the second system is trained to determine the damage severity. Both final network systems are tested with the testing data set. The performance of the first network system trained by backpropagation (for failure mechanism determination) is as high as 96% accuracy. The performance of the second network system (for damage severity determination) is only 44% accuracy if trained by backpropagation method. However, if the network system is trained by the PNN method, the performance increases to 74% accuracy. Summaries of the performance of the final network systems are shown in Fig. 8.23 and 8.24.

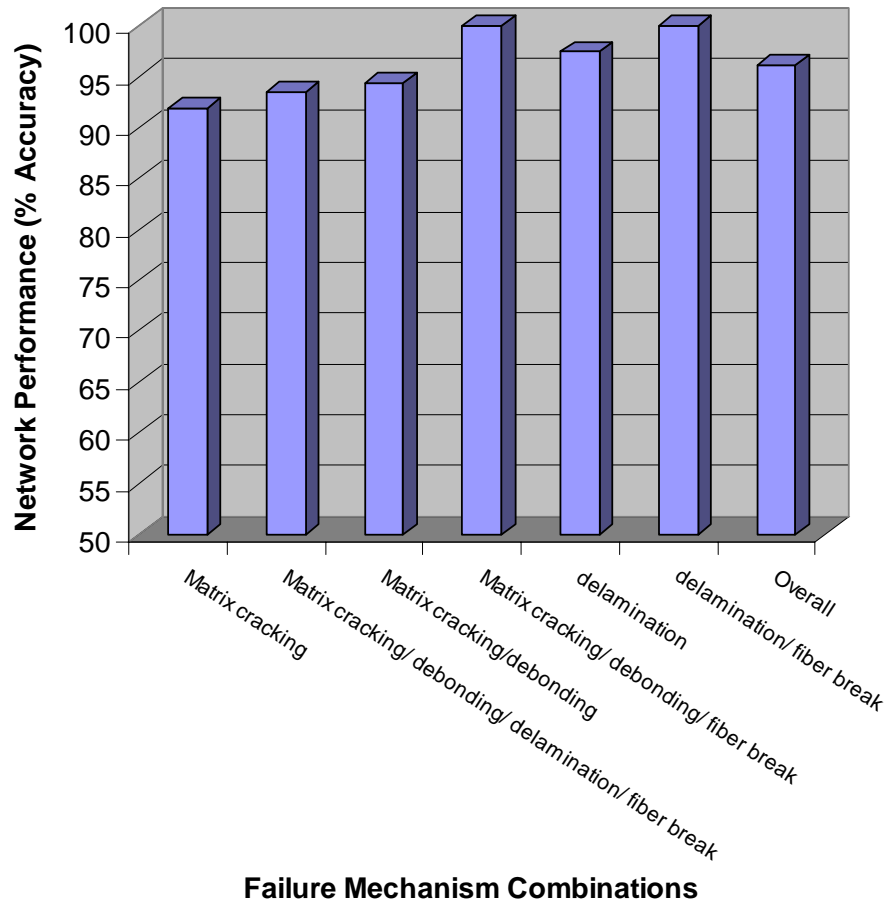


Figure 8.23: Performance of Final Network for Failure Mechanism Determination

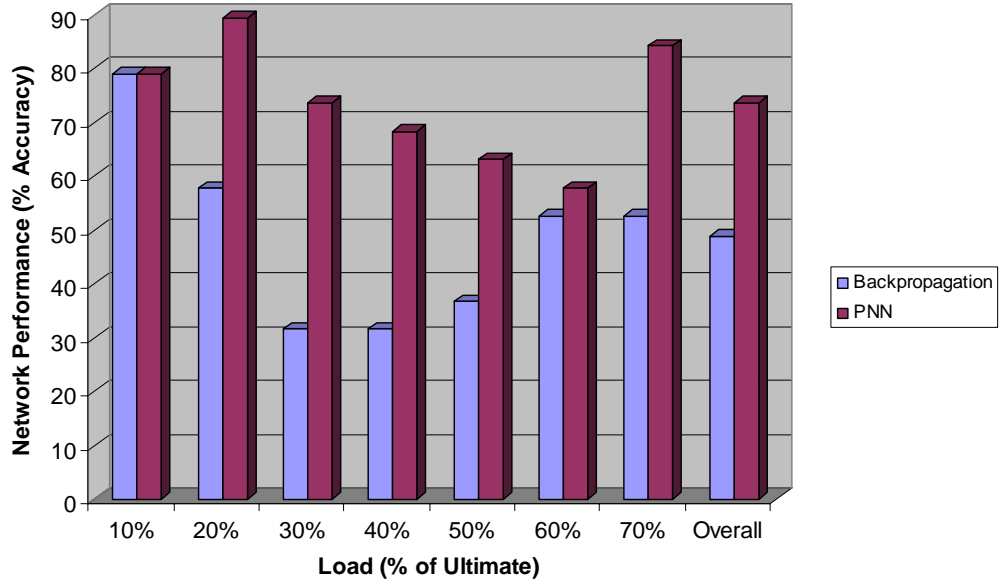


Figure 8.24: Performance of Final Network for Level of Load Determination

CHAPTER 9

Neural Network Applications

In this chapter, the neural network systems developed in Chapter 8 are applied to determine failure mechanisms and damage severity of additional test specimens. One specimen is a full-scale trapezoidal FRP girder, which was subjected to a three-point bending test. The other specimens are FRP coupons subjected to a three-rail shear test. The results from the network are compared with the actual from visual inspection. This way, the network performance and the network consistency can be evaluated

9.1 TRAPEZOIDAL GIRDER

The trapezoidal girder (TK1) was fabricated by Tankinetics Inc. It was made with DerakaneTM 411-350 vinyl ester resin reinforced with glass fibers. The entire specimen was fabricated by the contact molding method.

The test setup of the trapezoidal girder is discussed below. The results of the test, including visually observed physical results, AE results, and failure-mechanisms determined by the neural networks are also reported.

9.1.1 Test Setup and Instrumentations

The overall length of the girder was 30 ft. It had a constant depth of 18 in. The central 10 ft. of the girder had a constant cross section, while the cross sections of the 10-ft long portions at each end were tapered from the middle towards the ends. The girder had web connectors on the top flanges to provide a shear connection for a concrete deck. However, this test was performed without a concrete deck. The dimension of the overall specimen and its cross section at midspan and at the ends are given in Figures 9.1 and 9.2.

Design of the girder was such that the concrete deck provided lateral stability to the webs. In the absence of the deck, additional measures were needed to prevent the girder from premature web buckling during the test. Two FRP square tubes were used to brace the webs at the center of the girder. Details are shown in Figure 9.3. The tubes had 3 in. x 3 in. cross-section and were 111 in. long. The tubes were tied to each other by a steel through-rod at the center and at both ends. Teflon sheets were inserted between the interface of the girder and the tubes to prevent friction noises, which would interfere with the genuine AE.

Three steel rods were also used to clamp the webs together where the point load is applied. In addition to the tubes and steel rods, four carpenter clamps were used to brace the webs. Two clamps were placed along each tapered portion. Details of the bracing tubes, steel rods and carpenter clamps are shown in Figures 9.4, and 9.5 respectively.

The girder was loaded in three-point bending. The point load was applied at a location 37 in. from the south end of the girder. A spreader beam was used to apply the load to both webs. Figure 9.6 shows the experimental set up for the girder. Loading was applied to the girder in a stepwise schedule. The specified load schedule is shown in Fig. 9.7.

AE was monitored during testing. Ten R15I sensors were mounted on the webs and bottom of the specimen. The AE data acquisition system used was the Transportation Instrument. Figure 9.8 shows the sensor locations on the girder.

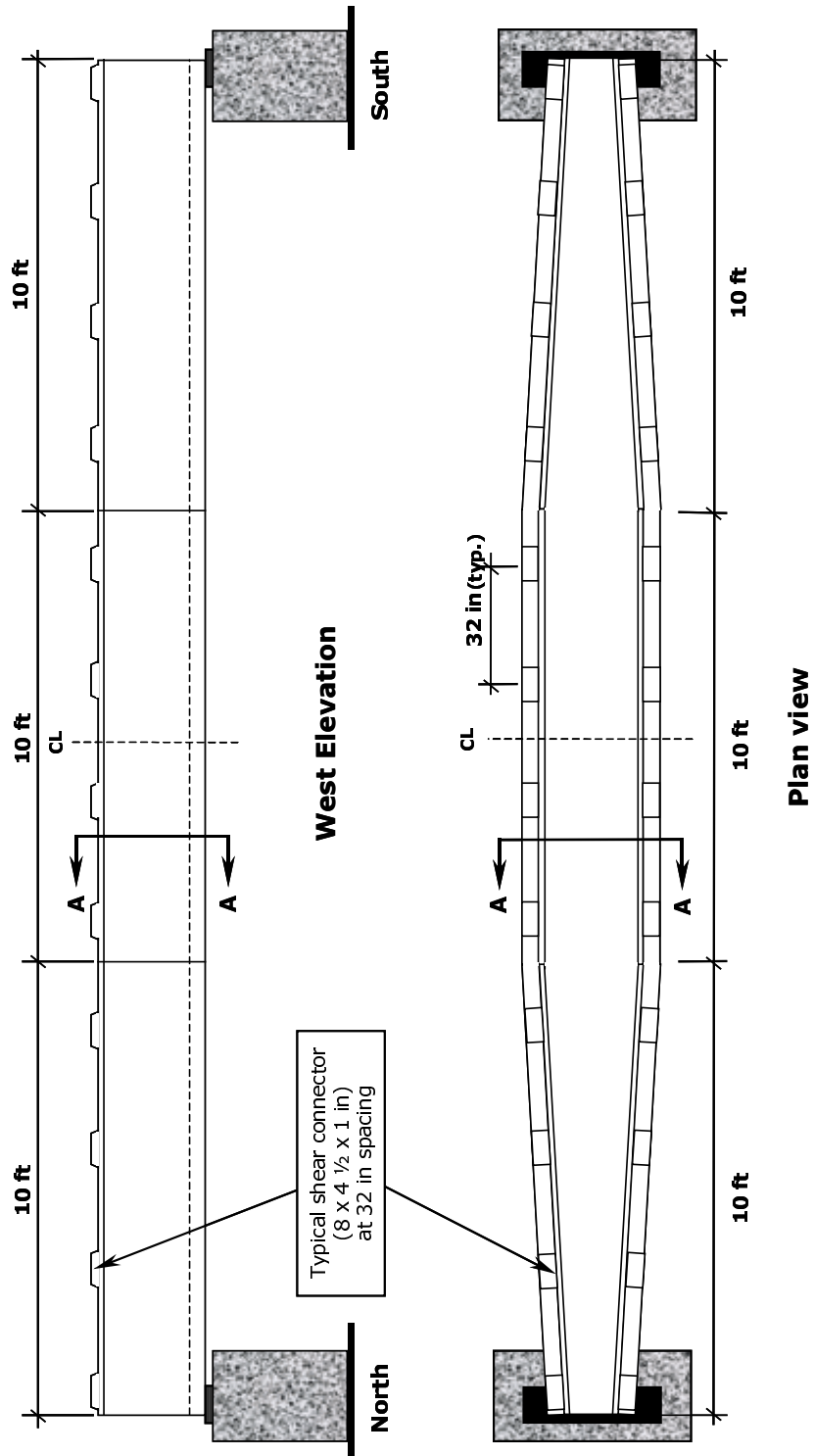


Figure 9.1: Dimensions of Specimen TK1 (Ulloa, 2002)

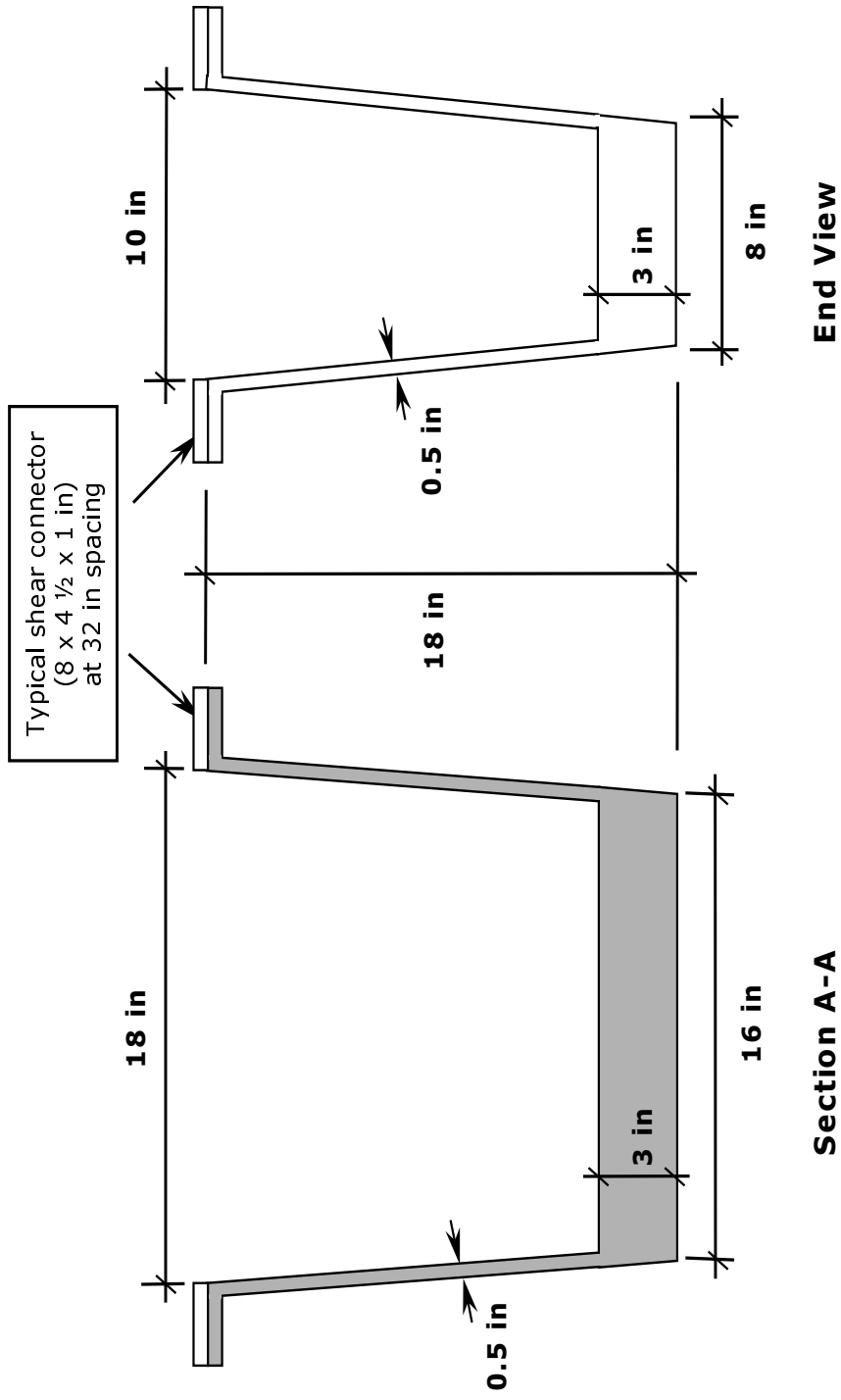


Figure 9.2: Specimen TK1 Cross Sections (Ulloa, 2002)

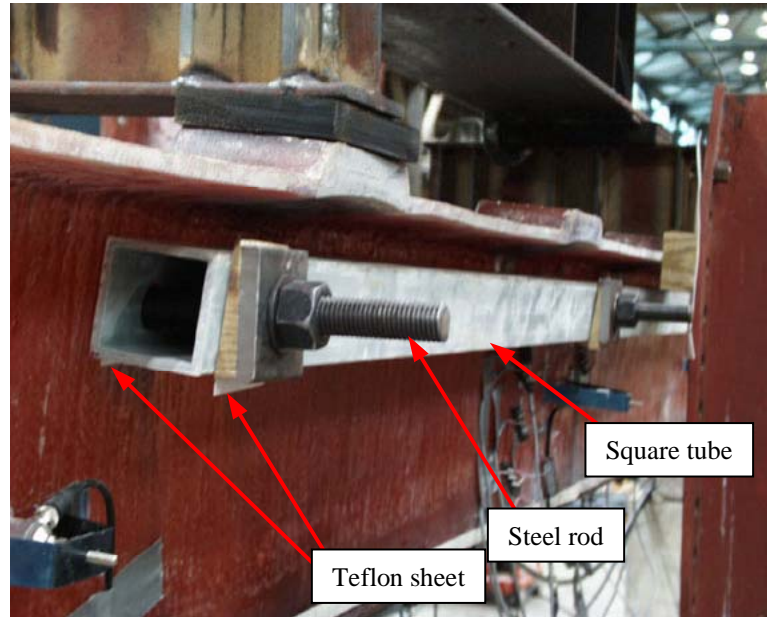


Figure 9.3: Bracing FRP Tubes of Specimen TK1

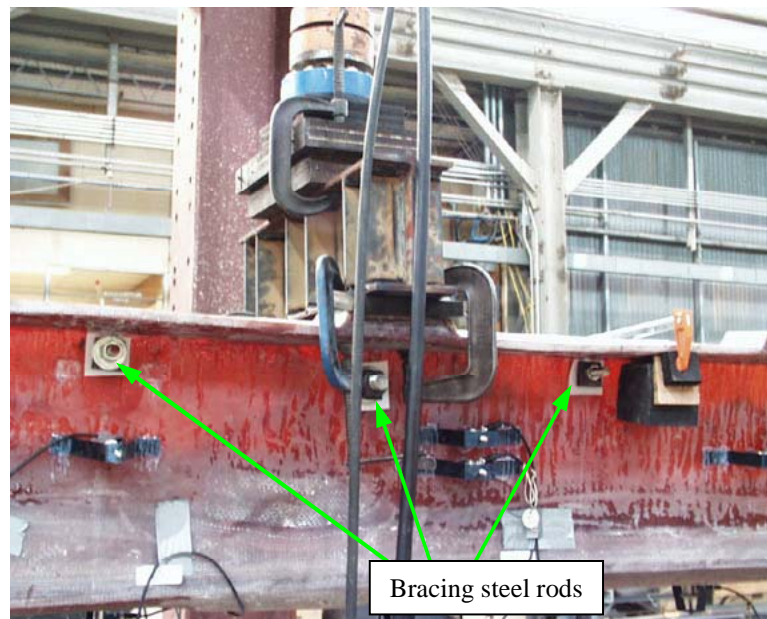


Figure 9.4: Three Bracing Steel Rods on Specimen TK1

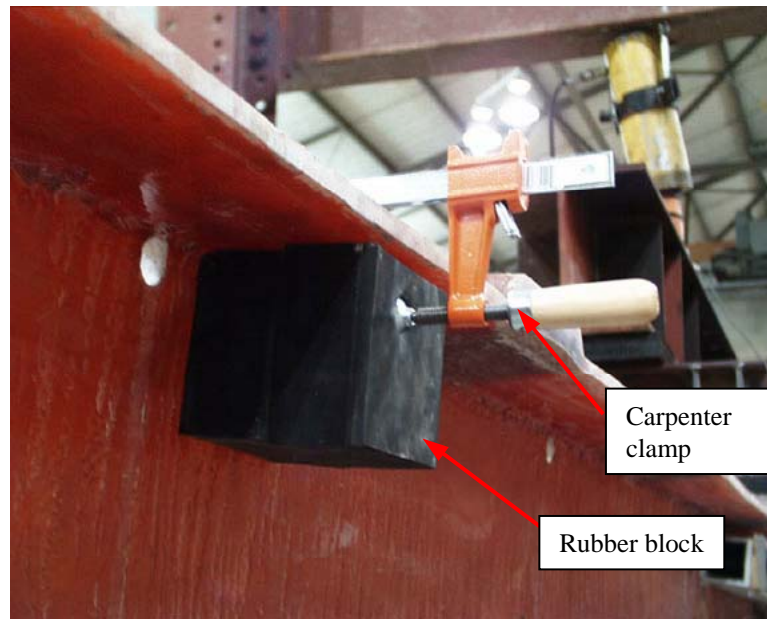


Figure 9.5: Carpenter Clamp on Specimen TK1

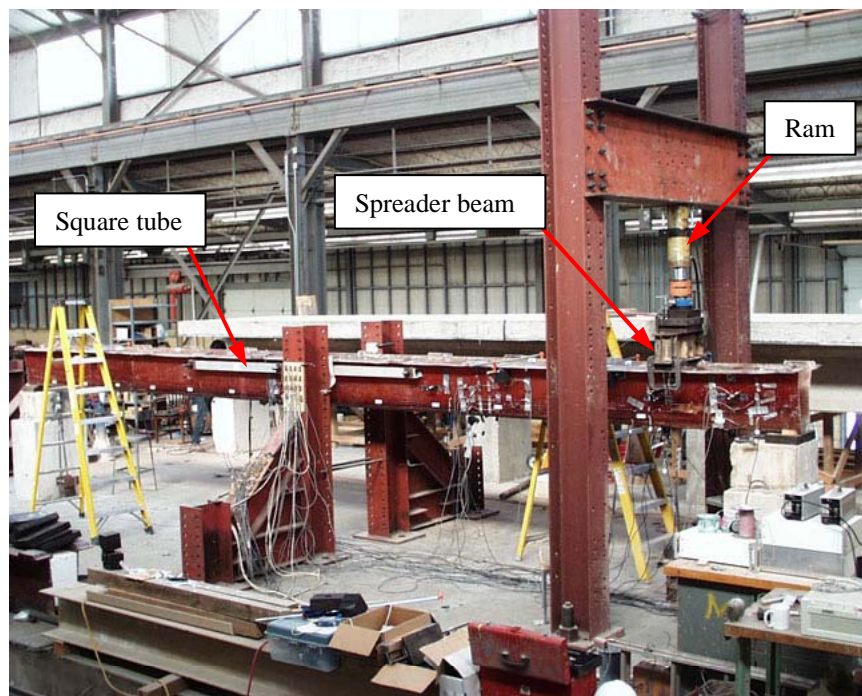


Figure 9.6: Specimen Test Setup

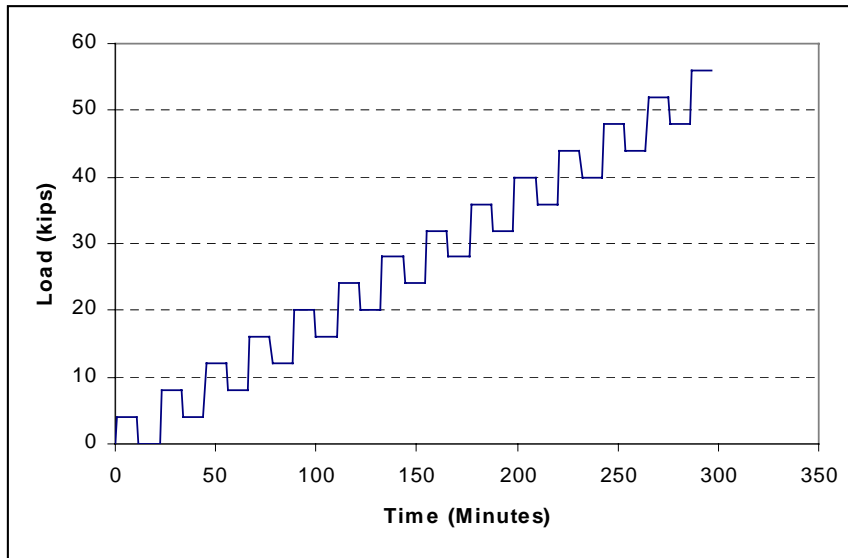


Figure 9.7: Specified Load Schedule

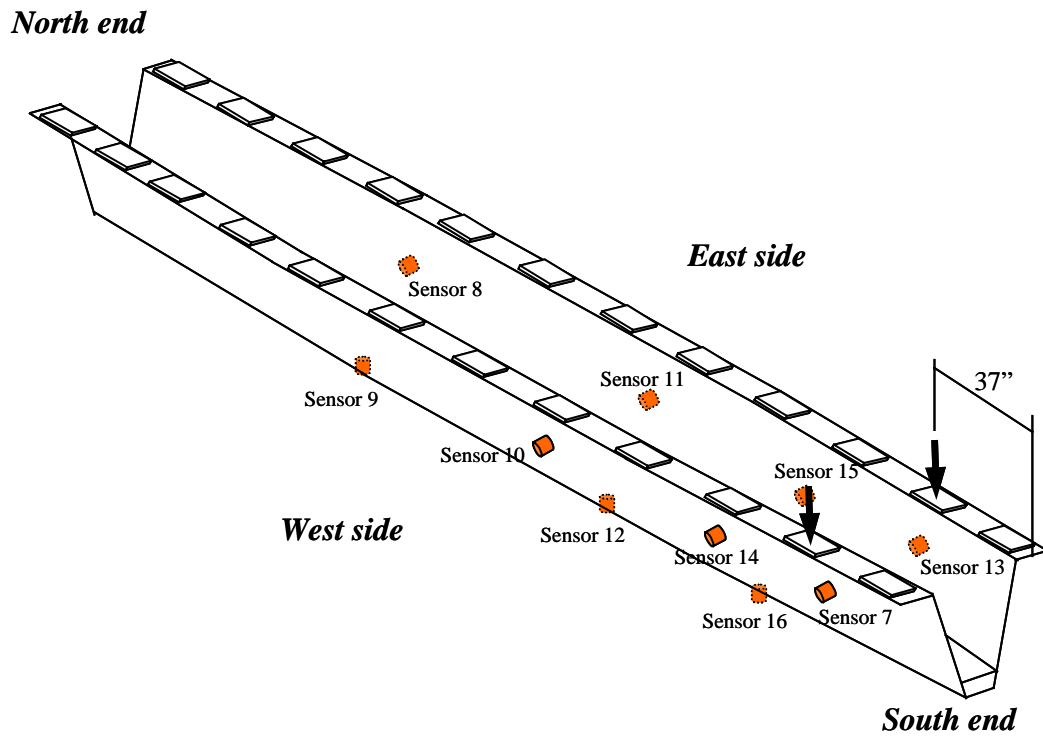


Figure 9.8: Sensor Locations of Specimen

9.1.2 Test Results

The loading was applied stepwise to the girder until failure. The ultimate load at failure was 56 kips. The load-deflection at midspan shows a linear relationship from the beginning of load application to the ultimate load (see Fig. 9.9). Noises were audible during a load hold at 52 kips. A series of noises was heard again during the 56 kips load before the specimen failed at the same load. A buckling delamination failure occurred at the east flange under the point load (see Fig. 9.10). Underneath the top flange where the delamination occurred, a significant numbers of matrix cracks involving fiber breaks were observed (see Fig. 9.11). In addition, several other cracks at surrounding locations could be seen. Cracks near the steel rod are shown in Fig. 9.12. Cracks in the web where the web joins with the bottom flange of the girder are shown in Fig. 9.13. All the damage occurring on the east web and flange of the girder were observed to be associated with fiber breaks.

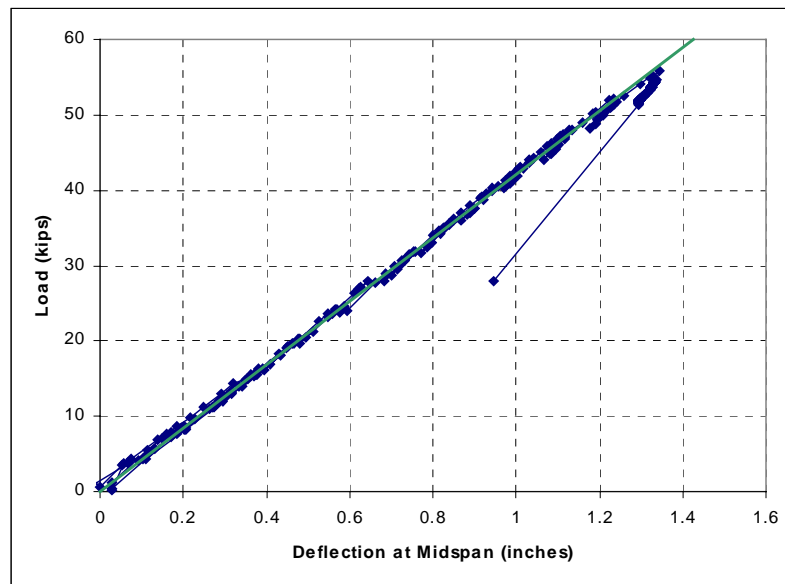


Figure 9.9: Load-Deflection Response at Midspan

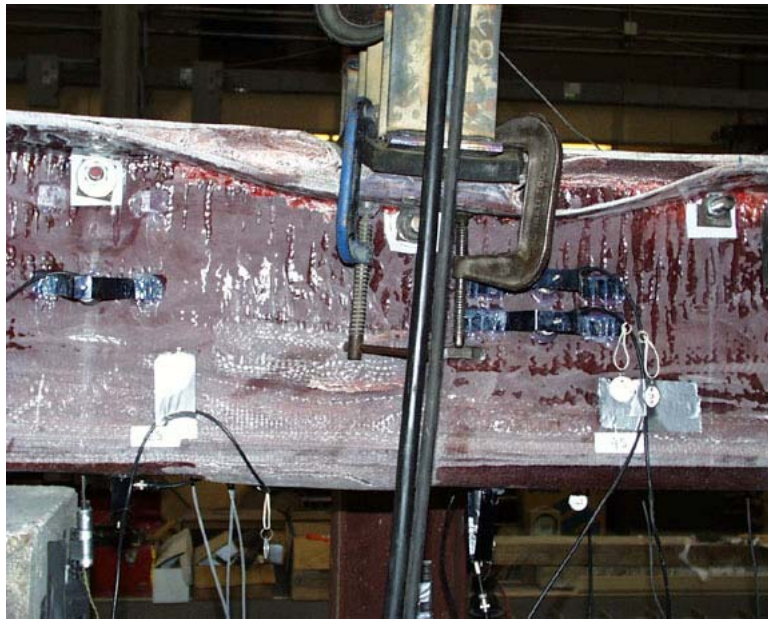


Figure 9.10: Buckling Delamination at Top Flange (East Side)

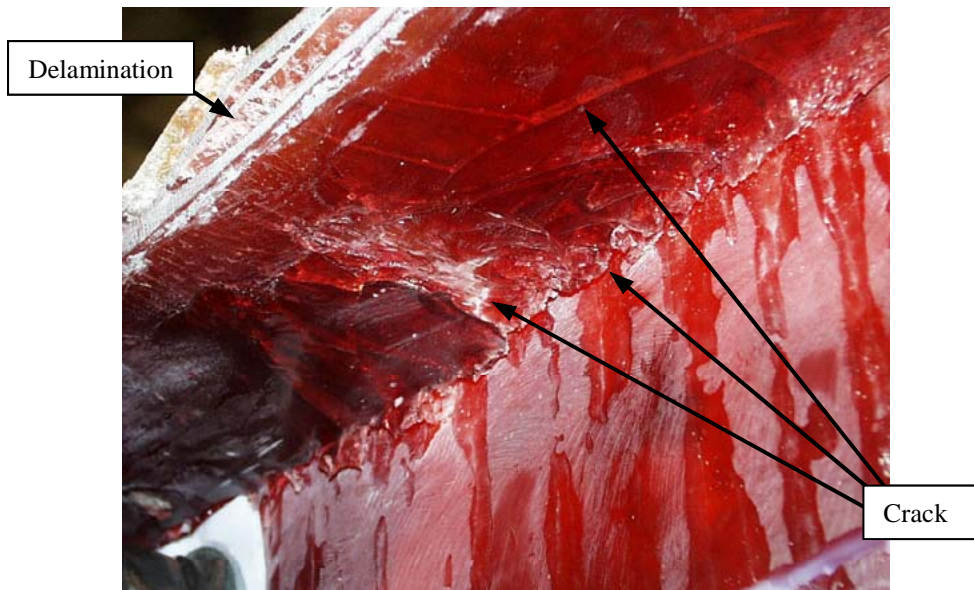


Figure 9.11: Cracks Under Top Flange Where Delamination Occurred (East Side)

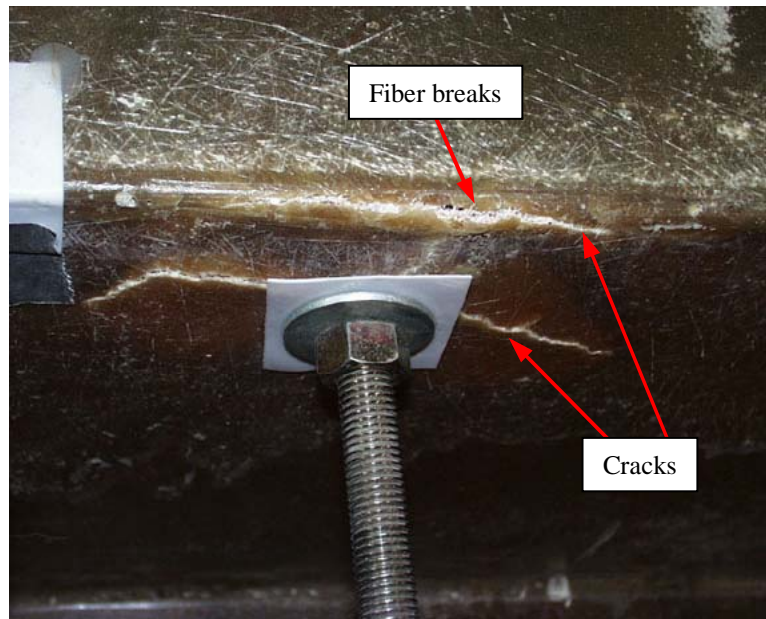


Figure 9.12: Cracks at Steel Rod (East Side)

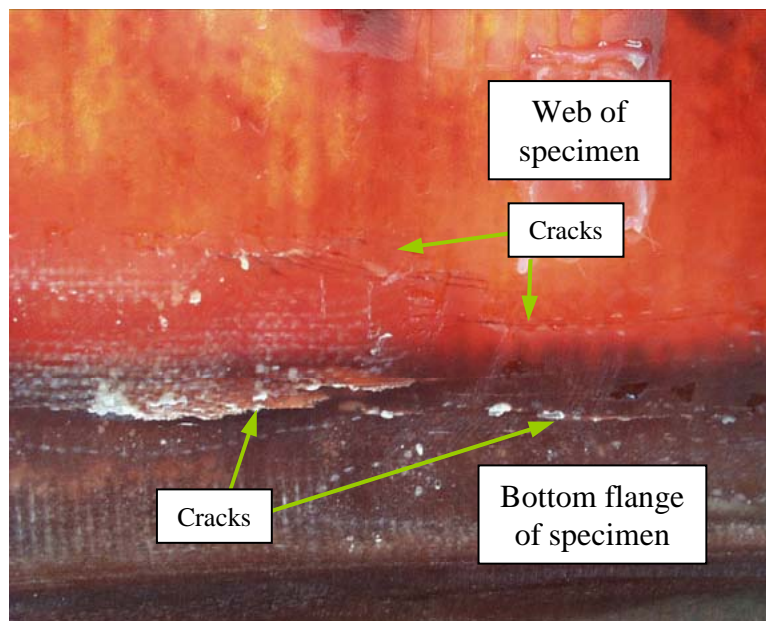


Figure 9.13: Cracks at Web Where Web Joins Bottom Flange of Girder (East Side)

9.1.3 Failure Mechanism and Damage Severity Determined by Neural Networks (Only Backpropagation Training Method)

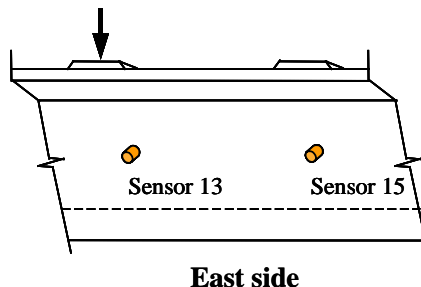
The final network systems developed in Chapter 8 are applied to the AE data of the trapezoidal girder. Based on visual inspection, all of the damage that occurred during testing was located on the east web under the point load. Accordingly, to be able to validate the failure mechanisms determined by the network with the actual damages, data from sensors 13 and 15 (mounted on the east web) are evaluated first by the network. The results of the network determination are presented in Table 9.1.

From Table 9.1, the severity results are disappointing, but the results of the failure mechanism determination are clean, meaning that there is no jumping around of the result numbers. The damage development is clearly comprehensible, which starts from delamination and changes to delamination/matrix cracking/ debonding/ fiber break.

As expected, the failure mechanism results from sensor 15 follow behind the development of the damage in the area of sensor 13. This is due to the fact that sensor 15 is located 2 feet away from the sensor 7 where the center of visual damage occurs. Therefore, it indicates that this failure mechanism results are quite reasonable.

After 70% of the ultimate load, the determination ideally should remain at 70% severity due to the use of the third input scheme of this network system (see Section 8.3.2.1 of Chapter 8). This scheme only considers data up to 70% of ultimate.

Table 9.1: Network Determination of Sensors 13 and 15 (East Side of Girder)



Actual Load (% of Ultimate)	Determination from Network			
	Sensor 13		Sensor 15	
	Failure mechanism	Damage severity	Failure mechanism	Damage severity
10%	5	70%	5	10%
20%	5	70%	5	10%
30%	5	70%	5	20%
40%	5	70%	5	10%
50%	5	70%	5	10%
60%	2	70%	5	10%
70%	2	70%	5	30%
80%	2	70%*	2	70%*
90%	2	70%*	2	70%*
100%	2	70%*	2	70%*

Note: Failure Mechanism combinations

1 = Matrix cracking

4 = Matrix cracking/ debonding/ fiber break

2 = Matrix cracking/ debonding/ delamination/ fiber break

5 = Delamination

3 = Matrix cracking/ debonding

6 = Delamination/ fiber break

* The network used for this analysis is intended for use at lower loads and will not register a damage severity greater than 70%

For a complex structure and test setup like the trapezoidal girder, the damage severity is expected to increase with load, but not necessarily from 10%

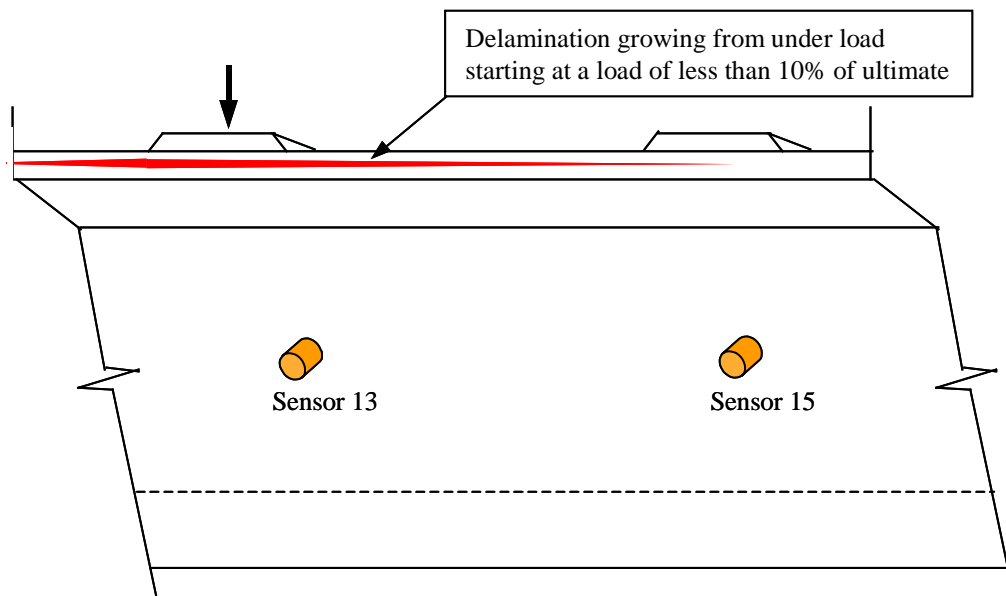
severity at the 10% load level. Also, the rate of increase is not necessarily gradual. It can increase so quickly from 0% to 70% severity within a 10% increment of the applied load. This depends on how far the sensor is located from the damage site and how the damage propagates. Based on visual inspection experience, delamination can propagate so rapidly from one location of the specimen to another possibly making severity rise rapidly. Also, even though the damage reaches 70% severity, it may damage the structure only in a small local area. The entire structure may remain stable and may be able to take a considerable amount of additional load.

Note that, based on the testing performance of the network in determining damage severity as discussed in Chapter 8, the network has 44% accuracy to give correct results. However, this number increases to 81% accuracy if the network prediction that falls within 10% of the actual severity is counted as a correct prediction.

The delamination severity in the area of sensor 13 developed so quickly from 0% to 70% severity within the first 10% of the ultimate load. It is because sensor 13 is located near the center of the delamination failure. The delamination severity in the area of sensor 15 developed much slower from 0% to 30% severity during load span of 0% to 70% of the ultimate. This is also because sensor 15 is located 2 feet away from the center of the damage.

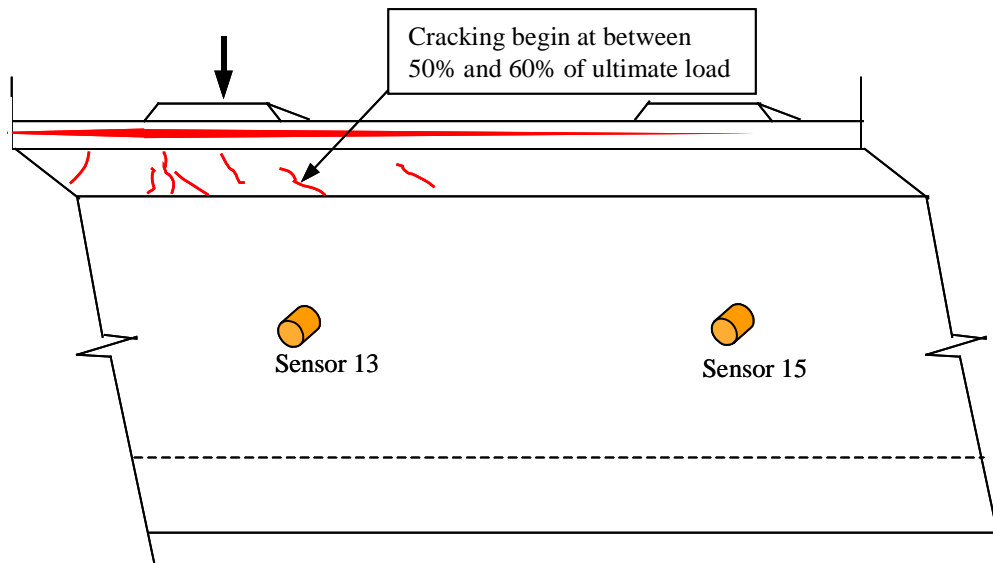
Together with both the failure mechanism and the damage severity results given by the network, a clear picture of the damage propagation in the east web area can be illustrated (Fig. 9.14). The delamination began first under the load, close to the area where sensor 13 is mounted. This delamination began at a load as low as 10% of the ultimate. Delamination also extended close to the area of sensor 15, but with low severity (Fig. 9.14a). Once the load was increased more, the delamination grew, became more severe and cracking, which is associated

with matrix cracking/ debonding/ delamination/ fiber break, underneath the flange occurred near sensor 13. At this point, only delamination remained in the area of sensor 15, with a low severity (Fig. 9.14b). After 70% of the ultimate load, cracks underneath the flange propagated to occur in the area of sensor 15 with a high severity (Fig. 9.14c). These results agree with the damage from visual inspection confirming that the network results are reliable.

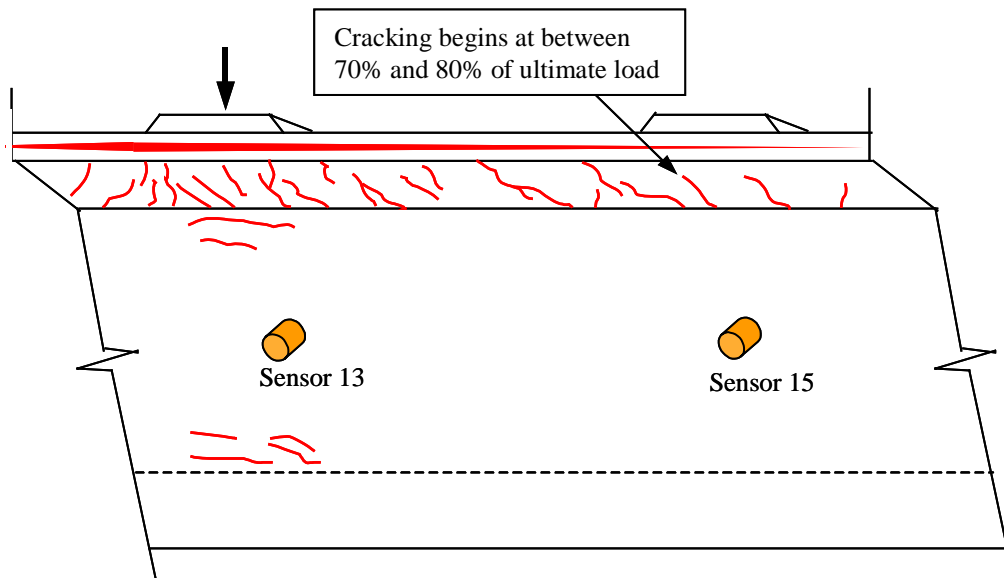


a) Delamination at Flange Under Point Load Extending to Sensor 15

Figure 9.14: Illustration of Damage Propagation on East Side of Girder



b) Cracking Occurring Underneath Top Flange Close to Sensor 13



c) Cracking Propagation Near Sensor 15

Figure 9.14 (cont'd): Illustration of Damage Propagation on East Side of Girder

Damage on the west side of the girder could not be seen by the eye, thus, the determination results from the network on this side of the girder cannot be validated. However, the failure mechanisms determined from the network can be related with the damage of the east side of the girder. This is because both webs girder are loaded in the same manner and theoretically should be subjected to the same damage development.

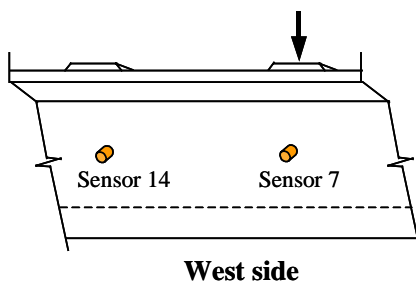
The network is applied to the AE data from sensors 7 and 14, which were mounted on the west web of the girder close to the point load. The results of the network determination of both sensors are presented in Table 9.2.

The results follow the same general pattern as sensors 13 and 15 discussed previously. This starts with delamination, and finally changes to matrix cracking/ debonding/ delamination/ fiber break at the ultimate load. Damage at sensor 7 develops slower than the damage at sensor 13 and has more matrix cracking and fiber breakage. This suggests that there is not a clear delamination at sensor 7 as was the case with sensor 13. This was confirmed by visual observation. Damage at sensor 14 develops faster than the damage at sensor 15 and has more matrix cracking and debonding. The absence of fiber breaks in the area of sensor 14 until 80% of the ultimate load confirms that the damage in the area of sensor 14 develops with a slower rate than that in the area of sensor 7. This is attributed to the effect of damage propagation on the specimen.

The failure mechanism results have only a small amount of scatters at 100% of the ultimate load for sensor 7 and at 70% of the ultimate load for sensor 14. The damage severity increases to 30% at 20% of the ultimate load for sensor 14, but returns to 20% for subsequent load increases.

It can be seen that the damage development in the area of sensor 14 follows behind that in the area of sensor 7, with a slower rate. This is similar to the damage development of the east side of the girder.

Table 9.2: Network Determination of Sensors 7 and 14 of Specimen TK1



Actual Load (% of Ultimate)	Determination from Network			
	Sensor 7		Sensor 14	
	Failure mechanism	Damage severity	Failure mechanism	Damage severity
10%	5	30%	5	10%
20%	4	50%	5	30%
30%	4	70%	5	20%
40%	4	70%	5	20%
50%	4	70%	3	20%
60%	4	70%	3	20%
70%	2	70%	5	20%
80%	2	70%*	2	70%*
90%	2	70%*	2	70%*
100%	4	70%*	2	70%*

Note: Failure Mechanism combinations

1 = Matrix cracking

4 = Matrix cracking/ debonding/ fiber break

2 = Matrix cracking/ debonding/ delamination/ fiber break

5 = Delamination

3 = Matrix cracking/ debonding

6 = Delamination/ fiber break

* The network used for this analysis is intended for use at lower loads and will not register a damage severity greater than 70%

At this point, it is shown that the network results give a clear picture of the damage propagation on the west side of the girder, which follows the same damage development on the east side of the girder. Thus, it can be concluded that the network results on this side of the specimen is reliable and as was expected.

9.2 RAIL SHEAR TESTS

This test is designed for determining the in-plane shear properties of high-modulus FRP specimens. The test setup and procedure follow the ASTM D 4255, Procedure B (three-rail shear test). The test was monitored with AE. The final network system developed in Chapter 8 will be applied to this AE data to determine the failure mechanisms and damage severity. The results of the network analysis are reported in this section.

9.2.1 Test Setup and Instrumentations

The test setup consists of three pairs of parallel rails, which were attached to the specimen by through bolts (see Fig. 9.15). The exterior pairs of rails were attached to the base plate. The middle pair of rails was inserted through a slot in the top of the base fixture and was loaded in compression so as to apply a shear load to the specimen.

Three FRP specimens were tested for this research. The first and the second specimens (SHEAR1 and SHEAR2) were cut from beam IKG, which was made of vinyl ester reinforced with glass fibers. The third specimen (SHEAR3) was cut from a glass/isophthalic polyester FRP plate. The fiber structure of this plate consisted mainly of continuous strand fiber layers. Also, the fiber structure had five unidirectional fiber layers. However, these unidirectional fiber layers were observed to be very thin compared to the unidirectional fiber layers in beam IKG.

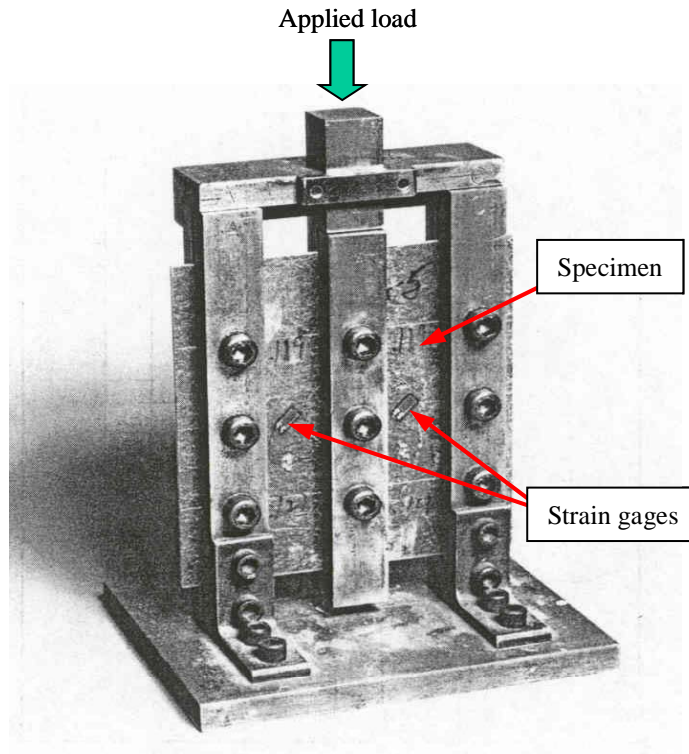


Figure 9.15: Three-Rail Shear Test Setup (ASTM D 4255)

The specimens were placed in the test setup such that the fibers in the unidirectional layer were oriented horizontally (perpendicularly to the applied load). The dimensions of the specimen are shown in Fig. 9.16.

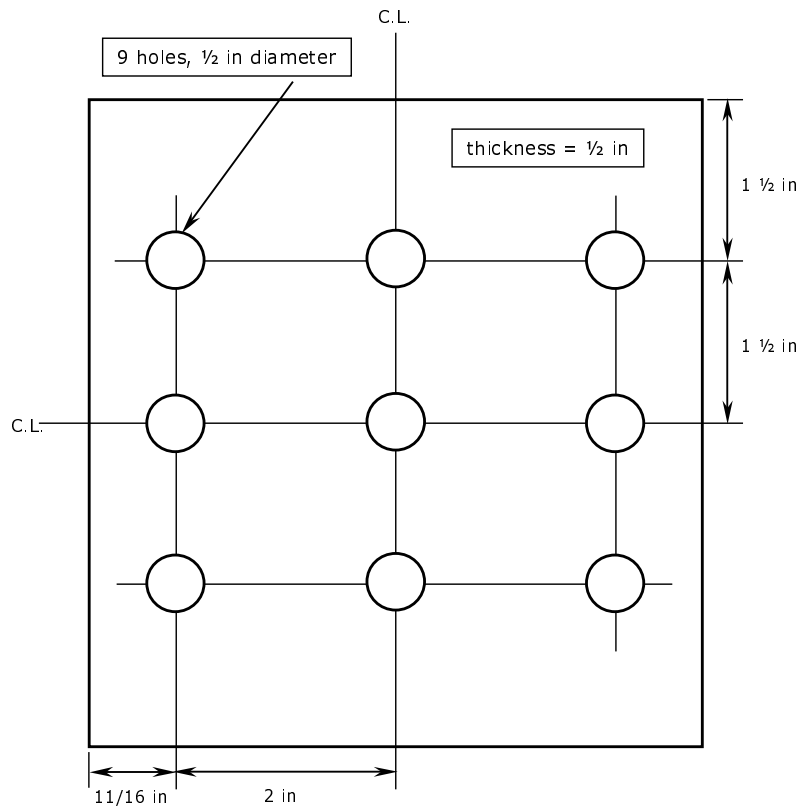


Figure 9.16: Specimen Layout and Dimensions (Ulloa, 2002a)

Two strain gages were attached to the specimen at the center of the exposed areas between the middle and exterior rails. The gages were placed with an orientation of 45 degree to the vertical axis (Fig. 9.14). One gage was aligned along the direction of the tension stress and one along the direction of the compression stress. AE was monitored during testing with a R15 sensor and with the Mistras AE data acquisition system.

9.2.2 Test Results

Loading was applied monotonically to specimens SHEAR1 and SHEAR2, and applied stepwise as load/ unload/ reload cycles to specimen SHEAR3. The

ultimate loads, shear stresses, and shear strains of all three specimens are presented in Table 9.3. It is noticed that the ultimate shear stresses of all specimens are in the same range, but the ultimate strain of specimen SHEAR3 was lower than the other specimens. This is because the isophthalic polyester resin in specimen SHEAR3 is known to have low ductility. Shear stress vs. strain curves of specimens SHEAR2 and SHEAR3 are shown in Fig. 9.17 and 9.18.

Table 9.3: Physical Results of Three-Rail Shear Test

Specimen	Resin	Primary glass reinforcement	Ultimate load (kips)	Ultimate shear stress (ksi)	Ultimate shear strain (microstrains)
SHEAR1	Vinyl ester	Unidirectional transverse to load	21.5 (monotonic)	3.58	270
SHEAR2	Vinyl ester	Unidirectional transverse to load	20.5 (monotonic)	3.42	265
SHEAR3	Isophthalic polyester	Unidirectional transverse to load and continuous fiber mat	22.1 (stepwise)	3.68	55

The damage progression during testing could not be inspected, because only limited areas of the specimen were exposed to view. The failures of specimen SHEAR2 and SHEAR3, after the tests were completed, are shown in Fig. 9.19 and 9.20, respectively. It was observed that the cracks in specimens SHEAR1 and SHEAR2 consisted mainly of cracks parallel to the unidirectional fibers (horizontal cracks) and a few cracks perpendicular to the unidirectional fibers (vertical cracks). For specimen SHEAR3, inclined cracks were mainly observed. Vertical and horizontal cracks were also found.

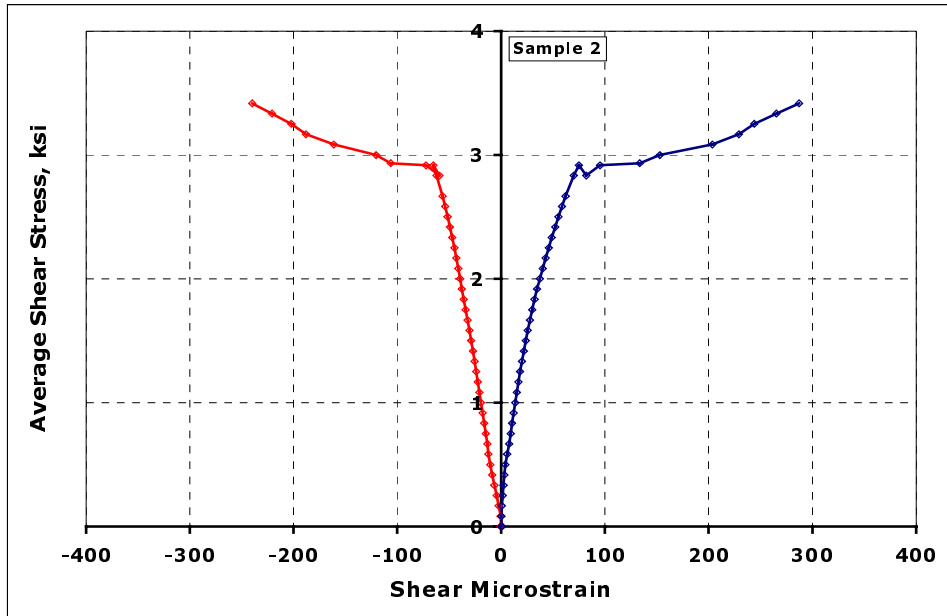


Figure 9.17: Shear Stress vs. Strain Curve of Specimen SHEAR2

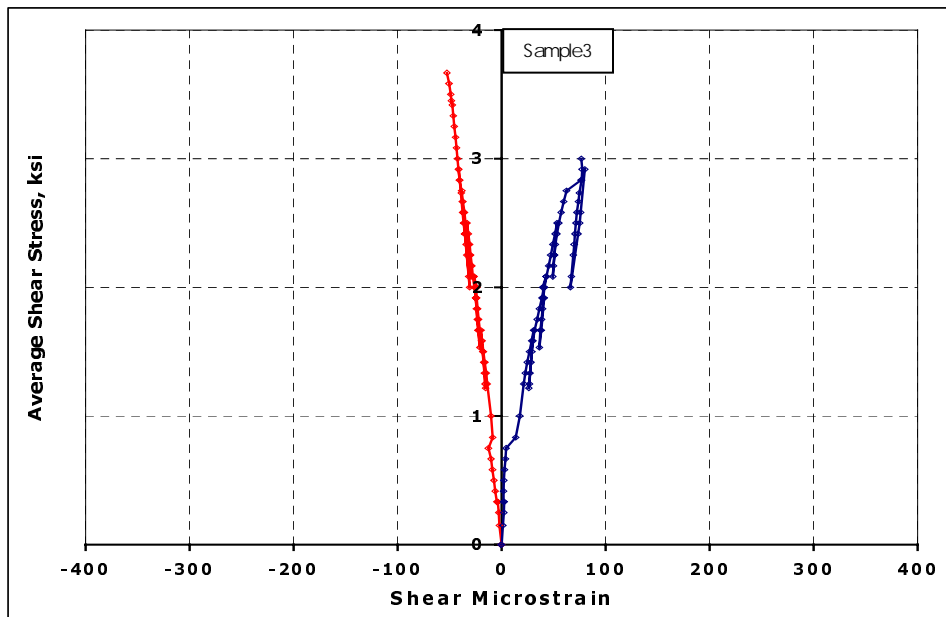


Figure 9.18: Shear Stress vs. Strain Curve of Specimen SHEAR3

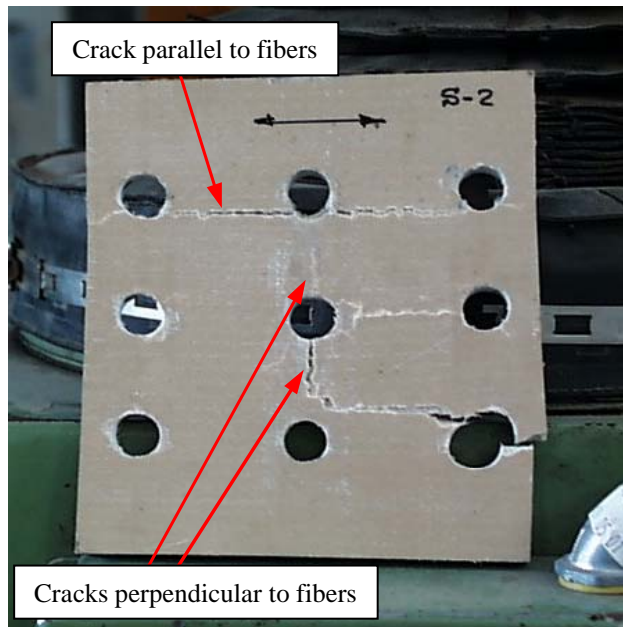


Figure 9.19: Specimen SHEAR2 After Testing

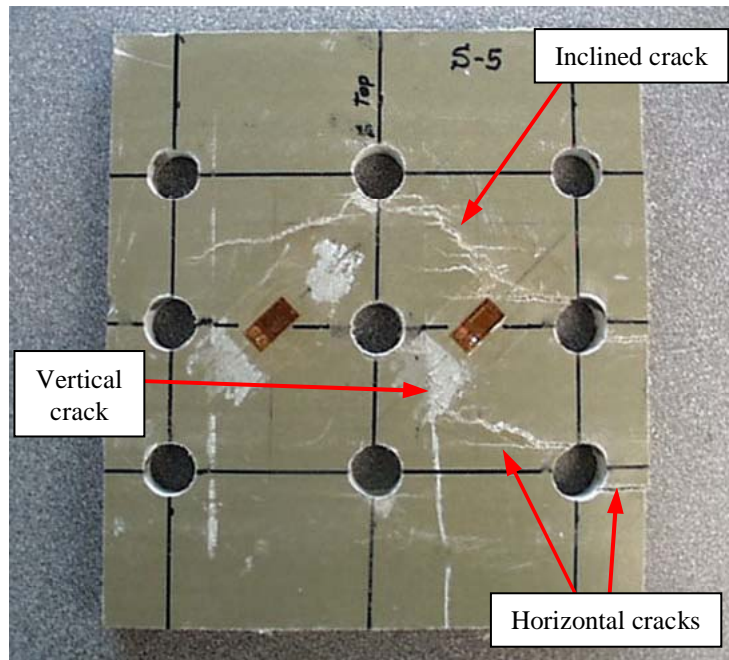


Figure 9.20: Specimen SHEAR3 After Testing

An autopsy of specimen SHEAR3 was conducted. It was found that the part of the specimen, in which horizontal and vertical cracks were observed externally, consisted of an inclined crack internally (see Fig. 9.21). It could be explained that even though the exterior layers of the specimen were unidirectional fibers, the main fiber structure in specimen SHEAR3 was continuous strand random fibers. This made the interior part of the specimen act as an isotropic material, which caused a failure plane of 45 degree by the shear stress.

The vertical cracks on the exterior layer of the specimen were observed to be mainly of fiber breaks. These fiber breaks were in the exterior unidirectional fiber layers. The picture of the fiber breaks of a vertical crack is also shown in Fig. 9.21.

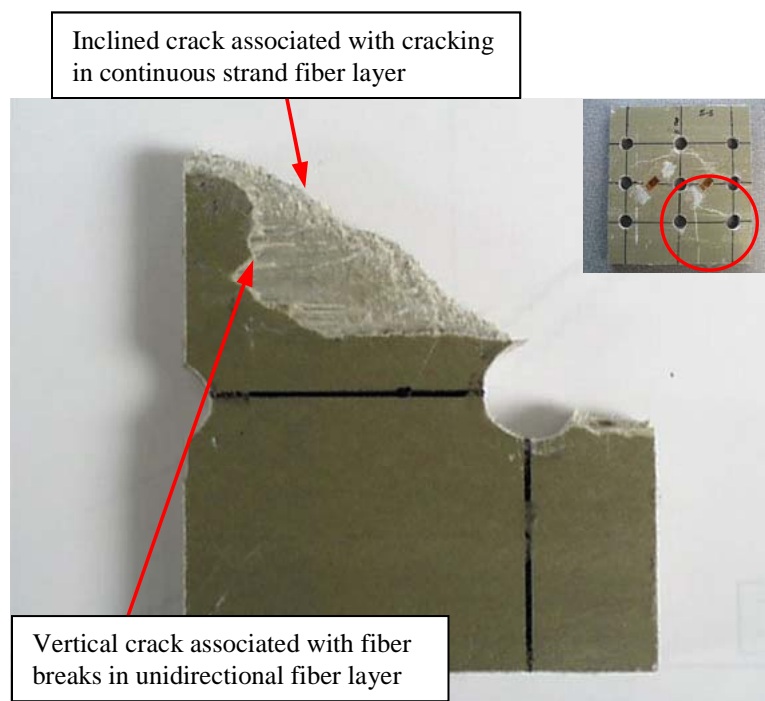


Figure 9.21: Autopsy of specimen SHEAR3 Showing Interior Inclined Crack and Exterior Vertical and Horizontal Crack

9.2.3 Failure Mechanism and Damage Severity Determined by Neural Networks (Only Backpropagation Training Method)

The final network systems developed in Chapter 8 were also applied to the AE data from the shear tests. The characteristics of the cracks occurring in specimens SHEAR1, SHEAR2, and SHEAR3 are similar to those in the tensile specimen tested perpendicular and parallel direction to the unidirectional fibers (e.g. specimens TGV and LGV1). Therefore, it is expected that the network results should be primarily involved failure mechanisms found in those specimens. The results of the network determination are presented in Table 9.4.

From the table, it is noticed that the network results, both failure mechanism and damage severity, are quite clean meaning only one scattered result is found. This is the damage severity result of specimen SHEAR3 at 20% of the ultimate load, in which the value should not be lower than the severity result of the same specimen at 10% of the ultimate load. The failure mechanism results of specimens SHEAR1 and SHEAR2 are identical, and their damage severity results are similar. Specimens SHEAR 1 and SHEAR2 were made of the same material and tested with the same testing procedure. This indicates that the network has reproducibility.

Table 9.4: Network Determination of Three-Rail Shear Specimens

Actual Load (% of Ultimate)	Determination from Network					
	SHEAR1		SHEAR2		SHEAR3	
	Failure mechanism	Damage severity	Failure mechanism	Damage severity	Failure mechanism	Damage severity
10%	5	20%	5	40%	1	20%
20%	2	70%	2	70%	1	10%
30%	2	70%	2	70%	1	70%
40%	2	70%	2	70%	2	70%
50%	2	70%	2	70%	2	70%
60%	2	70%	2	70%	2	70%
70%	2	70%	2	70%	2	70%
80%	2	70%*	2	70%*	2	70%*
90%	2	70%*	2	70%*	2	70%*
100%	2	70%*	2	70%*	2	70%*

Note: Failure Mechanism combinations

1 = Matrix cracking

4 = Matrix cracking/ debonding/ fiber break

2 = Matrix cracking/ debonding/ delamination/ fiber break

5 = Delamination

3 = Matrix cracking/ debonding

6 = Delamination/ fiber break

* The network used for this analysis is intended for use at lower loads and will not register a damage severity greater than 70%

The failure mechanism in specimen SHEAR1 and SHEAR2 starts with delamination. Local delamination between layers is to be expected as load is transferred through the specimen. After that, the damage severity increase rapidly to 70% severity and the failure mechanisms of matrix cracking/ debonding/ delamination/ fiber break took place from 20% to the ultimate load. This explains that the vertical cracks, which caused this failure mechanism combination (see Chapter 4 for details), starts to occur at the early stage of the test. The network results of the specimen SHEAR1 and SHEAR2 are checked with the amplitude

vs. load plot (Fig. 9.22). The plot shows that high amplitude hits (amplitude of 80 dB or higher), indicators of fiber breaks, were detected just above 10% to the ultimate load. This agrees with the failure mechanism determined by the network.

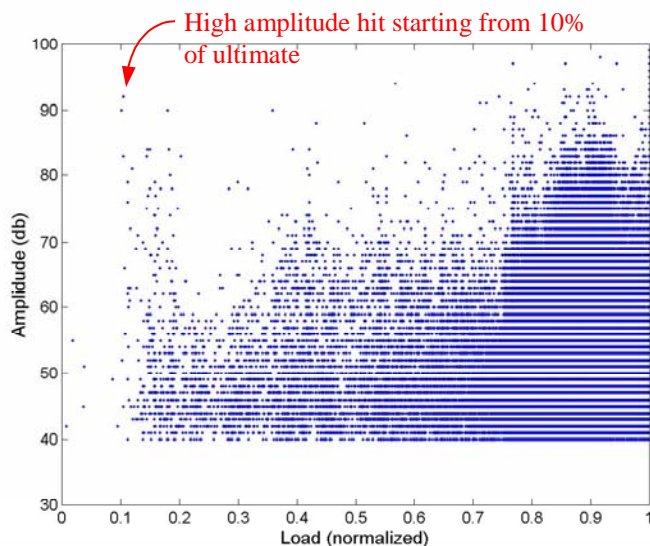


Figure 9.22: Amplitude vs. Load Plot of Specimen SHEAR1

In specimen SHEAR3, matrix cracking is determined as a primary failure mechanism from the beginning to 30% of the ultimate load. After that, a combination of matrix cracking/ debonding/ delamination/ fiber break is determined as the main failure mechanism until failure. This damage evolution is almost similar to the evolution of the specimen tested in tension perpendicular to the fiber direction (e.g. specimen LGI1). This is because the majority of the cracks in the specimen are inclined cracks and the failure mechanisms of the inclined crack develops the same way as that of the specimen tested in tension perpendicular to the fiber direction.

The failure mechanism results of specimen SHEAR3 are checked with the AE plot of amplitude vs. load (see Fig. 9.23). The plot shows that high amplitude hits (amplitude of 76 dB or higher), indicating fiber breakage, began to occur slightly after 20% to the ultimate load. This slightly conflicts with the network results, which show that the fiber breaks began to occur after 30% of the ultimate load.

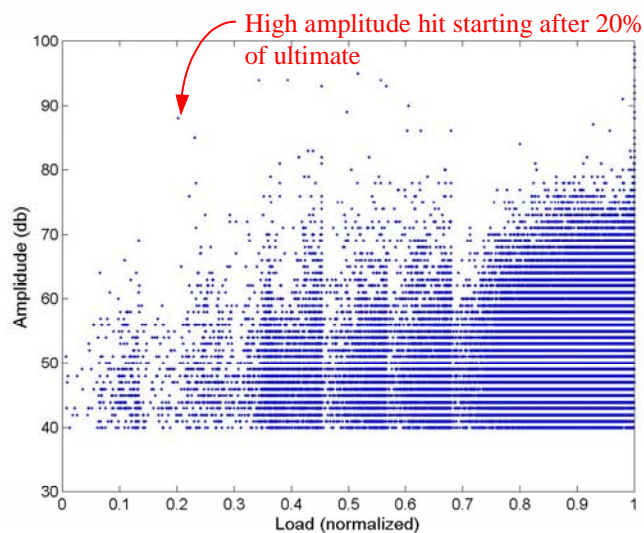


Figure 9.23: Amplitude vs. Load Plot of Specimen SHEAR3

The main difference between damage development of specimen SHEAR3 and specimens SHEAR1 and SHEAR2 is the delay of fiber break occurrence. In specimen SHEAR3, fiber breaks start to occur after 30% of the ultimate load, while they start to occur after 10% of the ultimate load in specimens SHEAR1 and SHEAR2. This can be explained by two postulations:

1. The fiber structure of specimen SHEAR3 consists mainly of continuous strand fibers and thin layers of unidirectional fiber. Therefore, its

characteristics are similar to those of specimen Chop (see Chapter 6). Fiber breaks in specimen Chop start to occur in the later stage of the load compared to the fiber break occurrence in the unidirectional FRP with the same resin material (see Chapter 4).

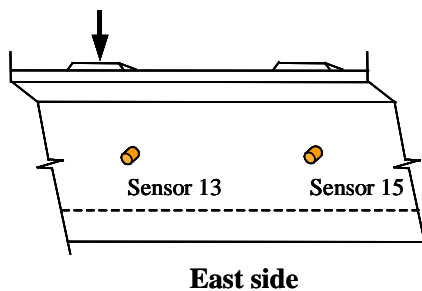
2. Specimen SHEAR3 was made of glass fibers with isophthalic polyester resin. Experience shows that fiber breaks of this type in FRP always occur in a later stage when tested in tension perpendicular to the fiber direction. On the other hand, fiber breaks in vinyl ester FRP tend to occur earlier (see Chapter 4 for details).

Even though all three specimens are subject to 70% severity damage at between 10% and 40% of the ultimate load, the specimens can continue to carry the rest of the load. This conflicts with the behavior of the simple-fundamental specimens tested for the AE database of the neural network. This behavior is reflects the complexity of the rail-shear test setup that allows the specimens to take more loads after the severe crack has occurred.

9.3 COMPARISON OF DAMAGE SEVERITY DETERMINED BY BACKPROPAGATION AND PNN NETWORKS

In this section, the network system that is trained by the PNN method (which, in Chapter 8, shows a better performance with the testing data set) is used to determined damage severity of specimens TK1, SHEAR1, SHEAR2, and SHEAR3. The results are compared with the resulted determined by the backpropagation networks. The comparison summary is shown in Tables 9.5 and 9.6 for specimen TK1, and in Table 9.7 for specimen SHEAR1 to SHEAR3.

Table 9.5: Network Determination of Sensors 13 and 15 of Specimen TK1 (East Side of Girder)



Actual Load (% of Ultimate)	Determination from Network					
	Sensor 13			Sensor 15		
	Failure mode	Damage severity (backprop)	Damage severity (PNN)	Failure mode	Damage severity (backprop)	Damage severity (PNN)
10%	5	70%	10%	5	10%	10%
20%	5	70%	10%	5	10%	10%
30%	5	70%	10%	5	20%	40%
40%	5	70%	10%	5	10%	10%
50%	5	70%	10%	5	10%	30%
60%	2	70%	10%	5	10%	10%
70%	2	70%	50%	5	30%	10%
80%	2	70%*	70%*	2	70%*	40%*
90%	2	70%*	70%*	2	70%*	50%*
100%	2	70%*	40%*	2	70%*	40%*

Note: Failure Mechanism combinations

1 = Matrix cracking

4 = Matrix cracking/ debonding/ fiber break

2 = Matrix cracking/ debonding/ delamination/ fiber break

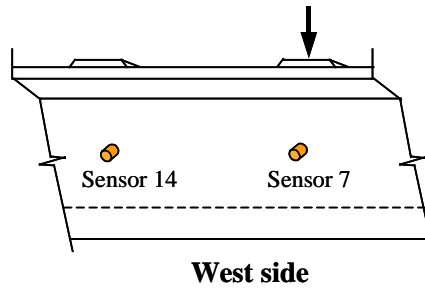
5 = Delamination

3 = Matrix cracking/ debonding

6 = Delamination/ fiber break

* The network used for this analysis is intended for use at lower loads and will not register a damage severity greater than 70%

Table 9.6: Network Determination of Sensors 7 and 14 of Specimen TK1



Actual Load (% of Ultimate)	Determination from Network					
	Sensor 7			Sensor 14		
	Failure mode	Damage severity (backprop)	Damage severity (PNN)	Failure mode	Damage severity (Backprop)	Damage severity (PNN)
10%	5	30%	10%	5	10%	10%
20%	4	50%	10%	5	30%	10%
30%	4	70%	10%	5	20%	40%
40%	4	70%	10%	5	20%	30%
50%	4	70%	10%	3	20%	10%
60%	4	70%	10%	3	20%	30%
70%	2	70%	10%	5	20%	40%
80%	2	70%*	50%*	2	70%*	50%*
90%	2	70%*	50%*	2	70%*	20%*
100%	4	70%*	10%*	2	70%*	50%*

Note: Failure Mechanism combinations

1 = Matrix cracking

4 = Matrix cracking/ debonding/ fiber break

2 = Matrix cracking/ debonding/ delamination/ fiber break

5 = Delamination

3 = Matrix cracking/ debonding

6 = Delamination/ fiber break

* The network used for this analysis is intended for use at lower loads and will not register a damage severity greater than 70%

Table 9.7: Network Determination of Three-Rail Shear Specimens

Actual Load (% of Ultimate)	Determination from Network											
	SHEAR1				SHEAR2				SHEAR3			
	Failure mode	Damage severity (backprop)	Damage severity (PNN)	Failure mode	Damage severity (backprop)	Damage severity (PNN)	Failure mode	Damage severity (backprop)	Damage severity (PNN)	Failure mode	Damage severity (backprop)	Damage severity (PNN)
10%	5	20%	10%	5	40%	10%	1	20%	10%	1	20%	20%
20%	2	70%	10%	2	70%	60%	1	10%	60%	1	10%	20%
30%	2	70%	40%	2	70%	10%	1	70%	10%	1	70%	10%
40%	2	70%	50%	2	70%	10%	2	70%	10%	2	70%	60%
50%	2	70%	50%	2	70%	10%	2	70%	10%	2	70%	70%
60%	2	70%	50%	2	70%	50%	2	70%	50%	2	70%	10%
70%	2	70%	50%	2	70%	50%	2	70%	50%	2	70%	10%
80%	2	70%	40%	2	70%	70%	2	70%	70%	2	70%	70%
90%	2	70%	70%	2	70%	70%	2	70%	70%	2	70%	50%
100%	2	70%	70%	2	70%	70%	2	70%	70%	2	70%	50%

Note: Failure Mechanism combinations

1 = Matrix cracking

2 = Matrix cracking/ debonding/ delamination/ fiber break 5 = Delamination

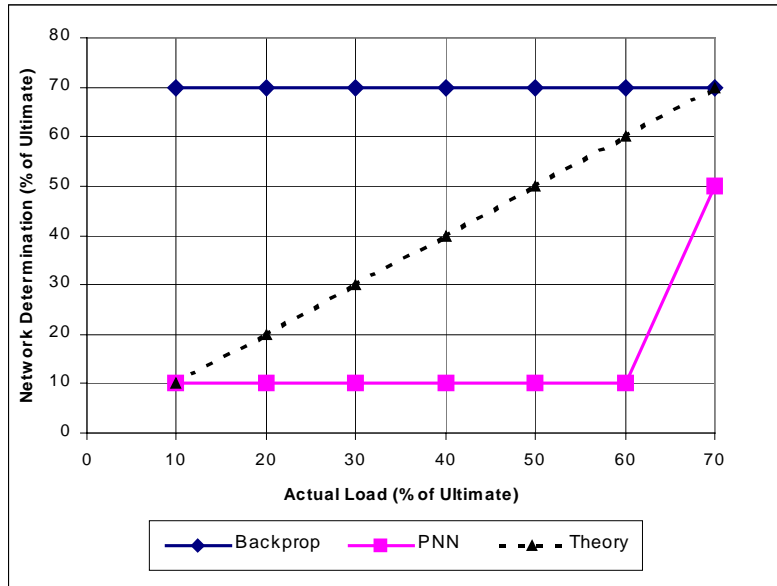
3 = Matrix cracking/ debonding

4 = Matrix cracking/ debonding/ fiber break

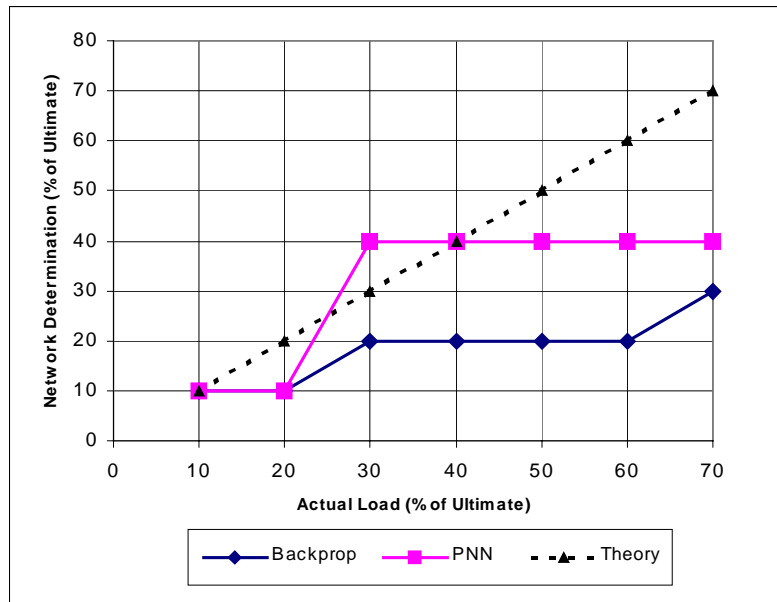
6 = Delamination/ fiber break

In general, the PNN network gives results that have a lower value of damage severity than the backpropagation network. Also, with increasing load, the results from the PNN networks fluctuate up and down, which is not as expected. To remedy this problem, the peak hold method is applied to the results from the network with PNN. The peak hold does not permit damage severity to drop below a previously attained value, instead, it is held at the maximum value that it has achieved. With the peak hold method, the results from PNN network will either remain constant or increase. Figures 9.24 and 9.25 show example plots of the PNN network results with peak hold compared with the backpropagation results with peak hold and the actual value (theory) for each sensor.

The network determination beyond 70% of the ultimate load is not included in these plots since it is out of the range of interest. The plots show that, with the peak hold method, PNN network performs slightly better than backpropagation network. This shows that PNN network results are very encouraging and has potential to be improved by further research. The PNN network also performs with high accuracy (74% accuracy) when tested with the testing data set. This means that the PNN network will predict damage severity well if the specimen under test is the same type of specimen and uses the same test setup as those used in the testing data set. This leads to the recommendation that PNN network performance can be improved by training with data from more specimen types and test setups.

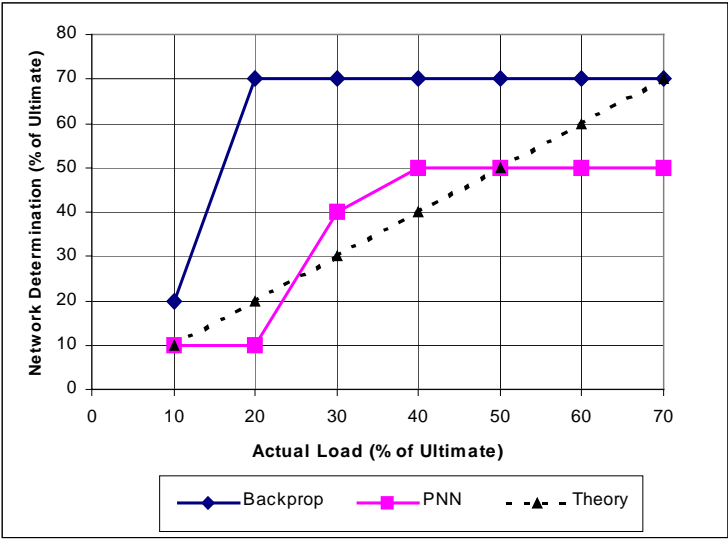


a) Sensor 13

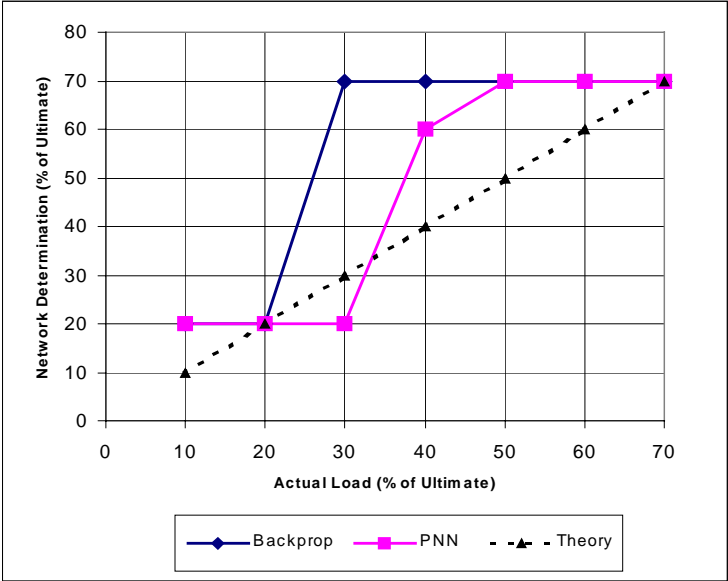


b) Sensor 15

Figure 9.24: Comparison of Backpropagation Network Results with Peak Hold, PNN Network Results with Peak Hold, and Theory of Specimen TK1



a) SHEAR1



b) SHEAR3

Figure 9.25: Comparison of Backpropagation Network Results with Peak Hold, PNN Network Results with Peak Hold, and Theory of Specimens SHEAR1 and SHEAR3

9.4 SUMMARY

The network systems developed in Chapter 8 are applied to determine failure mechanism and severity of damage from two types of tests. The first test is a full-scale trapezoidal girder subjected to a three-point bending test. Only damage was observed visually on the east web of the girder. The network results of the east web of the girder yield a good agreement with the actual damage. The network results of the west web of the girder cannot be directly validated since no damage was observed visually in the west web of the girder. However, the network results are validated indirectly by relating the results with the damage on the east web of the girder. It is shown that the damage development of the west side determined by the network follows the same path as that of the east side. This is as expected since the girder cross section is symmetric and the stresses, as well as damage development, on both webs should be similar. This indicates that the network results are reliable. In addition to the validation of the network results, the damage propagation from one location on the specimen to another can be interpreted from the network results

In the second section, three FRP coupons were subjected to a three-rail shear test. The network results have an agreement with the damage from visual inspection. The network results shows that the damage development of specimens SHEAR1 and SHEAR2 are almost identical. This indicates that this method of pattern recognition is reproducible since specimens SHEAR1 and SHEAR2 were made of the same materials and tested with the same testing procedure. The damage development of specimen SHEAR3 is different than that of specimens SHEAR1 and SHEAR2. The network results suggest that this is attributed to the difference of resins used and the fiber structures.

When the backpropagation network is compared with the PNN network for damage severity determination of these applications, the PNN network results

initially show considerable scatter. However, with the peak hold method, the PNN network results show slightly better performance than the backpropagation network. Therefore, the PNN network for damage severity determination has a potential to be improved by further research.

CHAPTER 10

Summary and Conclusions

10.1 SUMMARY

The objective of this research is to develop reliable methods to determine AE signatures of defects in FRP structures based on AE data. The study consists of two parts. The first part is collecting AE data of different failure mechanisms. This involves testing of specimens and observations of defects. The specimens tested include:

- Unidirectional FRP specimens tested in tension parallel to the fiber direction. The specimens include coupons and full-scale components.
- Unidirectional FRP specimens tested in tension perpendicular to the fiber direction.
- Specimens in which delamination governs the failure mode. Two types of specimens were tested. The first type of specimens had a low span-to-depth ratio and were subjected to a four-point bending test (short beam shear test). The second type of specimens were made of two “T” sections bonded together with a resin. Also, there was a Teflon strip inserted at the center of the bond line to initiate cracking. These specimens were tested with the bond line in tension.
- Specimens having other common types of fiber structures such as chopped strand fiber and woven roving. These specimens were subjected to a direct tension test.

- Specimens with complex failure mechanisms. These specimens were double-web sections subjected to a compression test and a full-scale girder subjected to a four-point bending. These specimens failed by buckling, but experienced additional secondary failures.

The observation of macro-defect mechanisms were performed by visual inspection, whereas the observation of micro-defect mechanisms were performed with the aid of SEM. With these observations, basic failure mechanisms were identified and were correlated with the AE data. An AE database with reliable information of failure mechanisms was built.

The second part of the research focused on analyses of AE data for pattern recognition. Two methods were selected to perform this task: visual pattern recognition and neural network pattern recognition. The visual pattern recognition involved creating 16 AE correlation plots for each specimen and visually comparing the plot dissimilarities between specimens. Also, there were some techniques to help visualize the patterns such as the slope of the cumulative amplitude distribution (b-value) and the “knee” of the cumulative emission curves. The analysis showed many distinctions between the AE signatures for different defects.

The neural network technique was also used to perform AE pattern recognition. Two networks were trained to perform two tasks. The first task was to determine failure mechanism types and the second task was to determine damage severity of specimens. The networks yielded good results for failure mechanism determination, and showed promising results for the damage severity determination. The neural networks were then applied to determine failure mechanism and damage severity of additional test specimens. These specimens were a trapezoidal girder subjected to a three-point bending test and three coupon

specimens tested by three-rail shear. The results agreed with the visual observation showing good network performance.

10.2 SIGNIFICANT FINDINGS

The significant findings from the research on AE signatures of failure mechanisms are reported. This includes the findings from conducting AE database collection, visual pattern recognition, and applying neural networks for pattern recognition.

10.2.1 AE Database Collection

The conclusions and findings based on experimentation of unidirectional specimens loaded in tension parallel to the fibers are:

1. The main failure mechanism occurring in these specimens is fiber breaks
2. Fiber breakage is associated with high amplitude AE hits. This is based on closely relating the AE data with the number of fiber breaks occurring in the specimens at different load levels. The number of fiber breaks is observed with SEM.
3. The shape of the plot of cumulative signal strength vs. load is closely related to the plot of the cumulative number of fiber breaks vs. load.
4. Based on the low-amplitude filtering technique, the borderline amplitudes, which separate between AE hits from fiber break and AE hits from other failure mechanisms, are:
 - a. 76 dB for glass/isophthalic polyester FRP
 - b. 80 dB for glass/vinyl ester FRP
 - c. 68 dB for glass-carbon/vinyl ester FRP

5. Fiber breaks occur with a continuation of matrix cracking or fiber/matrix debonding (debonding). Delamination is often found after fiber breaks occur.
6. AE data recorded before the first occurrence of a fiber break is associated with matrix cracking.

The conclusions and findings based on experimentation of unidirectional specimens loaded in tension perpendicular to the fibers are:

1. The main failure mechanisms of these specimens are matrix cracking and debonding.
2. Matrix cracking and debonding occur almost simultaneously. It is not possible to identify the AE data from individual failure mechanisms.
3. Fiber breaks also occur in this type of specimen and are observed to be associated with high amplitude hits.
4. AE data recorded before the first occurrence of a fiber break are associated with matrix cracking and debonding.
5. AE data recorded after the first occurrence of a fiber break are associated with fiber breaks as well as matrix cracking and debonding.

The conclusions and findings based on experimentation of unidirectional specimens tested in short beam shear are:

1. Delamination is the main failure mechanism of these specimens and occurs between lamina or/and within a chopped strand fiber layer.
2. Delamination in the glass fiber reinforced specimens is visually observed at the ultimate load. Glass fiber breaks also occur in addition to the delamination when the load is approaching failure.

3. Multiple delaminations are visually observed before the ultimate load is reached for hybrid specimens. In addition to the delamination, carbon fiber breaks occur a very early stage of the test (7% of the ultimate load).
4. The AE data recorded before the first occurrence of a fiber break is associated with delamination and the data after the first occurrence of a fiber break is associated with delamination/fiber break.

The conclusions and findings based on the bond tests of the “T” specimens are:

1. Delamination is the main failure mechanism of these specimens and occurs at the bond line, which is essentially a tension failure of the resin.
2. Delamination initiates suddenly at the maximum load, then the delamination propagates to both ends of the bond line.
3. Fiber breaks are observed from the beginning of the test (from 0% of the ultimate load). Therefore, the entire AE data recorded is associated with delamination/fiber break.

10.2.2 AE Visual Pattern Recognition

Sixteen plots of twelve representative specimens are used for this analysis. The significant AE signatures and patterns of failure mechanisms are listed below:

1. Vinyl ester resin is more flexible and elongates more than isophthalic polyester resin. This allows more fibers in the vinyl ester FRP to break prior to failure than in the isophthalic polyester FRP when the tensile stress is applied parallel to the fibers.

2. High amplitude hits begin at a lower load (40% of ultimate) in the vinyl ester specimens than in the isophthalic polyester specimens (80% of ultimate) tested in tension parallel to the unidirectional fibers.
3. Vinyl ester resin is flexible and allows the tensile stress to redistribute to the adjacent fibers or matrix after a fiber is broken. For this reason, the departure from linearity of the stress vs. strain curve appears long before failure for the vinyl ester FRP tested in tension parallel to the fibers.
4. When a tension load is applied parallel to the fibers, the onset of AE is at a higher load for the glass/isophthalic polyester FRP than for the glass/vinyl ester FRP. Onset of copious emission (knee in the curve) is also at a higher load for the glass/isophthalic polyester FRP.
5. When a tension load is applied perpendicular to the fibers, the onset of AE is at a higher load for the glass/vinyl ester FRP than the glass/isophthalic polyester FRP. This is because the vinyl ester is more flexible than the isophthalic polyester (Ziehl, 2000). However, onset of copious emission is at a higher load for the glass/isophthalic polyester FRP.
6. Isophthalic polyester resin is brittle and does not allow stress redistribution as much as vinyl ester resin after a fiber is broken. For this reason, the departure from the linearity of the stress vs. strain curve appears close to failure for isophthalic polyester FRP.
7. In the hybrid specimens, very early fiber breaks occur during the test. It is believed that this is due to the brittle property of the carbon fibers, which are susceptible to damage during the fabrication process. In turn, this leads to premature fiber breakage.
8. Carbon fiber breaks have less effect to the stiffness of the structure than the same number of glass fiber breaks. This is because a carbon fiber has a

smaller cross section than a glass fiber and each fiber carries a smaller proportion of the total load.

9. Fiber breaks, as evidenced by high amplitude hits, do not occur in the chopped strand FRP until 90% of the ultimate load in tension. Two factors contribute to this behavior. The first is the short length of the fibers, which permits them to pull out of the resin matrix rather than break. The second is that there are fewer fibers in the direction of maximum stress than with a unidirectional fabric loaded parallel to the fibers. When fibers start to break, the strength of the FRP starts to degrade rapidly.
10. The woven nature of the fibers in woven roving FRP means that the fibers are initially wavy with air voids where the fiber bundles cross. Thus, the fibers are not efficiently configured to carry a tensile load. The woven roving FRP does not show fiber breaks at as low a load as unidirectional FRP. As load is applied, the woven roving fibers are straightened and can take tensile stress. This explains the reason that fiber breaks in woven roving FRP occur at a load of 60% of the ultimate, which is higher than the unidirectional FRP but lower than the chopped strand FRP.
11. The stress vs. strain relationship of woven roving FRP shows a sharp rise near failure. This is also because of the fiber straightening, which increases the stiffness of the FRP considerably.
12. The slope of the amplitude distribution plot and cumulative amplitude distribution plot is independent to the sensor-to-source distance. In contrast, the peak amplitude of the amplitude distribution plot is dependent to the sensor-to-source distance. Also, the amplitude where the plot changes slope is dependent to the sensor-to-source distance.
13. b-values and the corresponding failure mechanisms are found and presented in table 10.1.

14. The slope of the amplitude distribution plot for a coupon specimen is likely to be different than that of a full-scale specimen of the same material due to the reflection effect.
15. Delamination failure of glass FRP occurs very suddenly. Only a few AE hits are detected before the delamination occurs.
16. The stress vs. strain relationship of specimens associated with delamination remains linear until delamination occurs. This applies to both glass and carbon FRP.
17. High amplitude/long duration hits (duration of 30,000 microseconds and higher) are found only in the tension specimens tested parallel to the unidirectional fiber direction. They occur when the load is approaching to failure. A high amplitude/long duration hit is attributed to a fiber break followed immediately by another failure mechanism, which may be fiber pullout or more likely simultaneous fiber breaks. The signal strengths of these hits are higher than 5,000.

Table 10.1: Summary of b-Values of Failure Mechanisms Found in Research Program

Failure mechanism	b-value
Matrix cracking	2.3-3.0
Matrix cracking/ debonding	3.3-3.84
Delamination (only for glass fibers)	1.04-1.50
Fiber breakage involved	< 1.24 in high amplitude zone

10.2.3 Neural Network for AE Pattern Recognition

Neural networks are developed using AE correlation plots to model the input data. As part of the network development process, the networks are

used to determine failure mechanisms of chopped strand fiber FRP and woven roving fiber FRP, which are subjected to a longitudinal tension test. The AE data and failure mechanism information of these specimens are also added to the AE database to train the final networks. The following conclusions are based on development of the neural networks for failure mechanism determination and damage severity determination.

1. The network results are shown to be very reliable in determining failure mechanisms.
2. The network results show a promise in determining damage severity.
3. Backpropagation is a slightly better method than PNN for training the networks for this application. The network trained by the backpropagation method yields a performance 3% higher than that of the network trained by the PNN method.
4. Network systems with two level networks, primary and secondary networks, are proven to achieve higher performance than one-layer networks. This is because the secondary network combines the strength of each primary network and processes the results to produce the output.
5. For the damage severity determination network, having failure mechanism information as input data (beside AE and material information) yields the better network performance. Also, training the network by using AE data from 0% to 70% of the ultimate load slightly increases network performance.
6. The performance of the network trained for failure mechanism determination is 96%, while the performance of the network trained for damage severity determination is 44%.

The performance of the primary networks is governed by:

1. Types of AE correlation plot that is used to model the data input.

For failure mechanism determination:

- a. Amplitude vs. duration plot yields the highest network performance with PNN.
- b. Amplitude vs. duration plot with log conversion yields the highest network performance with backpropagation.
- c. Historic index and severity plot yield the lowest network performance with both training method.

For damage severity determination with backpropagation training method:

- a. Cumulative signal strength plot yields the highest network performance.
- b. Historic index and severity plot yields the lowest network performance.

2. Normalization method: Normalization by using the maximum value of the plot as a reference yields a higher network performance than normalization by using the total value of the plot (area under the curve) as a reference.
3. Format of number used: Network with backpropagation training method yields a better performance if the input data is in a simpler format (using linear or log conversion). In contrast, network with PNN training method yield a better performance if the input data is in a more complex format (without conversion).

The conclusions obtained from applying the developed network to determine failure mechanisms of additional tests are:

1. The network results are in good agreement with the actual damage. This means that the network results are reliable.
2. The network results are reproducible.

10.3 DIRECTIONS FOR FUTURE RESEARCH

Most of the tests reported in this research were conducted by monotonic loading. However, in real applications, the structure will experience many service loading cycles. It is recommended that the AE data from subsequent loadings be studied and added as training sets for the neural networks.

A key component of this research was observation of actual failure mechanisms at different load levels. In this research, the neural network was used to determine failure mechanisms in two FRP specimens, which were the chopped strand FRP and the woven roving FRP. SEM observation should be conducted to more accurately identify failure mechanisms in these specimens. SEM is limited to observation of failure mechanisms on the surface of the specimens. Recently developed technology can perform the interior observation of the object on a micro scale. An example of such a technique is high resolution X-ray CT (computed tomography).

The specimens tested in this research program were made of isophthalic polyester and vinyl ester resins. Epoxy is another commonly used and it would be beneficial to expand the database to include this resin.

Other type of neural networks should be researched for use in these applications. The unsupervised training methods, such as self-organizing map, has shown good performance for many other applications and should be evaluated for this type of research (Mehrotra, 1997).

References

1. American Society for Nondestructive Testing, 1982, "Nondestructive Testing Handbook—Second Edition, Volume 3, Radiography and Radiation Testing," Bryant, L.E. (tech. ed.), McIntire, P. (ed.), American Society for Nondestructive Testing, Metals Park, Ohio.
2. American Society for Nondestructive Testing, 1982, "Nondestructive Testing Handbook—Second Edition, Volume 6, Magnetic Particle Testing," Schmidt, J.T. (tech. ed.), Skeie, K. (tech. ed.), McIntire, P. (ed.), American Society for Nondestructive Testing, Metals Park, Ohio.
3. American Society for Nondestructive Testing, 1982, "Nondestructive Testing Handbook—Second Edition, Volume 7, Ultrasonic Testing," Birks, A.S. (tech. ed.), Green Jr., R.E. (tech. ed.), McIntire, P. (ed.), American Society for Nondestructive Testing, Metals Park, Ohio.
4. American Society for Nondestructive Testing, 1982, "Nondestructive Testing Handbook—Second Edition, Volume 4, Electromagnetic Testing," Mester, M.L. (tech. ed.), McIntire, P. (ed.), American Society for Nondestructive Testing, Metals Park, Ohio.
5. American Society for Nondestructive Testing, 1982, "Nondestructive Testing Handbook—Second Edition, Volume 1, Leak Testing," Jackson, C.N. Jr. (tech. ed.), Sherlock, C.N. (tech. ed.); Moore, P.O. (ed.), American Society for Nondestructive Testing, Metals Park, Ohio.
6. American Society for Nondestructive Testing, 1982, "Nondestructive Testing Handbook—Second Edition, Volume 8, Visual and Optical Testing," Allgaier, M.W. (tech. ed.), Ness, S. (tech. ed.), McIntire, P. (ed.),

- Moore, P.O. (ed.), American Society for Nondestructive Testing, Metals Park, Ohio.
7. American Society for Nondestructive Testing, 1993, "Recommended Practice for Acoustic Emission Testing of Pressurized Highway Tankers Made of Fiberglass Reinforced Plastic with Balsa Core", American Society for Nondestructive Testing, Columbus, Ohio, 1993.
 8. American Society for Nondestructive Testing, 1999, "Nondestructive Testing Handbook—Third Edition, Volume 2, Liquid Penetrant Testing," Tracy, N., Moore P.O., American Society for Nondestructive Testing, Metals Park, Ohio.
 9. American Society for Testing Materials, ASTM E 1316, "Standard Terminology for Nondestructive Examinations," Annual Book of ASTM Standards, Nondestructive Testing, Vol. 03, Philadelphia, American Society for Testing and Materials.
 10. American Society for Testing Materials, ASTM E 2076, "Examination of Fiberglass Reinforced Plastic Fan Blades Using Acoustic Emission," American Society for Testing and Materials, West Conshohocken, PA.
 11. American Society for Testing Materials, ASTM F 914, "Standard Test Method for Acoustic Emission for Insulated Aerial Personnel Devices," Preprinted from the Annual Book of ASTM Standards, American Society for Testing and Materials, West Conshohocken, PA.
 12. American Society for Testing Materials, ASTM E 1067, "Standard Practice for Acoustic Emission Examination of Reinforced Plastic Resin (FRP) Tanks/Vessels," Preprinted from the Annual Book of ASTM Standards, American Society for Testing and Materials, West Conshohocken, PA.
 13. American Society for Testing Materials, ASTM E 1118, "Standard Practice for Acoustic Emission Examination of Reinforced Thermosetting Resin

Pipe (RTRP),” Preprinted from the Annual Book of ASTM Standards, American Society for Testing and Materials, West Conshohocken, PA.

14. American Society of Civil Engineers, Structural Plastics Design Manual Volume 1, American Society of Civil Engineers, New York, New York, 1982.
15. ASME Section V, Article 11, “Acoustic Emission Examination of Fiber Reinforced Plastic Vessels, Boiler and Pressure Vessel Code,” American Society of Mechanical Engineers, New York, NY.
16. ASME Section X, “Acceptance Test Procedure for Class II Vessels, Article RT-6, Section X, Boiler and Pressure Vessel Code,” American Society of Mechanical Engineers, New York, NY.
17. Association of American Railroads, 1999, “Procedure for Acoustic Emission Evaluation of Tank Cars and IM101 Tanks, Issue 8,” Association of American Railroads, Mechanical Division Washington, DC.
18. Barnes, C.A., Ramirez, G., 1998, “Acoustic Emission Testing of Carbon Fiber Composite Offshore Drilling Risers,” The sixth International Symposium on Acoustic Emission from Composite Materials AECM-6, American Society for Nondestructive Testing, Inc., San Antonio, Texas, June 1-4, pp.13-22.
19. Belchamber, R.M, et.al., 1983, “Looking for Patterns in Acoustic Emissions,” First International Symposium on Acoustic Emission from Reinforced Composites, The Society of the Plastics Industry, Inc., July 19-21, Session 1, pp.1-5.
20. Berthelot, J.M., and Billaud, J., 1983, “Analysis of the Fracture Mechanisms in Discontinuous Fibre Composites Using Acoustic Emission,” First International Symposium on Acoustic Emission from

- Reinforced Composites, The Society of the Plastics Industry, Inc., July 19-21, Session 2, pp.1-10.
21. Berthelot, J.M., and Rhazi, J., 1986, "Different Types of Amplitude Distributions in Composite Materials," Second International Symposium on Acoustic Emission from Reinforced Composites, The Society of the Plastics Industry, Inc., Reinforced Plastics/Composites Institute, Montreal, Canada, July 21-25, pp.96-103.
 22. Boogaard, J., and Van Dijk, G.M., 1989, "Acoustic Emission a Review," Non-Destructive Testing (Proc. 12th World Conference), Elsevier Science Publishers B.V., Amsterdam, April 23-28, pp. 429-434.
 23. Bray, D.E., and Stanley, R.K., 1997, Nondestructive Evaluation: A Tool in Design, Manufacturing, and Service, Revised Edition, CRC Press, New York.
 24. CARP, 1999, "Recommended Practice for Acoustic Emission Evaluation of Fiber Reinforced Plastic (FRP) Tanks and Pressure Vessels," The Committee on Acoustic Emission for Reinforced Plastics (CARP), A Division of the Technical Council of The American Society for Nondestructive Testing, Inc., Columbus, Ohio, Draft I, October 1999.
 25. Chawla, K.K., Composite Materials: Science and Engineering, Second Edition, Springer, New York, 1998.
 26. Chen, F., Hiltner, A., and Baer, E., 1992, "Damage and Failure Mechanism of Continuous Glass Fiber Reinforced Polyphenylene Sulfide," Journal of Composite Materials, Vol. 26, No. 15, pp. 2289-2306.
 27. Chen, H.L., and Chen, C.L., 1992, "Applying Neural Network to Acoustic Emission Signal Processing," Forth International Symposium on Acoustic Emission from Composite Materials AECM-4, Seattle, WA, July 27-31, pp.273-281.

28. Chotickai, P., 2001, "Acoustic Emission Monitoring of Prestressed Bridge Girders with Premature Concrete Deterioration," Thesis Presented for Degree of Master of Science in Engineering, The University of Texas at Austin.
29. Crosbie, G.A., Guild, F.J., and Phillips, M.G., 1983, "Acoustic Emission Studies in Glass Fibre-Polyester Composites with Rubber Toughened Matrices," First International Symposium on Acoustic Emission from Reinforced Composites, The Society of the Plastics Industry, Inc., July 19-21, Session 1, pp.1-7.
30. Crump, T.N., 1981, "Acceptance Criteria for Acoustic Emission Testing of FRP Tanks," SPI/CARP Meeting Paper, June 25, 1981, Atlanta, Georgia.
31. Crump, T.N., Droge, M.A., 1979, "The Characterization of Fiberglass Reinforced Plastics Using Acoustic Emission," Managing Corrosion with Plastics, Volume IV, National Association of Corrosion Engineers, Houston, Texas, pp. 91-95.
32. Dickens, J.R., Bray, D.E., 1994, "Human Performance Considerations in Nondestructive Testing," Materials Evaluation, September 1994, Vol. 52, No. 9, pp. 1033-1041.
33. Droge, M., 1983, "Recommended Practice for Acoustic Emission Testing of Fiberglass Reinforced Plastic Piping Systems," First International Symposium on Acoustic Emission from Reinforced Composites, The Society of the Plastics Industry, Inc., July 19-21, Session 4, pp.1-17.
34. Duke, J.C., Lesko, J., and Weyers, R., 1996, "Nondestructive Evaluation of Critical Composite Material Structural Elements," Nondestructive Evaluation of Bridges and Highways, SPIE 2946, 1996, pp. 206-210.
35. Elmore, W.C., and Heald, M.A., 1969, Physics of Waves, Dover Publications, Inc., NY.

36. Ely, T.M., and Hill, E.v.K., 1992, "Characterization of Failure Mechanisms in Graphite/Epoxy Tensile Test Specimens Using Acoustic Emission Data," Forth International Symposium on Acoustic Emission from Composite Materials AECM-4, Seattle, WA, July 27-31, pp.187-199.
37. Endo, K., 2000, "A Study on the Application of the Acoustic Emission Method for Steel Bridges," Thesis Presented for Degree of Master of Science in Engineering, The University of Texas at Austin.
38. Fausett, L., 1994, Fundamentals of Neural Networks: Architectures, Algorithms, and Applications, Prentice Hall, Englewood Cliffs, New Jersey.
39. Favre, J.P., and Laizet, J.C., 1989, "Acoustic Analysis of the Accumulation of Cracks in CFRP Cross-Ply Laminates Under Tensile Loading," Third International Symposium on Acoustic Emission from Composite Materials AECM-3, Paris, France, July 17-21, pp.278-285.
40. Fisher, M.E., and Hill, E.v.K., 1998, "Neural Network Burst Pressure Prediction in Fiberglass Epoxy Pressure Vessels Using Acoustic Emission," Material Evaluation, Vol. 56, No. 12, December 1998, pp.1395-1401.
41. Fowler, D.W., 1998, Class Note for CE 351 Construction Materials, The University of Texas at Austin, Fall.
42. Fowler, T. J., 1977, "Acoustic Emission Testing of Fiber Reinforced Plastics", Preprint 3092, Fall Convention, San Francisco, CA, American Society of Civil Engineers, New York.
43. Fowler, T. J., 1986, "Acoustic Emission Testing of Process Industry Vessels and Piping", Proceedings, 5th International Symposium on Loss Prevention and Safety Promotion in the Process Industries, Cannes, France,

- European Federation of Chemical Engineering, Société de Chimie Industrielle, Paris, France, September 1986.
44. Fowler, T. J., and Gray, E., 1979, "Development of an Acoustic Emission Test for FRP Equipment", Preprint 3593, Annual Convention, Boston, MA, American Society of Civil Engineers, New York, April 1979.
 45. Fowler, T.J., 1979, "Acoustic Emission of Fiber Reinforced Plastics," Journal of the Technical Councils of the American Society of Civil Engineers, proceedings of the American Society of Civil Engineers, Vol. 105, No. TC2, New York, December 1979, pp. 281-289.
 46. Fowler, T.J., 1999, "Inspecting FRP Composite Structures with Nondestructive Testing," Project Agreement Between the Texas Department of Transportation and the University of Texas at Austin, Center for Transportation Research and Texas A&M University, Texas Transportation Institute, Project 0-1892, Center of Transportation Research, The University of Texas at Austin.
 47. Fowler, T.J., 1999, Class Note for CE 397N Structural Plastics Design, The University of Texas at Austin, Summer.
 48. Fowler, T.J., Blessing, J.A., and Conlisk, P.J., 1989, "New Directions in Testing," Third International Symposium on Acoustic Emission from Composite Materials AECM-3, Paris, France, July 17-21, pp. 16-27.
 49. Fowler, T.J., Blessing, J.A., and Conlisk, P.J., 1989, "New Directions in Testing," Third International Symposium on Acoustic Emission from Composite Materials AECM-3, Paris, France, July 17-21, pp.16-27.
 50. Fowler, T.J., et al., 1989, "The MONPAC System," Journal of Acoustic Emission, Vol. 8, No. 3.
 51. Gere, J.M., and Timoshenko, S.P., 1984, Mechanics of Materials, Third Edition, PWS-KENT Publishing, Boston, Massachusetts.

52. Gorman, M.R., and Foral, R.F., 1986, "Acoustic Emission Studies of Fiber/Resin Double Cantilever Beam Specimens," Second International Symposium on Acoustic Emission from Reinforced Composites, The Society of the Plastics Industry, Inc., Reinforced Plastics/Composites Institute, Montreal, Canada, July 21-25, pp.104-109.
53. Gorman, M.R., and Rytting, T.H., 1983, "Long Duration AE Events in Filament Wound Graphite/Epoxy in the 100-300 KHz Band Pass Region," First International Symposium on Acoustic Emission from Reinforced Composites, The Society of the Plastics Industry, Inc., July 19-21, Session 6, pp.1-5.
54. Grabec, I., and Sachse, W., 1988, "Application of an intelligent Signal Processing System to Acoustic Emission Analysis," Progress in Acoustic Emission IV, The Japanese Society for Non-destructive Inspection.
55. Grabec, I., Sachse, W., 1997, Synergetics of Measurement, Prediction and Control, Springer-Verlag Berlin Heidelberg, Germany.
56. Grabec, I., Sachse, W., and Govekar, E., 1991, "Solving AE Problems by a Neural Network," Acoustic Emission: Current Practice and Future Directions, ASTM STP 1077, W. Sachse, J. Roget and K. Yamaguchi, Eds. American Society for Testing and Materials, Philadelphia.
57. Guild, F.J., et. al., 1983, "Amplitude Distribution Analysis of Acoustic Emission from Composites: The development of a Data Collection and Procession System," First International Symposium on Acoustic Emission from Reinforced Composites, The Society of the Plastics Industry, Inc., July 19-21, Session 5, pp.1-7.
58. Guild, F.J., Phillips, M.G., and Harris, B., 1983, "Acoustic Emission from Composites: The Influenced of Reinforcement Pattern," First International

- Symposium on Acoustic Emission from Reinforced Composites, The Society of the Plastics Industry, Inc., July 19-21, Session 3, pp.1-9.
59. Guild, F.J., Phillips, M.G., and Harris, B., 1985, "Amplitude of Distribution Analysis of Acoustic Emission from Composites: A New Method of Data Presentation," *Journal of Materials Science Letter*, Vol. 4, No. 11, pp. 1375-1378.
60. Halmshaw, R., 1991, Non-Destructive Testing, Second Edition, Edward Arnold, London.
61. Hamstad, M.A., 1983, "Results Obtained During Acoustic Emission Monitoring of Proof Testing of a Large Kevlar/Epoxy Rocket Motor Case," First International Symposium on Acoustic Emission from Reinforced Composites, The Society of the Plastics Industry, Inc., July 19-21, Session 4, pp.1-13.
62. Harper, C.A., 1996, Handbook of Plastics, Elastomers, and Composites, Third Edition, McGraw-Hill.
63. Harvey, D. W., 2001, "Acoustic Emission in an Aerospace Composite", Thesis presented for degree of Master of Science in Engineering, The University of Texas at Austin.
64. Hill, E.v.K., Israel, P.L., and Knotts, G.L., 1993, "Neural Network Prediction of Aluminum-Lithium Weld Strengths from Acoustic Emission Amplitude Data," *Materials Evaluation*, Vol.51, No.9, September 1993, pp.1040-1045.
65. Hill, E.v.K., Walker II, J.L., and Rowel, G.H., 1995, "Burst Pressure Prediction in Graphite/Epoxy Pressure Vessels Using Neural Networks and Acoustic Emission Amplitude Data," *Material Evaluation*, Vol. 54, No. 6, March 1995, pp.744-748.

66. Kwon, O., and Yoon, D.J., 1989, "Energy Distribution Analysis of Acoustic Emission Signals from the Tensile Testing of CFRP," Third International Symposium on Acoustic Emission from Composite Materials AECM-3, Paris, France, July 17-21, pp.298-303.
67. Li, L. and Zhao, J.H., 1986, "The Monitoring Damage Growth Processes in Glass Fiber Reinforced Composite by Amplitude Analyses," Second International Symposium on Acoustic Emission from Reinforced Composites, The Society of the Plastics Industry, Inc., Reinforced Plastics/Composites Institute, Montreal, Canada, July 21-25. pp.90-95.
68. Masson, J.J., and Valentin, D., 1989, "Proof Testing of Unidirectional GFRP Using Acoustic Emission Technique," Third International Symposium on Acoustic Emission from Composite Materials AECM-3, Paris, France, July 17-21, pp. 200-206.
69. McGowan, P.T., 1983, "Analysis of Failure Mechanisms in Glass Fiber Reinforced Plastic and Acoustic Emission Correlation with a Transverse Resin Crack Model," First International Symposium on Acoustic Emission from Reinforced Composites, The Society of the Plastics Industry, Inc., July 19-21, Session 3, pp.1-12.
70. Mehrotra, K., Mohan, C.K., and Ranka, S., 1997, Elements of Artificial Neural Networks, MIT Press, Cambridge, Massachusetts.
71. Meilke, W., et al., 1989, "Analysis of AE-Events from Single Fibre Pull-Out Experiments," Third International Symposium on Acoustic Emission from Composite Materials AECM-3, Paris, France, July 17-21, pp.323-331.
72. Meisel, W.S., 1972, Computer-Oriented Approaches to Pattern Recognition, Academic Press, New York, New York.

73. Merienne, M.C., and Favre, J.P., 1989, "Identification of the Acoustic Signals Generated by the Rupture of SIC Fibre/Metallic Matrix Composites," Third International Symposium on Acoustic Emission from Composite Materials AECM-3, Paris, France, July 17-21, pp.304-312.
74. Miikkulainen, 1999. Neural Networks Notes: Class Notes for CS 342 Neural Networks, The University of Texas at Austin, Fall.
75. MONPAC-PLUS, 1992, "MONPAC-PLUS Procedure for Acoustic Emission Testing of Metal Tanks/Vessels," Monsanto Company, St. Louis, Missouri, Draft D, August.
76. NeuralWare, 2000, "Using NeuralWorks: A Tutorial for NeuralWorks Professional II/PLUS," NeuralWare, Carnegie, PA.
77. Niese, J., and Ahluwalia, H., 2001, "A Practical Guide to Field Inspection of FRP Equipment and Piping," MTI Project 129-99, Materials Technology Institute of the Chemical Process Industries, Inc., St. Louis, Missouri.
78. Physical Acoustic Corporation, 1995, "Design and Fabrication of a Prototype Portable Acoustic Emission Monitoring System," A proposal Submitted to U.S. Department of Transportation Federal Highway Administration, Princeton, NJ, May 1995.
79. Pickering F.H., 1983, "Design of High Pressure Fiberglass Downhole Tubing: A Proposed New ASTM Specification," First International Symposium on Acoustic Emission from Reinforced Composites, The Society of the Plastics Industry, Inc., July 19-21, Session 4, pp.1-11.
80. Pollock, A.A., 1978, "Physical Interpretation of AE/MA Signal Processions," Second Conference on Acoustic Emission/Microseismic Activity in Geologic Structures and Materials, Pennsylvania State University, November 13-15.

81. Pollock, A.A., 1978, "Physical Interpretation of AE/MA Signal Processing," Proceedings Second Conference on AE/Microseismic Activity in Geologic Structures and Materials, Pennsylvania State University, November 13-15. pp. 399-421.
82. Pollock, A.A., 1981, "Acoustic Emission Amplitude Distributions," International Advances in Nondestructive Testing, Vol. 7, pp.215-239.
83. Promboon, Y., 2000, "Acoustic Emission Source Location", Dissertation presented for degree of Doctor of Philosophy, The University of Texas at Austin.
84. Prosser, W.H., Jackson, K.E., Kellas, S., Smith, B.T., McKeon, J., and Friedman, A., 1995, "Advanced, Waveform Based AE Detection of Matrix Cracking in Composites," Materials Evaluation, Vol. 53, No. 9, September, pp. 1052-1058.
85. Roman, I., et al., 1986, "Mechanical Behavior and Acoustic Emission Characterization of Kevlar-Epoxy Composites Loaded in Tension," Second International Symposium on Acoustic Emission from Reinforced Composites, The Society of the Plastics Industry, Inc., Reinforced Plastics/Composites Institute, Montreal, Canada, July 21-25. pp.85-89.
86. Rosen, W.B., 1964, "Tensile Failure of Fibrous Composites," AIAA Aerospace Sciences Meeting, New York, January 20-22, pp.1985-1991.
87. Rotem, A., and Eliezer, A., 1979, "Fracture Modes and Acoustic Emission of Composite Materials," Journal of Testing and Evaluation, JTEVA, Vol. 7, No. 1, January, pp. 33-40.
88. Sakakibara, S., et al., 1984, "Evaluation of Structural Integrity of Piping Components for Fast Breeder Reactor by Acoustic Emission Signals," Progress in Acoustic Emission II, Proceeding of The 7th International Acoustic Emission Symposium, Zao, Japan, October 23-26, pp. 278-284.

89. Sato, N., and Kurauchi, T., 1997, "Interpretation of Acoustic Emission Signal from Composite Materials and its Application to Design of Automotive Composite Components," *Research in Nondestructive Evaluation*, Vol. 9, pp. 119-136.
90. Scarpellini, R.S., Swanson, T.L., and Fowler, T.J., 1983, "Acoustic Emission Signatures of RP Defects," *First International Symposium on Acoustic Emission from Reinforced Composites*, The Society of the Plastics Industry, Inc., July 19-21, Session 3, pp.1-6.
91. Shiwa, M., et. al., 1986, "Acoustic Emission during Tensile, Loading-Holding, and Unloading-Reloading Testing in Fiberglass-Epoxy Composites," *Second International Symposium on Acoustic Emission from Reinforced Composites*, The Society of the Plastics Industry, Inc., Reinforced Plastics/Composites Institute, Montreal, Canada, July 21-25. pp.44-49.
92. Specht, D.F., 1990, "Probabilistic Neural Networks," *Neural Networks*, Vol. 3, pp. 109-118.
93. Strongwell Corporation, Extren Design Manual, Strongwell Corporation, Bristol, Virginia.
94. Surrel, Y., and Vautrin, A., 1989, "Acoustic Emission Amplitude Analysis by Logarithmic Rate Cartography," *Third International Symposium on Acoustic Emission from Composite Materials AECM-3*, Paris, France, July 17-21, pp.365-374.
95. Suzuki, H., et al., 2000, "Integrity Evaluation of Glass-Fiber Composites with Varied Fiber/Matrix Interfacial Strength Using AE," *NDT&E International*, Vol. 33, pp. 173-180.

96. Tinkey, B. V., 2000, "Nondestructive testing of Prestressed Bridge Girders with Distributed Damage," Thesis Presented for Degree of Master of Science in Engineering, The University of Texas at Austin.
97. Tinkey, B. V., 2000, "Nondestructive testing of Prestressed Bridge Girders with Distributed Damage," Thesis Presented for Degree of Master of Science in Engineering, The University of Texas at Austin.
98. Trade Association for the Pulp and Paper Industry, " Guidelines for Inspecting Used FRP Equipment," Technical Information Paper - TIP 0402-28, Atlanta, GA.
99. TxDOT, 2002, "Fabrication Specification for FRP Beams," Rev. 2, Texas Department of Transportation, Corpus Christi District, pp.1-9.
100. Ulloa, F.V., Fowler, T.J., and Ativitavas, N., 2002, "Use of the Rail Shear Test to Measure In-Plane Shear Properties of Composite Lamina and Laminates," ASME Code-Section X, Document, November 2002.
101. Valentin, D., 1985, "A Critical Analysis of Amplitude Histograms Obtained During Acoustic Emission Tests on Unidirectional Composites with an Epoxy and a PSP Matrix," Composites, vol. 16, No.3, July 1985, pp.225-230.
102. Valentin, D., and Bunsell, A.R., 1983, "Acoustic Emission and Damage Accumulation in Carbon Fibre Epoxy Composites," First International Symposium on Acoustic Emission from Reinforced Composites, The Society of the Plastics Industry, Inc., July 19-21, Session 2, pp.1-7.
103. Valentin, D., Bonniau, Ph., and Bunsell, A.R., 1983, "Failure Mechanism Discrimination in Carbon Fibre-Reinforced Epoxy Composites," Composites, Vol. 14, No. 4, October 1983, pp. 345-351.
104. Valentin, D., Ponsot, B., and Bunsell, A.R., 1984, "Qualitative and Quantitative Evaluation of Damage in CFRP by Acoustic Emission During

- Structural Loading,” Polymer NDE, Proceedings of European Workshop on Non-Destructive Evaluation of Polymers and Polymer Matrix Composites, Termar Do Vimeiro, Portugal, September 4-5, 1984, pp.146-160.
105. Wagner, J., et al., 1992, “Interpretation of Optically Detected Acoustic Emission Signals,” Forth International Symposium on Acoustic Emission from Composite Materials AECM-4, Seattle, WA, July 27-31, pp.282-291.
106. Walker, J.L., Hill, E.v.K., 1992, “Amplitude Distribution Modeling and Ultimate Strength Prediction of ASTM D-3039 Graphite/Epoxy Tensile Specimens,” Forth International Symposium on Acoustic Emission from Composite Materials AECM-4, Seattle, WA, July 27-31, pp.115-131.
107. Whalley, G.S., Cole, P.T., 1983, “Development of Acoustic Emission Techniques for Quantitative Use on Aerospace C.F.R.P. Structures,” First International Symposium on Acoustic Emission from Reinforced Composites, The Society of the Plastics Industry, Inc., July 19-21, Session 4, pp.1-7.
108. Yamaguchi, K., et al., 1984, “Advanced Acoustic Emission Monitoring System by Distributed Processing of Waveform Microdata,” Progress in Acoustic Emission II, Proceeding of The 7th International Acoustic Emission Symposium, Zao, Japan, October 23-26, pp. 366-373.
109. Yamaguchi, K., et al., 1984, “Generation Characteristics of Acoustic Emission from Fatigue Crack in FBR Piping Component at Room Temperature,” Progress in Acoustic Emission II, Proceeding of The 7th International Acoustic Emission Symposium, Zao, Japan, October 23-26, pp. 262-269.
110. Ziehl, P.H., 1998, “Use of Acoustic Emission to Determine Damage Initiation of Fiber Reinforced Polymers,” The sixth International

Symposium on Acoustic Emission from Composite Materials AECM-6, American Society for Nondestructive Testing, Inc., San Antonio, Texas, June 1-4.

111.Ziehl, P.H., 2000, "Development of A Damage Based Design Criterion for Fiber Reinforced Vessels," Dissertation presented for degree of Doctor of Philosophy, The University of Texas at Austin.

112.Zweben, C., 1968, "Tensile Failure of Fiber Composites," AIAA 6th Aerospace Sciences Meeting, New York, January 22-24, pp.2325-2331.

VITA

Nat Ativitavas was born in Bangkok, Thailand on October 23, 1974, the son of Payungyuth Ativitavas and Naree Ativitavas. After completing his work at Samsen Wittayalai School, Bangkok, in March 1991, he entered Chulalongkorn University in Bangkok, Thailand. He received the degree of Bachelor of Science in Civil Engineering in July 1995. During a following year, he worked as a civil engineer at Petroleum Authority of Thailand (PTT) where he was awarded a scholarship to earn a Master's degree. In September 1996, he entered the graduate school of The University of Texas at Austin and worked on a research project under the supervision of Professor David W. Fowler. He received the degree of Master of Science in Engineering in August 1998. After that, he began to pursue the Doctoral Degree under the supervision of Professor Timothy J. Fowler. He plans to work at PTT after he graduates.

Permanent Address: 213 Soi Suwandee 3
Rimklongprapa Road Bangsue
Bangkok 10800 Thailand

This dissertation was typed by the author.